Development, characterization and miniaturization of a trace gas detection system for NO_2 in air based on photoacoustic spectroscopy

Dissertation

zur Erlangung des Doktorgrades der Naturwissenschaften
(Dr. rer. nat.)
der Fakultät für Chemie und Pharmazie
der Universität Regensburg

vorgelegt von
Thomas Rück
aus Günzburg
im Jahr 2017

Die vorgelegte Dissertation entstand in der Zeit von September 2012 bis Juni 2017 in Kooperation des Instituts für Analytische Chemie, Chemo- und Biosensorik der naturwissenschaftlichen Fakultät IV- Chemie und Pharmazie - der Universität Regensburg (UR)

und

des Sensorik-Applikationszentrums (SappZ) der Ostbayerischen Technischen Hochschule (OTH) Regensburg.

Die Arbeit wurde angeleitet von: Prof. Dr. habil. Frank-Michael Matysik
Prof. Dr. rer. nat. Rudolf Bierl

Das Promotionsgesuch wurde eingereicht am: 28.06.2017
Termin des Kolloquiums: 14.08.2017

Vorsitz des Prüfungsausschusses übernimmt Prof. Dr. habil. Achim Göpferich. Erstgutachter ist Prof. Dr. habil. Frank-Michael Matysik, Zweitgutachter Prof. Dr. rer. nat. Rudolf Bierl und Drittprüfer ist Prof. Dr. habil. Alkwin Slenczka.

Ich möchte mich an dieser Stelle bei allen bedanken,
die mich auf dem Wege der Promotion unterstützt und begleitet haben.

I want to thank everyone
involved in supporting and accompanying me on my way toward my doctorate.

"Der Schall erklingt und der Äther schwingt,
wenn der Leuchtturm blinkt"
(Claus Lüer)

Contents

Person

Full name	Thomas Rück
E-Mail	thomas.rueck@oth-regensburg.de
Date and place of birth	3rd June 1981 in Günzburg

Education

09/2012–07/2017	Doctorate at the University of Regensburg Faculty of Chemistry and Pharmacy, Institute of Analytical Chemistry, Chemosensors and Biosensors
04/2009–03/2010	Diploma studies in cooperation of the University of Regensburg, Faculty of Chemistry and Pharmacy, Institute of Physical and Theoretical Chemistry with Continental Automotive AG

Positions and Employment

01/2014	Company foundation, SEMSTec UG (limited liability)
since 04/2010	Research associate at the Ostbayerische Technische Hochschule (OTH) Regensburg and coordination of two consortium projects
04/2008–02/2009	Scientific assistent at the University of Regensburg Institute of Physical and Theoretical Chemistry Research focus interferometry
10/2007–03/2008	Scientific assistent at the University of Regensburg Institute of Physical and Theoretical Chemistry Research focus spectroscopy
01/2007–09/2007	Scientific assistent at the University of Regensburg Institute of Physical and Theoretical Chemistry Research focus thermodynamics

Co-authored publications

Oliver Zech, Stefan Thomaier, Pierre Bauduin, Thomas Rück, Didier Touraud and Werner Kunz. Microemulsions with an ionic liquid surfactant and room temperature ionic liquids as polar pseudo-phase. *Journal of Physical Chemistry B*, 113(2):465-473, 2009

Martin Hofmann, Rudolf Bierl, and Thomas Rück. Implementation of a dual-phase lock-in amplifier on a TMS320C5515 digital signal processor. In *EDERC 2012 - Proceedings of the 5th European DSP in Education and Research Conference*, pages 20-24, 2012

Oral presentations

"Micromechanical designed sensor applications",
Thomas Rück
Presented at the *AVL List GmbH Research Networking Day* in February 2014 (Graz, Austria)

Poster presentations

"Development of a miniaturized photoacoustic multigas sensing system for trace gas measurement",
T. Rück, F. Landgraf, J. Unger, T. Hero, M. Hofmann, R. Bierl
Presented at the *17th International Conference on Photoacoustic and Photothermal Phenomena (ICPPP17)* in October 2013 (Suzhou, China)

"Development of a miniaturized photoacoustic multigas sensing system for trace gas measurement",
T. Rück, F. Landgraf, J. Unger, M. Hofmann, F.-M. Matysik, R. Bierl
Presented at the *Analytica Conference 2014* in April 2014 (Munich, Germany)

"Comparison of acoustic detectors for use in miniaturized photoacoustic devices designed for nitrogen dioxide trace gas measurement",
T. Rück, F.-M. Matysik, R. Bierl
Presented at the *ANAKON Conference 2015* in March 2015 (Graz, Austria)

"Specification of an improved photoacoustic setup for high-sensitive, low-cost NO_2 trace gas detection",
T. Rück, F. Landgraf, I. Läpple, J. Unger, F.-M. Matysik, R. Bierl
Presented at the *18^{th} International Conference on Photoacoustic and Photothermal Phenomena (ICPPP18)* in September 2015 (Novi Sad, Serbia)

The authors' original publications

Parts that were adapted from the authors' publications form the basis of chapter "Results and Discussion". The adapted text parts are indicated by [P1]–[P3]. This section lists the abstracts of the original publications.

[P1]

Development and characterization of a laboratory setup for photoacoustic NO_2 determination based on the excitation of electronic $^2B_2$ and $^2B_1$ states using a low cost semiconductor laser

Thomas Rück, Rudolf Bierl, Frank-Michael Matysik

in *Sensors and Actuators A* 258 (**2017**) 193–200

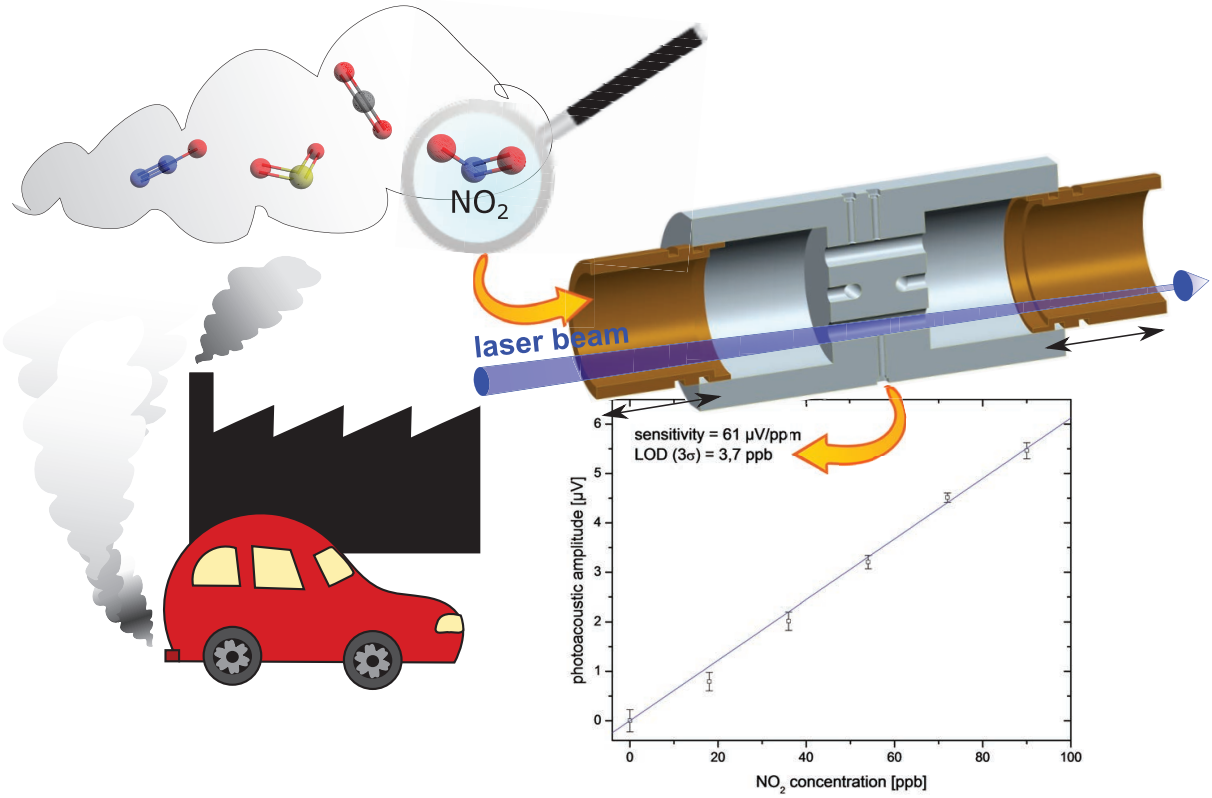

Abstract

This work gives a detailed characterization of a laboratory setup for photoacoustic NO_2 trace gas detection at the ppbV level. The signal generation

For the contents of this publications refer to chapter 4.1 on page 150

is based on the excitation of electronic $^2B_2$ and $^2B_1$ states using a low-cost semiconductor laser emitting at 450 nm. An acoustic resonator was used for signal amplification and the modulation frequency of the laser was determined to 3395 Hz in order to gain maximum signal amplification. The quality of resonant amplification was determined to 7.9. The gas samples were NO_2 calibration gases diluted with pure nitrogen. The signal-to-noise ratio (SNR) dependency on the flow rate Q and the lock-in time constant τ_{LIA} was investigated, respectively, and the optimum values were specified to $Q = 500$ mL/min and $\tau_{\mathrm{LIA}} = 2$ s. In case of ambient noise, increasing τ_{LIA} to 10 s was evaluated as sufficient for SNR preservation. The noise level was measured in the absence of NO_2 and it was determined to be composed of 51 % electronic noise and 49 % gas flow noise. With the analyte concentration ranging from 300 ppbV to 100 ppmV, the linear dependency of the photoacoustic amplitude on the NO_2 concentration was specified, the sensitivity was determined to 110 µV/ppmV and the maximum measurement error was calculated to ± 0.8 %. The detection limit was determined to 2.0 ppbV. Furthermore, the stability of the signal was investigated and a maximum drift of ± 1 % was observed within a measuring period of 30 min. The response time τ_{90} was specified to 58 s. All results considered, this photoacoustic measuring system, which is based on low-cost signal generation and detection units, provides an excellent basis in view of developing a portable device for photoacoustic trace gas detection.

[P2]
Low-cost photoacoustic NO_2 trace gas monitoring at the pptV-level

Thomas Rück, Rudolf Bierl, Frank-Michael Matysik

submitted to *Sensors and Actuators A* in March **2017**

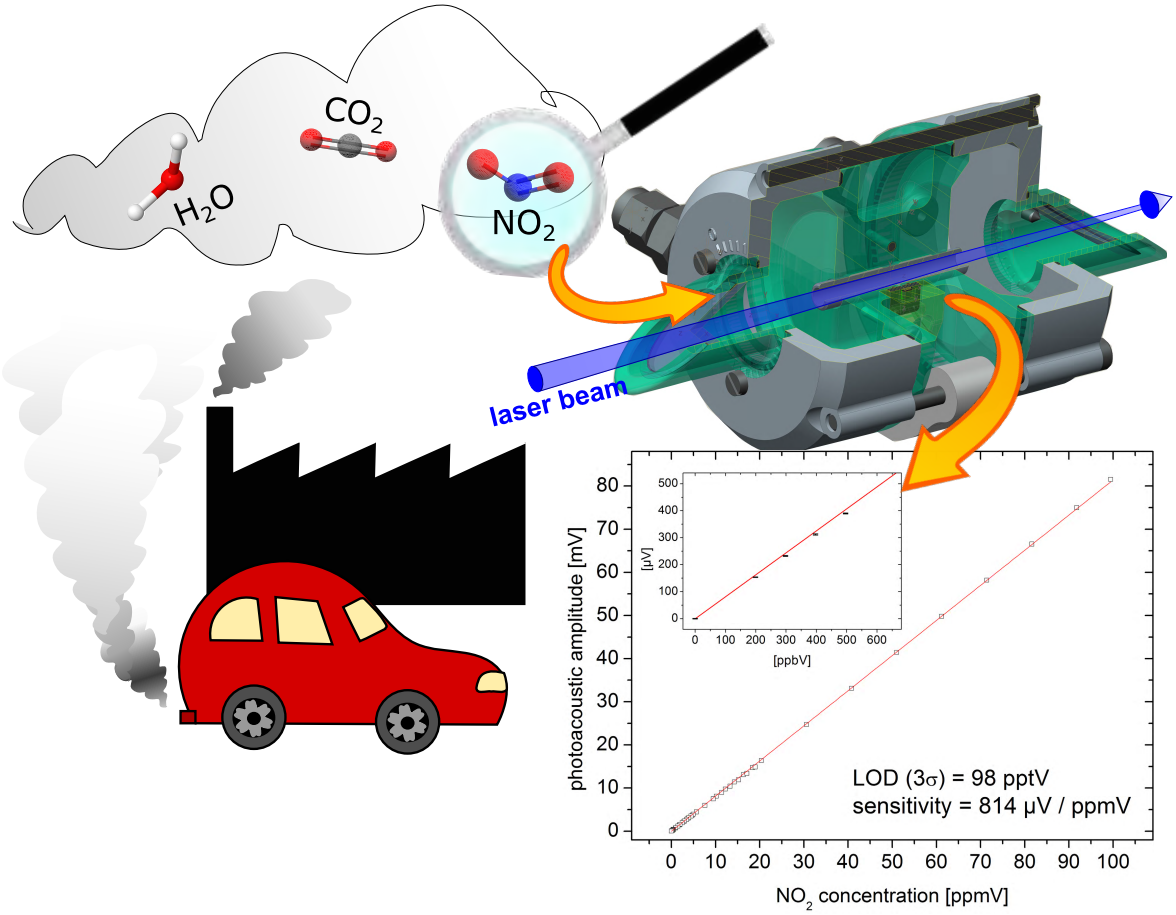

Abstract

We present the development and the characterization of a photoacoustic NO_2 trace gas detection system. The system is based on the implementation of low-cost components, i.e. a mass-produced blue diode laser and a standard MEMS microphone which is commonly built into smartphones, for example. An optimized cell design was realized by means of 3D printing. The linearity of the photoacoustic signal dependency on the analyte concentration was verified from 200 ppbV to 100 ppmV NO_2. The detection limit (1σ) was determined to 33 pptV and the normalized noise equivalent

For the contents of this publications refer to chapter 4.2 on page 168

absorption coefficient was calculated to $7.0 \cdot 10^{-10}$ W cm^{-1} Hz$^{-1/2}$. The dynamic range of the system was verified to be linear over three magnitudes of order and the sensitivity was calculated to 814 µV/ppmV. The system was characterized in view of optimal operating parameters, i.e. lock-in time constant τ_{LIA} and total mass flow rate, optical performance and signal stability. The mass flow depended response time of the system was specified to 19 s and an idealized step response to a quasi-Heaviside step function was quantified as a function of τ_{LIA}. The quality factor of acoustic resonance was determined to 21.9 and an empirical expression regarding acoustic node shifting is provided. The expression takes into account the radius of the resonator pipe and the radius of the hole, which was drilled into the pipe for microphone coupling. Furthermore, we studied the cross-sensitivity of the photoacoustic signal towards H_2O and CO_2, respectively.

[P3]

NO_2 trace gas monitoring in air using off-beam quartz enhanced photoacoustic spectroscopy (QEPAS) and interference studies towards CO_2, H_2O and acoustic noise

Thomas Rück, Rudolf Bierl, Frank-Michael Matysik

submitted to *Sensors and Actuators B* in April **2017**

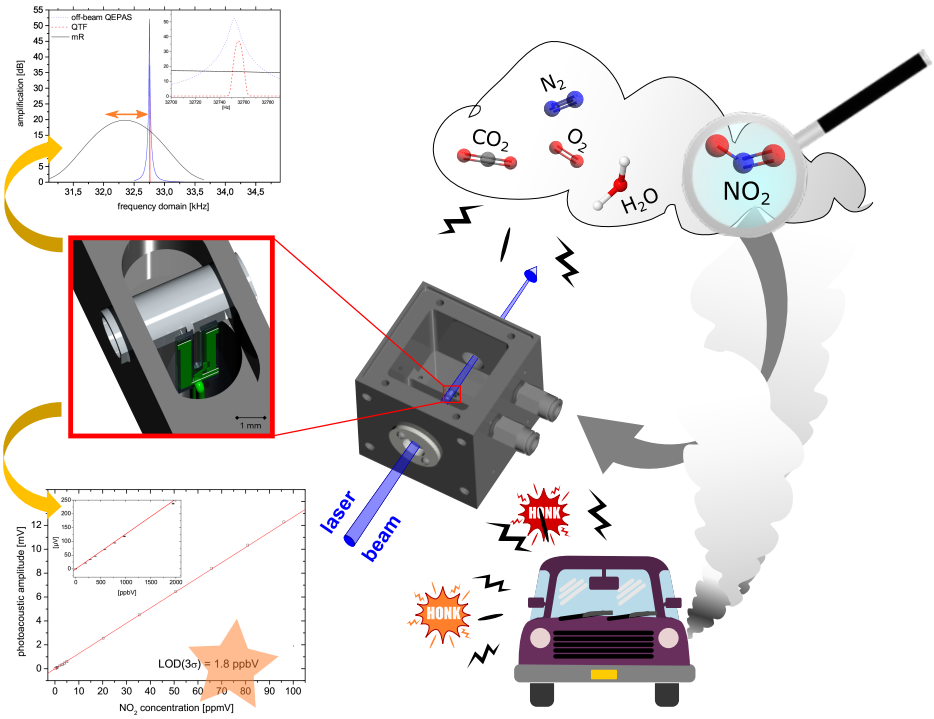

Abstract

We present the development and characterization as well as comprehensive interference studies of a photoacoustic NO_2 trace gas detection system. The system is based on an off-beam quartz enhanced photoacoustic scheme (off-beam QEPAS) and signal generation was initiated by amplitude modulating a low-cost diode laser emitting at 450 nm. The QEPAS sensor element features double-resonant amplification, still it is only about 5 x 5 x 2.5 mm in size. The individual and combined resonance characteristics were investigated and specified to 52 dB amplification, adding up 15 dB acoustic- and 37 dB mechanical-resonance amplification. The linearity of the pho-

For the contents of this publications refer to chapter 4.3 on page 190

toacoustic signal dependency on the analyte concentration was verified from 200 ppbV to 100 ppmV NO_2 in synthetic air and the detection limit (3σ) was determined to 1.8 ppbV. The stability of the signal was investigated over time and a slight drift by 1 ‰ was observed after 30 minutes without temperature stabilizing the photoacoustic cell (PAC). Noise analysis was performed by means of Allan deviation and the inverse dependency of response time and precision of the system on the lock-in time constant was outlined. We performed interference analyses towards N_2, O_2, CO_2, H_2O and acoustic noise, respectively. Although neither spectral interferences nor losses due to slow NO_2 VT-relaxation were observed, O_2 was identified to cause a 15 % signal drop due to $VV_{NO2\text{-}O2}$–relaxation. Changing H_2O concentrations were found to cause acoustic detuning, which cannot be compensated by adjusting the frequency of modulation, because of the double-resonant feature of the PAC. However, alternative approaches of compensation were discussed. Finally, we carried out heavy traffic noise simulations and determined the QEPAS setup to be 46 times less susceptible towards ambient noise compared to standard microphone-based photoacoustic setups.

Declaration of collaboration

Most of the theoretical and experimental scientific work that is presented within this thesis was done independently by the author. In some cases, however, the practical implementation of concepts and the performance of measurements was carried out in collaboration with other researchers and individuals. In any case, assistance was guided and supervised by the author. In accordance with § 7 Abs. 3 Satz 3 of *Ordnung zum Erwerb des akademischen Grades eines Doktors der Naturwissenschaften (Dr. rer. nat.) an der Universität Regensburg vom 18. Juni 2009 (Änderungssatzung vom 6. Februar 2014)*, this section gives a detailed declaration of those collaborations.

Gas stream
(section 3.1.1, p.135)
The concept of the gas mixing unit was created solely by the author. The implementation was mainly done by the student assistant Andreas Zagler.

Neutral density filter array
(section 3.2.2, p.145)
A neutral density filter array was designed in order to attenuate OPO laser radiation in order to facilitate optical alignment. All calculations and simulations were performed by the author. The transfer from concept to design drawing was assisted by Ignaz Läpple.

Photoacoustic cell design (2$^{\text{nd}}$ generation cell)
(section 4.2.2, p.170)
The concept and dimensioning of the 2$^{\text{nd}}$ generation photoacoustic cell (PAC) was conceived by the author. The transfer from concept studies to design drawing was done in collaboration with Ignaz Läpple.

Photoacoustic cell design (3$^{\text{rd}}$ generation cell)
(section 4.3.2, p.193)
In view of the 3$^{\text{rd}}$ generation cell design various simulations were performed by the author. The results of simulation form the basis for PAC devel-

opment, which was done by Martin Hofmann in the course of his master studies.

Miniaturized sensor element μPAS
(section 4.4, p.215)
The concept design of the micromechanical sensor element μPAS was developed by the author. The process-technological implementation and the appropriate clean room production steps were mainly realized by Johannes Unger and in parts by Ferdinand Landgraf during their master studies.
A functional housing was developed for adjusting a laser source and a microphone, as well as for applying the sensor element to the test-gas flow. The concept of this housing was designed in collaboration with Ignaz Läpple.
The measurements were carried out with the assistance of Markus Bodensteiner during his Bachelor studies.

Portable NO_2 measuring device
(section 4.5, p.226)
A portable trace gas monitoring device for NO_2 was developed. The demands on the application as well as the overall concept was specified in collaboration with Simon Gassner during his bachelor studies. Various development steps were mainly carried out by Mr. Gassner in close collaboration and after consultation with the author.
In terms of signal processing, a lock-in amplification algorithm was implemented on a field programmable gate array (FPGA) by Stefan Weigl in the course of his master studies. Further development, improvement and measurements were carried out in collaboration with Peter Gaida during his master studies.

Funding
Within the scope of the German governments' 6^{th} Energy-Research-Program, the Federal Ministry of Economics and Technology (BMWi) has provided essential financial support for this work. The funding codes of the grant projects are 03ET1137A and 03ET1317A.

List of abbreviations

µPAS	miniaturized photoacoustic sensor chip
3D	three-dimensional
AC	alternating current
ADC	analog to digital converter
AM	amplitude modulation
AM-PA	amplitude modulated photoacoustics
AS	absorption spectroscopy
ASCII	American standard code for information interchange
BPI	base peak intensity
CEAS	cavity-enhanced absorption spectroscopy
CEPAS	cantilever enhanced photoacoustic spectroscopy
CLD	chemiluminescence detector
CPU	central processing unit
CRDS	cavity ring down spectroscopy
cw	continuous wave
DA	direct absorption
DAS	direct absorption spectroscopy
dB	decibel
DC	direct current
DGA	dissolved gas analysis
DL	diode laser
DSP	digital signal processing, double side polished
E-MOCAM	electrical modulation cancellation method
e.g.	*exempli gratia* (for example)
EU	European Union
EWMA	exponentially weighted moving average
FERS	fiber-enhanced Raman spectroscopy

FG ..... frequency generator
FM ..... frequency modulation
FPGA ..... field programmable gate array
FWHM .... full width at half maximum
GC ..... gas chromatograph
GPIB ..... general purpose interface bus
high-Q .... high quality
HITRAN .. high-resolution transmission molecular absorption
HWHM ... half width at half maximum
i.e. ..... *id est* (that is)
ICL ..... interband cascade laser
IR ..... infrared
LAS ..... laser absorption spectroscopy
LED ..... laser emitting diode
LIA ..... lock-in amplifier
LOD ..... limit of detection
low-Q ..... low quality
LWIR ..... long wavelength infrared
MA ..... moving average
MEMS .... microelectromechanical system
MFC ..... mass flow controller
MIC ..... microphone
MOCAM .. modulation cancellation method
MOS ..... metal oxide semiconductor
mR ..... micro resonator
MS ..... mass spectrometer
ND ..... neutral density
Nd:YAG ... neodymium-doped yttrium aluminum garnet; Nd:$Y_3Al_5O_{12}$
NDFA ..... neutral density filter array
NDIR ..... non-dispersive infrared
NIR ..... near infrared
NL ..... normalized level
NNEA ..... normalized noise equivalent absorbance
OA-ICOS .. off-axis integrated cavity output spectroscopy

OPO ..... optical parametric oscillator
PA ..... photoacoustic
PAC ..... photoacoustic cell
PAS ..... photoacoustic spectroscopy
PC ..... personal computer
PECVD ... plasma enhance chemical vapor deposition
PM ..... power meter
ppbV ..... parts per billion by volume
ppmV ..... parts per million by volume
pptV ..... parts per trillion by volume
PSR ..... phase sensitive rectifier
PTR-MS .. proton transfer reaction mass spectrometry
QCL ..... quantum cascade laser
QEPAS .... quartz enhanced photoacoustic spectroscopy
QTF ..... quartz tuning fork
RAM ..... residual amplitude modulation
rh ..... relative humidity
RIE ..... reactive ion etching
RT ..... retention time
SIFT-MS .. selected-ion flow-tube mass spectrometer
SIM ..... selected ion mode
SL ..... sample loop
SNR ..... signal-to-noise-ratio
SOI ..... silicon on insulator
SPL ..... sound pressure level
SPR ..... surface plasmon resonance spectroscopy
SSP ..... single side polished
TCP/IP ... transmission control protocol / Internet protocol
TDL ..... tunable diode laser
TDLS ..... tunable diode laser spectroscopy
TIA ..... transimpedance amplifier
TIC ..... total ion current
UI ..... user interface
USB ..... universal serial bus

UV ..... ultraviolet
Vis ..... visible
VOC ..... volatile organic compound
VT ..... vibrational-translational
VV ..... vibrational-vibrational
WM ..... wavelength modulation
WMAS .... wavelength modulation absorption spectroscopy
z. B. ..... zum Beispiel

Introduction

Human beings by nature possess an efficient sense for trace gas detection, namely olfaction. Among many other benefits this sense of smell serves as an early warning system for hazardous substances. Nevertheless, there is also a variety of volatile contaminants, which cannot be perceived at all or not until a concentration, that might already be harmful. Detecting these substances in the context of health and safety surveillance is one potential application area for trace gas monitoring [1]. Apart from that, trace gas sensing is of great interest regarding numerous other fields of application as well. These include indoor air quality monitoring (e.g. CO_2, VOCs) [2], atmospheric chemical science (e.g. O_3, NO_x, fine particulate air pollution) [3], industrial production plants (e.g. propene, H_2O_2) [4], medical and clinical diagnostics (e.g. acetone in human breath as marker for diabetes) [5], natural gas quality monitoring (e.g. hydrocarbons) [6], gas certification, animal facilities (e.g. NH_3, CO_2) [7] and early fire detection (e.g. NH_3, HCN, C_2H_2) [8], to name but a few. In search of the most suitable measuring technique, several factors generally have to be considered. Essential factors are ambient conditions, e.g. temperature and pressure, the composition of the sample and, in particular, the target range of analyte concentration. Concerning the concentration range, the term "trace gas" usually encompasses analyte volume ratios of ~ 100 ppmV (*parts per million*, 10^{-6}) down to a few pptV (*parts per trillion*, 10^{-12}).
Some well-known techniques, which are capable of monitoring concentrations that small, are solid-state metal oxide semiconductor (MOS) based sensors [9], cavity ring down spectroscopy (CRDS) [10], cavity-enhanced absorption spectroscopy (CEAS) [11, 12], selected-ion flow-tube mass spectrometry (SIFT-MS) [5, 13], laser absorption spectroscopy (LAS) [14], surface plasmon resonance spectroscopy (SPR) [15], interferometry [16, 17], fiber-enhanced Raman spectroscopy (FERS) [18], chemiluminescence detectors (CLD) [19] and photoacoustic spectroscopy (PAS) [8, 20–22], respectively. Except for MOS and SIFT-MS, all of these are optical methods. The most crucial advantage of optical based techniques is their potential of highly sensitive trace gas detection, while at the same time featuring low cross sensitivities to other species. Hodgkinson and Tatam [23] provided a comprehensive review, where the most common optical techniques were

compared with respect to their suitability for trace gas sensing. Concluding their literature research, they classified optical methods regarding their normalized noise equivalent absorbance (NNEA) and the required optical path. As a result, they specified photoacoustic spectroscopy, wavelength modulation absorption spectroscopy and off-axis integrated cavity output spectroscopy (OA-ICOS), which is a special CEAS technique, to ensure minimum detectable concentrations (NNEA $\sim 10^{-7}$ $\mathrm{Hz}^{-0.5}$). While common WMAS applications are based on path lengths of $\sim$ 100 cm to $\sim$ 100 m, OA-ICOS configurations even require optical pathways of $\sim$ 100 m up to $\sim$ 10 km. By comparison, the dimensions of common measuring cells for PAS are only $\sim$ 2 to 10 cm. Actually, the optical path length is no limiting factor regarding photoacoustic applications, as the photoacoustic signal correlates with the length-to-volume ratio of a tube shaped cell, i.e. the reciprocal cross section, rather than with the length of the tube itself. Therefore, plenty of PAS applications have already been reported to afford single-digit ppbV- [24–28] or even pptV-detection [29, 30], while utilizing tube lengths $<$ 1 cm. Since the intention of this work was not only to realize a laboratory trace gas detection system for research purposes, but also to pave the way for highly integrated miniaturized sensor development, photoacoustic spectroscopy turned out to be the method of choice.

Although in the medium term a multi-component monitoring device is to be developed, the fundamentals of the photoacoustic technique as well as the influence of the photoacoustic cell (PAC) design was studied on the basis of a primary target species, namely nitrogen dioxide (NO_2). This gas was selected as the analyte for two reasons. On the one hand it features electronic excitation by using visible light sources, thus facilitating optical alignment and minimizing cross sensitivities, on the other hand recent events have lent new significance to NO_2 trace gas sensing. In particular the Volkswagen emission scandal, which was made public when Thiruvengadam et al. [31] presented their research results about real-life NO_2 emissions of diesel vehicles by the end of 2015, led to current relevance and public awareness. Photoacoustic NO_2 detection based on electronic excitation has already been demonstrated to feature astonishing detection limits (1σ) of 200 pptV [32], 50 pptV [33] and 54 pptV [34] by utilizing cell designs of 9 to 10 cm in

length. Even when applying miniaturized quartz enhanced photoacoustic spectroscopy (QEPAS), detection limits of 1.3 ppbV [26] and 18 ppbV [24] have been reported so far. This thesis further presents two world records, i.e. a detection limit of 33 pptV using a low-cost 3D printed PAC with 4 cm in length as well as a minimum detectable concentration of 600 pptV utilizing a QEPAS setup. Besides QEPAS based miniaturization, this work also demonstrates a further step towards developing a downscaled and highly integrated sensor chip for photoacoustic NO_2 trace gas detection.

References

[1] M. Stefanidou, S. Athanaselis and C. Spiliopoulou, Health Impacts of Fire Smoke Inhalation, *Inhalation Toxicology*, 20(8):761–766 (2008), ISSN 0895-8378, doi:10.1080/08958370801975311, URL `http://www.tandfonline.com/doi/full/10.1080/08958370801975311`.

[2] S.-O. Baek, Y.-S. Kim and R. Perry, Indoor air quality in homes, offices and restaurants in Korean urban areas-indoor/outdoor relationships, *Atmospheric Environment*, 31(4):529–544 (1997), ISSN 1352-2310, doi:http://dx.doi.org/10.1016/S1352-2310(96)00215-4, URL `http://www.sciencedirect.com/science/article/pii/S1352231096002154`.

[3] S. Sillman, O3-NOx -VOC sensitivity and NOx-VOC indicators in Paris: Results from models and Atmospheric Pollution Over the Paris Area (ESQUIF) measurements, *Journal of Geophysical Research*, 108(D17):8563 (2003), ISSN 0148-0227, doi:10.1029/2002JD001561, URL `http://doi.wiley.com/10.1029/2002JD001561`.

[4] Demonstrationsprojekt zur Evaluierung der Mikroreaktionstechnik in industriellen Systemen (DEMiS) (Schlussbericht), Technical report, Technische Universität Chemnitz (2005), doi:10.2314/GBV:514961546, URL `https://www.tib.eu/suchen/id/TIBKAT:514961546/`.

[5] P. Španěl, K. Dryahina and D. Smith, A general method for the calculation of absolute trace gas concentrations in air and breath from selected ion flow tube mass spectrometry data, *International Journal of Mass Spectrometry*, 249-250:230–239 (2006), ISSN 13873806, doi:10.1016/j.ijms.2005.12.024.

[6] A. Varga, Z. Bozóki, M. Szakáll and G. Szabó, Photoacoustic system for on-line process monitoring of hydrogen sulfide (H2S) concentration in natural gas streams, *Applied Physics B: Lasers and Optics*, 85(2-3):315–321 (2006), ISSN 09462171, doi:10.1007/s00340-006-2388-6.

[7] T. G. Ooms, J. E. Artwohl, L. M. Conroy, T. M. Schoonover and J. D. Fortman, Concentration and emission of airborne contaminants in a laboratory animal facility housing rabbits, *Journal of the American Association for Laboratory Animal Science*, 47(2):39–48 (2008), ISSN 1559-6109.

[8] A. A. Kosterev, F. K. Tittel and G. Bearman, Advanced Quartz-Enhanced Photoacoustic Trace Gas Sensor for Early Fire Detection, *SAE Int. J. Aerosp.*, 1:331–336 (2008), doi: 10.4271/2008-01-2091, URL http://doi.org/10.4271/2008-01-2091.

[9] C. Christofides and A. Mandelis, Solid-state sensors for trace hydrogen gas detection, *Journal of Applied Physics*, 68(6) (1990), ISSN 00218979, doi:10.1063/1.346398.

[10] R. T. Jongma, M. G. H. Boogaarts, I. Holleman and G. Meijer, Trace gas detection with cavity ring down spectroscopy, *Review of Scientific Instruments*, 66(4):2821–2828 (1995), ISSN 00346748, doi:10.1063/1.1145562.

[11] J. M. Langridge, S. M. Ball, A. J. L. Shillings and R. L. Jones, A broadband absorption spectrometer using light emitting diodes for ultrasensitive, in situ trace gas detection, *Review of Scientific Instruments*, 79(12) (2008), ISSN 00346748, doi:10.1063/1.3046282.

[12] R. Peeters, G. Berden, A. Apituley and G. Meijer, Open-path trace gas detection of ammonia based on cavity-enhanced absorption spectroscopy, *Applied Physics B*, 71(2):231–236 (2000), ISSN 0946-2171, doi:10.1007/s003400000302, URL http://dx.doi.org/10.1007/s003400000322.

[13] D. Smith and P. Spanel, The novel selected-ion flow tube approach to trace gas analysis of air and breath, *Rapid Communications in Mass Spectrometry*, 10(10):1183–1198 (1996), ISSN 09514198, doi:10.1002/(SICI)1097-0231(19960731)10:10⟨1183::AID-RCM641⟩3.0.CO;2-3.

[14] M. R. McCurdy, Y. Bakhirkin, G. Wysocki, R. Lewicki and F. K. Tittel, Recent advances of laser-spectroscopy-based techniques for applications in breath analysis, *Journal of Breath Research*, 1(1):014001 (2007), ISSN 1752-7155, doi:10.1088/1752-7155/1/1/014001, URL http://stacks.iop.org/1752-7163/1/i=1/a=014001?key=crossref.82b41ff4727096647a9d0b285dace327.

[15] M. J. Jory, P. S. Vukusic and J. R. Sambles, Development of a prototype gas sensor using surface plasmon resonance on gratings, *Sens. Actuators, B*, 17(3):203–209 (1994), ISSN 0925-4005, doi:10.1016/0925-4005(93)00871-U, URL http://www.sciencedirect.com/science/article/pii/092540059300871U.

[16] G. Bentini, M. Bianconi, A. Cerutti, M. Chiarini, G. Pennestri, C. Sada, N. Argiolas, M. Bazzan and P. Mazzoldi, Integrated Mach-Zehnder micro-interferometer on LiNbO3, *Optics and Lasers in Engineering*, 45(3):368–372 (2007), ISSN 01438166, doi:10.1016/j.optlaseng.2005.05.006, URL http://linkinghub.elsevier.com/retrieve/pii/S0143816606000728.

[17] X. Liu, H. Wu, Y. Liu, L. Dong, W. Ma, L. Zhang, W. Yin and S. Jia, All-optical Trace Gas Detection Method by use of Fiber Mach-Zehnder Interferometer with a Tuning Fork, in *Light, Energy and the Environment 2015*, page JTu5A.36 (Optical Society of America, 2015), doi:10.1364/PV.2015.JTu5A.36, URL http://www.osapublishing.org/abstract.cfm?URI=PV-2015-JTu5A.36.

[18] S. Hanf, R. Keiner, D. Yan, J. Popp and T. Frosch, Fiber-Enhanced Raman Multigas Spectroscopy: A Versatile Tool for Environmental Gas Sensing and Breath Analysis, *Analytical Chemistry*, 86(11):5278–5285 (2014), doi:10.1021/ac404162w, URL `http://dx.doi.org/10.1021/ac404162w`.

[19] Z. Zhang, S. Zhang and X. Zhang, Recent developments and applications of chemiluminescence sensors, *Analytica Chimica Acta*, 541(1-2):37–47 (2005), ISSN 00032670, doi:10.1016/j.aca.2004.11.069.

[20] A. Elia, P. M. Lugarà, C. di Franco and V. Spagnolo, Photoacoustic techniques for trace gas sensing based on semiconductor laser sources, *Sensors*, 9(12):9616–9628 (2009), ISSN 14248220, doi:10.3390/s91209616.

[21] A. Miklós, P. Hess and Z. Bozóki, Application of acoustic resonators in photoacoustic trace gas analysis and metrology, *Review of Scientific Instruments*, 72(4):1937–1955 (2001), ISSN 00346748, doi:10.1063/1.1353198.

[22] M. W. Sigrist, Trace gas monitoring by laser photoacoustic spectroscopy and related techniques (plenary), *Review of Scientific Instruments*, 74(1 II):486–490 (2003), ISSN 00346748, doi:10.1063/1.1512697.

[23] J. Hodgkinson and R. P. Tatam, Optical gas sensing: a review, *Measurement Science and Technology*, 24(1):012004 (2013), ISSN 0957-0233, doi:10.1088/0957-0233/24/1/012004.

[24] H. Yi, K. Liu, W. Chen, T. Tan, L. Wang and X. Gao, Application of a broadband blue laser diode to trace NO2 detection using off-beam quartz-enhanced photoacoustic spectroscopy., *Optics letters*, 36(4):481–483 (2011), ISSN 0146-9592, doi:10.1364/OL.36.000481.

[25] L. Dong, V. Spagnolo, R. Lewicki and F. K. Tittel, Ppb-level detection of nitric oxide using an external cavity quantum cascade laser based QEPAS sensor, *Optics Express*, 19(24):24037 (2011), ISSN 1094-4087, doi:10.1364/OE.19.024037.

[26] H. Zheng, L. Dong, X. Yin, X. Liu, H. Wu, L. Zhang, W. Ma, W. Yin and S. Jia, Ppb-level QEPAS NO2 sensor by use of electrical modulation cancellation method with a high power blue LED, *Sensors and Actuators, B: Chemical*, 208(2):173–179 (2015), ISSN 09254005, doi:10.1016/j.snb.2014.11.015, URL `http://dx.doi.org/10.1016/j.snb.2014.11.015`.

[27] L. Dong, R. Lewicki, K. Liu, P. R. Buerki, M. J. Weida and F. K. Tittel, Ultra-sensitive carbon monoxide detection by using EC-QCL based quartz-enhanced photoacoustic spectroscopy, *Applied Physics B: Lasers and Optics*, 107(2):275–283 (2012), ISSN 09462171, doi:10.1007/s00340-012-4949-1.

[28] A. A. Kosterev, Y. A. Bakhirkin and F. K. Tittel, Ultrasensitive gas detection by quartz-enhanced photoacoustic spectroscopy in the fundamental molecular absorption bands region, *Applied Physics B*, 80(1):133–138 (2005), ISSN 0946-2171, doi:10.1007/s00340-004-1619-y.

[29] V. Spagnolo, P. Patimisco, S. Borri, G. Scamarcio, B. E. Bernacki and J. Kriesel, Part-per-trillion level detection of SF6 using a single-mode fiber-coupled quantum cascade laser

and a quartz enhanced photoacoustic sensor (2013), doi:10.1117/12.2001638, URL http://dx.doi.org/10.1117/12.2001638.

[30] Y. Ma, R. Lewicki, M. Razeghi and F. K. Tittel, QEPAS based ppb-level detection of CO and N2O using a high power CW DFB-QCL., *Optics express*, 21(1):1008–19 (2013), ISSN 1094-4087, doi:10.1364/OE.21.001008, URL http://www.ncbi.nlm.nih.gov/pubmed/23388995.

[31] A. Thiruvengadam, M. C. Besch, P. Thiruvengadam, S. Pradhan, D. Carder, H. Kappanna, M. Gautam, A. Oshinuga, H. Hogo and M. Miyasato, Emission rates of regulated pollutants from current technology heavy-duty diesel and natural gas goods movement vehicles, *Environmental Science and Technology*, 49(8):5236–5244 (2015), ISSN 15205851, doi:10.1021/acs.est.5b00943.

[32] J. Kalkman and H. W. Van Kesteren, Relaxation effects and high sensitivity photoacoustic detection of NO2 with a blue laser diode, *Applied Physics B: Lasers and Optics*, 90(2):197–200 (2008), ISSN 09462171, doi:10.1007/s00340-007-2895-0.

[33] J. Peltola, T. Hieta and M. Vainio, Parts-per-trillion-level detection of nitrogen dioxide by cantilever-enhanced photo-acoustic spectroscopy, *Opt Lett*, 40(13):2933–2936 (2015), ISSN 0146-9592, doi:10.1364/OL.40.002933, URL http://www.ncbi.nlm.nih.gov/pubmed/26125335.

[34] X. Yin, L. Dong, H. Wu, H. Zheng, W. Ma, L. Zhang, W. Yin, S. Jia and F. K. Tittel, Sub-ppb nitrogen dioxide detection with a large linear dynamic range by use of a differential photoacoustic cell and a 3.5 W blue multimode diode laser, *Sensors and Actuators B: Chemical*, 247:329–335 (2017), ISSN 09254005, doi:10.1016/j.snb.2017.03.058, URL http://linkinghub.elsevier.com/retrieve/pii/S0925400517304756.

Chapter 1

Theory

1.1 Absorption Spectroscopy (AS)

Several phenomena are known, where light interacts with matter in a way that energy gets transferred. In view of quantifying gaseous analytes, three of these inelastic effects may be considered, namely Raman* scattering [1], absorption processes [2, 3] and fluorescence processes [4]. However, absorption phenomena were discovered first and are still most used with regard to trace gas analysis, as they generally offer major cross-sections [5].

1.1.1 Beer – Lambert Law

Since the establishment of quantum mechanics as one of the most important theories in modern physics, molecules are known to adopt defined energetic states. This quantization of energy levels constitutes the characteristic absorption spectra of molecules. Whether exciting ro-vibronic states, i.e. interaction of rotational, vibrational and electronic degrees of freedom, or ro-vibrational states, i.e. interactions between rotational and vibrational degrees of freedom, molecules absorb only those amounts of electromagnetic energy that equal the change in molecular state $\bar{\nu}_{01}$.

$$\bar{\nu}_{\mathrm{ph}} = \frac{\nu_{\mathrm{ph}}}{\mathrm{c}_0} = \bar{\nu}_{01} = \bar{\nu}_1 - \bar{\nu}_0 \tag{1.1}$$

In equation 1.1, c_0 is the speed of light in vacuum, $\bar{\nu}_{\mathrm{ph}}$ and ν_{ph} is the wavenumber and the frequency of radiation, respectively. The strength of absorption, i.e. the absorbance $a(\bar{\nu})$, can be obtained by illuminating an absorbing sample and monitoring the intensity used for illumination $I_0(\bar{\nu})$ as well as the transmitted intensity $I(\bar{\nu})$.

$$\frac{I(\bar{\nu})}{I_0(\bar{\nu})} = e^{-a(\bar{\nu})} \tag{1.2}$$

Equation 1.2 is named the Beer† – Lambert‡ Law and it constitutes the basis of absorption processes.

*Chandrasekhara Venkata Raman (1888-1970)
†August Beer (1825-1863)
‡Johann Heinrich Lambert (1728-1777)

By knowing the optical path length of illumination ΔL_{op}, the absorption coefficient $\alpha(\bar{\nu})$ can be calculated via

$$a(\bar{\nu}) = \alpha(\bar{\nu}) \cdot \Delta L_{\mathrm{op}} \tag{1.3}$$

The absorption coefficient [cm^{-1}] is defined as the volume number density ρ_i of absorbing molecules multiplied by their absorption cross-section $\sigma(\bar{\nu})$ [cm^2] at a given wavelength.

$$\alpha(\bar{\nu}) = \rho_i \cdot \sigma(\bar{\nu}) \tag{1.4}$$

The volume number density can be written as

$$\rho_i = N_i \cdot \frac{\mathrm{N_A}}{V_{\mathrm{mol}}} \tag{1.5}$$

where N_i is the volume ratio of absorbing molecules, $\mathrm{N_A}$ is the Avogadro constant and V_{mol} is the molar volume of the sample. In terms of trace gas analysis, the volume ratio of absorbing molecules is typically indicated by pptV, ppbV or ppmV, i.e. parts per trillion (10^{-12}), billion (10^{-9}) and million (10^{-6}), respectively.

1.1.2 Line width broadening

However, in reality absorption spectra of molecules do not show explicit absorption lines corresponding to molecular transitions. Instead, they exhibit absorption profiles with finite line width broadening. Integrating the absorption cross-section over such a symmetrically broadened profile gives the line strength S_{01}.

$$S_{01} = \int_0^\infty \sigma(\bar{\nu}) \mathrm{d}\bar{\nu} \tag{1.6}$$

The line strength specifies the spectral line intensity for a single molecule, per unit volume. S_{01} depends on temperature and pressure and its dimensions are $\left[\frac{\mathrm{cm}^{-1}}{\mathrm{molecule \cdot cm}^{-2}}\right]$, which can be simplified to [cm]. By knowing the

line-shape function of broadening $f_{\mathrm{LS}}(\bar{\nu}_{01}, \bar{\nu}, T, p_0)$, the cross-section at the absorption peak can thus be calculated to

$$\sigma(\bar{\nu}_{01}) = S_{01} \cdot f_{\mathrm{LS}}(\bar{\nu} - \bar{\nu}_{01}) \tag{1.7}$$

The phenomenon of broadening is reducible to three different effects, namely natural broadening, Doppler broadening and collision broadening.

Natural broadening results from the intrinsic lifetime of excited states, which is subject to a considerable uncertainty. According to the energy-time uncertainty relation that was firstly reported by Heisenberg*, the lifetime of an excited state τ_{e} is probabilistically limited, as excited molecular states decay due to spontaneous emission after a certain period of time.

$$\tau_{\mathrm{e}} \Delta E \geq \hbar \tag{1.8}$$

$$\Delta\bar{\nu}_{\mathrm{nat}} \geq (2\pi\tau_{\mathrm{e}} \mathrm{c}_0)^{-1} \tag{1.9}$$

Therein, ΔE is the energy of molecular transition, $\hbar$ is the reduced Planck† constant ($\hbar = \frac{\mathrm{h}}{2\pi}$) and $\Delta\bar{\nu}_{\mathrm{nat}}$ is the natural broadening width. Quantum physics provide a correlation of lifetime τ_{e} and energy of transition, where Einstein‡ coefficients are used in order to quantify transition probabilities [6]. As a result, natural broadening width can also be written as

$$\Delta\bar{\nu}_{\mathrm{nat}} \geq \frac{32\pi^3 \bar{\nu}_{01}^3}{6\varepsilon_0 \mathrm{h} \mathrm{c}_0^3} |\mu|^2 \tag{1.10}$$

where ε_0 is the vacuum permittivity and μ is the transition dipole moment. Considering equations 1.9 and 1.10, natural line width broadening is proportional to τ_e^{-1} and $\bar{\nu}_{01}^3$, respectively. Typical frequency values of natural broadening are $\sim$ 30 MHz in terms of vibronic excitation and $\sim$ 10 kHz in terms of vibrational excitation [7].

*Werner Karl Heisenberg (1901-1976)
†Max Karl Ernst Ludwig Planck (1858-1957)
‡Albert Einstein (1879-1955)

Doppler broadening results from the movement of molecules relative to the direction of photon propagation whilst excitation. Once molecules exhibit positive velocity components in the direction of photon propagation (movement towards the detector) the transition energy gets blue-shifted, while negative components lead to a red-shift. Molecules within a gaseous sample show Brownian* motion, where the velocities are governed by a Maxwell†–Boltzmann‡ distribution. According to that, the most probable velocity $v_{\mathrm{p},i}$ of absorbing analyte molecules is

$$v_{\mathrm{p},i} = \sqrt{\frac{2\mathrm{R}T}{M_i}} \tag{1.11}$$

where R is the gas constant, T is the thermodynamic temperature and M_i is the molar mass of the analyte. Doppler broadening width $\Delta\bar{\nu}_{\mathrm{dop}}$ then is given by [6]

$$\Delta\bar{\nu}_{\mathrm{dop}} = \frac{\bar{\nu}_{01}}{\mathrm{c}_0}\sqrt{\frac{2\mathrm{R}T\ln 2}{M_i}} \tag{1.12}$$

Typical values of Doppler broadening are ~ 200 MHz for near infrared (NIR) transitions and ~ 30 MHz for long wavelength infrared (LWIR, $\lambda \sim 10$ µm) transitions [7].

Collision broadening results from molecular motion as well. More precisely, broadening occurs when collisions of analyte molecules take place with any other kind of molecule during the process of absorption. Collisions of molecules mean a continuous change in distance of collision partners, while converging results in continuous redistribution of kinetic and potential energy. A further discussion of molecular collisions in the context of sound propagation is given in chapter 1.4.1. The degree of line width broadening due to collisions directly relates to the collision rate, i.e. the re-

*Robert Brown (1773-1858)
†James Clerk Maxwell (1831-1879)
‡Ludwig Boltzmann (1844-1906)

ciprocal quantity of the collision-free average time τ_{ii} of an analyte molecule [8],

$$\tau_{ii}^{-1} = \rho_i v_{\mathrm{m},ii} \sigma_{ii} \tag{1.13}$$

where $v_{\mathrm{m},ii}$ is the relative mean velocity of two molecules of species i whilst collision and σ_{ii} is the collision cross-section of the colliding particles. The volume number density ρ_{i} is specified in 1.5. Assuming ideal gas behavior, the molar volume is

$$V_{\mathrm{mol}} = \frac{\mathrm{R}T}{p_0} \tag{1.14}$$

where p_0 is the pressure of the sample. The relative mean velocity of molecules is given by

$$v_{\mathrm{m},ii} = \frac{2\sqrt{2}}{\sqrt{\pi}} \cdot v_{\mathrm{p},i} = \sqrt{2} \cdot \sqrt{\frac{8\mathrm{R}T}{\pi M_i}} \tag{1.15}$$

and the collision cross-section can be calculated by [8]

$$\sigma_{ij} = \pi(r_i + r_j)^2 \tag{1.16}$$

where r_i and r_j are the molecular radii of the collision partners. Considering only one species of molecules, i.e. $i = j$, the cross-section thus becomes $4\pi r_i^2$. Combining equations 1.13 – 1.16, the collision rate can be written as*

$$\tau_{ii}^{-1} = \sqrt{\frac{\pi}{\mathrm{k_B} T m_i}} \cdot p_0 \cdot (4r_i)^2 \tag{1.17}$$

As broadening directly correlates with the pressure of the sample, the phenomenon is also called pressure broadening. In addition to the impact of the molecules relative mean velocity on the broadening width, it also affects the averaged potential distortion and, therefore, may also lead to a peak shift of transition energy (not only broadening). This peak shifting effect is more complex than the broadening effect, which was discussed above, because it additionally depends on the molecules distance affecting the shape of the potential energies of the ro-vibrational states. As a consequence,

*considering $N_i = 1$, i.e. pure substance i

the phenomenon may either result in positive or in negative shifting of the transition peak energy.
However, this effect is the reason why literature provides slightly differing dependencies of [6]

$$\Delta\bar{\nu}_{\text{dop}} \propto T^{-n_T} p_0 \tag{1.18}$$

with $0.5 \leq n_T \leq 0.8$, compared to the ones resulting from 1.17:

$$\Delta\bar{\nu}_{\text{dop}} \propto T^{-0.5} p_0 \tag{1.19}$$

Typical values for collision broadening at standard conditions are ~ 2 GHz.

Summing up the different effects of line width broadening regarding rovibrational transitions, natural broadening may be neglected as its contribution is about five magnitudes of order less than in terms of collision broadening. Actually, at standard conditions, collision broadening provides the largest contribution, which exceeds Doppler broadening by approximately one magnitude of order.
Consequently, the best option to counteract line width broadening, e.g. in order to increase selectivity and sensitivity of an optical sensor, is to create vacuum. Increasing temperature may also reduce line width broadening to some extent. However, as soon as Doppler broadening gains weight, further increasing temperature will have an opposite effect and thus increase broadening. Moreover, according to equation 1.12, Doppler broadening by light-weight molecules such as H_2O or CH_4 is more pronounced than in terms of NO_2 for example. Additional collision broadening results from inelastic collisions that cause depopulation of the excited state by increasing the kinetic energy of the sample. This explains the broad chaotic absorption spectrum of NO_2 centered at 400 nm, which is addressed in chapter 4.1.2.
The line-shape function of broadening is Gaussian in case of Doppler broadening and Lorentzian in case of natural and collision broadening, respec-

tively. Equations 1.20 and 1.21 give a mathematical representation of offset-free ($y_0 = 0$) Gaussian and Lorentzian peak shape functions, respectively.

$$f_{\mathrm{G}} = \frac{A \cdot \exp - \dfrac{4 \ln 2 (x - x_{\mathrm{c}})^2}{w_{\mathrm{G}}^2}}{w_{\mathrm{G}} \cdot \sqrt{\dfrac{\pi}{4 \ln 2}}} \tag{1.20}$$

$$f_{\mathrm{L}} = \frac{2A}{\pi} \cdot \frac{w_{\mathrm{L}}}{4(x - x_{\mathrm{c}})^2 + w_{\mathrm{L}}^2} \tag{1.21}$$

Therein, A is the peak area and x_{c} is the peak center, respectively. At conditions where both, Doppler and collision broadening, have to be considered, total broadening might best be approximated by the Voigt function, i.e. the convolution $f_{\mathrm{V}} = (f_{\mathrm{L}} * f_{\mathrm{G}})(x)$.* Olivero and Longbothum [9] provided an approximation of total broadening $\Delta\bar{\nu}_{\mathrm{tot}}$ on the basis of Voigt profile improvement and specified the maximal inaccuracy to ± 0.01 %:

$$\Delta\bar{\nu}_{\mathrm{tot}} = 0.5346 \Delta\bar{\nu}_{\mathrm{col}} + \sqrt{0.2166 \Delta\bar{\nu}_{\mathrm{col}}^2 + \Delta\bar{\nu}_{\mathrm{dop}}^2} \tag{1.22}$$

Finally, figure 1.1 shows the graphical representation of such Gaussian (solid black line) and Lorentzian (dashed red line) line-shape functions with same FWHM ($w_{\mathrm{G}} = w_{\mathrm{L}}$), as well as the resulting Voigt profile (dash-dotted blue line). All profiles are normalized with regard to peak area.

1.1.3 Drawbacks of the technique

Depending on the particular application, there are essentially three techniques available in order to perform trace gas analysis on the basis of absorption spectroscopy. These are UV/Vis–, NDIR (nondispersive infrared)– and TDL (tunable diode laser)–spectroscopy, respectively. While UV/Vis methods rest on the excitation of ro-vibronic states using ultraviolet or visible light, NDIR– and TDL–spectroscopy are generally based on the excitation of ro-vibrational states by means of infrared radiation. The main difference between NDIR and TDLS is the source of infrared radiation, i.e.

*At standard atmospheric conditions, collision broadening predominates and, therefore, Lorentz shape often can be assumed in good approximation.

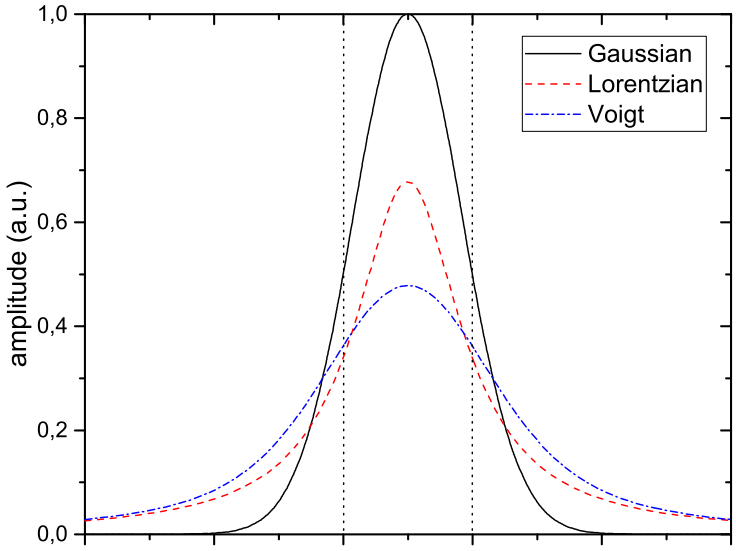

Figure 1.1: Graphical representation of Gaussian (solid black line), Lorentzian (dashed red line) and Voigt profile (dash-dotted blue line).

broadband emitters and spectral filters in terms of NDIR and monochromatic semiconductor lasers in TDLS applications. Classical arrangements of these techniques all base on direct absorption spectroscopy (DAS), which was already discussed in chapter 1.1.1. However, DAS suffers from some general drawbacks, which are discussed hereinafter.

i. DAS has to be considered an indirect method, as two quantities have to be determined, i.e. $I(\bar{\nu})$ and $I(\bar{\nu_0})$ (see equation 1.2), and the analyte concentration has to be calculated from their difference. Especially in terms of trace gas analysis, which deals with low analyte concentrations, this difference is small due to minor total absorption, whereas the measurands themselves are high. This causes significant losses in resolution, as the dynamic range of the ADC (analog-to-digital converter) has to be suited to the high intensities.

ii. The measured intensities and the analyte concentration show a non-linear, but exponential dependency.

iii. According to equation 1.3, the optical path has to be preferably long in order to achieve adequate absorbance in terms of low analyte concentrations. This limits the approach of miniaturizing the sensor element.

Typical path lengths in TDLS are 1 m up to 100 m [10], which are commonly realized by means of multipass cells, e.g. Herriott cells. Therein, the laser beam gets reflected between two mirrors several times in order to increase the effective optical path length. Mondelain et al. [11] for example described a Herriott cell with an optical path length of 5.3 m, where the distance of the mirrors was set to 140 mm.

iv. Trace gas DAS is highly sensitive to scattering effects, since losses in intensity due to scattering can not be separated from losses due to absorption.

v. The sensitivity of direct absorption tunable diode laser spectroscopy (DA-TDLS) is often limited by low frequency laser intensity noise, which is referred to as $1/f$-noise [12, 13].

vi. Infrared spectra at atmospheric conditions are known to show high peak densities and peak overlapping due to collision broadening (refer to chapter 1.1.2). Therefore, infrared DAS often suffers from cross-sensitivities, e.g. towards H_2O. In order to identify most suitable ro-vibrational transitions, chapter 2.5.1 deals with the simulation of absorption spectra with regard to different analytes in a variety of matrix compositions.

In order to circumvent some of these drawbacks, namely iv. to vi., there are a variety of modulation techniques presented in literature, where the most common one is wavelength modulation absorption spectroscopy (WMAS). In literature this technique is often abbreviated as WMS, which is not unambiguous as there exist other spectroscopic schemes that are also based on wavelength modulation. However, this work deals with the detection of NO_2 based on amplitude modulated photoacoustic spectroscopy (AM-PAS) (refer to chapter 4). Although it does not involve wavelength modulation (WM) approaches, the following section is meant to discuss the basics of this technique for two reasons:
Firstly, AM-PA detection of NO_2 in the visible range is a special case and current expansion of the technique to other analytes takes advantage of WM as well.* Apart from that, PAS techniques are often compared to

*Actually, wavelength modulation is currently implemented in our lab as well in terms of N_2O, CH_4, C_2H_6 and C_3H_8 detection, respectively.

DAS, which is not appropriate as both methods (AS and PAS) are usually based on wavelength modulation approaches. Thus the basics of WM have to be discussed for substantiated comparison of both techniques.

1.1.4 Improvement by wavelength modulation

This section aims at understanding the principles of wavelength modulation on the basis of TDLS, as well as at highlighting the advantages of the technique. Whilst ignoring the red dotted parts, figure 1.2 shows a schematic drawing of a standard DA-TDLS setup.

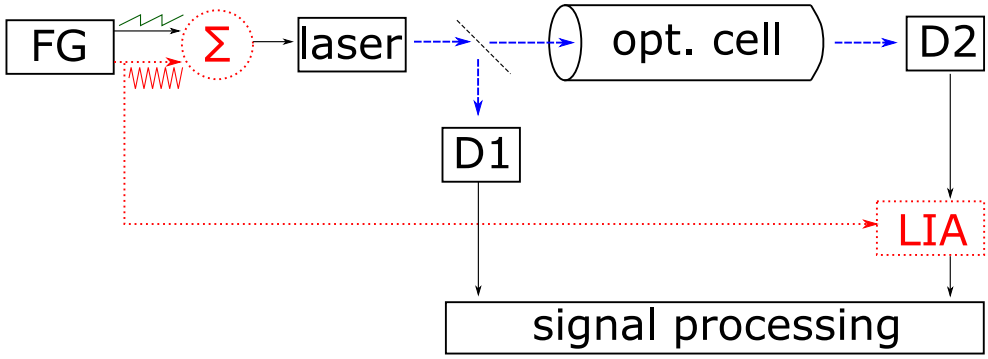

Figure 1.2: Schematic drawing of a DA-TDLS (ignoring the red dotted parts) and a WM-TDLS (taking into account all parts) setup, respectively. The laser beam is illustrated by blue dashed arrows. FG: frequency generator, D1 and D2: detectors 1 and 2, LIA: lock-in amplifier.

A function generator (FG) is used to modulate the DC injection current to the diode laser (DL) with a sawtooth signal of frequency $f_\mathrm{r} = \omega_\mathrm{r}/2\pi$. Due to the nature of diode lasers, this enables to tune the wavenumber of emission (i.e. the reciprocal wavelength) by $\Delta\bar{\nu}_\mathrm{ph}$, thus scanning an absorption peak of interest. While a minor part of radiation is reflected into a detector D1 by means of a semitransparent mirror, the majority of the laser light is used for illuminating an optical cell of length ΔL_op. Afterwards, the transmitted intensity is monitored by D2 and both signals S_1 and S_2 are amplified, converted and post-processed.
Now considering the red dotted parts in figure 1.2, wavelength modulation approaches are based on additionally modulating a sine wave to the DL

injection current. In terms of WMAS, the frequency of modulation f_{wm} usually is in the range of kHz [14], given that

$$f_{\mathrm{wm}} >> f_{\mathrm{r}} \tag{1.23}$$

and its peak-to-peak amplitude causes a modulation depth $\delta_s \bar{\nu}_{\mathrm{ph}}$, which is smaller than the width of the absorption peak $\Delta\bar{\nu}_{\mathrm{tot}}$ and the scanning range $\Delta_{\mathrm{r}}\bar{\nu}_{\mathrm{ph}}$.

$$\delta_s \bar{\nu}_{\mathrm{ph}} < \Delta\bar{\nu}_{\mathrm{tot}} < \Delta_{\mathrm{r}}\bar{\nu}_{\mathrm{ph}} \tag{1.24}$$

The modulation depth is commonly specified by the modulation index η_{mod}, which besides considers the half-width-at-half-maximum (HWHM) of the absorption feature:

$$\eta_{\mathrm{mod}} = \frac{\delta_s \bar{\nu}_{\mathrm{ph}}}{\frac{\Delta\bar{\nu}_{\mathrm{tot}}}{2}} \tag{1.25}$$

There is plenty of literature that deals with the investigation of optimum modulation indices, which were specified to $\eta_{\mathrm{mod}} = 2.2$ in terms of collision broadening [15, 16] and $\eta_{\mathrm{mod}} = 2.11$ considering Doppler broadening dominance [13], respectively.

Superimposed modulation and n*f* demodulation

Figure 1.3 visualizes the superimposed modulation that is applied in WMAS applications. It illustrates a Lorentzian-shaped molecular transition (black) that is scanned by means of sawtooth tuning (green). However, the illustration indicates a snapshot, where the current center wavelength of tuning matches the peak of absorption $\bar{\nu}_{01}$ (blue crosses). Rapid wavelength modulation of the laser around its center emission is highlighted by a red sine wave. This wavelength modulation around the absorption peak results in a symmetric signal, which is illustrated by another blue sine wave. This raw signal is characterized by a frequency that is twice the frequency of wavelength modulation f_{wm}, because the peak absorption is passed through two times during one period of sine wave. Therefore, the raw signal gets demodulated at two times f_{wm} by means of a lock-in amplifier, which basics

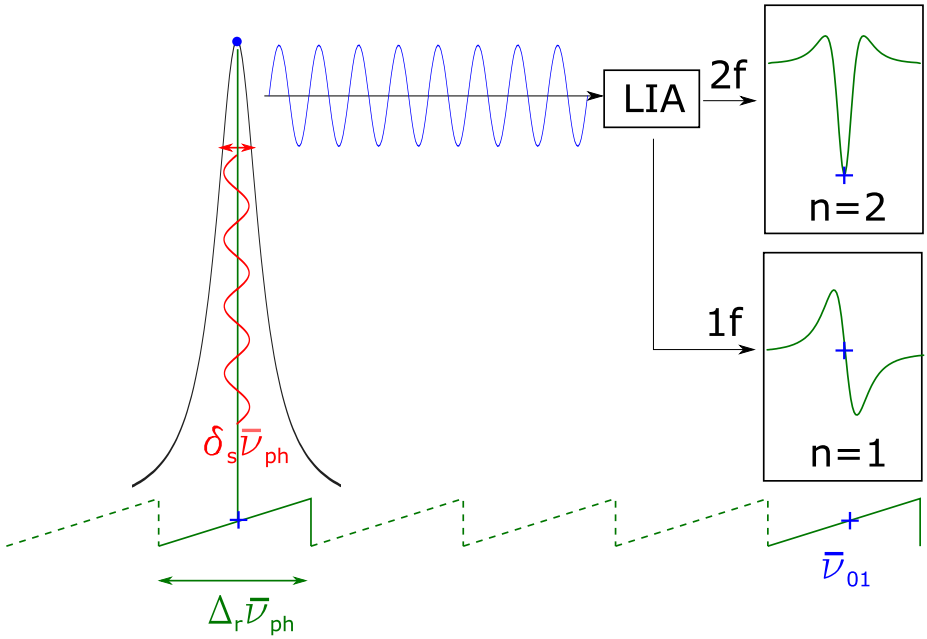

Figure 1.3: Schematic drawing of the functional principle of the wavelength modulation technique. $\delta_s\bar{\nu}_{ph}$: wavelength modulation depth (red), $\Delta_r\bar{\nu}_{ph}$: range of emission center line scanning (green), $\bar{\nu}_{01}$: current value of emission center line (blue).

are discussed in chapter 1.3.4. However, successive sawtooth detuning away from the center of the absorption feature increases the number of different frequency components within the raw signal, which in turn weakens the $2f$ signal, i.e. shown top right in figure 1.3 (n=2). Below this $2f$ signal, the drawing additionally outlines the shape of the signal after $1f$ demodulation (n=1). At the time when the center line of emission matches up with the absorption maximum, this $1f$ signal exhibits a zero point passage, where the $2f$ signal peaks (in a negative value). In case of non-distorted symmetrical absorption profiles, those demodulated signals almost exactly represent the n^{th} derivative of the absorption feature. Therefore, WMAS is often referred to as derivative spectroscopy.

However, demodulation at $2f_{wm}$ has a significant advantage compared to other multiples of the modulation frequency. Just like higher harmonics, $2f$ signals do not suffer from background drifts resulting from unwanted residual amplitude modulation (RAM). Due to the nature of diode lasers, RAM is a consequence of current modulation that was originally applied in order to perform wavelength modulation [10, 14, 17–19]. While $1f$ signals

are distorted by background drifts, $2f$ signals only undergo offset shifting due to amplitude modulation. This offset shift increases with modulation depth and has to be compensated by self referencing the $2f$ peak value to the $2f$ background beyond its foothills [10]. In fact, $2f$ signals might be distorted as well, not because of RAM per se, but for non-linearities in the response of amplitude modulation to current changes [17]. However, higher harmonics might be even less susceptible to external effects such as RAM, but they also have smaller amplitudes.

Signal normalization ($2f/1f$)

Another approach in view of signal enhancement presented in literature is referred to as $2f/1f$ normalization. Normalizing the $2f$- to the $1f$-signal brings several improvements [15]:

i. Offset compensation that originates from RAM

ii. Canceling of scattering losses

iii. Less susceptibility to mechanical vibrations and beam attenuation

iv. Less sensitivity to window fouling and beam steering

Wavelength tracking

Besides normalization reasons, most common WM-TDLS applications simultaneously utilize $1f$ or $3f$ demodulation for controlling the center wavelength of emission. As odd harmonics exhibit zero point passages at the absorption peak, they are well suited for detection and adjustment of detuning, which might result from temperature drifts for example. Although $3f$ signals offer some benefits for the purpose of wavelength control [10], most applications still rest on $1f$ wavelength tracking, as many laboratory PA systems still utilize SR810 or SR830 lock-in amplifiers from Stanford Research Systems (California, US), which are limited to a frequency of 102.4 kHz. In such case, utilizing $3f$ demodulation would mean a maximum frequency of wavelength modulation of $f_{\mathrm{wm,max}} = 34$ kHz.

Simplified mathematical description

Equations 1.26 and 1.27 give mathematical expressions for wavelength and concomitant residual amplitude modulation, respectively, while non-linearities in RAM response are neglected [19].

$$\bar{\nu}_{\mathrm{ph}}(t) = \bar{\nu}_{\mathrm{ph}} + \frac{\delta_s \bar{\nu}_{\mathrm{ph}}}{2} \cdot \cos(\omega_{\mathrm{wm}} t) \tag{1.26}$$

$$I_0(t) = I_0 + \frac{i_0}{2} \cdot \cos(\omega_{\mathrm{wm}} t + \Psi) \tag{1.27}$$

Therein, $\bar{\nu}_{\mathrm{ph}}$ is the center emission resulting from DC current I_0 and the modulation depth $\delta_s \bar{\nu}_{\mathrm{ph}}$ is adjusted by the amplitude of current modulation i_0 that in turn causes RAM. Besides, ω_{wm} is the angular frequency of wavelength modulation and Ψ is the phase shift between AM and WM, which is assumed to be zero in subsequent derivations.
With regard to mathematical description of WM signals, most sources in literature assume optical thin sample approximation, which turns the exponential dependency in equation 1.2 into a linear one [17].

$$e^{-\alpha(\bar{\nu})} \sim 1 - \alpha(\bar{\nu}) \tag{1.28}$$

However, this so-called thin-sample approximation is not restricted to wavelength modulation techniques only. Figure 1.4 verifies this approximation taking the example of NO_2 absorption at 450 nm ($\sigma = 4.3 \cdot 10^{-23}$ m^2 [20]) and an optical path length of 10 m. As a result of this calculation, the approximation was determined to cause a relative error of 0.6 % for a volume ratio of 10 ppmV NO_2 and thus the approximation is considered valid in view of trace gas concentrations. However, within some literature sources this linear dependency is considered an advantage of WMAS compared to DAS (see enumeration ii. on p.17), which is not correct, as optical thin sample approximation might be applied to DAS as well.
According to 1.26, the time and wavenumber dependent absorbance can be written as

$$a(\bar{\nu}_{\mathrm{ph}}, t) = a\left[\bar{\nu}_{\mathrm{ph}} + \frac{\delta_s \bar{\nu}_{\mathrm{ph}}}{2} \cdot \cos(\omega_{\mathrm{wm}} t)\right] \tag{1.29}$$

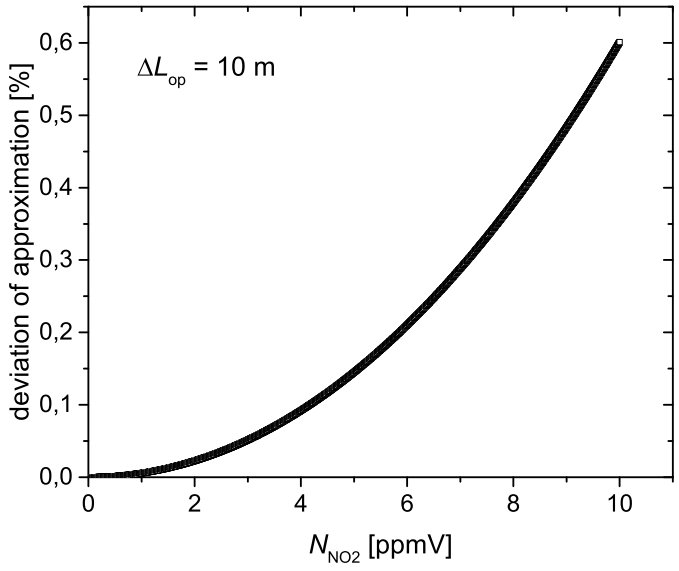

Figure 1.4: Validation of the optical thin sample approximation $\exp^{-\alpha(\bar{\nu})} \sim 1 - \alpha(\bar{\nu})$ in example of NO_2 absorption at 450 nm.

which is a periodic even function in ωt that can be expanded in a Fourier cosine series [17]:

$$-a\left[\bar{\nu}_{\mathrm{ph}} + \frac{\delta_s \bar{\nu}_{\mathrm{ph}}}{2} \cdot \cos(\omega_{\mathrm{wm}} t)\right] = \sum_{k=0}^{\infty} H_k(\bar{\nu}_{\mathrm{ph}}, \delta_s \bar{\nu}_{\mathrm{ph}}) \cos(k\omega_{\mathrm{wm}} t) \tag{1.30}$$

Combining equations 1.3, 1.4 and 1.30, the Fourier coefficients of the modulated signal can be written as [16]

$$H_k(k>0) = -\frac{\rho_{\mathrm{i}} \Delta L_{\mathrm{op}}}{\pi} \int_{-\pi}^{\pi} \sigma\left[\bar{\nu}_{\mathrm{ph}} + \frac{\delta_s \bar{\nu}_{\mathrm{ph}}}{2} \cdot \cos(\omega_{\mathrm{wm}} t)\right] \cos(k\omega_{\mathrm{wm}} t) \mathrm{d}(\omega t) \tag{1.31}$$

$$H_0 = -\frac{\rho_{\mathrm{i}} \Delta L_{\mathrm{op}}}{2\pi} \int_{-\pi}^{\pi} \sigma\left[\bar{\nu}_{\mathrm{ph}} + \frac{\delta_s \bar{\nu}_{\mathrm{ph}}}{2} \cdot \cos(\omega_{\mathrm{wm}} t)\right] \mathrm{d}(\omega t) \tag{1.32}$$

Based on these coefficients, the $2f$ signal is represented by [19]

$$S_2(\bar{\nu}_{\mathrm{ph}}) = \frac{i_0}{2} H_3(\bar{\nu}_{\mathrm{ph}}, \delta_s \bar{\nu}_{\mathrm{ph}}) + I_0 H_2(\bar{\nu}_{\mathrm{ph}}, \delta_s \bar{\nu}_{\mathrm{ph}}) + \frac{i_0}{2} H_1(\bar{\nu}_{\mathrm{ph}}, \delta_s \bar{\nu}_{\mathrm{ph}}) \tag{1.33}$$

In order to quantify the peak height, it is adequate to take into account the 2^{nd} harmonic only. Including equation 1.7, it follows

$$H_2 = -\frac{S_{01}\rho_{\text{i}}\Delta L_{\text{op}}}{\pi}\int_{-\pi}^{\pi} f_{\text{LS}}\left[\bar{\nu}_{\text{ph}} + \frac{\delta_s\bar{\nu}_{\text{ph}}}{2}\cdot\cos(\omega_{\text{wm}}t)\right]\cos(2\omega_{\text{wm}}t)\text{d}(\omega t) \quad (1.34)$$

where the peak height is only complicated by the line shape function f_{LS}, which is given by equation 1.20 and 1.21 for Doppler- and collision-broadening, respectively.

Wavelength- vs. frequency-modulation

Besides WM techniques, there is an alternative method of modulation, i.e. frequency modulation (FM). This section is only meant to briefly address the differences between both techniques, as they often get mixed up in literature. Actually, in a spectroscopic view WM and FM describe the same phenomenon, since both methods consider the frequency of light as carrier frequency. The only difference is that WM is based on adequate modulation frequencies (typically a few kHz to a few MHz) and large modulation depths, i.e. high modulation indices, whereas FM rests on modulation frequencies exceeding 100 MHz and small modulation depths [13, 18, 21, 22]. In theory, FM techniques are preferable as they show superior signal-to-noise ratios (SNR), which may even be "shot"- or quantum-noise limited only [23]. However, huge efforts have to be made in view of technical implementation, e.g. integrating electro-optical modulators, thus common trace gas applications almost exclusively base upon wavelength modulation.

Advanced literature

In order to not go beyond the scope of this thesis, details of modulation techniques are not further discussed, but only summarized and referenced:

i. Development of extended theoretical models including non-ideal behavior (e.g. non-zero laser linewidths, non-linear RAM response) [17, 24]

ii. Numerical calculation of expressions for harmonic spectra of Voigt profiles, which are based on convolution of the absorption feature with a fixed function using Chebyshev polynomials [25]

iii. WMAS using multiplexed diode lasers [19]

iv. Investigation of temperature and pressure effects as well as the influence of modulation indices [15, 16]

v. Compensation of $2f$ signal offsets by pre-processing instead of post-processing [19]

vi. Discussion of different sideband schemes of frequency modulation [13]

vii. Noise limitation of FM applications due to the emergence of optical fringes [10, 12, 23, 26]

Advantages of WMAS

Referring to drawbacks of direct absorption spectroscopy that were already discussed on p.16, WMAS methods offer three main advantages, which are [15]

- ✓ lower susceptibility to light scattering,
- ✓ enhanced SNR due to noise suppression by lock-in amplification and
- ✓ less spectral cross-sensitivity.

Some literature sources additionally claim the advantage of being a direct method in contrast to DAS. However, this conclusion is a fallacy. While it is correct, that the $2f$ signal is small after demodulation (which improves the resolution of DA conversion), the detector itself still has to be capable of dealing with small variations of high intensities.
However, WM based techniques rely on the availability of light sources that can be modulated in wavelength. Therefore, concluding chapter 1.1, table 1.1 provides an overview of a variety of light sources and their intrinsic potential to be used in wavelength modulation based applications.
Despite the rapidly growing availability of semiconductor lasers covering ever-increasing spectral ranges, still many applications cannot be realized on the basis of WM for a lack of suitable sources or due to major technical effort required for implementation. For this reason, absorption based applications still often rely on direct absorption spectroscopy.

Table 1.1: List of a variety of light sources and their intrinsic potential to be used in wavelength modulation based applications. FP: Fabry-Pérot laser, LED: light emitting diode, cw-QCL: continuous wave quantum cascade laser, DFB-DL: distributed feedback diode laser, ICL: interband cascade laser, OPO: optical parametric oscillator, SG-DBR: sampled-grating distributed Bragg reflector laser, EC-QCL: external cavity quantum cascade laser, VCSEL: vertical cavity surface emitting laser.

Light source	thermal emitter[a]	III-V FP[b]	LED	cw-QCL	DFB-DL[c]	ICL	lead-salt
WM applicable	–	✓ [27]	–	✓ [28]	✓ [29]	✓ [30]	✓ [31]

Light source	OPO	dye laser	gas laser[e]	SG-DBR	EC-QCL	VCSEL	III-V DFB[f]
WM applicable	(–) [d]	–	–	✓ [32]	✓ [33]	✓ [34]	✓ [31]

[a] i.e. broadband emitter
[b] antimonide-based
[c] InGaAsP-based
[d] Lindsay et al. [22] realized OPO wavelength tuning by implementing an additional DBRL
[e] e.g. He-Ne or CO_2
[f] InP based diode laser for telecommunication

However, the presented work bases on the measuring principle of photoacoustic spectroscopy (PAS), which fundamentals are discussed in the following chapter 1.2. Even in those cases, where WM is not applicable, photoacoustic spectroscopy offers all advantages of WMAS despite of less spectral cross-sensitivity.* Moreover,

- ✓ PAS can be considered a direct method,
- ✓ its measurand, i.e. the amplitude of acoustic pressure, is directly proportional to the analyte concentration and
- ✓ it offers the option of miniaturization, as its sensitivity does not correlate with the optical path length (refer to equation 1.3).

*Actually, WM based PAS obviously offers this advantage too.

References

[1] C. V. Raman, A new radiation, *Indian Journal of Physics*, 2:387–398 (1928), ISSN 03700089, doi:10.1007/BF03052651.

[2] P. Bouguer, Essai d'optique sur la gradation de la lumière, Technical report (1729).

[3] J. H. Lambert, *Photometria sive De mensura et gradibus luminis, colorum et umbrae* (Sumptibus viduae Eberhardi Klett, typis Christophori Petri Detleffsen, 1760).

[4] G. G. Stokes, On the Change of Refrangibility of Light, *Philosophical Transactions of the Royal Society of London*, 143(January):463–562 (1852), ISSN 0261-0523, doi:10.1098/rstl.1853.0016, URL `http://rstl.royalsocietypublishing.org/content/142/463.full.pdf`.

[5] H. Inaba, *Detection of atoms and molecules by Raman scattering and resonance fluorescence*, pages 153–236 (Springer Berlin Heidelberg, Berlin, Heidelberg, 1976), ISBN 978-3-540-38239-3, doi:10.1007/3-540-07743-X_19, URL `http://dx.doi.org/10.1007/3-540-07743-X_19`.

[6] M. Mattiello, *Gas Traces Measurement by Photoacoustic Spectroscopy Using Helmholtz Resonator-Based Sensors*, Ph.D. thesis, University of Lausanne (2008).

[7] J.-P. Besson, *Photoacoustic spectroscopy for multi-gas sensing using near infrared lasers*, Ph.D. thesis, University of Lausanne (2006).

[8] H. A. Beck, *Anwendung der Photoakustischen Spektroskopie in der Prozess- und Umweltanalytik*, Ph.D. thesis, TU München (2003).

[9] J. J. Olivero and R. L. Longbothum, Empirical Fits to the Voigt Line Width: A Brief Review, *Journal of Quantitative Spectroscopy and Radiative Transfer*, 17:233–236 (1977).

[10] J. Hodgkinson and R. P. Tatam, Optical gas sensing: a review, *Measurement Science and Technology*, 24(1):012004 (2013), ISSN 0957-0233, doi:10.1088/0957-0233/24/1/012004.

[11] D. Mondelain, C. Camy-Peyret, A. W. Mantz, E. Tang and A. Valentin, Performance of a Herriott cell, designed for variable temperatures between 296 and 20 K, *Journal of Molecular Spectroscopy*, 241(1):18–25 (2007), ISSN 00222852, doi:10.1016/j.jms.2006.10.012.

[12] P. Werle, R. Mücke and F. Slemr, The limits of signal averaging in atmospheric trace-gas monitoring by tunable diode-laser absorption spectroscopy (TDLAS), *Applied Physics B Photophysics and Laser Chemistry*, 57(2):131–139 (1993), ISSN 07217269, doi:10.1007/BF00425997.

[13] H. Wenz, *Laserabsorptionsspektroskopie im nahen Infrarot mit höchster Empfindlichkeit*, Ph.D. thesis, University of Kaiserslautern (2001).

[14] J. Chen, *Compact Laser-Spectroscopic Gas Sensors using Vertical-Cavity Surface-Emitting Lasers*, Ph.D. thesis, Technical University of Munich, Germany (2010).

[15] G. B. Rieker, *Wavelength-Modulation Spectroscopy for Measurements of Gas Temperature and Concentration in Harsh Environments*, Ph.D. thesis, Stanford University (2009).

[16] M. M. Jozdani, A. Khorsandi and S. G. Sabouri, Modulation index optimization for wavelength modulation spectroscopy, *Optica Applicata*, XLVI(4):639–650 (2016), doi:10.5277/oa160411.

[17] H. Li, G. B. Rieker, X. Liu, J. B. Jeffries and R. K. Hanson, Extension of wavelength-modulation spectroscopy to large modulation depth for diode laser absorption measurements in high-pressure gases., *Applied optics*, 45(5):1052–1061 (2006), ISSN 0003-6935, doi:10.1364/AO.45.001052.

[18] F. S. Pavone and M. Inguscio, Frequency- and wavelength-modulation spectroscopies: Comparison of experimental methods using an AlGaAs diode laser, *Applied Physics B Photophysics and Laser Chemistry*, 56(2):118–122 (1993), ISSN 07217269, doi:10.1007/BF00325250.

[19] J. T. C. Liu, J. B. Jeffries and R. K. Hanson, Wavelength modulation absorption spectroscopy with 2f detection using multiplexed diode lasers for rapid temperature measurements in gaseous flows, *Applied Physics B: Lasers and Optics*, 78(3-4):503–511 (2004), ISSN 09462171, doi:10.1007/s00340-003-1380-7.

[20] J. T. C. Liu, R. K. Hanson and J. B. Jeffries, High-sensitivity absorption diagnostic for NO2 using a blue diode laser, *Journal of Quantitative Spectroscopy and Radiative Transfer*, 72(2):655–664 (2002).

[21] D. S. Bomse, A. C. Stanton and J. A. Silver, Frequency modulation and wavelength modulation spectroscopies:comparison of experimental methods using a lead-salt diode laser, *Appl. Opt.*, 31(6):718–731 (1992), doi:10.1364/AO.31.000718, URL `http://ao.osa.org/abstract.cfm?URI=ao-31-6-718`.

[22] I. D. Lindsay, P. Groß, C. J. Lee, B. Adhimoolam and K. Boller, Modulation Spectroscopy With a Pump-Modulated Singly-Resonant Optical Parametric Oscillator, 14(25):12341–12346 (2006), ISSN 10944087, doi:10.1364/OE.14.012341.

[23] H. I. Schiff, G. I. Mackay and J. Bechara, The Use of Tunable Diode-Laser Absorption-Spectroscopy for Atmospheric Measurements, *Res. Chem. Intermed.*, 20(3-5):525–556 (1994), ISSN 0922-6168, doi:10.1163/156856794X00441.

[24] A. Hangauer, J. Chen and M. C. Amann, Modeling of the n-th harmonic spectra used in wavelength modulation spectroscopy and their properties, *Applied Physics B: Lasers and Optics*, 90(2):249–254 (2008), ISSN 09462171, doi:10.1007/s00340-007-2902-5.

[25] M. Peric and H. J. Halpern, Fitting of the Derivative Voigt ESR Line under Conditions of Modulation Broadening, *Journal of Magnetic Resonance, Series A*, 109(2):198–202 (1994), ISSN 1064-1858, doi:http://dx.doi.org/10.1006/jmra.1994.1155, URL `http://www.sciencedirect.com/science/article/pii/S1064185884711557`.

[26] B. Xiong, Z. Du and J. Li, Modulation index optimization for optical fringe suppression in wavelength modulation spectroscopy, *Review of Scientific Instruments*, 86(11):113104 (2015), ISSN 0034-6748, doi:10.1063/1.4935920, URL `http://scitation.aip.org/content/aip/journal/rsi/86/11/10.1063/1.4935920`.

[27] P. Werle and A. Popov, Application of antimonide lasers for gas sensing in the 3-4-microm range., *Applied optics*, 38(9):1494–1501 (1999), ISSN 0003-6935, doi:10.1364/AO.38.001494.

[28] B. W. M. Moeskops, S. M. Cristescu and F. J. M. Harren, Sub-part-per-billion monitoring of nitric oxide by use of wavelength modulation spectroscopy in combination with a thermoelectrically cooled, continuous-wave quantum cascade laser., *Optics letters*, 31(6):823–825 (2006), ISSN 0146-9592, doi:10.1364/OL.31.000823.

[29] V. Weldon, J. O'Gorman, P. Phelan, J. Hegarty and T. Tanbun-Ek, H2S and CO2 gas sensing using DFB laser diodes emitting at 1.57 um, *Sensors and Actuators: B. Chemical*, 29(1-3):101–107 (1995), ISSN 09254005, doi:10.1016/0925-4005(95)01669-4.

[30] G. Wysocki, Y. Bakhirkin, S. So, F. K. Tittel, C. J. Hill, R. Q. Yang and M. P. Fraser, Dual interband cascade laser based trace-gas sensor for environmental monitoring, *Appl. Opt.*, 46(33):8202–8210 (2007), doi:10.1364/AO.46.008202, URL `http://ao.osa.org/abstract.cfm?URI=ao-46-33-8202`.

[31] P. Werle, F. Slemr, K. Maurer, R. Kormann, R. Mücke and B. Jänker, Near- and mid-infrared laser-optical sensors for gas analysis, *Optics and Lasers in Engineering*, 37(2-3):101–114 (2002), ISSN 01438166, doi:10.1016/S0143-8166(01)00092-6.

[32] D. Weidmann, A. a. Kosterev, F. K. Tittel, N. Ryan and D. McDonald, Application of a widely electrically tunable diode laser to chemical gas sensing with quartz-enhanced photoacoustic spectroscopy., *Optics letters*, 29(16):1837–9 (2004), ISSN 0146-9592, doi:10.1364/OL.29.001837, URL `http://www.ncbi.nlm.nih.gov/pubmed/15357332`.

[33] G. Hancock, J. H. Van Helden, R. Peverall, G. A. D. Ritchie and R. J. Walker, Direct and wavelength modulation spectroscopy using a cw external cavity quantum cascade laser, *Applied Physics Letters*, 94(20):14–16 (2009), ISSN 00036951, doi:10.1063/1.3141521.

[34] A. Hangauer, J. Chen, R. Strzoda, M. Ortsiefer and M.-C. Amann, Wavelength modulation spectroscopy with a widely tunable InP-based 2.3 μm vertical-cavity surface-emitting laser, *Optics Letters*, 33(14):1566 (2008), ISSN 0146-9592, doi:10.1364/OL.33.001566, URL `http://ol.osa.org/abstract.cfm?URI=ol-33-14-1566`.

1.2 Photoacoustic spectroscopy (PAS)

Analogous to classical AS, PAS (photoacoustic spectroscopy*) is a detection technique that is based on the absorption of light. The main difference between PAS and AS, however, is the concept of signal detection. Whereas classical AS bases on the detection of transmitted light that is not absorbed within a sample, PAS provides the opportunity to directly reveal the absorbed energy. In fact, the photoacoustic signal quantifies the heat input into the sample resulting from absorption of light, thus representing a calorimetric measurement [1]. As a consequence of this comparison, AS is often considered an indirect method, while Photoacoustic Spectroscopy constitutes a direct measuring technique.
The history of photoacoustics dates back to 1880, when Bell [2]† discovered the photoacoustic effect while investigating the interaction between chopped light and solids. However, for a lack of suitable light emitters, sound detectors and electronics, it lasted more than half a century until Viegerov [3] applied the technique for gas analysis. The first laser based photoacoustic system was presented by Kerr and Atwood [4]. However, Dewey et al. [5] and Kamm [6] demonstrated the first photoacoustic systems based on modulated laser excitation and acoustic resonance amplification, which are nowadays referred to as classical photoacoustic (PA) setups.

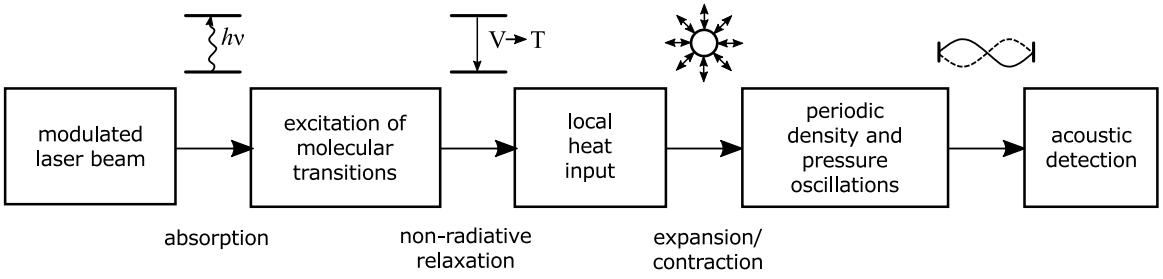

Figure 1.5: Schematic drawing of the functional principle of photoacoustic signal generation.

*For historical reasons sometimes also referred to as Optoacoustic Spectroscopy.
†Alexander Graham Bell (1847-1922)

Figure 1.5 illustrates the functional principle of photoacoustic signal generation. Analogous to classical absorption techniques, monochromatic light is used in order to excite ro-vibronic or ro-vibrational molecular transitions. The most crucial difference in signal generation is that PA systems require chopped, i.e. amplitude modulated* (AM), light, while standard AS applications are based on continuous wave (cw) illumination of the sample. However, alternative modulation techniques (refer to chapter 1.1.4) may be equally applied to both, AS and PAS, thus offering the advantage of reducing spectral cross-sensitivities.
There are three basic pathways for excited molecules to release their energy and return to initial state, namely chemical reaction, radiative relaxation (spontaneous or stimulated emission) and non-radiative relaxation, respectively. However, only non-radiative processes (hereinafter entitled VT-relaxation) contribute to photoacoustic signal generation. This model of deactivation rests on molecular collisions of excited analyte molecules. During these collisions, energy stored from absorption gets transfered into translational, i.e. kinetic, energy of the collision partners, thus causing a local heat input into the sample.†. In this process, the collision partners do not necessarily have to be analyte molecules as well. As a consequence of modulation, this heat input is repetitive and, therefore, causes density oscillations within the sample. Density oscillation in turn cause pressure oscillations, which are synonymic for acoustic wave generation. Finally, the acoustic pressure is detected by means of a microphone, as its amplitude is directly proportional to the analyte concentration.

1.2.1 Rate equation of a two-level system

A simplified model of photoacoustic signal generation can be derived from a two-level system consisting of a molecular ground state S_0 and an excited state S_1. Considering the volume number density ρ_i and an illuminated

*AM modulation depth from threshold to operating current. In literature it is sometimes also referred to as intensity modulation (IM).
†A more detailed discussion of VT relaxation processes will be given in chapter 1.4.2

volume of the sample V_{il}, the total number of analyte molecules χ can be calculated by

$$\chi = \rho_{\mathrm{i}} \cdot V_{\mathrm{il}} \tag{1.35}$$

and according to conservation law, this total number can be divided over the population densities χ_0 and χ_1 following

$$\chi = \chi_0 + \chi_1 \tag{1.36}$$

Furthermore, the continuous gas flow Q through the photoacoustic cell (PAC) is considered sufficiently low, so that no temporal change of the total number of analyte molecules within the PAC is assumed during one cycle of absorption and relaxation processes.

$$\frac{\mathrm{d}\chi}{\mathrm{d}t} = 0 \tag{1.37}$$

This assumption was verified using the example of two miniaturized PACs that are discussed in chapter 4.3 and 4.4, respectively, while considering a gas flow rate of $Q = 500\,[\mathrm{mL/min}]$. Those PACs, hereinafter referred to as QEPAS (quartz enhanced photoacoustic spectroscopy) and µPAS (microfabricated photoacoustic sensor element) setups, feature small sample volumes, still the relative time-dependent removal of molecules $\mathrm{d}\chi$ was calculated to merely ~ 0.3 ‰ and ~ 0.6 ‰, respectively.

An universal rate equation that takes into account the excitation by absorption A_{01} and collision C_{01}, as well as the relaxation by collision C_{10}, stimulated emission E_{st} and spontaneous emission E_{sp} can be written as [7]

$$\frac{\mathrm{d}\chi_1}{\mathrm{d}t} = (A_{01} + C_{01}) \cdot (\chi - \chi_1) - (C_{10} + E_{\mathrm{st}} + E_{\mathrm{sp}}) \cdot \chi_1 \tag{1.38}$$

The absorption rate A_{01} is calculated from the absorption cross-section $\sigma(\bar{\nu})$ and the photon flux $\Psi_0[\mathrm{s}^{-1}\mathrm{m}^{-2}]$ via

$$A_{01} = \sigma(\bar{\nu}) \cdot \Psi_0 \tag{1.39}$$

where the photon flux depends on the optical power of the emitter P_0 and the diameter of the collimated circular beam profile d_b.

$$\Psi_0 = \frac{I_0}{\mathrm{h}\nu_\mathrm{ph}} = \frac{P_0}{\mathrm{h}c_0\bar{\nu}_\mathrm{ph} \cdot \pi \left(\frac{d_\mathrm{b}}{2}\right)^2} \tag{1.40}$$

Excitation and relaxation rates due to molecular collisions show Boltzmann distribution, [7, 8]

$$C_{01} = C_{10} \cdot e^{-\frac{\mathrm{h}\nu}{\mathrm{k_B}T}} \tag{1.41}$$

which relates the energy $\mathrm{h}\nu$ that is necessary for molecular transition to thermal energy $\mathrm{k_B}T$. Calculating 1.41 for a vibronic NO_2 transition at $\bar{\nu}_{01} = 22\,222.\bar{2}$ cm^{-1} revealed that the excitation due to molecular collisions can be considered negligible. Based on the calculations, even at a temperature of 10 000 °C, excitation comprises only 4.5 % of relaxation.

The total lifetime of the excited state τ_e is the reciprocal sum of the lifetime of non-radiative τ_n and radiative relaxation processes τ_r, where τ_r considers stimulated and spontaneous emission.

$$\tau_\mathrm{e}^{-1} = \tau_\mathrm{n}^{-1} + \tau_\mathrm{r}^{-1} \tag{1.42}$$

The lifetime of radiative relaxation processes in the infrared region is roughly in the order of $\tau_\mathrm{r} \sim 10^{-3}$ up to 10^{-1} s and can be neglected towards non-radiative processes, which only last $\tau_\mathrm{r} \sim 10^{-9}$ to 10^{-6} s [9]. Even in terms of NO_2 excitation at 450 nm, a lifetime of $\tau_\mathrm{e} \sim 2$ µs [10] ensures at least 90 % efficiency in view of converting absorbed energy into thermal energy, which finally contributes to the photoacoustic signal [11]. Therefore, E_st and E_sp can be excluded from equation 1.38 as well.
It is further assumed, that the population of the excited state χ_1 is considerably lower than χ_0, thus it follows

$$\chi \sim \chi_0 \tag{1.43}$$

which is verified below (refer to figure 1.6). Taking into account these approximations, 1.38 simplifies to

$$\frac{\mathrm{d}\chi_1}{\mathrm{d}t} = A_{01} \cdot \chi - \frac{1}{\tau_\mathrm{n}} \cdot \chi_1 \tag{1.44}$$

Given that the light source is harmonically amplitude modulated at an angular frequency ω, the photon flux can be expressed as

$$\Psi = \Psi_0 \cdot \left(1 + e^{-j\omega t}\right) \tag{1.45}$$

while only the time-dependent second term has to be considered in view of photoacoustic signal generation [12].* After inserting 1.39, a solution of the partial differential equation in 1.44 is [13]

$$\chi_1(t) = \frac{\chi\sigma(\bar{\nu})\Psi_0\tau_\mathrm{n}}{\sqrt{1+(\omega\tau_\mathrm{n})^2}} \cdot e^{j(\omega t-\phi)} \tag{1.46}$$

where χ_1 is the population of the excited state, χ is the total number of analyte molecules within the illuminated volume, $\sigma(\bar{\nu})$ is the absorption cross-section of the analyte at the wavenumber of radiation $\bar{\nu}$, Ψ_0 is the photon flux, τ_n is the non-radiative lifetime†, ω is the angular frequency of modulation and ϕ is the phase difference between photon flux and population of the excited state, which is defined as

$$\phi = \arctan(\omega\tau_\mathrm{n}) \tag{1.47}$$

A simplified solution of 1.44 is obtained when a Heaviside step function is assumed for illumination instead [7]:

$$\chi_1(t) = \chi\sigma(\bar{\nu})\Psi_0\tau_\mathrm{n} \cdot \left(1 - e^{-\frac{t}{\tau_\mathrm{n}}}\right) \tag{1.48}$$

Actually, the assumption in 1.43 is only valid in terms of moderate absorption [14]. Since the photoacoustic experiments, which are presented in this work, are based on high power illumination ($P_0 = 1.4$ W at 450 nm), the

*j is the imaginary unit.
†that is assumed to equal τ_e

de facto population of χ_1 was calculated in order to proof this assumption. The calculations consider the excitation of nitrogen dioxide utilizing a square wave modulated laser with a beam diameter of 1 mm.

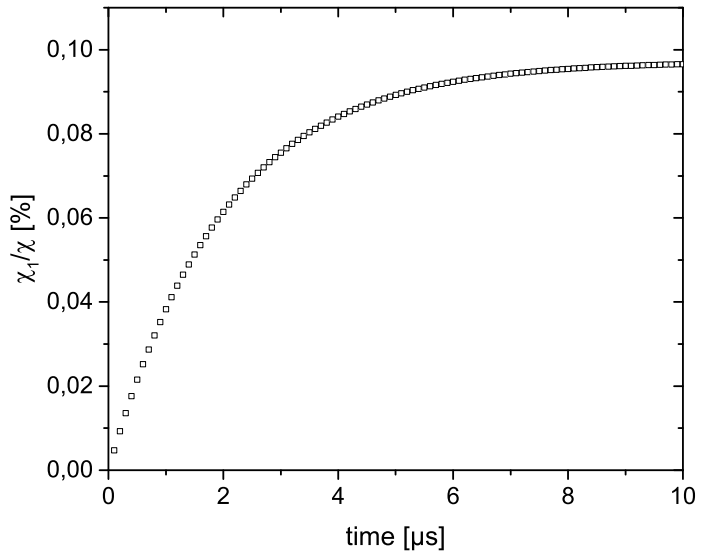

Figure 1.6: Calculation of the time-dependent relative population of the excited state for Heaviside step function illumination.

Figure 1.6 illustrates the time-dependent relative population of the excited state χ_1 calculated from 1.48.* It reveals a maximum population of less than 1‰ at steady state, which is suggested to meet the approximation in 1.43. Moreover, it reveals a minimum required excitation time of fivefold the relaxation time in order to achieve steady state condition. This generally limits the maximum frequency of modulation to

$$f_{\mathrm{mod}} \lesssim \frac{1}{10\tau_{\mathrm{e}}} \tag{1.49}$$

Further calculations were carried out on the basis of equation 1.48 in order to estimate critical values for beam diameter, optical power and lifetime of the excited state, respectively. These critical values, which demonstrate the limits of approximation 1.43 are presented in chapter 2.1.

*The beam diameter was defined at FWHM of the intensity profile. Therefore, the calculation depends on $\Psi = 2\Psi_0$ in order to satisfy twice the light intensity at maximum.

1.2.2 Heat production at thermal equilibrium

This section addresses the production of heat within the sample based on the time-dependent rate equation in 1.46 and 1.35. Given a 100 % efficiency of heat production, the time-dependent heat production rate per volume $\dot{H}(t)$ is specified by

$$\dot{H}(t) = \rho_1(t) \cdot \frac{\mathrm{hc}_0 \bar{\nu}_{\mathrm{ph}}}{\tau_{\mathrm{n}}} \tag{1.50}$$

where $\rho_1(t)$ is the time-dependent volume number density of excited analyte molecules. In contrast to χ, ρ does not depend on the volume of illumination (refer to 1.35). The unit of volume heat production rate (subsequently also referred to as power density) therefore is $[\mathrm{J}/(\mathrm{s} \cdot \mathrm{m}^3)]$. Analogous to 1.45, the time-dependent power density can also be considered a function of light modulation. Again only considering the time-dependent term results to

$$\dot{H}(t) = \dot{H}_0 \cdot e^{j(\omega t - \varphi)} \tag{1.51}$$

where $\dot{H}_0$ is the amplitude of power density. Substitution of 1.46 and 1.50 in 1.51 yields to

$$\dot{H}_0 = \frac{\rho \sigma(\bar{\nu}) \Psi_0 \mathrm{hc}_0 \bar{\nu}_{\mathrm{ph}}}{\sqrt{1 + (\omega \tau_{\mathrm{n}})^2}} \tag{1.52}$$

The denominator of equation 1.52 is considered negligible regarding moderate modulation frequencies, which was calculated to only cause an error of ~ 0.5 % for a frequency of $f_{\mathrm{mod}} (= \omega/2\pi) = 50\mathrm{kHz}$. Inserting 1.40 in 1.52 thus results to

$$\dot{H}_0 = \rho \sigma(\bar{\nu}) I_0 \tag{1.53}$$

1.2.3 Acoustic wave generation

Based on equation 1.53, literature generally provides three different approaches to introduce photoacoustic signal generation, i.e. acoustically [1, 7, 8, 12, 13, 15–18], thermodynamically/kinetically [1, 7, 9, 15, 19, 20] or electrodynamically [16, 21]. However, this chapter aims at an expression

for the PA signal derived from the principles of acoustics. The generation of photothermal and photoacoustic signals thus can be characterized by temperature, pressure, density and the velocity vector of particles. In order to determine these six quantities, the same number of equations is needed, which are assigned to [18]

- classical fluid-mechanics,
- classical thermodynamics,
- energy conservation law (heat diffusion),
- momentum conservation law (Navier-Stokes),
- mass conservation law (continuity) and
- thermodynamic equation of state.

The amplitudes of local oscillation in temperature, pressure and density (index a) due to PA signal generation are very small compared to their equilibrium values (index 0):

$$T(\vec{r},t) = T_0 + T_\mathrm{a}(\vec{r},t) \tag{1.54}$$

$$p(\vec{r},t) = p_0 + p_\mathrm{a}(\vec{r},t) \tag{1.55}$$

$$\rho(\vec{r},t) = \rho_0 + \rho_\mathrm{a}(\vec{r},t) \tag{1.56}$$

Therefore, the products of these small terms can be neglected and the equilibrium values can be considered constant. Thus a linearized Navier-Stokes equation is used in order to relate molecular motion to pressure oscillations:

$$\frac{\partial \vec{v}}{\partial t} = -\frac{1}{\rho_0}\vec{\nabla} \cdot p_\mathrm{a}(\vec{r},t) + \mu_\mathrm{d}\vec{\nabla}\left(\vec{\nabla} \cdot \vec{v}_\mathrm{l}\right) \tag{1.57}$$

Therein, $\vec{v}$ is the velocity vector and μ_d is the dynamic viscosity of the medium. The velocity vector can be separated into a transversal part ($\mathrm{div}\,\vec{v}_\mathrm{t} = 0$) and a longitudinal part ($\vec{\mathrm{rot}}\,\vec{v}_\mathrm{l} = 0$). Since heat-diffusion and continuity equations are coupled to the momentum conservation law only

by the non-rotational component of velocity, its transversal part was omitted in 1.57.
Mass conservation is satisfied by the continuity equation

$$\frac{\partial \rho_{\mathrm{a}}(\vec{r},t)}{\partial t} = -\rho_0 \vec{\nabla} \cdot \vec{v}_{\mathrm{l}} \tag{1.58}$$

Calculating the divergence of the pressure vector field in 1.57 and combining momentum and mass conservation thus eliminates the velocity vector and gives a modified wave equation, which links pressure and density:*

$$\Delta p_{\mathrm{a}}(\vec{r},t) = \frac{\partial^2}{\partial t^2}\rho_{\mathrm{a}}(\vec{r},t) - \mu_{\mathrm{d}}\Delta\left(\frac{\partial}{\partial t}\rho_{\mathrm{a}}(\vec{r},t)\right) \tag{1.59}$$

Thermodynamics provide an equation of state that describes density as a function of pressure and temperature

$$\begin{aligned}\rho_{\mathrm{a}}(\vec{r},t) &= \left(\frac{\partial \rho}{\partial p}\right)_{\mathrm{T}_0} p_{\mathrm{a}}(\vec{r},t) + \left(\frac{\partial \rho}{\partial T}\right)_{\mathrm{p}_0} T_{\mathrm{a}}(\vec{r},t) = \\ &= \frac{\gamma}{c_{\mathrm{s}}^2}\left(p_{\mathrm{a}}(\vec{r},t) - \frac{\beta_T}{\kappa_T} T_{\mathrm{a}}(\vec{r},t)\right)\end{aligned} \tag{1.60}$$

where γ is the heat capacity ratio, i.e. the ratio of specific isobar C_p and isochore C_V heat capacities, β_T is the coefficient of thermal expansion, κ_T is the isothermal compressibility and c_{s} is the speed of sound, which is defined as

$$c_{\mathrm{s}} = \sqrt{\frac{\gamma \mathrm{R} T}{M}} \tag{1.61}$$

Substituting 1.60 in 1.59 eliminates density and results in a wave equation, which only depends on temperature [12]:

$$\Delta p_{\mathrm{a}}(\vec{r},t) = \frac{\gamma}{c_{\mathrm{s}}^2}\left[\frac{\partial^2}{\partial t^2} - \mu_{\mathrm{d}}\Delta\frac{\partial}{\partial t}\right]\left(p_{\mathrm{a}}(\vec{r},t) - \frac{\beta_T}{\kappa_T} T_{\mathrm{a}}(\vec{r},t)\right) \tag{1.62}$$

*Caution: No Greek Delta occurs within the formulae of section 1.2.3. Those are all Laplace operators!

Variations of pressure are always accompanied by variations of temperature. This can be expressed by the heat diffusion equation,

$$\frac{k}{\rho_0 \mathrm{C}_p} \Delta T_\mathrm{a}(\vec{r},t) = \frac{\partial}{\partial t}\left(\frac{\gamma-1}{\gamma\beta_T}\kappa_T p_\mathrm{a}(\vec{r},t)\right) - \frac{\dot{H}(\vec{r},t)}{\rho_0 \mathrm{C}_p} \tag{1.63}$$

which contains the thermal conductivity k and the local power density $\dot{H}(\vec{r},t)$, which was derived in chapter 1.2.2. Solving the coupled equations 1.62 and 1.63 yields to two independent solutions of a plane wave equation [13]:

1st solution is a strongly dampened thermal wave with sub-millimeter length, thus not propagating far beyond its point of origin. This solution is usually applied in order to describe the generation of **photothermal** phenomena.

2nd solution is a slightly dampened acoustic wave. Its length exceeds the thermal wavelength by roughly three magnitudes of order. This solution is further considered in view of **photoacoustic** signal generation.

This second solution dampened wave equation is represented by

$$\Delta p_\mathrm{a}(\vec{r},t) - \frac{1}{c_\mathrm{s}^2}\left[\frac{\partial^2 p_\mathrm{a}(\vec{r},t)}{\partial t^2} + \underbrace{\mu_\mathrm{d}\frac{\partial}{\partial t}\Delta p_\mathrm{a}(\vec{r},t)}_{loss\ term}\right] = \underbrace{-\frac{\gamma-1}{c_\mathrm{s}^2}\frac{\partial \dot{H}(\vec{r},t)}{\partial t}}_{source\ term} \tag{1.64}$$

The dampening results from losses due to the viscosity of the medium. It is specified by a loss term, which prevents an analytical solution. Therefore, losses are neglected in view of further derivation and added again later on as an excess term [1, 12]. The resulting non-dampened inhomogeneous wave equation can be solved by Fourier transformation and it follows [22]

$$\left(\Delta + \frac{\omega^2}{c_\mathrm{s}^2}\right) p_\mathrm{a}(\vec{r},\omega) = \left(\frac{\gamma-1}{c_\mathrm{s}^2}\right) j\omega \dot{H}(\vec{r},\omega) \tag{1.65}$$

with

$$p_{\mathrm{a}}(\vec{r},t) = \int_{-\infty}^{\infty} p_{\mathrm{a}}(\vec{r},\omega)e^{-j\omega t}\mathrm{d}\omega \tag{1.66}$$

$$\dot{H}(\vec{r},t) = \int_{-\infty}^{\infty} \dot{H}(\vec{r},\omega)e^{-j\omega t}\mathrm{d}\omega \tag{1.67}$$

Equation 1.65 connects the frequency-dependent heat production rate resulting from absorption, which was derived in section 1.2.1, with the generation of an acoustic wave. In order to obtain the oscillation modes of this acoustic wave, the boundary conditions have to be selected appropriate to the actual geometry of the photoacoustic cell, wherein the PA signal is generated [18]. As the geometry of the PAC contributes to resonant signal amplification, this derivation is continued in chapter 1.3.1.

References

[1] A. Rosencwaig, *Photoacoustics and photoacoustic spectroscopy* (John Wiley and Sons, 1980), volume 57 edition, ISBN 0-471-04495-4.

[2] A. G. Bell, On the production and reproduction of sound by light, *American Journal of Science*, s3-20(118):305–324 (1880), ISSN 0002-9599, doi:10.2475/ajs.s3-20.118.305, URL `http://www.ajsonline.org/cgi/doi/10.2475/ajs.s3-20.118.305`.

[3] M. L. Viegerov, Eine Methode der Gasanalyse, beruhend auf der optisch-akustischen Tyndall-röntgenerscheinung, in *Dokl. Akad. Nauk SSSR*, volume 19, pages 687–688 (1938).

[4] E. L. Kerr and J. G. Atwood, The Laser Illuminated Absorptivity Spectrophone: A Method for Measurement of Weak Absorptivity in Gases at Laser Wavelengths, *Applied Optics*, 7(5):915 (1968), ISSN 0003-6935, doi:10.1364/AO.7.000915, URL `https://www.osapublishing.org/abstract.cfm?URI=ao-7-5-915`.

[5] C. F. Dewey, R. D. Kamm and C. E. Hackett, Acoustic amplifier for detection of atmospheric pollutants, *Applied Physics Letters*, 23(11):633–635 (1973), ISSN 00036951, doi:10.1063/1.1654774.

[6] R. D. Kamm, Detection of weakly absorbing gases using a resonant optoacoustic method, *Journal of Applied Physics*, 47(8):3550–3558 (1976), ISSN 00218979, doi:10.1063/1.323153.

[7] O. Schulz, *Bestimmung physikalischer und technischer Randbedingungen zur Umsetzung eines photoakustischen Gassensors in der Mikrosystemtechnik*, Ph.D. thesis, University Ilmenau (2008).

[8] B. Baumann, B. Kost, M. Wolff and H. Groninga, Modeling and Numerical Investigation of Photoacoustic Resonators, *Recent Advances in Modelling and Simulation*, pages 17–38 (2008).

[9] P. L. Meyer and M. W. Sigrist, Atmospheric pollution monitoring using CO2 laser photoacoustic spectroscopy and other techniques, *Review of Scientific Instruments*, 61(7):1779–1807 (1990), ISSN 0034-6748, doi:10.1063/1.1141097, URL `http://scitation.aip.org/getpdf/servlet/GetPDFServlet?filetype=pdf&id=RSINAK000061000007001779000001&idtype=cvips&doi=10.1063/1.1141097&prog=normalhttp://aip.scitation.org/doi/10.1063/1.1141097`.

[10] J. Kalkman and H. van Kesteren, Relaxation effects and high sensitivity photoacoustic detection of NO2 with a blue laser diode, *Applied Physics B*, 90(2):197–200 (2008), ISSN 0946-2171, doi:10.1007/s00340-007-2895-0, URL `http://link.springer.com/10.1007/s00340-007-2895-0`.

[11] J. Saarela, *Gas-Phase Photoacoustic Spectroscopy: Advanced Methods for Photoacoustic Detection and Signal Processing*, Ph.D. thesis, Tampere University of Technology, Tampere (2011).

[12] J.-P. Besson, *Photoacoustic spectroscopy for multi-gas sensing using near infrared lasers*, Ph.D. thesis, University of Lausanne (2006).

[13] M. Mattiello, *Gas Traces Measurement by Photoacoustic Spectroscopy Using Helmholtz Resonator-Based Sensors*, Ph.D. thesis, University of Lausanne (2008).

[14] H. A. Beck, *Anwendung der Photoakustischen Spektroskopie in der Prozess- und Umweltanalytik*, Ph.D. thesis, TU München (2003).

[15] Y.-H. Pao, *Optoacoustic spectroscopy and detection* (Academic Press, New York, 1977), ISBN 9780323158817.

[16] A. Miklós, P. Hess and Z. Bozóki, Application of acoustic resonators in photoacoustic trace gas analysis and metrology, *Review of Scientific Instruments*, 72(4):1937–1955 (2001), ISSN 0034-6748, doi:10.1063/1.1353198, URL `http://aip.scitation.org/doi/10.1063/1.1353198`.

[17] A. V. Masurkar, *Extensions of quartz-enhanced photoacoustic spectroscopy*, Ph.D. thesis, Massachusetts Institute of Technology. Dept. of Physics. (2009), URL `http://dspace.mit.edu/handle/1721.1/51579`.

[18] A. Miklós, S. Schäfer and P. Hess, Photoacoustic Spectroscopy , Theory, *Encyclopedia of Spectroscopy and Spectrometry*, pages 1815–1822 (1999).

[19] G. Wysocki, A. A. Kosterev and F. K. Tittel, Influence of molecular relaxation dynamics on quartz-enhanced photoacoustic detection of CO2 at 2um, *Applied Physics B: Lasers and Optics*, 85(2-3):301–306 (2006), ISSN 09462171, doi:10.1007/s00340-006-2369-9.

[20] N. Barreiro, A. Vallespi, A. Peuriot, V. Slezak and G. Santiago, Quenching effects on pulsed photoacoustic signals in NO2-air samples, *Applied Physics B: Lasers and Optics*, 99(3):591–597 (2010), ISSN 09462171, doi:10.1007/s00340-010-3936-7.

[21] M. Tavakoli, A. Tavakoli, M. Taheri and H. Saghafifar, Design, simulation and structural optimization of a longitudinal acoustic resonator for trace gas detection using laser photoacoustic spectroscopy (LPAS), *Optics and Laser Technology*, 42(5):828–838 (2010), ISSN 00303992, doi:10.1016/j.optlastec.2009.12.012, URL `http://dx.doi.org/10.1016/j.optlastec.2009.12.012`.

[22] P. M. Morse and K. U. Ingard, *Theoretical acoustics* (Princeton University Press, Princeton and NJ, 1986), 1 edition, ISBN 9780691024011.

1.3 Signal enhancement

The vast majority of photoacoustic applications is based on some kind of signal amplification. The variety of different physical* amplification techniques can basically be divided into

i. photoacoustic cell designs that offer constructive acoustic interference, i.e. standing wave generation, and
ii. sensor elements that feature mechanical amplification by resonant oscillation.

While acoustic amplification is discussed in section 1.3.1 in detail, mechanical amplification is treated in section 1.3.2. A combination of both (i.) and (ii.), i.e. a double resonant system allowing for even higher amplification, is addressed in section 1.3.3. Concluding chapter 1.3, section 1.3.4 shortly deals with the principle of lock-in amplification, which is a standard method that is applied to virtually all photoacoustic systems, and besides, it addresses the concept of phase sensitive offset correction.

1.3.1 Acoustic amplification

Within the last decades a variety of photoacoustic cell (PAC) designs featuring acoustic resonance amplification was presented. The most commonly used designs can be assigned to

- Helmholtz resonators and
- tube-shaped PACs [1].

Within these categories, many different schemes were realized. In order to name only some of them, the former category includes standard Helmholtz resonators [2–6], differential Helmholtz resonators [7] and T-cell designs [8, 9], while the latter covers standard tube-shaped cavity resonators [10–12] as well as differential– [13], cavity enhanced– [14] or horn-like shaped–resonators [15].

*light amplification techniques prior to PA signal generation as well as electronic amplification or signal post-processing techniques are not included.

However, all five different cell designs that are presented in this work (refer to chapters 4.1 to 4.5) can be considered one-dimensional two-side open-ended resonator tubes. A theoretical description of such cell designs is provided in literature [3, 4, 10, 11, 16–19]. Those theoretical considerations will be used in the following to resume the derivation from equation 1.65 and thus finally present a definition of the photoacoustic signal.

One-dimensional tube-shaped PACs are characterized by openings, whose dimensions are much smaller than the wavelength of resonant amplification, i.e. the tube length L_r exceeds the tube diameter $2r_\mathrm{r}$. As already mentioned at the end of chapter 1.2.3, appropriate boundary conditions of the PAC are required in order to determine the normal mode solutions $p_k(\vec{r})$ of the homogeneous wave equation presented in 1.70. Therefore, the walls of the tube are considered rigid (see 1.68) and the openings are assumed to constitute zero acoustic impedance (see 1.69) [3].

$$\nabla_\perp p(\vec{r})|_{r=r_\mathrm{r}} = 0 \tag{1.68}$$

$$p(\vec{r})|_{z=0,L_\mathrm{r}} = 0 \tag{1.69}$$

$$\left[\Delta + \left(\frac{\omega_k}{c_0}\right)^2\right] p(\vec{r}) = 0 \tag{1.70}$$

While neglecting losses, the solutions of 1.70 are orthonormal and can be normalized to the volume of the cell V_r [10].

$$\int p_q^*(\vec{r}) p_k(\vec{r}) = \delta_{qk} V_\mathrm{r} \tag{1.71}$$

Considering orthogonality and using cylinder coordinates, expressions for $p_k(\vec{r})$ can be found by means of Bessel functions [19]. These expressions involve three different kinds of acoustic modes that might generally form within a tube-shaped cavity, namely radial, azimuthal and longitudinal (in-

dexed by m, n and n_z), respectively [11]. The eigenfrequencies of the pressure modes can then be calculated via

$$f_{\mathrm{m,n,n_z}} = \frac{c_\mathrm{s}}{2}\sqrt{\left(\frac{\alpha_{\mathrm{m,n}}}{r_\mathrm{r}}\right)^2 + \left(\frac{\mathrm{n_z}}{L_\mathrm{r}}\right)^2} \tag{1.72}$$

where $\alpha_{\mathrm{m,n}}$ are the zero derivatives, i.e. saddle or turning points, of those Bessel functions. Literature provides graphical visualizations and tabular values to envisage and calculate such acoustic modes, respectively [3, 11]. However, since this work is only based on tube-shaped PACs, only longitudinal solutions are of interest, because radial and azimuthal ones are excited at much higher frequencies. This was verified by calculating the respectively first modes at the example of the PAC presented in chapter 4.2 to $f_{100} = 108\,970$ Hz, $f_{010} = 52\,352$ Hz and $f_{001} = 4\,559$ Hz. Thus, modified cell dimensions with decreased length-to-diameter ratio are suggested in order to excite radial or azimuthal pressure modes [10]. By setting $\mathrm{m} = \mathrm{n} = 0$, 1.72 simplifies to

$$f_{\mathrm{n_z}} = \frac{\mathrm{n_z} c_\mathrm{s}}{2 L_\mathrm{r}} \tag{1.73}$$

Considering the general relation that links velocity of propagation c, frequency f and length λ of waves,

$$c = \lambda \cdot f \tag{1.74}$$

equation 1.73 can be converted to the well known resonance criteria for longitudinal resonance amplification within a tube:

$$L_\mathrm{r} = \mathrm{n_z} \cdot \frac{\lambda_\mathrm{s}}{2} \tag{1.75}$$

All measurements presented in this work are based on fundamental longitudinal mode excitation, i.e. $\mathrm{n_z} = 1$, which is visualized in figure 1.7. The image is color-coded. While red color means high pressure amplitude and small particle velocity, the blue colored regions at the tube openings illustrate nodes of acoustic pressure and maxima of particle velocity, respectively.

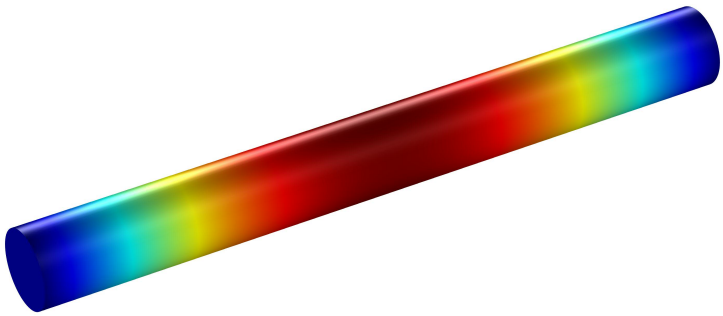

Figure 1.7: Color-coded conditions for fundamental longitudinal pressure mode within a tube. Red color means high pressure amplitude and small particle velocity, respectively.

At this point it is unavoidable to address a phenomenon that is well known from empirical analysis of longitudinal mode excitation, i.e. the effect of acoustic pressure node shifting. In reality the half length of the first longitudinal mode of an two-side open-ended tube tends to exceed the ideal tube length L_r, which is calculated by 1.75 [10]. Different mathematical excess terms were presented in order to account for the effect of node shifting [10, 20]. However, acoustic resonance studies of a variety of PACs, which are presented in chapter 4, revealed none of these excess terms to satisfy the empirical data. Since no analytical representation could be found that quantifies this node shifting with regard to the different investigated PACs, a PAC specific excess factor is introduced in chapter 4.2.3. The complexity of this phenomenon is due to the variety of contributing effects:

- Equation 1.75 is based on the assumption of a one-dimensional tube [10], thus the finiteness of openings causes the pressure nodes to shift from the tube openings into the bulk volume.
- Additionally, these bulk volumes (buffer volumes) are assumed to be infinite compared to the resonator cross-section. Decreasing the volumes was identified to counteract the lengthening of the longitudinal mode (refer to the results of chapter 4.1.4).
- Cutting a hole into the tube at half its length for microphone coupling compensates this lengthening, too (refer to the simulations in chapter 2.2).[21]*

*Actually, in [21] the effect of microphone mounting overcompensated standard node shifting, which could not be reproduced on the basis of the PAC geometries, that are presented in this work.

- Classical attenuation effects, i.e. thermal and viscous boundary layer formation (refer to chapter 1.4.1), cause the speed of sound c_s to decrease, which in turn decreases the distance of the nodes compared to the ideally calculated tube length [12].
- Due to non-perfectly adiabatic behavior, real gases exhibit inherent pressure and a higher pressure leads to an increase in c_s to some extend, i.e. mode lengthening.

All these contributions which partly compensate each other, complicate an analytical definition of the phenomenon. However, by disregarding this node shifting effect, the sum of solutions from 1.70 can be considered to constitute the pressure wave $p_\mathrm{a}(\vec{r},\omega)$ [17]

$$p_\mathrm{a}(\vec{r},\omega) = \sum_k A_k(\omega) p_k(\vec{r}) \tag{1.76}$$

where $A_k(\omega)$ is the amplitude of mode k and $p_k(\vec{r})$ is the spatial distribution.* Assuming that $p_k(\vec{r})$ is a solution of the homogeneous wave equation, substituting 1.76 and 1.70 in 1.65 yields to [3]

$$\sum_k A_k \left(\omega^2 - \omega_k^2\right) p_k(\vec{r}) = (\gamma - 1) j\omega \dot{H}(\vec{r}) \tag{1.77}$$

and by further considering orthogonality (see 1.71), we obtain [17]

$$A_k(\omega) = \frac{j}{\omega - \dfrac{\omega_k^2}{\omega}} \cdot \frac{\gamma - 1}{V_\mathrm{r}} \cdot \int p_k^*(\vec{r}) \dot{H}(\vec{r}) \mathrm{d}V \tag{1.78}$$

While the first term in 1.78 includes the resonance criterion, i.e. the angular resonance frequency ω_k, the last term shows the overlap integral, which describes the coupling between heating source, i.e. represented by the spatial part of heat rate $\dot{H}(\vec{r})$, and the pressure mode $p_k(\vec{r})$.

*$p_k(\vec{r})$ does not have any dimension.

So far, the energy loss term of 1.64 was excluded from derivation and can now be added to 1.78 by means of an excess loss term, thus it follows [18, 19]

$$A_k(\omega) = \frac{j}{\omega - \frac{\omega_k^2}{\omega} + \underbrace{\frac{j\omega_k}{Q_k}}_{loss\ term}} \cdot \frac{\gamma - 1}{V_\mathrm{r}} \cdot \int p_k^*(\vec{r}) \dot{H}(\vec{r}) \mathrm{d}V \tag{1.79}$$

where Q_k is the resonance quality factor of the k^{th} normal mode. A physical interpretation of this quality factor is the ratio of accumulated and dissipated energy during one period of acoustic oscillation. Another interpretation that can be easily obtained from measurement is

$$Q_k = \frac{f_k}{\Delta f_{\mathrm{FWHM}}} \tag{1.80}$$

where Δf_{FWHM} is the width of the resonance profile at half maximum (FWHM: *full width at half maximum*). There is a variety of reasons for energy dissipation due to non-ideal conditions [3, 10, 16, 18], which can be generally divided into volume and surface effects. Volumetric losses result from non-perfectly adiabatic conditions and friction between bulk molecules, respectively. They are also referred to as Stokes-Kirchhoff losses [3], however, they contribute only a minor part at atmospheric conditions. In fact, dissipation caused by surface losses has to be considered the crucial part. Three main processes cause energy dissipation at surface boundaries, i.e.

i. scattering due to inner wall roughness,

ii. thermal losses caused by thermal conductivity of the wall and

iii. viscous effects at the surface boundary.

Viscous effects for example are caused by shear stress due to heterogeneous particle velocities*, thus finally causing dissipation by friction. Thermal- as well as viscous-losses can be calculated from boundary layer concepts, which, however, would go beyond the scope of this thesis. In the end, the best way to counteract these dissipation phenomena is to select an appropriate material for PAC development, which features smooth surfaces, still

*Actually, the tangential component of velocity next to the wall is zero.

showing poor thermal conductivity. Further losses due to molecular relaxation or acoustic detuning are discussed in chapter 1.4 in detail.

In order to finally establish a connection between illumination and acoustic pressure, the heat rate within 1.79 is replaced by the light intensity resulting from 1.53 and 1.51, thus it follows [16]

$$A_k(\omega) = \frac{j}{\omega - \frac{\omega_k^2}{\omega} + \frac{j\omega_k}{Q_k}} \cdot \frac{(\gamma-1)\rho\sigma(\bar{\nu})}{V_\mathrm{r}} \cdot \int p_k^*(\vec{r}) I_0(\vec{r}) \mathrm{d}V \tag{1.81}$$

Considering light intensity as the product of optical power P_0 and the normalized spatial distribution of the light beam intensity $g(\vec{r})$ [4], equation 1.81 becomes

$$A_k(\omega) = \frac{j}{\omega - \frac{\omega_k^2}{\omega} + \frac{j\omega_k}{Q_k}} \cdot \frac{(\gamma-1)\rho\sigma(\bar{\nu})P_0}{V_\mathrm{r}} \cdot \int p_k^*(\vec{r}) g(\vec{r}) \mathrm{d}V \tag{1.82}$$

With regard to Gaussian intensity distribution (see equation 1.20), which does not change while the beam propagates through the PAC, the integral can be written as [3]

$$\int p_k^*(\vec{r}) g(\vec{r}) \mathrm{d}V = L_\mathrm{r} p_k e^{-\mu_k} = L_\mathrm{r} I_k \tag{1.83}$$

where p_k is a normalization coefficient and μ_k is the reciprocal coupling factor that represents the strength of light-to-sound coupling.* I_k is simply referred to as coupling integral and it describes the normalized efficiency of light-to-sound energy transfer. By applying 1.83, equation 1.82 becomes

$$A_k(\omega) = \frac{j}{\omega - \frac{\omega_k^2}{\omega} + \frac{j\omega_k}{Q_k}} \cdot \frac{(\gamma-1)\rho\sigma(\bar{\nu})P_0 L_\mathrm{r}}{V_\mathrm{r}} \cdot p_k e^{-\mu_k} \tag{1.84}$$

*The appearance of L_r is because $g(\vec{r})$ only depends on $\mathrm{d}x$ and $\mathrm{d}y$, which means the intensity distribution does not change while propagating in z-direction, at least from $z = 0$ to $z = V_\mathrm{r}$.

Assuming the resonant case, where the modulation frequency ω equals the resonance frequency ω_k, the term that contains the resonance criterion gets simplified and the photoacoustic amplitude results to

$$A_k(\omega_k) = \frac{Q_k}{\omega_k} \cdot (\gamma - 1) \cdot \frac{L_\mathrm{r}}{V_\mathrm{r}} \cdot \rho\sigma(\bar{\nu})P_0 \cdot p_k e^{-\mu_k} \tag{1.85}$$

It is obvious that the photoacoustic amplitude is directly proportional to the volume number density and the absorption cross-section of the analyte, as well as to the optical power, which is used for excitation. Moreover, the PA signal increases with the quality of resonance amplification and decreases with frequency. As a result, striving for PACs that feature moderate resonance frequencies is not only preferable due to data acquisition– or molecular VT-relaxation (refer to chapter 1.4.2)–limitations, respectively, but due to intrinsic characteristics of the photoacoustic amplitude itself. The PA amplitude further increases with the length-to-volume ratio of the cell, which obviously is the reciprocal cross-section in terms of tube-shaped PACs.

Now decreasing the modulation frequency, while maintaining all other measuring conditions, i.e. gas composition, illumination, temperature, pressure and of course using the same PAC, leads to the non-resonant case, where the photoacoustic amplitude is specified by

$$A_0(\omega) = \frac{j}{\omega} \cdot (\gamma - 1) \cdot \frac{L_\mathrm{r}}{V_\mathrm{r}} \cdot \rho\sigma(\bar{\nu})P_0 \tag{1.86}$$

In view of finding an expression for the photoacoustic signal, the resonant case is considered again, and optimum light-to-sound coupling ($\mu_k << 1$) is assumed. Mounting a microphone at position* $\vec{r} = \vec{r}_\mathrm{m}$ and combining 1.83, 1.85 and 1.76 finally yields to

$$p_\mathrm{a}(\vec{r}_\mathrm{m}, \omega_k) = \underbrace{-(\gamma - 1)\frac{Q_k}{\omega_k} I_k p_k(\vec{r}_\mathrm{m}) \frac{L_\mathrm{r}}{V_\mathrm{r}}}_{cell\ \ constant} \cdot \rho\sigma(\bar{\nu})P_0 \tag{1.87}$$

*In case of 1st longitudinal mode excitation, this might be at $L_\mathrm{r}/2$, where the pressure amplitude reaches its maximum (refer to figure 1.7)

In order to improve the photoacoustic signal with regard to trace gas detection, i.e. low analyte concentrations ρ, it is suggested to

- ✓ find molecular transitions that feature major cross-sections $\sigma(\bar{\nu})$*,
- ✓ use high power light sources (P_0)†,
- ✓ apply high-quality ($Q_k \gtrsim 20$) resonant cell designs‡,
- ✓ find good compromise with regard to resonance frequency (long tubes = low frequencies = high signal $\overset{versus}{\Longleftrightarrow}$ miniaturization),
- ✓ apply small tube cross-sections§ and
- ✓ consider effective light-to-sound coupling, i.e. not focusing illumination to regions of pressure nodes, but rather to regions of pressure maxima instead.

1.3.2 Resonant acoustic transducers

Besides acoustic amplification due to standing wave generation, which was discussed within the previous chapter 1.3.1 in detail, amplification can also be achieved by utilizing mechanically resonant acoustic transducers. Regardless of which concept is chosen with respect to sound conversion, resonant transducers have to be designed in a way, that their dimensions¶ allow eigenmode excitation at the frequency of light modulation. Thus, analogous to exciting acoustic resonances within the PAC, the photoacoustic signal is amplified, while those acoustic noise components, that significantly differentiate from these eigenmodes in frequency, are not amplified. In fact, striving for such resonant transducers is the inverse approach to common microphone design, as microphones usually aim at linear frequency responses over preferably wide frequency ranges. As a consequence, standard microphones are not considered optimal sound detectors for photoacoustic applications.

*but minor cross-sensitivities towards other components within the matrix.
†still respecting the limitations from equation 1.43.
‡while stabilizing measuring conditions (such as temperature and pressure) in order to prevent detuning (refer to chapter 1.4.4).
§but consider beam collimation, as reflections at the inner walls cause photoacoustic background signal generation.
¶and of course the material coefficients of the substrate have to be considered, too.

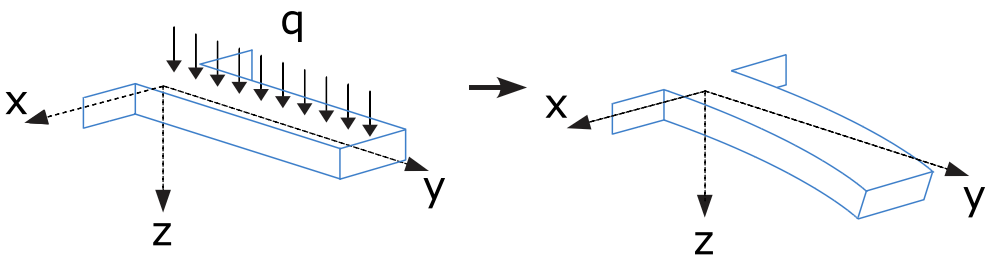

Figure 1.8: Drawing of a simple cantilever design. The beam is forced to flexural vibration by a line load q. The load causes deflection in z-direction.

Resonant cantilever enhanced photoacoustic spectroscopy (CEPAS)

One conceivable and simple geometry in view of mechanical resonant amplification is a cantilever design that features a fixed end and a free oscillating end, respectively.* Photoacoustic applications that utilize such cantilevers for sound conversion are referred to as cantilever enhanced photoacoustic spectroscopic (CEPAS) devices. However, most cantilever based photoacoustic systems do not operate at resonant conditions [22–30]†. There are only two resonant CEPAS systems presented in literature so far,‡ i.e. a piezoelectric cantilever microphone operating at 20 Hz [31] and an AFM (atomic force microscopy) cantilever operating at $\sim$5.3 kHz [32], respectively.

Figure 1.8 illustrates a simple cantilever geometry that is forced to flexural vibration by a line load q.§ The cantilever is of length L (y-direction), width w (x-direction) and thickness t (z-direction), and the load acts uniformly and perpendicular on his top site, i.e. its symmetry axis in xy-plane. The flexural modes of vibration can be derived from Euler¶–Bernoulli‖ beam theory [33–35]. This is a static approach that bases on equilibrium of force and momentum. In general, it takes into consideration the bending moment,

*Besides our team is also developing resonant membranes for photoacoustic applications, which, however, are not part of this thesis.

†These references are all based on the same system, which was developed at the institutes of Prof. Kauppinen (Aalto University of Helsinki, Finland) and Prof. Tittonen (University of Turku, Finland). The system is based on interferometric read-out, thus it is also referred to as an optical microphone.

‡to the best of the authors knowledge

§The dimensions of q are [N/m].

¶Leonhard Euler (1707-1783)

‖Daniel Bernoulli (1700-1782)

the line load and the shear force in order to calculate the curvature radius of the bending line. However, this thesis is not meant to give a detailed derivation of the theory, but only to shortly address the approximations that were assumed, which are:

- Only flexural modes are excited (no torsional vibration).
- The line load causes only moderate deflection, thus perpendicularity can be assumed during vibration.
- No damping effects are considered.
- No deformation occurs due to shear stress.
- The beam is of rectangle shape (top-site) and cross-section, respectively.
- The width is much smaller than the length of the cantilever.

Based on these assumptions, the area moment of inertia is specified to

$$I_y = \frac{1}{12} w t^3 \tag{1.88}$$

This moment can be further used to calculate the curvature radius and finally yields to an expression for the maximal deflection $\Delta z_{\max}$ at the tip of the beam

$$\Delta z_{\max} = \frac{qL \cdot L^3 3}{E w t^3 2} \tag{1.89}$$

where E is the elastic modulus of the substrate. The eigenfrequencies (j^{th}-harmonics) of flexural vibration of a cantilever can be derived from theory of harmonic oscillators

$$f_j = \frac{j}{2\pi} \cdot \sqrt{\frac{k}{m}} \tag{1.90}$$

where m is the vibrating mass and k is considered the spring constant of Hooke's law, that is

$$k = \frac{F}{\Delta z_{\max}} \tag{1.91}$$

Therein, F is the force acting on the beam, which is defined as $F = qL$. By combining 1.88, 1.89 and 1.91, the spring constant can either be expressed by the area moment of inertia (left side) or directly by the beam parameters (right side):

$$k = \frac{8EI}{L^3} = \frac{2}{3}\frac{Ewt^3}{L^3} \tag{1.92}$$

The mass of a rectangle-shaped cantilever is calculated from its density ρ

$$m = \rho V = \rho Lwt \tag{1.93}$$

and by substituting 1.93 and 1.92, 1.90 thus becomes [36]

$$f_j = \frac{j}{2\pi} \cdot \frac{t}{L^2} \cdot \sqrt{\frac{2E}{3\rho}} \tag{1.94}$$

Considering equation 1.94, the resonance frequency of a cantilever is found to linearly increase with thickness and quadratically decrease with length, while it does not depend on the width of the beam*.
Assuming a **point load at the tip** of the cantilever, rather than the line load depicted in figure 1.8, theory provides expressions for spring constant and resonant frequency that differ from 1.92 and 1.94. Those are [36–38]

$$k = \frac{3EI}{L^3} = \frac{1}{4}\frac{Ewt^3}{L^3} \tag{1.95}$$

$$f_j = \frac{j}{4\pi} \cdot \frac{t}{L^2} \cdot \sqrt{\frac{E}{\rho}} \tag{1.96}$$

and considering a **point load** that acts **at a distance l_1** away from the fixed end of the beam, k and f_j become [39]

$$k = \frac{3EI}{l_1^3} = \frac{1}{4}\frac{Ewt^3}{l_1^3} \tag{1.97}$$

$$f_j = \frac{j}{4\pi} \cdot t \cdot \sqrt{\frac{E}{\rho l_1^3 L}} \tag{1.98}$$

*under idealized conditions

Quartz enhanced photoacoustic spectroscopy (QEPAS)

An alternative and more widely used approach, where mechanical resonant detectors are applied in photoacoustic systems, is the so-called quartz enhanced photoacoustic spectroscopy (QEPAS) technique. The method was for the first time reported [40] in 2002 and patented in 2007 by Kosterev [41] and still constitutes the basis for most commonly used photoacoustic systems [42–44].
QEPAS based applications utilize clock generators featuring high Q-factors ($Q \approx 9000$ in air), namely quartz tuning forks (QTF), for PA signal detection. QTFs are fabricated from quartz monocrystals which feature piezoelectric properties, thus responding to mechanical deformation with a charge displacement. This displacement causes a change in potential at surfaces that are positioned at opposite sides of a polar axis of the substrate. Electrodes are applied on top of these surfaces, thus oscillation of the QTF can be monitored by a current signal. Actually, the alternating current (AC) signal is amplified and converted to an AC voltage signal by means of a transimpedance amplifier (TIA).

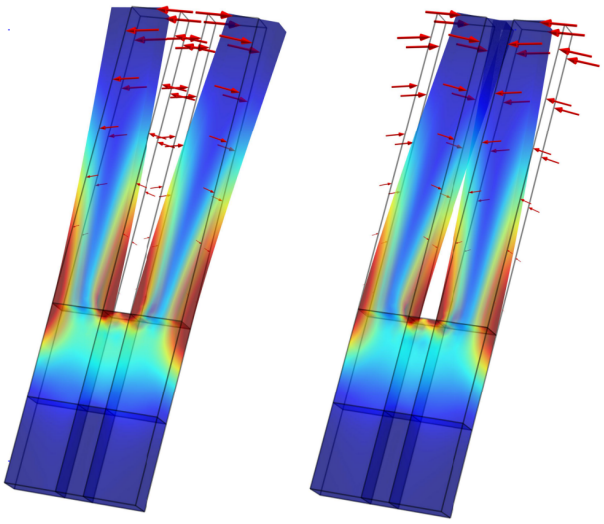

Figure 1.9: Color-coded illustration of the fundamental flexural vibration of a quartz tuning fork, where the tines oscillate in opposite directions. Red color means maximal mechanical stress, while red arrows represent deflection.

Figure 1.9 visualizes the fundamental anti-symmetrical vibration of a QTF, where the tines oscillate in opposite directions. The red-colored regions in-

dicate maximal mechanical stress, while the red arrows illustrate the deflection of the tines. Standard commercially available tuning forks are encapsulated and the frequency of fundamental anti-symmetrical flexural vibration is specified to 32 768 Hz* in vacuum. The tines of the QTF are 3.7 mm in length, 600 µm in width and 270 µm thick. The spacing between the tines is 300 µm. Utilizing such tuning forks for QEPAS setups is done by focusing a laser beam between the tines of the fork at an optimum distance of 0.7 mm from its opening† [45]. Therefore, the actual volume that is available for photoacoustic signal generation is astonishing small (~ 0.008 mm^3), still it satisfies the requirements for trace gas analysis.
QTFs can be interpreted as two clamped cantilevers, thus the eigenfrequencies can be derived from Euler–Bernoulli beam theory and calculated using equation 1.94, too. However, the direction of motion has to be considered, thus the width of the QTF corresponds to the thickness t of the cantilever in 1.94.‡ Considering a density of 2.65 g/cm^3 and a yx-cutting plane of the quartz crystal [46], i.e. an elastic modulus of $(97 + 76.5)/2 = 86.75$ GPa, the frequency of first in-plane vibration is calculated to 32 586 Hz. The deviation of ∼0.6 % between theory and specifications might be due to approximations/limitations of theory (refer to the key points on page 54).

1.3.3 Double-resonant systems

Regarding sections 1.3.1 and 1.3.2, it seems obvious to combine acoustic- and mechanical-amplification in order to further increase the sensitivity of trace gas monitoring applications.
Figure 1.10 accordingly illustrates two commonly used photoacoustic concepts, incorporating acoustic resonators with mechanical resonant detectors. Those are referred to as on-beam (figure (a) on the left) and off-beam (figure (b) on the right) QEPAS, which for the first time were presented by Kosterev et al. [49] in 2005 and by Liu et al. [50] in 2009, respectively. In terms of on-beam setups, the acoustic resonator is assembled from two tubes, which are mounted in front and behind the QTF, respectively, while

*i.e. 2^{15} Hz
†i.e. its free oscillating end
‡By analogy, the thickness of the QTF corresponds to the width of the beam.

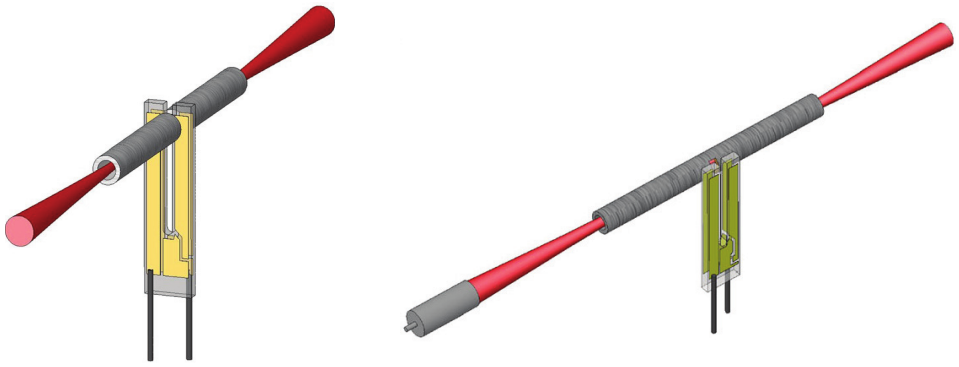

Figure 1.10: Schematic drawing of two different photoacoustic concepts featuring acoustic- and mechanical-amplification. (a): On-beam QEPAS (taken from [47]), (b): Off-beam QEPAS (taken from [48]).

the laser beam still has to be focused between the tines of the fork. In contrast, off-beam QEPAS arrangements resemble standard PA systems. Thus, a focused or collimated laser beam illuminates a tube, with an opening at half its length, where the QTF is mounted from the outside. Such a scheme entails the advantage, that the light does not have to be focused between the tines of the fork. This is considered an advantage, as directly illuminating the tines strongly affects photoacoustic background signal generation [51], thus on-beam setups are considerably more susceptible towards mechanical vibrations of the system whilst operation. Therefore, the off-beam scheme was chosen as a preliminary step towards developing a miniaturized photoacoustic trace gas application for the detection of nitrogen dioxide (refer to chapter 4.3). A further development stage, which is referred to as µPAS (miniaturized photoacoustic sensor chip), is presented in chapter 4.4. Therein, a concept is described, where a tube was etched into a borofloat glass substrate for acoustic resonance amplification, while a resonant silicon cantilever was bonded on top of the glass substrate for sound conversion. The excitation of NO_2, however, was achieved by bottom-up illumination of this MEMS (micro-electromechanical systems) sensor chip, instead of aligning the laser beam with the acoustic micro-resonator (mR). To the best of the authors knowledge, such a double-resonant photoacoustic system, which is based on signal amplification by means of a resonant cantilever, has not

been reported so far. Both the off-beam QEPAS and the μPAS concept can be considered feedback-free double-resonant systems, i.e. no feedback occurs from QTF or cantilever oscillation to standing wave generation within the acoustic resonator. Therefore, the signal resulting from double-resonance amplification is tantamount to the product of both discrete signals at a given frequency of light modulation.*

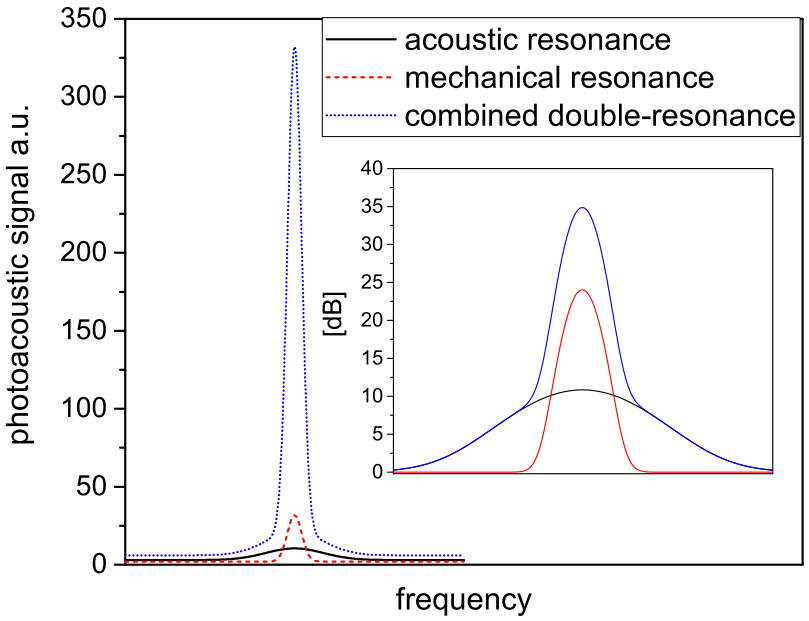

Figure 1.11: Theoretical two-resonance signal combination (blue dotted line) from acoustic (black solid line) and mechanical (red dashed line) amplification. The inset represents the corresponding amplification factors which are calculated via equations 1.99 and 1.100.

Figure 1.11 depicts such a hypothetical double-resonant system, consisting of an acoustic resonator (index k) and a resonant detector (index j). The resonance profiles $A_i(\omega)$ are assumed to show Gaussian shape (refer to equation 1.20) and the peak frequencies of mR (resulting from 1.87) and detector (resulting from 1.94) are expected to perfectly match up, i.e. $\omega_k = \omega_j = \omega_{mod}$. The PA signal due to acoustic $A_k(\omega)$, mechanical $A_j(\omega)$ and total amplification $A_{k*j}(\omega)$ is illustrated by a black solid, a red dashed and a blue dotted line, respectively. The fictitious offset (out of resonance) values were $A_k(\omega_{mod} \neq \omega_k) = 3$ and $A_j(\omega_{mod} \neq \omega_j) = 2$, the peak values

*Resonant PA systems can generally be considered as oscillators that are forced by the frequency of light modulation.

were $A_k(\omega_{mod} = \omega_k) = 10$ and $A_j(\omega_{mod} = \omega_j) = 30$, and the peak widths (FWHM) were set to $w_k = 4$ and $w_j = 1$. Moreover, the inset plot in figure 1.11 illustrates the amplification values $F_i(\omega)$ of the single amplification profiles derived by

$$F_i = 20 \cdot \log \frac{A_i(\omega)}{A_i(\omega_0)} \tag{1.99}$$

and of the double-resonance profile $F_{k*j}(\omega)$ resulting from

$$F_{k*j}(\omega) = \sum_i F_i(\omega) \tag{1.100}$$

The definition in equation 1.99 is valid for all field quantities, e.g. voltage or acoustic pressure, and its *quasi*-unit is dB (Decibel). This illustrative visualization of double-resonant amplification indicates the degree of improvement. However, double-resonance based schemes may also involve serious disadvantages, which will be addressed in chapter 1.4.4.

1.3.4 Phase-sensitive detection

In contrast to classical absorption spectroscopy (refer to chapter 1.1), virtually all photoacoustic applications utilize lock-in amplifiers (LIA), equally whether wavelength (WM) or amplitude modulation (AM) techniques are applied. The only difference in terms of lock-in amplification is, that WM rests on multiple harmonics demodulation (see figure 1.3), while only the $1f$ fundamental is considered in terms of AM.

Lock-in amplification (LIA)

The convenient opportunity of utilizing lock-in amplifiers relates to the fact that the frequency of the photoacoustic signal is known, as it corresponds to the frequency of light modulation. The modulation signal thus can be used as a reference for lock-in amplification. LIAs offer the advantage of reconstructing signals, which amplitudes might be several magnitudes of order smaller than the actual noise level. The fundamental principle of lock-in amplification is discussed hereinafter, however, references are provided in view of a more detailed theoretical consideration [52–56].

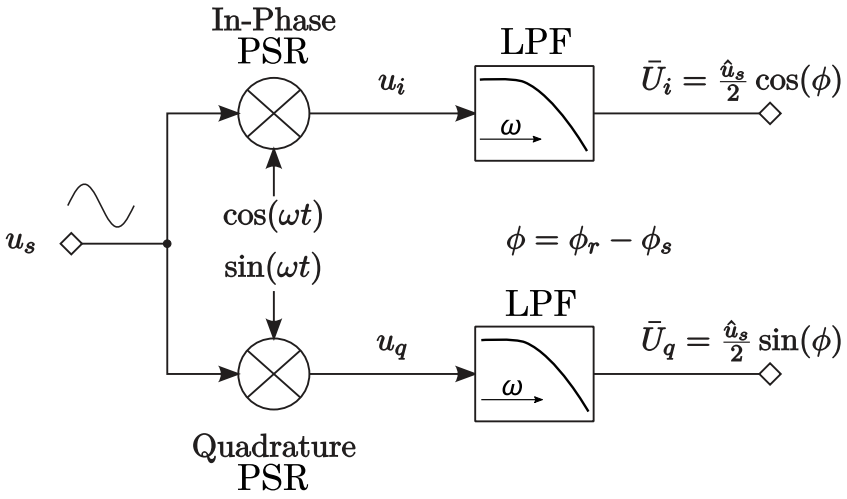

Figure 1.12: Functional diagram of a dual channel lock-in amplifier. u_s: AC input signal, PSR: phase sensitive rectifier, u_i: AC in-phase signal, u_q: AC quadrature signal, LPF: low-pass filter, $\bar{U}_i$: DC in-phase signal, $\bar{U}_q$: DC quadrature signal.

Figure 1.12 shows a functional diagram of a dual channel lock-in amplifier, that is typically used for photoacoustic detection. Considering the upper path, the photoacoustic input signal

$$u_s(t) = \hat{u}_s \cos(\omega_s t + \phi_s) \tag{1.101}$$

is modulated by the reference signal $u_r(t)$ by means of a phase sensitive rectifier (in-phase PSR)

$$\begin{aligned} u_i(t) &= u_s(t) \cdot \hat{u}_r \cos(\omega_r t + \phi_r) \\ &= \hat{u}_s \hat{u}_r \frac{1}{2}[\cos((\omega_r - \omega_s)t + (\phi_r - \phi_s)) \\ &+ \cos((\omega_r + \omega_s)t + (\phi_r + \phi_s))] \end{aligned} \tag{1.102}$$

and due to equifrequency condition ($\omega_s = \omega_r = \omega_{mod}$), 1.102 can be simplified to

$$u_i(t) = \underbrace{\frac{\hat{u}_s \hat{u}_r}{2}\cos(\phi_r - \phi_s)}_{\text{DC term}} + \frac{\hat{u}_s \hat{u}_r}{2}\cos(2\omega t + \phi_r + \phi_s) \tag{1.103}$$

The in-phase signal $u_i(t)$ is subsequently convoluted with a low-pass filter and thus the in-phase output signal $\bar{U}_i$ is the DC term of 1.103. Further eliminating the known amplitude of the reference $\hat{u}_r$, the in-phase output becomes

$$\bar{U}_i = \frac{\hat{u}_s}{2} \cos \Phi \tag{1.104}$$

where the phase difference between reference and signal is $\Phi = \phi_r - \phi_s$. Considering the lower path in figure 1.12, the photoacoustic signal is additionally modulated by the reference, which is previously shifted by 90° (quadrature PSR)

$$\begin{aligned} u_q(t) &= u_s(t) \cdot \hat{u}_r \cos\left(\omega_r t + \phi_r + \frac{\pi}{2}\right) \\ &= u_s(t) \cdot \hat{u}_r \sin(\omega_r t + \phi_r) \end{aligned} \tag{1.105}$$

and analogous to 1.103 and 1.104 it follows

$$\bar{U}_q = \frac{\hat{u}_s}{2} \cos\left(\Phi + \frac{\pi}{2}\right) = \frac{\hat{u}_s}{2} \sin \Phi \tag{1.106}$$

Based on 1.104 and 1.106, the photoacoustic amplitude can be reconstructed by the square root of the sum of the squares

$$\hat{u}_s = 2 \cdot \sqrt{\bar{U}_i^2 + \bar{U}_q^2} = 2 \cdot \frac{\hat{u}_s}{2} \underbrace{\sqrt{\cos^2 \Phi + \sin^2 \Phi}}_{=1} \tag{1.107}$$

and the phase difference between reference and signal is obtained by

$$\begin{aligned} \frac{\bar{U}_q}{\bar{U}_i} &= \frac{\sin \Phi}{\cos \Phi} = \tan \Phi \\ \rightarrow \Phi &= \arctan\left(\frac{\bar{U}_q}{\bar{U}_i}\right) \end{aligned} \tag{1.108}$$

The performance of a lock-in amplifier, i.e. its ability to reconstruct small signals that are superimposed by a certain noise level, is determined by the time constant τ_{LIA} and the roll-off ΔL [dB/decade] of the low-pass filter,

respectively. The filter cut-off frequency f_c is defined as the frequency, where only half of the power, i.e. $1/\sqrt{2}$ of the amplitude (field quantity), is remaining* and it is linked to τ_{LIA} by

$$f_c = \frac{1}{2\pi\tau_{\mathrm{LIA}}} \tag{1.109}$$

The roll-off [dB/decade], however, determines the attenuation in [dB] (refer to equation 1.99) per 10 times increase in frequency.†
When considering lock-in amplifiers as bandpass filters, equation 1.110 provides an expression, which depends on τ_{LIA} and ΔL‡, and allows to calculate the bandwidth B at which the signal amplitude is attenuated by a factor F_α. However, this formula is an approximation as it considers the low pass filter to be of 1st order and it additionally assumes the filter curve to linearly slope immediately after exceeding the cut-off frequency $f > f_c$.

$$B = \frac{1 + 10^{\dfrac{20\log F_\alpha - 10\log\sqrt{2}}{\Delta L}}}{\pi\tau_{\mathrm{LIA}}} \tag{1.110}$$

As an example, setting the time constant to 10 s and the roll-off to 20 dB/decade results to a filter bandwidth of 2.71 Hz, where the signal amplitude is attenuated by a factor 100.

Offset correction of photoacoustic signals

As a consequence of lock-in amplification, the obtained photoacoustic signal represents a vector quantity that is composed of the amplitude $\hat{u}_s$ (refer to 1.107)§ and the phase difference Φ (refer to 1.108) between reference and signal. Its complex notation is

$$\vec{u}_i = \begin{pmatrix} \mathbb{R}\mathrm{e}_i \\ \mathbb{I}\mathrm{m}_i \end{pmatrix} = \begin{pmatrix} \hat{u}_i \cos\Phi_i \\ \hat{u}_i \sin\Phi_i \end{pmatrix} \tag{1.111}$$

*Therefore, it is sometimes also referred to as the -3dB frequency. With regard to field quantities it rather might be called the -1.50515 frequency, see 1.110.

†or alternatively per 2 times increase in frequency when the roll-off is specified in [dB/octave]. Thus 20 dB/decade equals 6dB/octave.

‡in [dB/decade]

§which constitutes the length of the vector

The following paragraph is meant to discuss the context in which this complex notation gains in significance.
During calibration of a photoacoustic setup, the offset signal is recorded at standard measuring conditions and a gas flow including pure carrier gas only, i.e. zero analyte. Nevertheless, a small offset signal may occur, which primarily has to be attributed to interaction of light with the windows or the inner walls of the PAC. In terms of offset correcting the measured data with regard to this offset value, it is insufficient to only perform an offset amplitude subtraction, as the photoacoustic detection method is phase sensitive. Taking this phase information into account in view of signal evaluation is known to increase the SNR to some extend [57]. Besides it has the advantage to recognize signal drifts or signal fluctuations, e.g. due to ambient noise. Figure 1.13 shows the photoacoustic data of a concentration series of some analyte in Cartesian (a) and in polar coordinates (b), respectively.

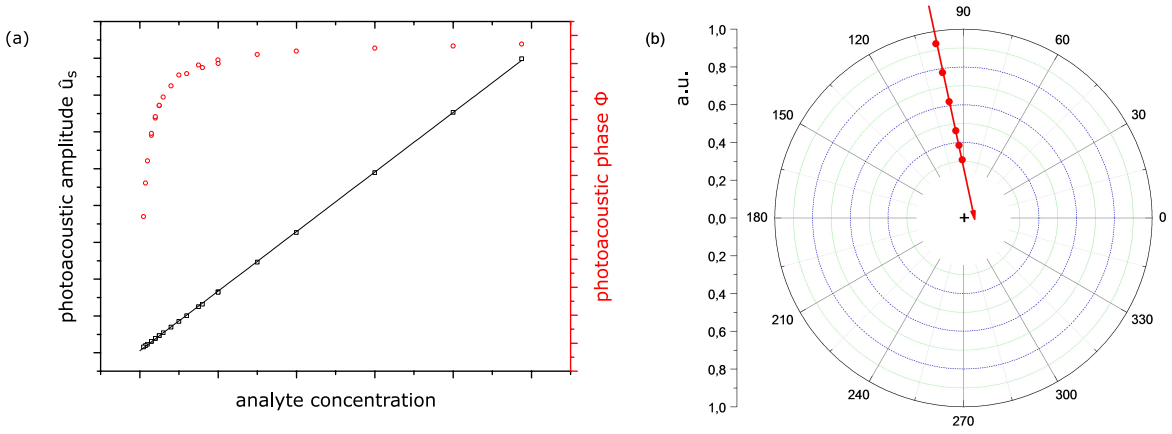

Figure 1.13: Calibration characteristics of a photoacoustic setup prior to offset correction. (a) Magnitude (black squares) and phase information (red circles) in Cartesian coordinates. (b) Vector signals in polar coordinates.

Considering figure (a), the red points illustrate the phase difference Φ_i and the black squares represent the magnitude $\hat{u}_i$ of measuring point i, respectively. Besides, the fitted black line depicts the calibration characteristics of the setup. While $\hat{u}_s$ shows good linearity with the analyte concentration, the phase difference obviously decreases regarding analyte concentration converging to zero. This shifting of Φ is attributed to the occurrence of a background signal at zero analyte. As a matter of fact, this background has

to be considered a vector quantity (with magnitude $\vec{u}_0$), too, and its phase relation to the reference Φ_0 does not equal the phase difference between PA signal and reference.* For better visualization of this increasing phase shift while converging to zero analyte, figure (b) additionally illustrates some of the measured values at low analyte concentrations in polar coordinates. The red arrow clearly identifies linearity, but the arrowhead does obviously not coincide with the origin of the coordinate system. In order to accordingly adjust the measured data, an offset correction has to be performed in vector space.† Offset correction (index *oc*) of a data point i can be implemented by

$$\vec{u}_{i,oc} = \vec{u}_i - \vec{u}_0 = \begin{pmatrix} \mathbb{R}\mathrm{e}_i \\ \mathbb{I}\mathrm{m}_i \end{pmatrix} - \begin{pmatrix} \mathbb{R}\mathrm{e}_0 \\ \mathbb{I}\mathrm{m}_0 \end{pmatrix} \tag{1.112}$$

Considering the definition for imaginary and real part of complex quantities

$$\tan \Phi_{i,oc} = \frac{\mathbb{I}\mathrm{m}_{i,oc}}{\mathbb{R}\mathrm{e}_{i,oc}} \tag{1.113}$$

and substituting 1.111 and 1.112 in 1.113 yields to an expression for the offset corrected phase

$$\Phi_{i,oc} = \left| \tan^{-1} \left[\frac{\hat{u}_i \sin \Phi_i - \hat{u}_0 \sin \Phi_0}{\hat{u}_i \cos \Phi_i - \hat{u}_0 \cos \Phi_0} \right] \right| \tag{1.114}$$

Considering the definition for the real part of a complex quantity from 1.111, the offset corrected magnitude thus becomes

$$\vec{u}_{i,oc} = \left| \frac{\mathbb{R}\mathrm{e}_{i,oc}}{\cos \Phi_{i,oc}} \right| = \left| \frac{\hat{u}_i \cos \Phi_i - \hat{u}_0 \cos \Phi_0}{\cos \Phi_{i,oc}} \right| \tag{1.115}$$

Figure 1.14 depicts the same data that was presented in figure 1.13, but after offset correction following equations 1.115 and 1.114. Looking at figure (a), the phase shift towards decreasing analyte concentrations obviously diminished. Actually, some over-compensation might be identified. Besides, the arrowhead in figure (b) fairly matches the origin of the polar coordinate

*The phase difference of the PA signal and the reference itself, however, does not change with analyte concentration.

†Furthermore it is important to ensure stability of the zero value, e.g. no divergence may appear due to temperature drifts.

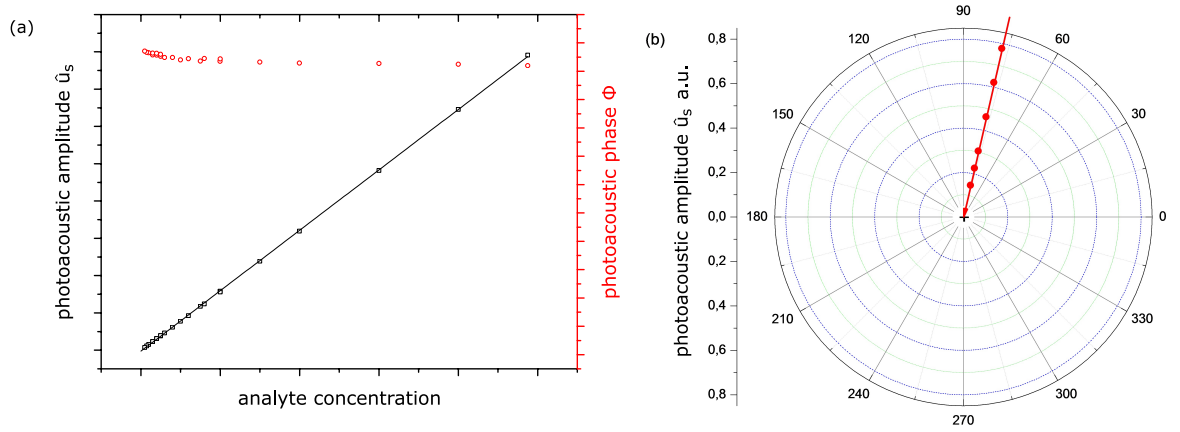

Figure 1.14: Calibration characteristics of a photoacoustic setup after offset correction. (a) Magnitude (black squares) and phase information (red circles) in Cartesian coordinates. (b) Vector signals in polar coordinates.

system. Unless otherwise specified, all measurements that are presented in chapter 4 are based on offset corrected data.

References

[1] M. Tavakoli, A. Tavakoli, M. Taheri and H. Saghafifar, Design, simulation and structural optimization of a longitudinal acoustic resonator for trace gas detection using laser photoacoustic spectroscopy (LPAS), *Optics and Laser Technology*, 42(5):828–838 (2010), ISSN 00303992, doi:10.1016/j.optlastec.2009.12.012, URL `http://dx.doi.org/10.1016/j.optlastec.2009.12.012`.

[2] S. Bernegger and M. Sigrist, *CO-laser photoacoustic spectrocopy of gases and vapors for trace gas analysis*, Phd thesis, ETH Zürich (1988).

[3] J.-P. Besson, *Photoacoustic spectroscopy for multi-gas sensing using near infrared lasers*, Ph.D. thesis, University of Lausanne (2006).

[4] M. Mattiello, *Gas Traces Measurement by Photoacoustic Spectroscopy Using Helmholtz Resonator-Based Sensors*, Ph.D. thesis, University of Lausanne (2008).

[5] T. Starecki, Influence of external acoustic noise on the operation of an open photoacoustic helmholtz cell, *Acta Physica Polonica A*, 114(6 A):199–204 (2008), ISSN 05874246.

[6] M. Suchenek, Influence of the duct shape on the Q-factor of a photoacoustic Helmholtz resonator, *International Journal of Thermophysics*, 32(4):886–892 (2011), ISSN 0195928X, doi:10.1007/s10765-010-0761-5.

[7] V. Zeninari, V. Kapitanov, D. Courtois and Y. Ponomarev, Design and characteristics of a differential Helmholtz resonant photoacoustic cell for infrared gas detection, *Infrared Physics and Technology*, 40(1):1–23 (1999), ISSN 13504495, doi:10.1016/S1350-4495(98)00038-3.

[8] B. Baumann, B. Kost, H. Groninga and M. Wolff, Eigenmodes of Photoacoustic T-Cells, in *COMSOL Multiphysics User's Conference 2005* (Frankfurt, Germany, 2005).

[9] A. Elia, V. Spagnolo, C. D. Franco, P. M. Lugarà and G. Scamarcio, Trace gas sensing using quantum cascade lasers and a fiber-coupled optoacoustic sensor: Application to formaldehyde, *Journal of Physics: Conference Series*, 214(1):012037 (2010), ISSN 1742-6596, doi:10.1088/1742-6596/214/1/012037, URL `http://stacks.iop.org/1742-6596/214/i=1/a=012037`.

[10] A. Miklós, P. Hess and Z. Bozóki, Application of acoustic resonators in photoacoustic trace gas analysis and metrology, *Review of Scientific Instruments*, 72(4):1937–1955 (2001), ISSN 0034-6748, doi:10.1063/1.1353198, URL `http://aip.scitation.org/doi/10.1063/1.1353198`.

[11] A. Miklós, S. Schäfer and P. Hess, Photoacoustic Spectroscopy , Theory, *Encyclopedia of Spectroscopy and Spectrometry*, pages 1815–1822 (1999).

[12] R. H. Johnson, R. Gerlach, L. J. Thomas III and N. M. Amer, Loss mechanisms in resonant spectrophones, *Applied Optics*, 21(1):81 (1982), ISSN 0003-6935, doi:10.1364/AO.21.000081, URL `http://www.ncbi.nlm.nih.gov/pubmed/20372405`.

[13] X. Yin, L. Dong, H. Wu, H. Zheng, W. Ma, L. Zhang, W. Yin, S. Jia and F. K. Tittel, Sub-ppb nitrogen dioxide detection with a large linear dynamic range by use of a differential photoacoustic cell and a 3.5 W blue multimode diode laser, *Sensors and Actuators B: Chemical*, 247:329–335 (2017), ISSN 09254005, doi:10.1016/j.snb.2017.03.058, URL `http://linkinghub.elsevier.com/retrieve/pii/S0925400517304756`.

[14] M. Hippler, C. Mohr, K. A. Keen and E. D. McNaghten, Cavity-enhanced resonant photoacoustic spectroscopy with optical feedback cw diode lasers: A novel technique for ultratrace gas analysis and high-resolution spectroscopy, *Journal of Chemical Physics*, 133(4) (2010), ISSN 00219606, doi:10.1063/1.3461061.

[15] B. Kost, B. Baumann, M. Germer, M. Wolff and M. Rosenkranz, Numerical shape optimization of photoacoustic resonators, *Applied Physics B: Lasers and Optics*, 102(1):87–93 (2011), ISSN 09462171, doi:10.1007/s00340-010-4170-z.

[16] Y.-H. Pao, *Optoacoustic spectroscopy and detection* (Academic Press, New York, 1977), ISBN 9780323158817.

[17] A. Rosencwaig, *Photoacoustics and photoacoustic spectroscopy* (John Wiley and Sons, 1980), volume 57 edition, ISBN 0-471-04495-4.

[18] B. Baumann, B. Kost, M. Wolff and H. Groninga, Modeling and Numerical Investigation of Photoacoustic Resonators, *Recent Advances in Modelling and Simulation*, pages 17–38 (2008).

[19] A. V. Masurkar, *Extensions of quartz-enhanced photoacoustic spectroscopy*, Ph.D. thesis, Massachusetts Institute of Technology. Dept. of Physics. (2009), URL http://dspace.mit.edu/handle/1721.1/51579.

[20] K. Liu, H. Yi, A. A. Kosterev, W. Chen, L. Dong, L. Wang, T. Tan, W. Zhang, F. K. Tittel and X. Gao, Trace gas detection based on off-beam quartz enhanced photoacoustic spectroscopy: Optimization and performance evaluation, *Review of Scientific Instruments*, 81(10):3–8 (2010), ISSN 00346748, doi:10.1063/1.3480553.

[21] M. Giglio, A. Sampaolo, P. Patimisco, H. Zheng, H. Wu, L. Dong, F. K. Tittel and V. Spagnolo, Single-tube on beam quartz-enhanced photoacoustic spectrophones exploiting a custom quartz tuning fork operating in the overtone mode, volume 10111, page 1011107 (2017), doi:10.1117/12.2252368, URL http://proceedings.spiedigitallibrary.org/proceeding.aspx?doi=10.1117/12.2252368.

[22] P. Sievilä, V.-P. Rytkönen, O. Hahtela, N. Chekurov, J. Kauppinen and I. Tittonen, Fabrication and characterization of an ultrasensitive acousto-optical cantilever, *Journal of Micromechanics and Microengineering*, 17(5):852–859 (2007), ISSN 0960-1317, doi:10.1088/0960-1317/17/5/002, URL http://stacks.iop.org/0960-1317/17/i=5/a=002?key=crossref.565a923b56a4f9fd65a01f3f41c7d152.

[23] R. E. Lindley, A. M. Parkes, K. A. Keen, E. D. McNaghten and A. J. Orr-Ewing, A sensitivity comparison of three photoacoustic cells containing a single microphone, a differential dual microphone or a cantilever pressure sensor, *Applied Physics B: Lasers and Optics*, 86(4):707–713 (2007), ISSN 09462171, doi:10.1007/s00340-006-2543-0.

[24] V. Koskinen, J. Fonsen, K. Roth and J. Kauppinen, Progress in cantilever enhanced photoacoustic spectroscopy, *Vibrational Spectroscopy*, 48(1):16–21 (2008), ISSN 09242031, doi:10.1016/j.vibspec.2008.01.013.

[25] J. Uotila, *Use Of The Optical Cantilever Microphone In Photoacoustic Spectroscopy* (2009), ISBN 9789512939114.

[26] J. Y. Tan, F. X. Li, D. Wu, Y. L. Luo and X. X. Yang, *Association of the C3 gene polymorphisms with susceptibility to adult asthma*, Ph.D. thesis, Aalto university, Helsinki, Finnland (2011), doi:10.3760/cma.j.issn.1003-9406.2011.02.018.

[27] C. Project and T. Theisen, Miniaturised photoacoustic gas sensor based on patented interferometric readout and novel photonic integration technologies (MINIGAS), Technical report, Summary report of an European joint project (2011).

[28] J. Peltola, M. Vainio, T. Hieta, J. Uotila, S. Sinisalo, M. Siltanen and L. Halonen, High sensitivity trace gas detection by cantilever- enhanced photoacoustic spectroscopy using a mid-infrared continuous-wave optical parametric oscillator, *Optics Express*, 21(8):2103–2109 (2013), ISSN 1094-4087, doi:10.1364/OE.21.010240.

[29] C. B. Hirschmann, S. Sinisalo, J. Uotila, S. Ojala and R. L. Keiski, Trace gas detection of benzene, toluene, p-, m- and o-xylene with a compact measurement system using cantilever enhanced photoacoustic spectroscopy and optical parametric oscillator, *Vibrational*

Spectroscopy, 68:170–176 (2013), ISSN 09242031, doi:10.1016/j.vibspec.2013.07.004, URL http://dx.doi.org/10.1016/j.vibspec.2013.07.004.

[30] J. Peltola, T. Hieta and M. Vainio, Parts-per-trillion-level detection of nitrogen dioxide by cantilever-enhanced photo-acoustic spectroscopy, *Opt Lett*, 40(13):2933–2936 (2015), ISSN 0146-9592, doi:10.1364/OL.40.002933, URL http://www.ncbi.nlm.nih.gov/pubmed/26125335.

[31] N. Ledermann, P. Muralt, J. Baborowski, M. Forster and J.-P. Pellaux, Piezoelectric Pb(Zr x , Ti 1-x)O3 thin film cantilever and bridge acoustic sensors for miniaturized photoacoustic gas detectors, *Journal of Micromechanics and Microengineering*, 14(12):1650–1658 (2004), ISSN 0960-1317, doi:10.1088/0960-1317/14/12/008, URL http://stacks.iop.org/0960-1317/14/i=12/a=008?key=crossref.4381152431a8f97385e0da3cab3330a3.

[32] B. D. Adamson, J. E. Sader and E. J. Bieske, Photoacoustic detection of gases using microcantilevers, *Journal of Applied Physics*, 106(11):2–5 (2009), ISSN 00218979, doi:10.1063/1.3271157.

[33] D. Gross, W. Hauger and W. Schnell, *Technische Mechanik: Band 2: Elastostatik*, Elastostatik (Springer, 2005), ISBN 9783540243120.

[34] J. Wittenburg, *Festigkeitslehre: ein Lehr-und Arbeitsbuch* (Springer-Verlag, 2011).

[35] J. Adam, *Festigkeitslehre und FEM-Anwendungen: Grundlagen der Festigkeitslehre und Einfuehrung in die Anwendung der Finite-Elemente-Methode* (Huethig, 1991), ISBN 9783778519998.

[36] M. Chaudhary and A. Gupta, Microcantilever-based Sensors, *Def. Sci. J.*, 59(6):634–641 (2009).

[37] M.-s. Kim, J.-h. Choi, J.-H. Kim and Y.-k. Park, Accurate determination of spring constant of atomic force microscope cantilevers and comparison with other methods, *Measurement*, 43(4):520–526 (2010), ISSN 02632241, doi:10.1016/j.measurement.2009.12.020, URL http://linkinghub.elsevier.com/retrieve/pii/S0263224109002681.

[38] N. Blanc, Scanning force microscopy in the dynamic mode using microfabricated capacitive sensors, *Journal of Vacuum Science and Technology B*, 14(2):901–905 (1996), ISSN 0734211X, doi:10.1116/1.589171.

[39] C.-C. Röhlig, *Evaluierung elastischer Eigenschaften von Mikro- und Nanostrukturen*, Ph.D. thesis, Albert-Ludwigs-Universität Freiburg (2011).

[40] A. A. Kosterev, Y. A. Bakhirkin, R. F. Curl and F. K. Tittel, Quartz-enhanced photoacoustic spectroscopy., *Optics letters*, 27(21):1902–1904 (2002), ISSN 0146-9592, doi:10.1364/OL.27.001902.

[41] A. A. Kosterev, United States Patent Patent No .: US 7,245,380 B2 Date of Patent : Jul. 17, 2007 (2007).

[42] A. A. Kosterev and F. K. Tittel, Ammonia detection by use of quartz-enhanced photoacoustic spectroscopy with a near-IR telecommunication diode laser., *Applied optics*, 43(33):6213–6217 (2004), ISSN 0003-6935, doi:10.1364/AO.43.006213.

[43] M. Horstjann, Y. Bakhirkin, A. Kosterev, R. Curl, F. Tittel, C. Wong, C. Hill and R. Yang, Formaldehyde sensor using interband cascade laser based quartz-enhanced photoacoustic spectroscopy, *Applied Physics B*, 79(7):799–803 (2004), ISSN 0946-2171, doi:10.1007/s00340-004-1659-3, URL http://link.springer.com/10.1007/s00340-004-1659-3.

[44] G. Wysocki, A. A. Kosterev and F. K. Tittel, Influence of molecular relaxation dynamics on quartz-enhanced photoacoustic detection of CO2 at 2um, *Applied Physics B: Lasers and Optics*, 85(2-3):301–306 (2006), ISSN 09462171, doi:10.1007/s00340-006-2369-9.

[45] N. Petra, J. Zweck, A. A. Kosterev, S. E. Minkoff and D. Thomazy, Theoretical analysis of a quartz-enhanced photoacoustic spectroscopy sensor, *Applied Physics B: Lasers and Optics*, 94(4):673–680 (2009), ISSN 09462171, doi:10.1007/s00340-009-3379-1.

[46] W. Briese and B. Neubig, Eigenschaften von Schwingquarzen, *Das große Quarzkochbuch* (1997).

[47] A. A. Kosterev, L. Dong, D. Thomazy, F. K. Tittel and S. Overby, QEPAS for chemical analysis of multi-component gas mixtures, *Applied Physics B: Lasers and Optics*, 101(3):649–659 (2010), ISSN 09462171, doi:10.1007/s00340-010-4183-7.

[48] L. Dong, A. A. Kosterev, D. Thomazy and F. K. Tittel, QEPAS spectrophones: Design, optimization, and performance, *Applied Physics B: Lasers and Optics*, 100(3):627–635 (2010), ISSN 09462171, doi:10.1007/s00340-010-4072-0.

[49] A. A. Kosterev, F. K. Tittel, D. V. Serebryakov, A. L. Malinovsky and I. V. Morozov, Applications of quartz tuning forks in spectroscopic gas sensing, *Review of Scientific Instruments*, 76(4):1–9 (2005), ISSN 00346748, doi:10.1063/1.1884196.

[50] K. Liu, X. Guo, H. Yi, W. Chen, W. Zhang and X. Gao, Off-beam quartz-enhanced photoacoustic spectroscopy, *Opt. Lett.*, 34(10):1594–1596 (2009), doi:10.1364/OL.34.001594, URL http://ol.osa.org/abstract.cfm?URI=ol-34-10-1594.

[51] A. A. Kosterev, Y. A. Bakhirkin and F. K. Tittel, Ultrasensitive gas detection by quartz-enhanced photoacoustic spectroscopy in the fundamental molecular absorption bands region, *Applied Physics B*, 80(1):133–138 (2005), ISSN 0946-2171, doi:10.1007/s00340-004-1619-y.

[52] R. Alonso, F. Villuendas, J. Borja and L. A. Barrag, Low-cost , digital lock-in module with external reference for coating glass transmission / reflection spectrophotometer, *Measurement Science and Technology*, 14(5):551–557 (2003).

[53] L. A. Barragán, J. I. Artigas, R. Alonso and F. Villuendas, A modular, low-cost, digital signal processor-based lock-in card for measuring optical attenuation, *Review of Scientific Instruments*, 72(1):247–251 (2001), ISSN 0034-6748, doi:10.1063/1.1333046, URL http://aip.scitation.org/doi/10.1063/1.1333046.

[54] a.a. Dorrington and R. Kunnemeyer, A simple microcontroller based digital lock-in amplifier for the detection of low level optical signals, *Proceedings First IEEE International Workshop on Electronic Design, Test and Applications '2002*, pages 0–2 (2002), doi:10.1109/DELTA.2002.994680.

[55] L. Qian, D. Cheng, J. Zhang, Y. Wang and G. Zheng, Design and analysis of digital lock-in sine-wave amplitude detector based on TMS320C6xEVM, *7th International Conference on Signal Processing*, 3:2545–2548 (2004), doi:10.1109/ICOSP.2004.1442300.

[56] M. Sonnaillon, R. Urteaga, F. Bonetto and M. Ordonez, Implementation of a high-frequency digital lock-in amplifier, in *Canadian Conference on Electrical and Computer Engineering, 2005.*, May, pages 1229–1232 (IEEE, 2005), ISBN 0-7803-8885-2, doi:10.1109/CCECE.2005.1557199, URL `http://ieeexplore.ieee.org/document/1557199/`.

[57] J. Saarela, T. Sorvajärvi, T. Laurila and J. Toivonen, Phase-sensitive method for background-compensated photoacoustic detection of NO2 using high-power LEDs, *Optics express*, 19 Suppl 4(2):A725–A732 (2011), ISSN 1094-4087, doi:10.1364/OE.19.00A725.

1.4 Attenuation effects

Photoacoustic techniques offer several advantages compared to entirely optical based methods, which are summarized on pages 26 and 27. However, PAS also suffers from two major drawbacks, i.e. susceptibility towards ambient noise and attenuation due to interferences with secondary components of the buffer matrix. While the influence of acoustic noise is discussed in chapter 4.1.7 and 4.3.5.3, respectively, the following sections are meant to address those composition dependent interferences.

Several attenuation effects were already considered in chapter 1.3.1 (refer to equation 1.80), as some of them limit the quality factor of acoustic resonators. Shortly summarized, these effects include [1–8]

- thermal and viscous losses due to boundary layer formation,
- diffusion processes,
- friction between bulk molecules,
- scattering caused by inner wall roughness and
- non-perfectly adiabatic sound propagation.

Key parameters of photoacoustic applications thus are the speed of sound c_s, the heat capacity ratio or adiabatic index γ, the thermal conductivity k, the dynamic viscosity μ and the bulk viscosity ξ [5]. However, serious attenuation also results from relaxation processes. In order to understand these contributions, it is unavoidable to treat the underlying mechanisms on a molecular level. By taking into account molecular relaxation, the list of key parameters is further extended by the energies $\mathrm{h}\nu$ and relaxation times τ_ν of the corresponding ro-vibronical states*.

1.4.1 Acoustic attenuation

Analogous to optical absorption (refer to equation 1.2), acoustic attenuation is specified by an attenuation coefficient $\alpha(\omega)$, which causes an initial

*Actually, the major contribution corresponds to vibrational states.

acoustic wave $\hat{p}_0$ to diminish to a final value $\hat{p}$ after propagating a distance x.

$$\hat{p} = \hat{p}_0 \cdot e^{-\alpha(\omega)x} \tag{1.116}$$

Consequently, the dimension of $\alpha(\omega)$ is m^{-1}, while it is mostly specified as the product $\alpha(\omega)\lambda_\mathrm{s}$, where λ_s is the length of the acoustic wave. This representation offers two advantages, i.e. the product is dimensionless and eliminated from baseline drift, which results from linear increase of attenuation with frequency ω_s. Overall acoustic attenuation can be separated into a classical part $\alpha_\mathrm{cl}(\omega)$ and the sum of all contributing molecular processes $\alpha_\nu(\omega)$.

$$\alpha(\omega) = \alpha_\mathrm{cl}(\omega) + \sum_\nu \alpha_\nu(\omega) \tag{1.117}$$

Classical attenuation primarily accounts for losses due to thermal and viscous boundary layer formation [5], thus an analytical expression is given by [6]

$$\alpha_\mathrm{cl}(\omega) = \frac{\omega_\mathrm{s}^2 \eta}{2c_\mathrm{s}} \cdot \left(\frac{4}{3} + \frac{\xi}{\eta} + \frac{\gamma - 1}{\mathrm{Pr}} \right) \tag{1.118}$$

where Pr is the Prandtl number, i.e. the ratio of viscous and thermal diffusion rates. However, this expression might loose its validity regarding frequencies that exceed ∼100 kHz. With regard to higher frequencies, relaxation of rotational states gains influence and has to be considered, too. Attenuation caused by excitation of a vibrational mode ν is represented by

$$\alpha_\nu(\omega) = \left[\frac{\pi(\nu - 1)}{\gamma} \cdot \frac{1}{\lambda_\mathrm{s}} \right] \cdot \left[\frac{\mathrm{c}_{\nu,\mathrm{V}}}{\mathrm{c}_\mathrm{V}} \right] \cdot \left[\frac{\omega_\mathrm{s}\tau_\nu}{1 + (\omega_\mathrm{s}\tau_\nu)^2} \right] \tag{1.119}$$

thus being proportional to the specific heat of the vibrational mode $\mathrm{c}_{\nu,\mathrm{V}}$ (normalized by the total specific heat c_V). Before going into detail of these molecular contributions, the general process of sound propagation has to be considered.

In chapter 1.2.3, the representation of an acoustic wave was derived from light absorption. Propagation of this sound wave through a gaseous medium

causes local areas of repetitive compression followed by dilatation. On a molecular level, these density oscillations result from collisions of molecules. In terms of sound propagation, the average Brownian motion of molecules is superimposed by oscillations about their rest positions, while the frequency equals the frequency of the acoustic wave. The momentum of vibrations is transmitted by molecular collisions, while the time- and location-dependent synergy of the variety of oscillations causes the macroscopic phenomenon of density variation. The momentary speed of the molecules vibrating about their rest positions is called the sound particle velocity. Just to get an idea about the dimensions, its maximum value at rest position is $\sim 5{\cdot}10^{-6}$ m/s in terms of the noise level in a library, while the speed of sound and the mean particle velocity are $\sim$ 350 m/s (refer to 1.61) and $\sim$ 470 m/s (resulting from the relative mean velocity in 1.15 divided by $\sqrt{2}$)* in N_2 at atmospheric conditions, respectively.
However, in order to quantify sound propagation on a molecular level, the rate of collisions Z_{ij} is an important variable, which is based on the relative mean velocity whilst collision. It can be derived from the kinetic theory of gases. Equation 1.15 already provides an expression for the collision of molecules of the same species within pure gas. With respect to a molecule of species i colliding with some molecule of species j, the collision rate takes into account the respective molecular radii r_i and r_j, as well as the masses m_i and m_j. Considering the reduced mass μ_{ij}

$$\mu_{ij} = \frac{m_i \cdot m_j}{m_i + m_j} \tag{1.120}$$

the relative mean velocity becomes

$$v_{\mathrm{m},ij} = \sqrt{\frac{8\mathrm{k_B}T}{\pi\mu_{ij}}} = \sqrt{\frac{8\mathrm{k_B}T(m_i + m_j)}{\pi m_i m_j}} \tag{1.121}$$

Substituting 1.121 and 1.16 in 1.13 yields to

$$Z_{ij} = \frac{1}{\tau_{ij}} = \rho_j \cdot (r_i + r_j)^2 \cdot \sqrt{\frac{8\pi\mathrm{k_B}T(m_i + m_j)}{m_i m_j}} \tag{1.122}$$

*The factor $\sqrt{2}$ takes the motion of the collision partners into consideration.

Taking the example of traces of NO_2 in nitrogen buffer gas, the relative mean velocity and the collision rate thus are calculated to 602 m/s and 9.22 GHz, respectively.* Further considering a relaxation time of NO_2 in N_2 of 2 µs [9], it would take about 18 500 collisions for an excited NO_2 molecule in order to release the internal energy stored from absorption into translational energy, i.e. heat production and photoacoustic signal generation.
Indeed, the kinetic theory of gases accounts for elastic collisions only. Besides transmission of translational energy, however, sound propagation further implies repetitive excitation and relaxation of ro-vibrational internal energy states. Therefore, the theory does not exclusively satisfy a fundamental representation of acoustic wave propagation. Furthermore, it is based on several assumptions, i.e. [3]

- molecules travel through space in a straight line,
- the particles are considered rigid spheres,
- interaction of electron clouds is neglected and
- it solely accounts for quasi-digital hit or miss situations and nothing in between.

To meet the demands of inelastic collisions, the redistribution of potential and kinetic energy whilst converging of two particles has to be considered. Assuming a Lennard-Jones potential (see equation 1.123), figure 1.15 visualizes the process of a non-vibrating ($\nu = 0$) molecule j approaching a vibrational excited ($\nu = 1$) but static molecule i with kinetic energy $1/2mv^2$.

$$V(z) = 4\epsilon \cdot \left[\left(\frac{\sigma_0}{z} \right)^{12} - \left(\frac{\sigma_0}{z} \right)^{6} \right] \tag{1.123}$$

Therein, z is the distance between the collision partners and ϵ is the depth of the potential well. When j approaches i, it gets accelerated by attractive London forces, that are represented by the second term in 1.123. As it passes point A, its velocity reaches a maximum value. After that, it gets decelerated, as the strong repulsive nuclear forces start to take effect (first

*The calculation of Z_{ij} is based on a NO_2 volume ratio of 1 ppmV, whereby N_i hardly affects Z_{ij} regarding volume ratios less than 1000 ppmV. The molecule diameters used for calculation were d(N_2)=3.7 Å and d(NO_2)=5.2 Å (calculated from the 2nd van der Waals coefficient).

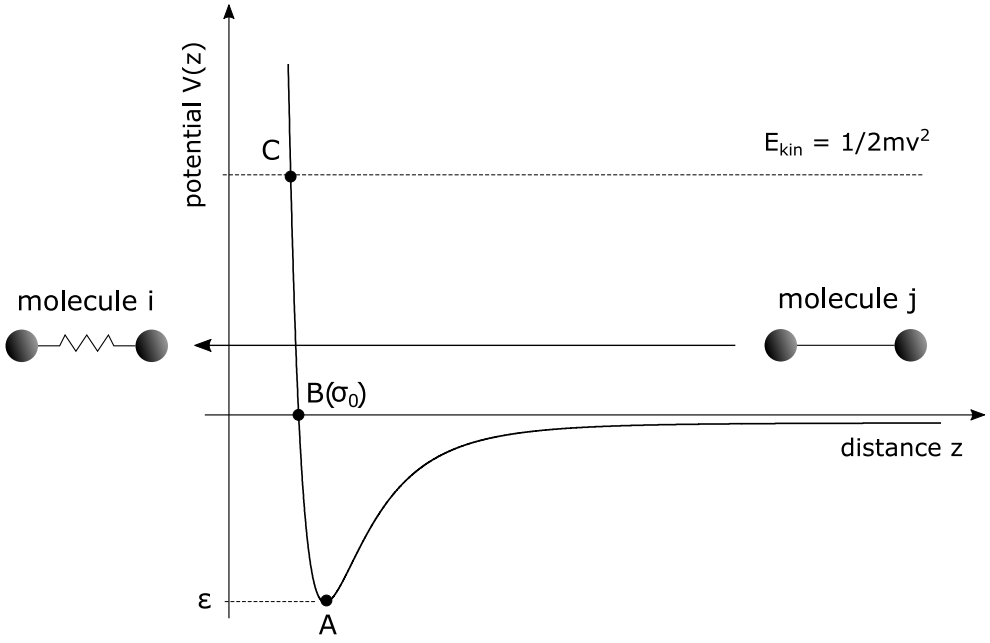

Figure 1.15: Schematic illustration of a molecule j approaching a vibrationally excited molecule i. At first, j experiences an attractive London force (van der Waals force), though by further approaching i, strong repulsive nuclear forces start to take effect. Interaction of both is represented by a Lennard-Jones potential.

term in 1.123). At a distance σ_0 (point B), the velocity of j equals its initial value. Further being decelerated, it finally reaches its turning point C, where the kinetic energy changes its sign and after which, molecule j starts to move away from i. Actually, this turning point is defined as the point of collision.
One of the first approaches to theoretically characterize such inelastic collisions was developed by Landau and Teller [10]. They neglected attractive forces and assumed a simplified potential of the the form

$$V(z) = V_0 \cdot e^{-\alpha z} \tag{1.124}$$

where α represents the strength of repulsive forces. Based on this potential and several further simplifications (for details refer to [3]), the probability P_{10} of a vibrational $\rightarrow$ translational (VT) energy transfer is obtained by

classical time-dependent perturbation theory

$$P_{10} = \exp\left[-3\left(\frac{2\pi^4\mu\nu^2}{\alpha^2 \mathrm{k_B} T}\right)^{\frac{1}{3}}\right] \tag{1.125}$$

where μ is the reduced mass and ν is the oscillator frequency. One important consequence of this equation is the fact, that VT-relaxation becomes less probable at higher oscillation frequencies, i.e. excitation of higher vibrational modes. The reciprocal product of this probability and the collision rate from 1.122 is defined as the VT lifetime of a vibrational excited molecule.

$$\tau_{\mathrm{VT}} = \frac{1}{P_{10} Z_{ij}} \tag{1.126}$$

Aiming at enhancing the Landau-Teller method in order to achieve better consistency with empirical data, various expansions were presented. Without going into detail, the still most commonly used theory was developed by Schwartz, Slawsky and Herzfeld (SSH theory) [11, 12] and further extended by Tanczos [13]. These enhancements obviously also increased the complexity of the model, which nevertheless suffer from discrepancies, especially in terms of distinct polarities or strong population of rotational modes. However, even if a perfect model would be available, the right solutions would still require knowledge about the actual shape of the potentials.

The essence of the last paragraphs is the contribution of molecular rovibrational transitions to the propagation of sound waves. This fact allows to understand what Pierce [14] already observed by the example of gaseous CO_2 in 1925. In terms of velocity measurements in CO_2 containing matrices, he noticed an increase in speed of sound when exceeding certain sound frequencies. One year later, Kneser and Zühlke [15] reproduced these findings on the basis of CO_2 and determined similar effects for N_2O. They made internal energy states accountable for this phenomenon, which is now known as sound dispersion. According to their interpretation, some internal states can not follow compression and dilatation anymore, once a certain frequency is exceeded. This interpretation can be quantified by considering

the dependency of the heat capacity ratio γ on the degrees of freedom d of a species [16]

$$\gamma = \frac{d+2}{d} \tag{1.127}$$

where $3N$ degrees of freedom are available to a molecule that contains N atoms. This definition takes into account three translational and at least two rotational states, while non-linear molecules* actually hold three rotational degrees as well. The remaining number, e.g. $3 \cdot 3 - 3 - 2 = 4$ in terms of CO_2,† corresponds to the vibrational modes that can be excited. Exceeding a given sound frequency, the VT relaxation (refer to 1.126) requires more time than available with respect to one interval of compression followed by dilatation. As a consequence, this VT transition is not further involved in the process of sound propagation. According to equation 1.127, this causes γ to increase, which in turn yields to an increase in speed of sound (refer to equation 1.61). Besides, dispersion comes along with a dissipation of energy.

With regard to figure 1.16, the acoustic frequency of maximum dissipation (black), i.e. the peak value of maximal acoustic attenuation, coincides with the frequency, where dispersion (red) exhibits a maximum in slope. As discussed above, this peak results from molecular attenuation (refer to equation 1.119), while the strong increase in dissipation regarding higher acoustic frequencies arises from classical attenuation (see equation 1.118). Increasing the acoustic frequency beyond the peak of molecular loss causes the attenuation to fall back to its initial value, while dispersion maintains a raised speed of sound.

Regarding CO_2, molecular attenuation peaks at a frequency of $\sim$ 40 kHz [17]‡ with an attenuation of $\alpha \sim 5.3 \cdot 10^{-3}$ m^{-1} considering 400 ppmV CO_2 in N_2 and an acoustic frequency of 32 755 Hz, which is the resonant frequency of the PAC presented in chapter 4.3. Assuming a mean distance of 2 mm, which the sound has to travel from its point of origin to the QTF detector, and further taking into account the resonance amplification of 53 dB (refer

*where N obviously has to be > 2

†i.e. two stretching and two bending vibrations, respectively.

‡considering pure CO_2

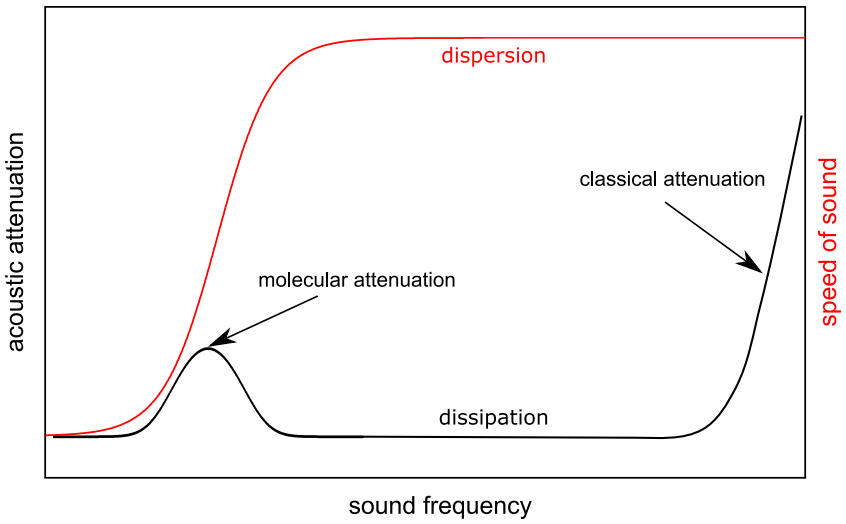

Figure 1.16: Schematic representation of energy dissipation (black) and dispersion (red) depending on frequency of sound. While dissipation causes acoustic attenuation, dispersion yields to an increase of the speed of sound.

to chapter 4.3.3), acoustic attenuation is calculated to cause a loss in photoacoustic signal of $\sim 0.5\%$, which is experimentally validated in chapter 4.3.5.1.
Concluding this section, classical acoustic attenuation can be usually neglected in good approximation in terms of photoacoustic measurements, as it gains significance only above ~ 100 kHz. In contrast, molecular attenuation was pointed out to potentially cause significant signal losses, depending on the concentration of the species, that is accountable for attenuation. However, signal losses due to slow VT processes are much more pronounced, as soon as VT relaxation not only contributes to the propagation of sound, but also constitutes an essential step in the process of photoacoustic signal generation. This issue is known to limit the sensitivity of many photoacoustic applications, hence it is addressed in the following section.

1.4.2 Vibrational-translational (VT) relaxation

Photoacoustic signal generation is generally based on the absorption of light due to excitation of ro-vibrational states. As discussed in section 1.4.1,

the relaxation rate of specific VT processes may be in the order of the modulation frequency, that is applied for PA signal generation. Once the modulation frequency f_{mod} approaches an involved VT relaxation rate, the corresponding internal energy exchange processes are not able to respond fast enough and the energy can not be returned to dilatational disturbance in phase with its oscillation. The critical value for the maximal modulation frequency $f_{\mathrm{mod,max}}$ can be estimated from 1.49. Figure 1.17 visualizes the loss in photoacoustic signal*, which results from exceeding this critical frequency.

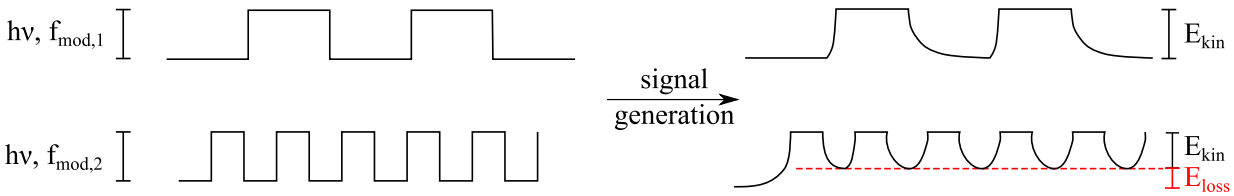

Figure 1.17: Schematic illustration of a signal dip due to exceeding a critical modulation frequency f_{mod}. hν: initial energy input into the system by absorption, E_{kin}: kinetic energy that is accountable for PA signal generation, E_{loss}: energy loss term.

The upper part in figure 1.17 outlines the process of complete conversion of absorbed into kinetic energy, when the criterion $f_{\mathrm{mod,1}} < f_{\mathrm{mod,max}}$ is satisfied. On the contrary, the bottom part illustrates, that increasing the frequency of light modulation beyond a critical value, i.e. $f_{\mathrm{mod,2}} \geq f_{\mathrm{mod,max}}$, causes the kinetic energy, which is released into the system, to diminish. The proportion that no longer contributes to the photoacoustic signal is designated E_{loss}.
In view of preventing such signal losses, table 1.2 provides a collection of several VT relaxation lifetimes gathered from literature and references therein. The relaxation times were either empirically or theoretically obtained, but always relate to a standard pressure of 1 atm. With regard to details about the vibrational modes, references to literature are provided. By knowing these individual relaxation lifetimes, equation 1.128 allows to calculate the total VT relaxation rate of an analyte i in a multi-component mixture,

*that is represented by a loss in kinetic energy

which additionally contain the species k, l and m in the relative concentration* $\rho_{i,k,l,m}$.†

Table 1.2: List of vibrational-translational lifetimes of several collision species. Vibrationally excited molecules are marked with an *. The values are either empirically or theoretically obtained, but always relate to standard pressure (1 atm).

Collision species	τ_{VT}	Collision species	τ_{VT}
$N_2^* + N_2$	1 s [3, 18]	$CO^* + CO$	10 - 100 ms [19]
	1 ms [20]	$CO^* + C_3H_6$	316 ns [21]
	300 µs [5]	$H_2O^* + H_2O$	37 ns [22]
$N_2^* + H_2O$	9.1 µs [3]	$H_2O^* + N_2$	714 ns [23]
$O_2^* + O_2$	16 ms [3]	$H_2O^* + O_2$	16.7 µs [23]
	1.6 ms [23]	$NO^* + NO$	500 ns [24]
	2 ms [5]	$NO^* + N_2$	300 µs [22, 24]
	15.9 ms [18]	$NO^* + air$	8 µs [24]
$O_2^* + N_2$	25 ms [3]	$NO^* + O_2$	1.5 µs [24]
	2.5 ms [23]	$NO^* + H_2O$	26 ns [24]
$O_2^* + H_2O$	910 ns [3, 18, 23]	$N_2O^* + N_2$	1.7 µs [25]
$O_2^* + CH_4$	1 µs [3, 18]	$N_2O^* + C_3H_6$	12 ns [21]
$O_2^* + He$	43 µs [3, 18]	$CH_4^* + CH_4$	1.25 µs [18]
$CO_2^* + CO_2$	5.7 µs [26]	$CH_4^* + N_4$	12.5 µs [18]
	2.9 - 21.8 µs [19]	$CH_4^* + O_2$	7.7 µs [18]
	3.53 µs [27]		200 ns [5, 18]
	5.6 µs [23]	$NH_3^* + NH_3$	112 ns [21]
$CO_2^* + N_2$	7, 11 µs [25]		98 ns [28]
	2 - 16 µs [19]	$C_3H_6^* + C_3H_6$	6 ns [21]
$CO_2^* + H_2O$	2 ns [19]		
	2.4 ns [23]		
$CO_2^* + He$	160 - 250 ns [19]		
$CO_2^* + air$	29 µs [23]		

*Actually, ρ is the volume number density, thus it follows $\sum_j \rho_j = 1$ (refer to equation 1.5).
†provided that intermolecular vibrational-vibrational transitions can be neglected (refer to section 1.4.3).

$$\frac{1}{\tau_i} = \rho_i \cdot \frac{1}{\tau_{ii}} + \rho_k \cdot \frac{1}{\tau_{ik}} + \rho_l \cdot \frac{1}{\tau_{il}} + \rho_m \cdot \frac{1}{\tau_{im}} \tag{1.128}$$

As an example, the relaxation rate of 1 ppmV NO in synthetic air (79% N_2 and 21% O_2) at 25° Celsius and a relative humidity of 50 %rh was calculated to 734 kHz, i.e. a relaxation lifetime of ~ 1.4 µs. Although all VT lifetimes that were used for this calculation were presented by Bernegger and Sigrist [24], the calculated lifetime still deviates from the value of 8 µs, which is listed for NO relaxation in air (refer to table 1.2). This discrepancy might be attributable to the fact, that this value was obtained for dry air, while the calculation resulting from 1.128 considers humidified air.
Indeed, H_2O is well known to support relaxation processes, thus it is often used as an additive in photoacoustic analysis. By this means, Dong et al. [29] were able to increase the PA signal whilst CO quantification by a factor of 10, when adding 2.2 % H_2O. They also identified no further supportive effect, once exceeding an amount of 0.2 % H_2O for CO_2 detection [30] and reported about H_2O causing a signal increase with regard to NO quantification as well [22]. Kosterev et al. [31] determined a signal enhancement by a factor of 30 when adding 1 % H_2O while N_2O and CO detection, respectively. Further references that deal with the acceleration of VT processes due to H_2O can be found in literature [18, 27, 32–36]. Finally, there are other components that were reported to have convenient effects on photoacoustic measurements as well, e.g. SF_6 [31, 37–39]*, C_2H_2 [40], CH_4 [3] or NH_3 [41]. Indeed, beyond slow relaxation of the analyte itself, intermolecular vibrational-vibrational (VV) transfer processes have to be considered, too. Several references report about fast VV energy transfer to components of the buffer gas, which for their part suffer from slow VT relaxation, thus subsequently causing a loss of photoacoustic amplitude. Therefore, the following section addresses VV processes that have to be considered.

*In [31], SF_6 was reported to support N_2O and CO_2, but not CO detection.

1.4.3 Vibrational-vibrational (VV) transfer processes and kinetic cooling

With regard to table 1.2, critical VT processes are self-quenching of N_2 and O_2 as well as relaxation of vibrationally excited O_2 by collision with N_2. As these are the main components in air, the sensitivity of photoacoustic air quality monitoring applications might be limited by slow VT processes of N_2 and O_2, whenever VV transfer to those two species occurs. In order to be able to estimate the hierarchy of ongoing processes, table 1.3 further lists several lifetimes of intermolecular and intramolecular (marked with an **!**) VV transitions, respectively.

Table 1.3: List of vibrational-vibrational lifetimes of several collision species. Vibrationally excited molecules are marked with an *, while the energy levels of the corresponding vibrations are indicated in brackets. The values relate to standard pressure (1 atm). Intramolecular transitions are labeled with an **!**, while the other processes represent intermolecular transitions.

Energy transfer reaction	τ_{VV}
! $HCl^*(\nu_2) + HCl \rightarrow 2\ HCl^*(\nu_1)$	14 ns [3]
$HCl^*(\nu_1) + O_2 \rightarrow HCl + O_2^*(\nu_1)$	12 µs [3]
$HCl^*(\nu_1) + N_2 \rightarrow HCl + N_2^*(\nu_1)$	1.5 µs [3]
$N_2^*(\nu_1) + H_2O \rightarrow N_2 + H_2O^*(\nu_2)$	10 µs [23]
$N_2^*(\nu_1) + O_2 \rightarrow N_2 + O_2^*(\nu_1)$	6.7 ms [23]
$H_2O^*(\nu_2) + O_2 \rightarrow H_2O + O_2^*(\nu_1)$	22 ns [23]
$O_2^*(\nu_1) + CH_4 \rightarrow O_2 + CH_4^*(\nu_4)$	50 ns [18]
$CH_4^*(\nu_4) + O_2 \rightarrow CH_4 + O_2^*(\nu_1)$	33 ns [18]
$CO_2^*(\nu_3) + N_2 \rightarrow CO_2 + N_2^*(\nu_1)$	56 ns [23]
! $CO_2^*(\nu_3) + CO_2 \rightarrow CO_2^*(\nu_2) + CO_2$	6.7 µs [23]
! $CO_2^*(\nu_3) + N_2 \rightarrow CO_2^*(\nu_2) + N_2$	16.7 µs [23]
! $CO_2^*(\nu_3) + O_2 \rightarrow CO_2^*(\nu_2) + O_2$	16.7 µs [23]
! $CO_2^*(\nu_1) + M \rightarrow CO_2^*(\nu_2) + M$ (M: N_2,O_2,CO_2)	2 ns [23]

The most intensively studied process of photoacoustic signal attenuation

due to VV transitions concerns the detection of CO_2 and is also referred to as kinetic cooling [3, 20, 23, 41]. Kinetic cooling is actually a special case, as it not only withdraws energy from successive PA signal generation, but also causes effective cooling of the sample, i.e. the loss of available energy exceeds the amount of energy that was initially absorbed. This might be surprising at first, but becomes comprehensible when considering hot band transitions of CO_2. Those transitions are a consequence of anharmonicity and they are generally based on the excitation of vibrational modes $\nu > 0$. Regarding kinetic cooling of CO_2, absorption yields to an $\nu_2 \rightarrow \nu_3$ transition, which has a short lifetime of 56 ns, before a VV exchange to N_2 takes place.* Referring to table 1.3, this process is faster than intramolecular VV exchange processes back to the ν_2 state and considering table 1.2, it is also faster than all VT processes of CO_2, except for collisions with H_2O, thus H_2O is often used to counteract kinetic cooling phenomena. Anyway, in cases where no supporting additive such as H_2O is present, the amount of energy that corresponds to a $\nu_0 \rightarrow \nu_3$ transition is no longer available for signal generation, although only the amount $\nu_2 \rightarrow \nu_3$ was supplied by absorption. This means that light absorption causes effective cooling rather than effective heating of the sample, which results in a phase shift of the photoacoustic signal by π. This phase shift can be observed by continuously adding H_2O to a mixture of CO_2 in N_2, as it lowers the probability of VV transitions to N_2 and thus induces a transition from effective cooling to effective heating. Simultaneous to a 180° phase shift, the photoacoustic amplitude might decrease to some extend, before it finally increases with H_2O concentration. This effect of signal drop prior to signal increase was determined to be even more pronounced at higher modulation frequencies [41].

Besides CO_2 detection, the quantification of further species was reported to suffer from kinetic cooling, too, e.g. CH_4 [42], CO or N_2O [31]. To be precise, these actually are no kinetic cooling effects, as they do not base on hot band transitions [3], i.e. no 180° phase shift occurs. Nevertheless, they were determined to cause some kind of effective cooling†, as the total vibrational

*The participating vibrational modes have very similar energies ($\nu_3(CO_2) = 2349\ cm^{-1}, \nu_1(N_2) = 2330\ cm^{-1}$).

†The degree of cooling is much less than in case of CO_2.

energy of the products exceeds the one of the educts. The required energy difference is borrowed from the bath of rotational and translational modes [31].
As mentioned above, the second major component in ambient air, namely oxygen, has already been identified to cause losses in photoacoustic signal due to VV energy exchange, too. Besson [3] for example reported the PA signal of CH_4 detection to decrease almost by two orders of magnitude, when replacing the buffer gas N_2 by O_2. Also with regard to NO_2 quantification, O_2 was previously stated responsible for PA signal attenuation. Kalkman and van Kesteren [9] identified a signal decrease of $\sim$ 20 % by adding 50 %V of O_2 to a mixture of NO_2 in N_2. Regarding the interpretation of their findings, they assumed an energy transfer from the vibrational ν_3 mode of the electronic $^2A_1$ state, i.e. 1617 cm^{-1}, to the ν_2 mode of O_2, i.e. 1556 cm^{-1}. Moreover, they formed a rate equation considering the VT and VV relaxation rates k_i of NO_2 collisions with N_2 and O_2, respectively, and determined

$$k_{\mathrm{VV,NO_2 \rightarrow O_2}} = 1.5 \cdot k_{\mathrm{VT,NO_2 \rightarrow N_2}} \tag{1.129}$$

$$k_{\mathrm{VV,NO_2 \rightarrow O_2}} = 0.3 \cdot k_{\mathrm{VT,NO_2 \rightarrow O_2}} \tag{1.130}$$

When considering a mixing ratio of N_2:O_2 that equals 1:1, 20 % of molecular collisions would cause a signal loss due to VV transition from NO_2 to O_2, while the remaining 80 % of collisions would contribute to heat production by VT relaxation of NO_2 with N_2. These conclusions coincide with the experimental data of photoacoustic NO_2 detection in air, which is presented in chapter 4.3.5.1. Concluding the theoretical chapter of this thesis, the following section shortly addresses a further pitfall of PA signal attenuation, i.e. acoustic detuning. Although detuning is more trivial than molecular relaxation effects, it might account for a major proportion of total signal loss in terms of photoacoustic trace gas air quality monitoring, if no remedial action is taken.

1.4.4 Acoustic detuning

Most common photoacoustic measuring schemes are based on acoustic resonance amplification (refer to chapter 1.3.1). Equation 1.72 provides an expression in order to calculate the frequencies of combined longitudinal, radial and azimuthal modes, which can be excited within a resonator tube. For the special case of solely 1$^{\text{st}}$ mode longitudinal excitation* (refer to figure 1.7 on page 47), equation 1.73 constitutes a simplified form, where f_{res} only depends on the speed of sound and the length of the tube. As the dimensions of the tube are fixed, acoustic detuning can only result from changes in the speed of sound c_{s}. According to 1.61, the proportionalities of c_{s} are stated to be $\propto T^{0.5}$, $\propto M^{-0.5}$ and $\propto (\text{C}_p/\text{C}_V)^{0.5}$.
Temperature effects either have to be avoided by controlling the temperature of the PAC or they have to be monitored and the modulation frequency has to be adjusted accordingly. In view of a varying buffer gas composition, which in turn causes changes in the mean molar mass M, monitoring becomes more complex, as every single component would have to be monitored separately. An alternative way to observe changes in composition might be to simultaneously exploit the phase information of the photoacoustic signal, as detuning also yields to a shifting in phase, rather than to signal attenuation only. Either way, suitable countermeasures are adjusting the modulation frequency or readjusting resonance by adapting the temperature of the PAC. For practical implementation regarding acoustic detuning due to variations in H_2O concentration within the buffer gas, refer to chapter 4.2.6.1. Although, adding H_2O to the mixture further inversely affects the heat capacity ratio, the increase in density overweights and thus the speed of sound decreases.
Moreover, the heat capacity ratio (and consequently the speed of sound) may increase in case of acoustic dispersion (refer to chapter 1.4.1 and especially to figure 1.16 therein). Since dispersion only has minor influence on PA signal loss compared to energy dissipation due to acoustic attenuation, however, it may be excluded from consideration in terms of air quality monitoring at standard conditions. Another quantity that might affect the speed of sound is the pressure of the sample. Considering air an ideal gas

*All of the PAC geometries that are presented in this work are based on solely longitudinal excitation.

(refer to 1.131), pressure p and density ρ changes act contrary on c_s (see 1.132), thus they are canceling each other out after all (refer to 1.133).

$$pV = n\mathrm{R}T \tag{1.131}$$

$$c_\mathrm{s} = \sqrt{\frac{\gamma p}{\rho}} \tag{1.132}$$

$$p = \frac{m}{V} \cdot \frac{1}{M} \cdot \mathrm{R}T = \rho \cdot \frac{\mathrm{R}T}{M} \tag{1.133}$$

Assuming non-ideal conditions, i.e. taking intermolecular interactions and the molar volume of the molecules into account, this pressure independence looses validity. By analogy with sound dispersion, perfect adiabatic conditions can be assumed, hence, pressure dependency is neglected in terms of photoacoustic analysis at standard conditions.
Having discussed the influences, that might cause detuning of acoustic resonators, it has to be noted, that countermeasures can not be applied that easily in terms of double resonant systems (refer to chapter 1.3.3 and especially to figure 1.11 therein). Common photoacoustic arrangements, which additionally utilize resonant detectors, e.g. QEPAS schemes (see chapter 1.10), feature high quality factors of mechanical resonance, compared to relatively low-Q acoustic amplification. If such systems are exposed to variations in the speed of sound, the photoacoustic signal attenuates as the total quality factor decreases, but the resonance frequency remains the one of high-Q mechanical amplification. Therefore, adjusting the frequency of modulation is not applicable. Chapter 4.3.5.2 relates to this issue and provides a detailed discussion.

References

[1] Y.-H. Pao, *Optoacoustic spectroscopy and detection* (Academic Press, New York, 1977), ISBN 9780323158817.

[2] A. Miklós, P. Hess and Z. Bozóki, Application of acoustic resonators in photoacoustic trace gas analysis and metrology, *Review of Scientific Instruments*, 72(4):1937–1955 (2001),

ISSN 0034-6748, doi:10.1063/1.1353198, URL http://aip.scitation.org/doi/10.1063/1.1353198.

[3] J.-P. Besson, *Photoacoustic spectroscopy for multi-gas sensing using near infrared lasers*, Ph.D. thesis, University of Lausanne (2006).

[4] B. Baumann, B. Kost, M. Wolff and H. Groninga, Modeling and Numerical Investigation of Photoacoustic Resonators, *Recent Advances in Modelling and Simulation*, pages 17–38 (2008).

[5] R. H. Johnson, R. Gerlach, L. J. Thomas III and N. M. Amer, Loss mechanisms in resonant spectrophones, *Applied Optics*, 21(1):81 (1982), ISSN 0003-6935, doi:10.1364/AO.21.000081, URL http://www.ncbi.nlm.nih.gov/pubmed/20372405.

[6] A. Cottet, Y. Neumeier, D. Scarborough, O. Bibik and T. Lieuwen, Acoustic absorption measurements for characterization of gas mixing, *The Journal of the Acoustical Society of America*, 116(4):2081 (2004), ISSN 00014966, doi:10.1121/1.1785631.

[7] S. G. Ejakov, S. Phillips, Y. Dain, R. M. Lueptow and J. H. Visser, Acoustic attenuation in gas mixtures with nitrogen: experimental data and calculations, *J Acoust Soc Am*, 113(4 Pt 1):1871–1879 (2003), ISSN 00014966, doi:10.1121/1.1559177, URL http://www.ncbi.nlm.nih.gov/pubmed/12703699.

[8] R. D. Kamm, Detection of weakly absorbing gases using a resonant optoacoustic method, *Journal of Applied Physics*, 47(8):3550–3558 (1976), ISSN 00218979, doi:10.1063/1.323153.

[9] J. Kalkman and H. van Kesteren, Relaxation effects and high sensitivity photoacoustic detection of NO2 with a blue laser diode, *Applied Physics B*, 90(2):197–200 (2008), ISSN 0946-2171, doi:10.1007/s00340-007-2895-0, URL http://link.springer.com/10.1007/s00340-007-2895-0.

[10] E. E. Nikitin and J. Troe, 70 years of Landau-Teller theory for collisional energy transfer. Semiclassical three-dimensional generalizations of the classical collinear model, *Phys. Chem. Chem. Phys.*, 10(11):1483–1501 (2008), ISSN 1463-9076, doi:10.1039/B715095D, URL http://xlink.rsc.org/?DOI=B715095D.

[11] R. N. Schwartz, Z. I. Slawsky and K. F. Herzfeld, Calculation of Vibrational Relaxation Times in Gases, *The Journal of Chemical Physics*, 20(10):1591–1599 (1952), ISSN 0021-9606, doi:10.1063/1.1700221, URL http://aip.scitation.org/doi/10.1063/1.1700221.

[12] J. T. Vanderslice and S. Weissman, On the Theory of Vibrational Energy Exchange, *The Journal of Chemical Physics*, 37(10):2247–2249 (1962), ISSN 0021-9606, doi:10.1063/1.1732993, URL http://aip.scitation.org/doi/10.1063/1.1732993.

[13] F. I. Tanczos, Calculation of Vibrational Relaxation Times of the Chloromethanes, *The Journal of Chemical Physics*, 25(3):439–447 (1956), ISSN 0021-9606, doi:10.1063/1.1742943, URL http://aip.scitation.org/doi/10.1063/1.1742943.

[14] G. W. Pierce, Piezoelectric Crystal Oscillators Applied to the Precision Measurement of the Velocity of Sound in Air and CO2 at High Frequencies, *Proceedings of the American Academy of Arts and Sciences*, 60(5):271–302 (1925), ISSN 01999818, URL `http://www.jstor.org/stable/25130055`.

[15] H. O. Kneser and J. Zühlke, Einstelldauer der Schwingungsenergien bei CO2 und N2O, *Zeitschrift für Physik*, 77(9-10):649–652 (1932), ISSN 1434-6001, doi:10.1007/BF01330888, URL `http://dx.doi.org/10.1007/BF01330888`.

[16] D. a. Bohn, Environmental effects on the speed of sound, *Journal of the Audio Engineering Society*, 36(4):223–231 (1988).

[17] B. Van der Weerd, *Entwicklung und Charakterisierung von CO2-Sensoren für die Bestimmung der CO2-Eliminierung während extrakorporaler Membranoxygenierung*, Ph.D. thesis, University of Regensburg (2016).

[18] S. Schilt, J.-P. Besson and L. Thévenaz, Near-infrared laser photoacoustic detection of methane: the impact of molecular relaxation, *Applied Physics B*, 82(2):319–328 (2006), ISSN 0946-2171, doi:10.1007/s00340-005-2076-y, URL `http://link.springer.com/10.1007/s00340-005-2076-y`.

[19] N. Truong, S. Buescher, F. Kuehnemann and M. A. Harith, Detecting Carbon Monoxide (CO) With Photoacoustic Spectroscopy: The Role of Molecular Collision Dynamics, *AIP Conference Proceedings*, 1172(1):3–8 (2009), doi:10.1063/1.3250106, URL `http://aip.scitation.org/doi/abs/10.1063/1.3250106`.

[20] F. J. Harren, G. Cotti, J. Oomens and S. t. L. Hekkert, Photoacoustic Spectroscopy in Trace Gas Monitoring, in *Encyclopedia of Analytical Chemistry*, pages 2203–2226 (John Wiley and Sons, Ltd, Chichester, UK, 2000), ISBN 0471976709, doi:10.1002/9780470027318.a0718, URL `http://doi.wiley.com/10.1002/9780470027318.a0718`.

[21] A. A. Kosterev, Y. A. Bakhirkin, F. K. Tittel, S. Blaser, Y. Bonetti and L. Hvozdara, Photoacoustic phase shift as a chemically selective spectroscopic parameter, *Applied Physics B: Lasers and Optics*, 78(6):673–676 (2004), ISSN 0946-2171, doi:10.1007/s00340-004-1519-1.

[22] L. Dong, V. Spagnolo, R. Lewicki and F. K. Tittel, Ppb-level detection of nitric oxide using an external cavity quantum cascade laser based QEPAS sensor, *Optics Express*, 19(24):24037 (2011), ISSN 1094-4087, doi:10.1364/OE.19.024037.

[23] P. L. Meyer and M. W. Sigrist, Atmospheric pollution monitoring using CO2-laser photoacoustic spectroscopy and other techniques, *Review of Scientific Instruments*, 61(7):1779–1807 (1990), ISSN 00346748, doi:10.1063/1.1141097.

[24] S. Bernegger and M. Sigrist, *CO-laser photoacoustic spectrocopy of gases and vapors for trace gas analysis*, Phd thesis, ETH Zürich (1988).

[25] A. Glière, J. Rouxel, M. Brun, B. Parvitte, V. Zéninari and S. Nicoletti, Challenges in the design and fabrication of a lab-on-a-chip photoacoustic gas sensor., *Sensors (Basel, Switzerland)*, 14(1):957–974 (2014), ISSN 14248220, doi:10.3390/s140100957.

[26] M. Wallmann, Die Einstelldauer der Schwingungswärme in CO2 in Abhängigkeit von Fremdgaszusätzen und vom Druck, *Annalen der Physik*, 413(7):671–681 (1935), ISSN 00033804, doi:10.1002/andp.19354130704, URL http://doi.wiley.com/10.1002/andp.19354130704.

[27] R. Lewicki, G. Wysocki, A. A. Kosterev and F. K. Tittel, Carbon dioxide and ammonia detection using 2 mu m diode laser based quartz-enhanced photoacoustic spectroscopy, *Applied Physics B-Lasers and Optics*, 87(1):157–162 (2007), ISSN 0946-2171, doi:10.1007/s00340-006-2474-9.

[28] N. Petra, J. Zweck, A. A. Kosterev, S. E. Minkoff and D. Thomazy, Theoretical analysis of a quartz-enhanced photoacoustic spectroscopy sensor, *Applied Physics B: Lasers and Optics*, 94(4):673–680 (2009), ISSN 09462171, doi:10.1007/s00340-009-3379-1.

[29] L. Dong, R. Lewicki, K. Liu, P. R. Buerki, M. J. Weida and F. K. Tittel, Ultra-sensitive carbon monoxide detection by using EC-QCL based quartz-enhanced photoacoustic spectroscopy, *Applied Physics B: Lasers and Optics*, 107(2):275–283 (2012), ISSN 09462171, doi:10.1007/s00340-012-4949-1.

[30] L. Dong, A. A. Kosterev, D. Thomazy and F. K. Tittel, Compact portable QEPAS multi-gas sensor, in M. Razeghi, R. Sudharsanan and G. J. Brown (editors), *Proc. SPIE 2011*, volume 7945, page 79450R (2011), ISBN 9780819484826, ISSN 0277786X, doi:10.1117/12.875108, URL http://proceedings.spiedigitallibrary.org/proceeding.aspx?articleid=722094.

[31] A. A. Kosterev, Y. A. Bakhirkin and F. K. Tittel, Ultrasensitive gas detection by quartz-enhanced photoacoustic spectroscopy in the fundamental molecular absorption bands region, *Applied Physics B*, 80(1):133–138 (2005), ISSN 0946-2171, doi:10.1007/s00340-004-1619-y.

[32] A. A. Kosterev, Y. A. Bakhirkin, F. K. Tittel, S. McWhorter and B. Ashcraft, QEPAS methane sensor performance for humidified gases, *Applied Physics B: Lasers and Optics*, 92(1):103–109 (2008), ISSN 09462171, doi:10.1007/s00340-008-3056-9.

[33] Y. Ma, R. Lewicki, M. Razeghi and F. K. Tittel, QEPAS based ppb-level detection of CO and N2O using a high power CW DFB-QCL., *Optics express*, 21(1):1008–19 (2013), ISSN 1094-4087, doi:10.1364/OE.21.001008, URL http://www.ncbi.nlm.nih.gov/pubmed/23388995.

[34] V. Spagnolo, A. A. Kosterev, L. Dong, R. Lewicki and F. K. Tittel, NO trace gas sensor based on quartz-enhanced photoacoustic spectroscopy and external cavity quantum cascade laser, *Applied Physics B-Lasers and Optics*, 100(1):125–130 (2010), ISSN 0946-2171, doi:10.1007/s00340-010-3984-z.

[35] G. Wysocki, A. A. Kosterev and F. K. Tittel, Influence of molecular relaxation dynamics on quartz-enhanced photoacoustic detection of CO2 at 2um, *Applied Physics B: Lasers and Optics*, 85(2-3):301–306 (2006), ISSN 09462171, doi:10.1007/s00340-006-2369-9.

[36] X. Yin, L. Dong, H. Wu, H. Zheng, W. Ma, L. Zhang, W. Yin, S. Jia and F. K. Tittel, Sub-ppb nitrogen dioxide detection with a large linear dynamic range by use of a differential photoacoustic cell and a 3.5 W blue multimode diode laser, *Sensors and Actuators B: Chemical*, 247:329–335 (2017), ISSN 09254005, doi:10.1016/j.snb.2017.03.058, URL http://linkinghub.elsevier.com/retrieve/pii/S0925400517304756.

[37] S. Gray, A. Liu, F. Xie and C.-e. Zah, Detection of nitric oxide in air with a 5.2 μm distributed-feedback quantum cascade laser using quartz-enhanced photoacoustic spectroscopy., *Optics express*, 18(22):23353–23357 (2010), ISSN 1094-4087, doi:10.1364/OE.18.023353.

[38] A. A. Kosterev, F. K. Tittel, D. V. Serebryakov, A. L. Malinovsky and I. V. Morozov, Applications of quartz tuning forks in spectroscopic gas sensing, *Review of Scientific Instruments*, 76(4):1–9 (2005), ISSN 00346748, doi:10.1063/1.1884196.

[39] M. M. J. W. Van Herpen, A. K. Y. Ngai, S. E. Bisson, J. H. P. Hackstein, E. J. Woltering and F. J. M. Harren, Optical parametric oscillator-based photoacoustic detection of CO2 at 4.23 um allows real-time monitoring of the respiration of small insects, *Applied Physics B: Lasers and Optics*, 82(4):665–669 (2006), ISSN 09462171, doi:10.1007/s00340-005-2119-4.

[40] J. H. Doty, A. A. Kosterev and F. K. Tittel, Recent Advances in Resonant Optothermalacoustic Detection, *Quantum*, 7945:1–5 (2011), ISSN 0277786X, doi:10.1117/12.875105.

[41] R. a. Rooth, a. J. Verhage and L. W. Wouters, Photoacoustic measurement of ammonia in the atmosphere: influence of water vapor and carbon dioxide., *Applied optics*, 29(25):3643–3653 (1990), ISSN 0003-6935, doi:10.1364/AO.29.003643.

[42] F. G. C. Bijnen, F. J. M. Harren, J. H. P. Hackstein and J. Reuss, Intracavity CO laser photoacoustic trace gas detection: cyclic CH4, H2O and CO2 emission by cockroaches and scarab beetles, *Applied Optics*, 35(27):5357 (1996), ISSN 0003-6935, doi:10.1364/AO.35.005357, URL https://www.osapublishing.org/abstract.cfm?URI=ao-35-27-5357.

Chapter 2

Simulation

Synopsis
Chapter 2 (Simulation) presents a variety of calculations and simulations, which were carried out in order to

- determine critical values of excitation (refer to section 2.1),
- enhance the concept of practical implementation regarding PAC design (refer to sections 2.2 – 2.4) and
- identify expedient approaches in view of further development steps (refer to section 2.5), respectively.

2.1 Critical values of excitation

Chapter 1.2.1 already dealt with the introduction of a simplified two-level rate equation, which provides the basis for a mathematical derivation of photoacoustic signal generation. Since various approximations were assumed during derivation, this section aims at identifying the limits of those approximations.
In equation 1.43, the ground state of this two-level system was supposed to be far more densely populated than the excited state at any point in time during signal generation. However, this assumption might be considered valid only in terms of moderate light intensities. As this work is based on photoacoustic NO_2 detection by utilizing a high power diode laser, the approximation was already verified in figure 1.6. This section moreover is intended to identify the maximum laser intensity, which must not be exceeded in terms of NO_2 excitation at 450 nm.
Equation 1.48 provides an expression for the time-dependent population of the excited state $\chi_1(t)$ as a function of the total number of analyte molecules χ within an illuminated volume V_{il} and of light intensity I_0, which in turn is defined* as the ratio of optical power P_0 and illuminated cross-sectional area† A_{b}, i.e. $\pi\,(d_{\mathrm{b}}/2)^2$. Thus, the population ratio $\chi_1(t)/\chi$ was calculated depending on one of the quantities P_0 and d_{b}, while the other was fixed to 1.4 W and 1 mm‡, respectively.

*A collimated beam is assumed for illumination.
†defined at FWHM of the intensity profile
‡Those are the set values of the experiments presented in chapter 4.

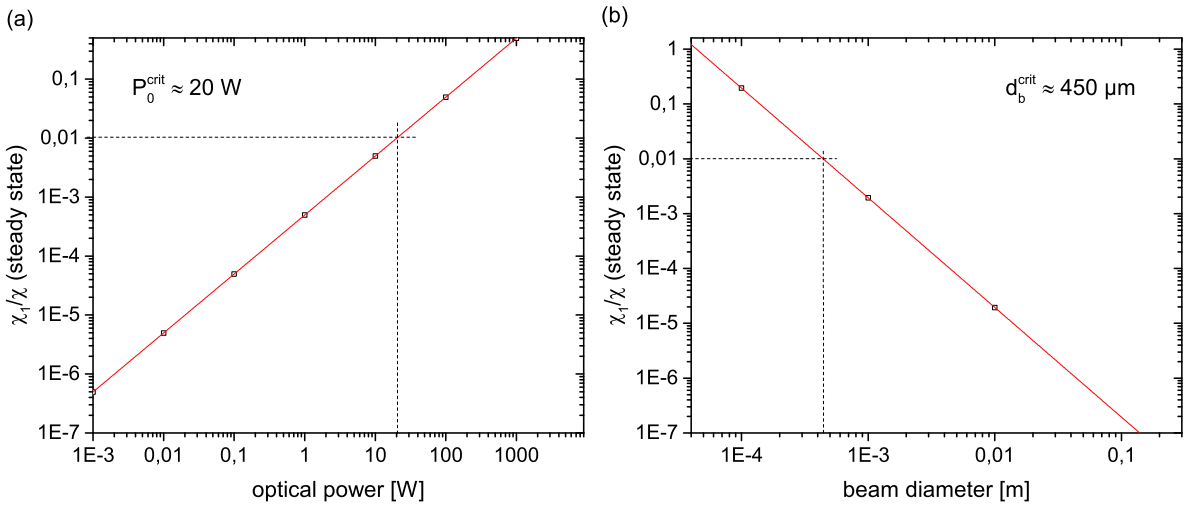

Figure 2.1: Critical values of illumination specified at 1 % steady state population of the excited state. Either optical power (a) or beam diameter (b) was changed, while the other was set to P_0=1.4 W and d_b=1 mm, respectively.

The critical values of laser power and beam diameter then were defined at 1 % population of the excited state for $\lim_{t\to\infty}(\chi_1(t)/\chi)$, i.e. steady state condition. Figure 2.1 depicts optical power and beam diameter affecting the population ratio. The critical values were specified to $P_0^{\mathrm{crit}} = 20$ W of laser power at 1 mm beam diameter and $d_\mathrm{b}^{\mathrm{crit}} = 450$ µm beam diameter at 1.4 W laser power, respectively. Going beyond these critical values is indicated to not further meet the requirement which is given by equation 1.43.

Equation 1.48 reveals another quantity which affects the population ratio, namely the lifetime of the excited state* τ_e. Regarding the calculations illustrated in figure 2.1, the lifetime of excited NO_2 molecules was considered $2 \cdot 10^{-6}$ s [1]. However, chapters 1.4.2 and 1.4.3 already provide a discussion about the phenomenon of decelerating non-radiative relaxation in the presence of certain components, e.g. H_2O or O_2. For this reason, the population ratio was additionally calculated depending on the relaxation time (for the given values of light intensity). Figure 2.2 outlines this dependency and illustrates a critical lifetime of $\tau_\mathrm{n}^{\mathrm{crit}} \approx 20$ µs.

*The lifetime of the excited state τ_e can be equated with the lifetime of non-radiative relaxation τ_n (refer to chapter 1.2.1).

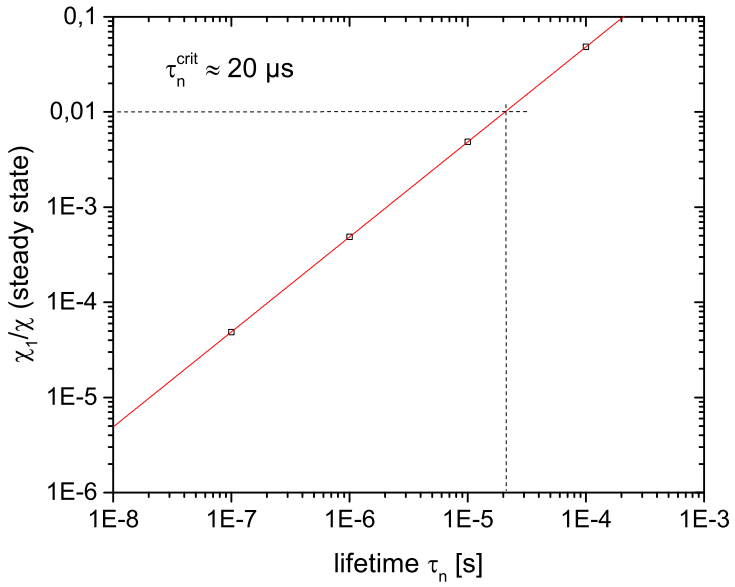

Figure 2.2: Critical lifetime of non-radiative relaxation τ_n^{crit} specified at 1 % steady state population. Optical power and beam diameter was set to P_0=1.4 W and d_b=1 mm, respectively.

Thus the lifetime of non-radiative relaxation may be increased by one magnitude of order without affecting the approximation which was stated in equation 1.43. This critical lifetime, however, corresponds to a maximum modulation frequency of 5 kHz according to equation 1.49. Exceeding this frequency would cause signal attenuation, as the analyte molecules would not be able to relax completely prior to de novo excitation (refer to chapter 1.4.2). As a consequence, critical lifetimes in photoacoustics are often limited by modulation instead of population ratio.

Minimum detectable increase in temperature

As already discussed in chapter 1.2, photoacoustic spectroscopy can be considered a calorimetric measurement, because photoacoustic signal generation results from the heat that is released into the medium after absorption. This section is meant to quantify the increase in temperature ΔT within a photoacoustic cell, resulting from heat input ΔH. Thermodynamics provide a general expression which links these quantities:

$$\mathrm{C_p} = \left(\frac{\partial H}{\partial T}\right)_{\mathrm{p,N}}$$
$$\mathrm{d}H = \int \mathrm{C_p}\mathrm{d}H$$

$$\Delta H = \mathrm{C_p}(T - T_0) = \mathrm{C_p}\Delta T \tag{2.1}$$

The isobar heat capacity $\mathrm{C_p}$ within 2.1 is defined as the product of specific molar heat $\mathrm{c_p}$ and the amount of substance. Considering the medium within the photoacoustic cell with volume V_{PAC} an ideal gas, it follows

$$\mathrm{C_p} = \mathrm{c_p} \cdot \frac{V_{\mathrm{PAC}}}{V_{\mathrm{m}}} \tag{2.2}$$

By further assuming that every analyte molecule, which was excited by absorption, releases its energy through molecular collisions, the corresponding heat input is given by

$$\Delta H = \lim_{t\to\infty} \chi_1(t) \cdot \mathrm{hc_0}\bar{\nu}_{\mathrm{ph}} \tag{2.3}$$

which again contains the steady state condition $\lim_{t\to\infty} \chi_1(t)$ (refer to 1.48). Substituting 2.3 together with 1.40 and 2.2 in 2.1 finally yields to

$$\Delta T = \frac{\chi\sigma(\bar{\nu})P_0\tau_{\mathrm{n}}}{\pi\left(\frac{d_{\mathrm{b}}}{2}\right)^2 \mathrm{c_p}\frac{V_{\mathrm{PAC}}}{V_{\mathrm{m}}}} \tag{2.4}$$

which can be further simplified by means of 1.5 and 1.35 to

$$\Delta T = \frac{4\mathrm{N_A}\sigma(\bar{\nu})P_0\tau_{\mathrm{n}}}{\mathrm{c_p}\pi d_{\mathrm{PAC}}^2} \cdot N_{\mathrm{i}} \tag{2.5}$$

Equation 2.5 thus can be used to calculate the increase in temperature depending on the analyte volume ratio N_{i}, where $\mathrm{N_A}$ is the Avogadro constant, $\sigma(\bar{\nu})$ is the absorption cross-section of the analyte at wavenumber $\bar{\nu}$, P_0 is the optical power of the light source*, τ_{n} is the lifetime of the excited state, $\mathrm{c_p}$ is the specific isobar molar heat capacity of the medium and d_{PAC} is the

*This must not be mistaken for the averaged mean power, i.e. only half P_0.

diameter of the photoacoustic tube-shaped cell. Equation 2.5 is considered valid in terms of moderate modulation frequencies (refer to equation 1.49), sufficiently short lifetimes of the excited state and moderate light intensities (refer to equation 1.43 and associated discussion). Moreover, no losses due to gas flow or transfer of heat with the walls of the PAC (i.e. non-adiabatic losses) were taken into consideration, which both would cause the calculated value of ΔT to further decrease.

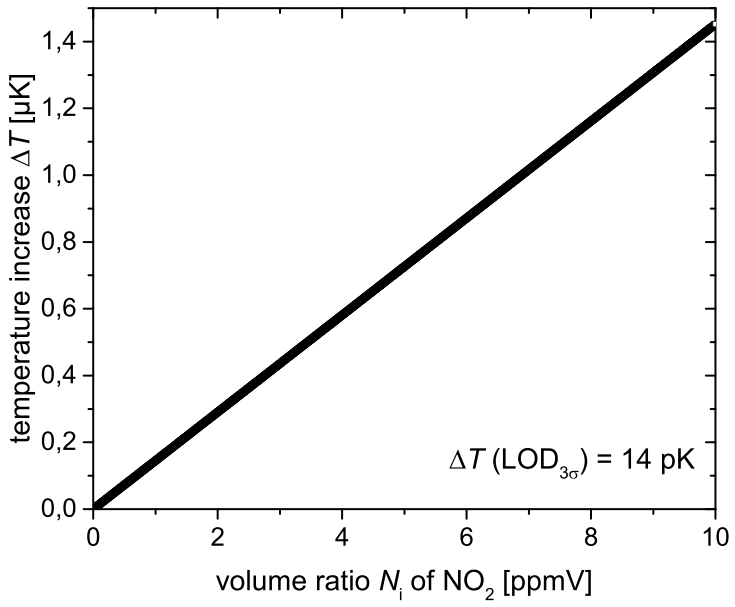

Figure 2.3: Calculation of the increase in temperature whilst photoacoustic detection of NO_2 using the PAC presented in chapter 4.2.

Figure 2.3 illustrates this dependency of ΔT at the example of a series of photoacoustic measurements that are presented in chapter 4.2.5.2. Therein, the limit of detection was empirically determined to 98 pptV (3σ) NO_2. By means of equation 2.5, this concentration was calculated to cause an increase in temperature of merely 14 pK (in words: "*pico Kelvin*"). This calculation points out the outstanding capabilities of photoacoustic techniques as they allow to measure such small energy input into a system, which only causes that astonishing small increase in temperature. Obviously, temperature increase on this scale cannot be dissolved by classical methods of thermometry.

2.2 Acoustic resonance amplification

All geometries of photoacoustic cells that are presented in chapter 4 are based on acoustic resonance amplification. More precisely, they are designed in a tube shape for first mode longitudinal resonance excitation. Equation 1.73 provides an expression to calculate the peak amplification frequencies of longitudinal resonances depending on the length of the tube. However, page 47 already contains a discussion regarding the phenomenon of node shifting, which may produce considerable deviations from 1.73. To shortly summarize, node shifting results from various effects, which individually cause the nodes of acoustic pressure either to move inside the tube, or away from its openings into the surrounding volume. This phenomenon is not actually relevant in view of solely acoustic amplification, as the peak frequency can be determined empirically and the laser modulation can be adjusted. In terms of double resonant amplification (for a theoretical consideration refer to chapter 1.3.3, for experimental results to chapters 4.3 and 4.4), however, the resonance frequencies of acoustic and mechanical amplification have to be harmonized. As a matter of cost and time, it is obviously untenable to perform successive frequency fine tuning without previous simulation. For this reason, a series of simulations was performed in preparation for developing the double resonant off-beam QEPAS scheme, that is presented in chapter 4.3. All eigenfrequency simulations were carried out using the software COMSOL Multiphysics (version 4.2, module *pressure acoustics*). The tubes were chosen to be cut from hypodermic needles, which were specified to consist of stainless steel, with an inner diameter of 1.5 mm and a wall thickness of 250 µm. In view of acoustic coupling to the mechanically resonant detector, i.e. a quartz tuning fork, it was envisaged to cut an opening slit into the resonator. The width of this slit was fixed to 150 µm regarding all simulations. In order to achieve realistic results, loss mechanisms were considered by defining a surrounding air volume at standard conditions, i.e. $p = 1$ atm and $T = 20$ °C. Based on those fixed starting values, the resonance frequency was supposed to be simulated depending on the tube length l_{tube} and the opening slit length l_{slit}, respectively. To obtain this three-dimensional dependency, two interlaced parametric sweeps were performed and the first three longitudinal eigenfrequencies of the system

were calculated for every pair of ($l_{\mathrm{tube}}/l_{\mathrm{slit}}$) variates. The values for l_{tube}- and l_{slit}-simulation ranged from 4 to 6 mm and from 0.4 to 0.8 mm, respectively. This resulted in a total of ∼1000 simulation cycles, yet only the 1$^{\mathrm{st}}$ modes of longitudinal resonance are addressed in this context.

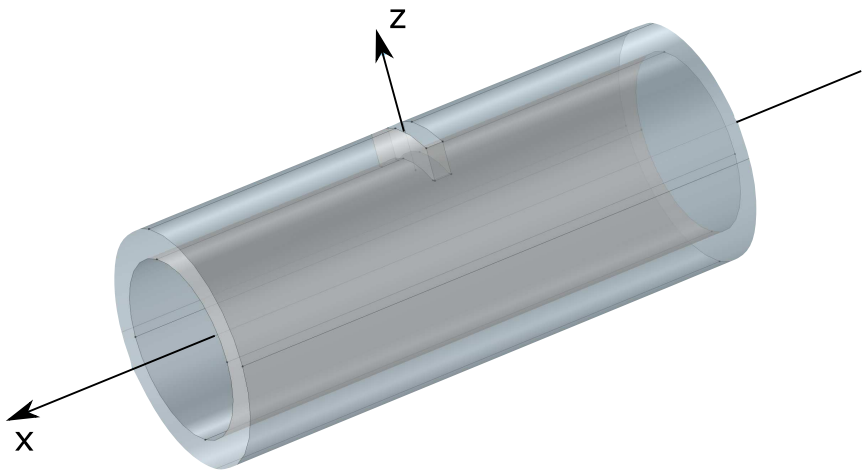

Figure 2.4: Drawing of a resonator tube, that was used for acoustic eigenfrequency simulation. The tube is orientated towards the cylinder axis x, its inner diameter is 1.5 mm and its wall thickness is 0.25 mm, respectively. An opening slit was added at half its length for acoustic coupling to the detector, which has to be conceived approaching from the z-axis.

Figure 2.4 illustrates the tube resonator, which constitutes the basis for simulation. The tube is orientated towards the cylinder axis x, while acoustic coupling by means of an opening slit is ensured towards the z-axis. For evaluation and presentation of the simulated data, a software routine was written in MATLAB-MathWorks. For this purpose, the data was exported in ASCII (American Standard Code for Information Interchange) format, thus be imported into the MATLAB routine as matrices. Actually, the routine offers two program modes:

i. The first mode allows to calculate one of the three variables f_{res}, l_{tube} and l_{slit} by specifying values for the remaining two quantities. The search value is then obtained by interpolation (command *griddata*).

The result matrix is presented in three-dimensional coordinates (command *scatter3*), while the search value is highlighted in color.

ii. The second mode enables the user to enter a target modulation frequency and in view of visualization, it can be switched between the functional dependencies $l_{\text{tube}} := \text{func}(l_{\text{slit}})$ and $l_{\text{slit}} := \text{func}(l_{\text{tube}})$. The results, i.e. all pairs of values that implicate the specified frequency, are presented three-dimensionally by the intersection of two surfaces, while the cutting edge of intersection is additionally plotted in two dimensions.

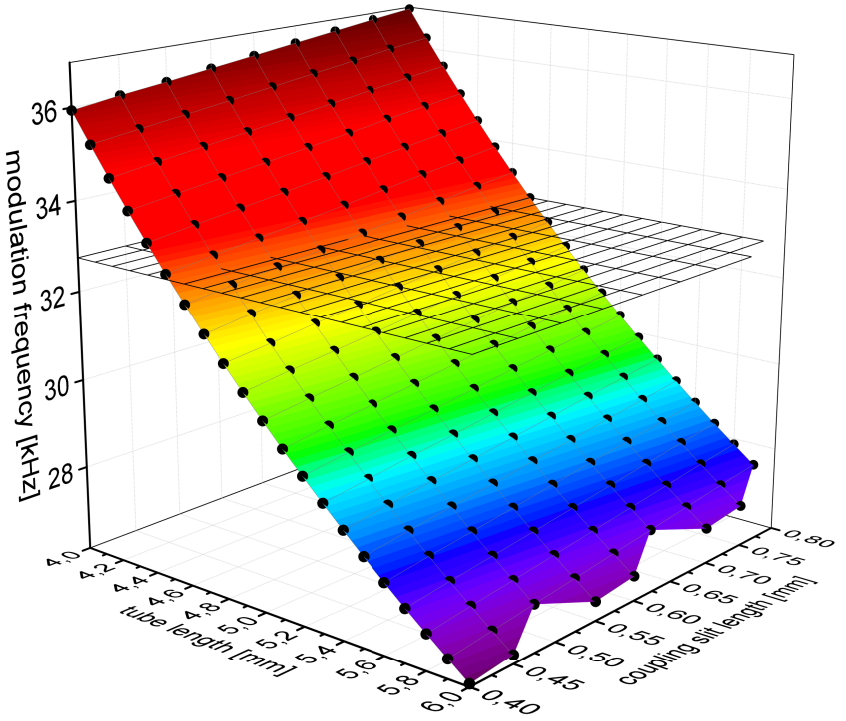

Figure 2.5: Three-dimensional colored surface plot, which illustrates the modulation frequency dependency on the tube- and the slit-length, respectively. The black spheres represent an interpolation of the elements of the simulation result matrix and the color coding further highlights the resonance frequency. The plane grid constitutes a constant frequency of 32 752.5 Hz.

Analogous to this second mode, Figure 2.5 illustrates the intersection of the simulated data with a plane depicting a constant frequency of 32 752.5 Hz. This is the frequency of resonant oscillation of the tuning forks in air, which

was experimentally determined in advance. Within figure 2.5, the result matrix elements are represented by black spheres and the color of the surface plot additionally highlights the modulation frequency. The intersection of the two surfaces is again plotted in two dimensions within figure 2.6.

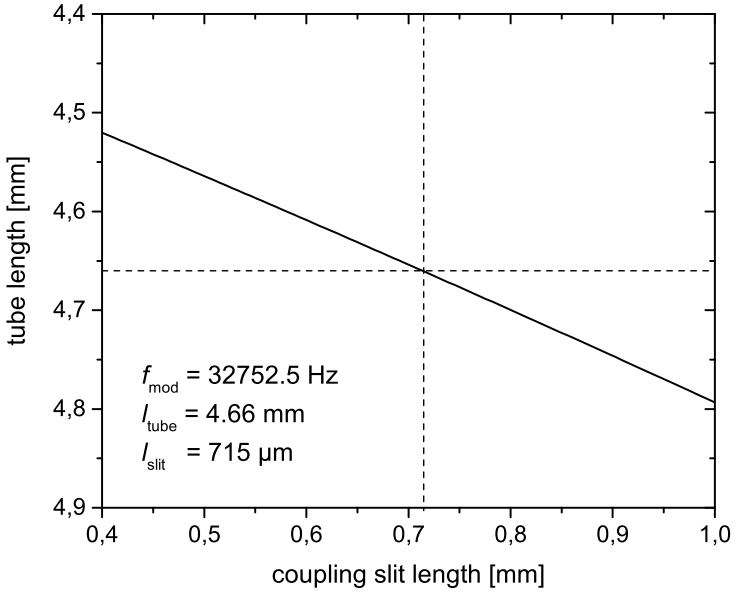

Figure 2.6: Delineation of those pairs of tube- and slit-lengths that ensure a resonance frequency of 32 752.5 Hz. In view of further development, the optimum values were defined to $l_{\mathrm{tube}} = 4.66$ mm and $l_{\mathrm{slit}} = 715$ µm.

More precisely, the functional dependencies of the intersection in figure 2.5 were identified to

$$l_{\mathrm{tube}} = 0.032502 \cdot l_{\mathrm{slit}}^2 + 0.40995 \cdot l_{\mathrm{slit}} + 4.351 \tag{2.6}$$

$$l_{\mathrm{slit}} = -0.35755 \cdot l_{\mathrm{tube}}^2 + 5.5243 \cdot l_{\mathrm{tube}} - 17.2651 \tag{2.7}$$

and figure 2.6 outlines an extrapolation of the upper dependency. Every pair of values represented by the plot in figure 2.6 is expected to ensure a resonance frequency of 32 752.5 Hz. In view of PAC development, the length of the tube was arbitrarily specified to 4.66 mm, thus the optimal length of the opening slit was calculated to 715 µm. The fabrication of resonator tubes was based on these values, however, a variety of tubes with values scattering about these medians were realized in order to experimentally proof

the validity of simulation. Indeed, within the PAC that is characterized in chapter 4.3, a resonator with a slit length of 890 µm was utilized, which was determined to cause the highest amplification. One potential cause The hypodermic needles, which were actually used as resonators, have a diameter of 1.6 mm instead of 1.5 mm, which was assumed for simulation. However, the deviation is not necessarily attributed to a mismatch of simulation and empirical data at all. For a lack of technical feasibility, it was neither possible to investigate the resonance characteristics of the individual tubes, nor can it be assumed with certainty that the mounting position of QTF and resonator was exactly the same with regard to the particular experiments. Since total amplification of double resonant systems also depends on the efficiency of sound coupling, the results of the experiments may also simply be attributed to more efficient acoustic coupling to some extend.

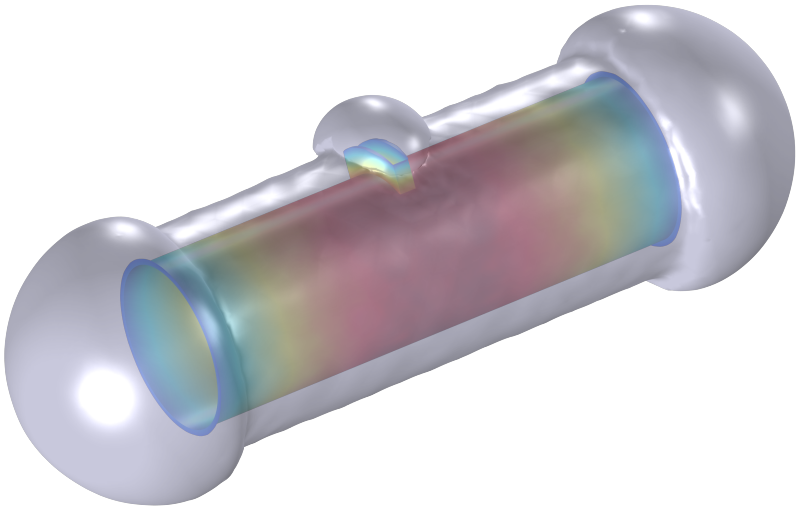

Figure 2.7: Graphical representation of the acoustic pressure field (highlighted in rainbow colors) within a resonator tube, superimposed by an isobaric surface.

Figure 2.7 visualizes the 1st longitudinal resonance of the tube geometry that was identified to cause the highest amplification in combination with a QTF detector. The acoustic pressure field that prevails inside the resonator is highlighted in rainbow colors and besides, it is superimposed by an isobaric surface. This graphical representation obviously illustrates the

phenomenon of node shifting, which was already discussed on page 47 in detail. Considering figure 2.7, it becomes clear that the tube openings cause the nodes of acoustic pressure to shift into the surrounding medium, which, however, is compensated by the coupling slit to some extend.

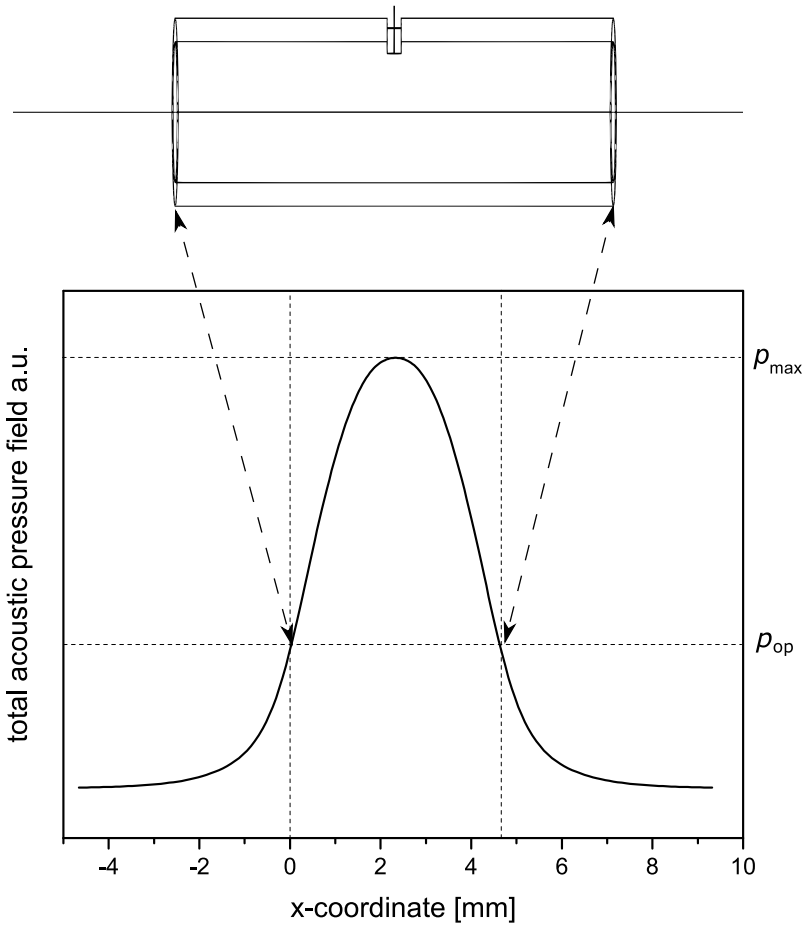

Figure 2.8: Qualitative graphical representation of the total acoustic pressure field along the cylinder axis of an acoustic resonator tube.

Another delineation that verifies node shifting is presented in figure 2.8. The upper part of the figure shows the tube in side view and below, the total acoustic pressure field is plotted along the x-axis (for orientation refer to 2.4). The diagram identifies, that the acoustic pressure p_{op} still remains to some extend at the tube openings (For comparison, p_{max} is the pressure peak value at half of the resonator length). By analogy, figure 2.9 further shows the pressure drop along the z-axis, i.e. the direction of sound coupling through the opening slit to the detector. Therein, p_{in} is the pressure on the

inside and p_{out} is the pressure on the outside of the resonator. Concluding this section, it has to be noted that figures 2.8 and 2.9 are by-products of eigenfrequency analysis. It is highly recommended not to interpret them in a quantitative way, as the pressure is normalized to some value that is not known to the author. In order to make quantitative statements about absolute pressure conditions within acoustic resonators, more complex simulations have to be performed, rather than only eigenfrequency studies.

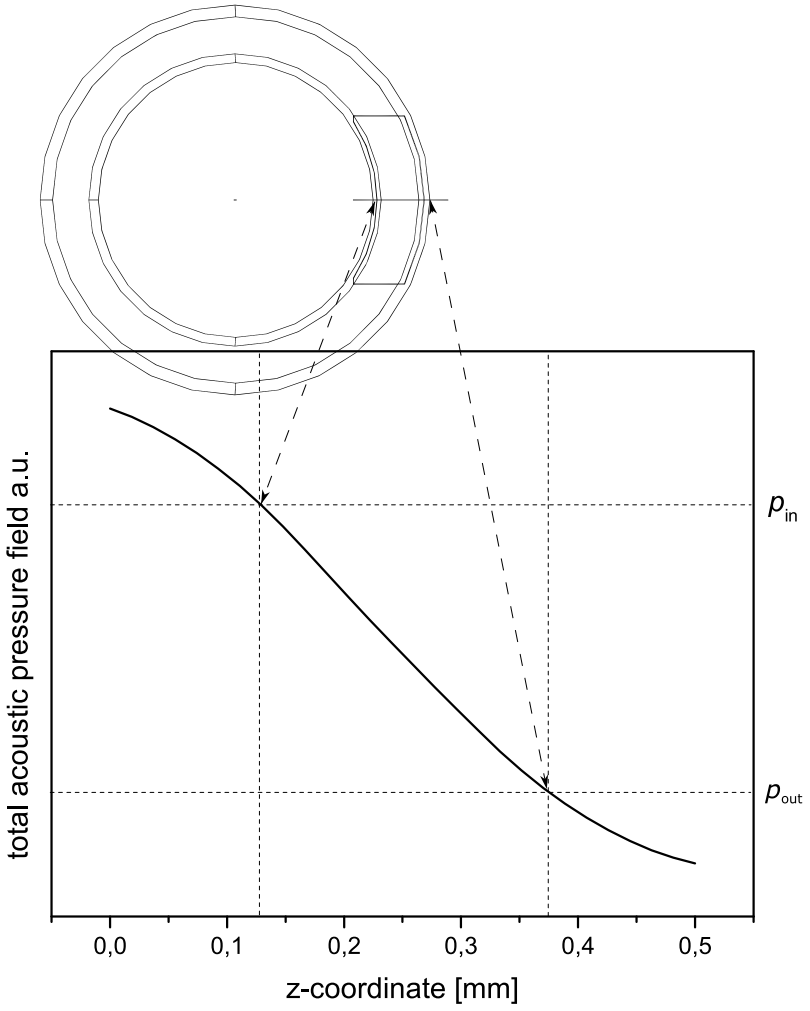

Figure 2.9: Qualitative graphical representation of the pressure drop along the z-axis, i.e. the direction of sound coupling through the opening slit to the detector.

2.3 Mechanical resonance amplification

This section introduces a further series of eigenfrequency simulations regarding a second double resonant photoacoustic system, which is presented in chapter 4.4. This double resonant scheme is referred to as μPAS (miniaturized photoacoustic sensor chip) and it is based on an arrangement that is commonly named CEPAS (cantilever enhanced photoacoustic spectroscopy) in literature. In accordance with the QEPAS scheme presented in 1.3.3, the μPAS design offers double resonant amplification by combining acoustic resonators and mechanically resonant detectors. In terms of eigenfrequency simulation of acoustic resonance, the methods described in chapter 2.2 were applied to a glass material, as the resonator is etched into a Borofloat substrate. This section further addresses the eigenfrequency simulation of mechanical resonant amplification, which is gained from a cantilever beam. Again, the software COMSOL Multiphysics was used to simulate the frequencies of resonant vibration of the beam. According to equation 1.94, these frequencies depend on the elastic modulus E and the density ρ of the material. As the cantilever is made of a silicon substrate in crystal face (110), E and ρ were set to 169 GPa and to 2329 kg/m^3, respectively.
A first approach of realistic simulation involved several attempts of defining a surrounding air volume on the lines of chapter 2.2. However, this did not lead to reasonable and reliable results. Without going into detail, neither about these simulation approaches nor about details regarding the issues that arose, the following enumeration is only meant to shortly list the problems that occurred:

i. The simulations yielded several resonant modes of the cantilever that were superimposed by wobbling of the air volume, whereby the actual beam vibration could hardly be identified.

ii. These modes that finally were assumed to specify cantilever vibration widely varied from those obtained by 1.94, whereas it is known from QTFs, that frequency blue-shifting due to loss mechanisms should not contribute that much.

iii. Not even the proportionalities of frequency dependence complied with theory.

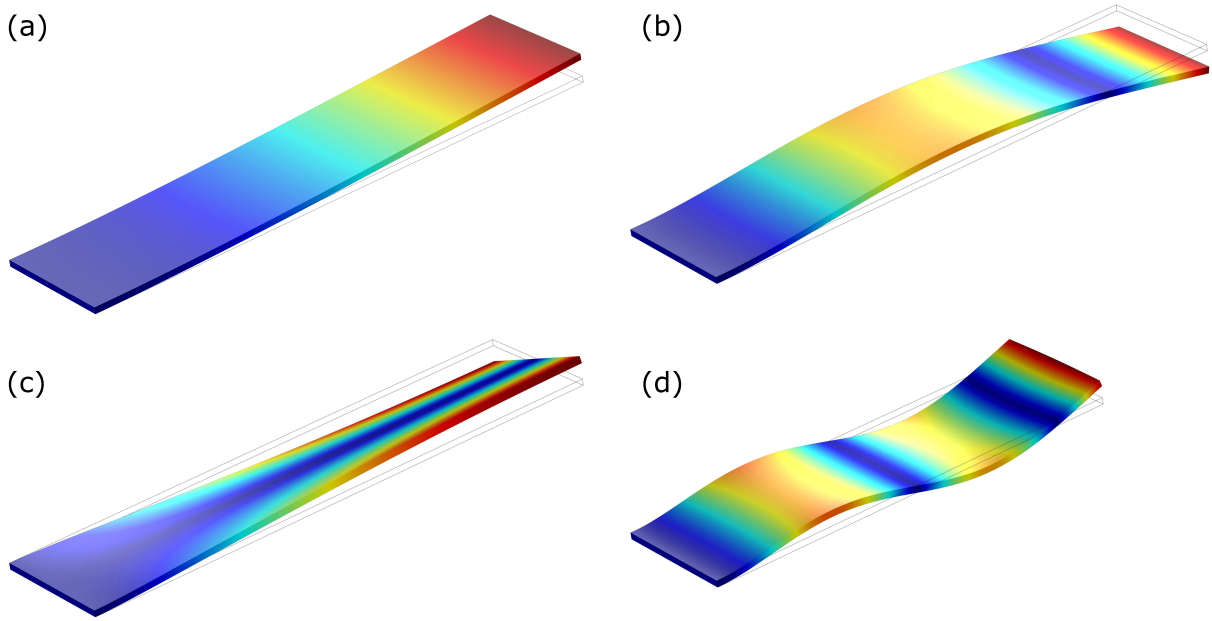

Figure 2.10: Illustration of the first four resonant vibrations of a cantilever beam. (a): 1st bending vibration. (b): 2nd bending vibration. (c): 1st torsional vibration. (d): 3rd bending vibration.

For these reasons, further simulations were performed assuming vacuum instead. Figure 2.10 visualizes the first four resonant vibrations of a cantilever beam, i.e. the first two bending, the fundamental torsional and third bending vibration. Considering a length of 1 mm, a width of 300 µm and a thickness of 15 µm, the corresponding resonance frequencies were simulated to 20 964 Hz, 130 983 Hz, 142 011 Hz and 388 320 Hz, respectively. Since the higher harmonics of vertical vibrations as well as the fundamental torsional vibration hold resonance frequencies exceeding 100 kHz, only the fundamental vertical vibration is further considered. With regard to equation 1.94, this 1st mode should not depend on the width of the cantilever, which could be verified by simulation in good approximation. Increasing the width from 100 µm to 300 µm was simulated to only cause a relative increase in frequency of 8 ‰.
In addition to the simulations, the frequency f_{mod} dependency on the thickness t and the length l of the cantilever was calculated by 1.94. In order to reduce temporal expenditure, a MATLAB script was written, that presents the data similar as described in section 2.2. Figure 2.11 illustrates this three-

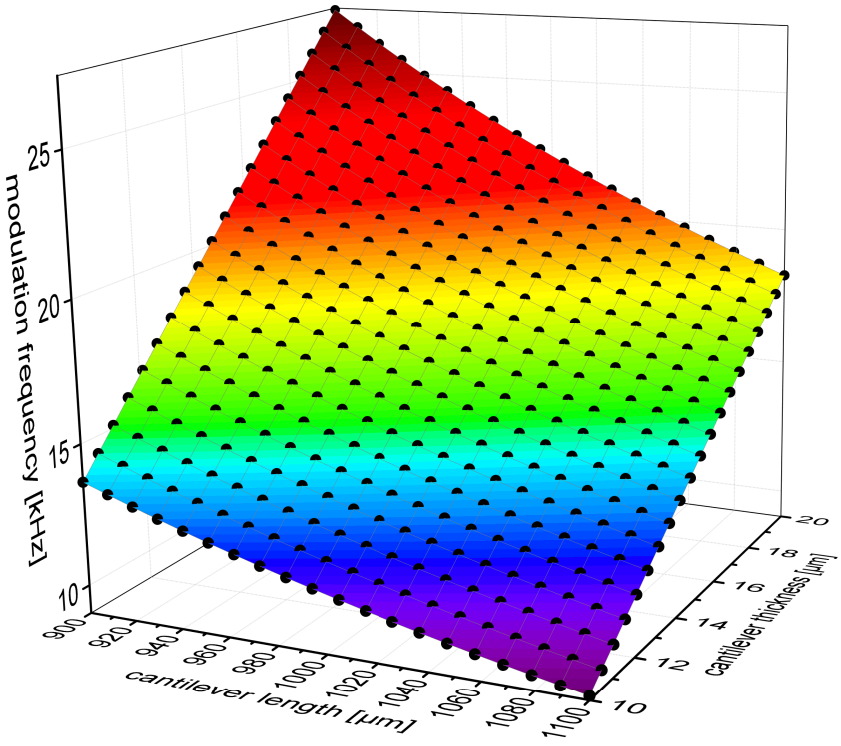

Figure 2.11: Three-dimensional visualization of the frequency dependency on the length and the thickness of the cantilever, respectively. The data was calculated by 1.94 using a MATLAB routine.

dimensional dependency for the length of the beam ranging from 900 to 1100 µm and its thickness ranging from 10 µm to 20 µm, respectively. Primary attempts intended to adjust the thickness of the beam by the etching period. Since the frequency of resonant vibration depends on the thickness of the cantilever to a great extend (the frequency increases by 1 107 kHz per thickness increase by 1 µm), these approaches yielded significant variance about the mean frequency. For this reason, further cantilever fabrication was based on a silicon-on-insulator (SOI) substrate, which facilitated a more homogeneous beam thickness of 15 ± 0.5 µm.

Figure 2.12 finally illustrates the frequency-length-dependency regarding a cantilever thickness of 15 µm. The values resulting from calculation are represented by red circles. For comparison, the values obtained from simulation are illustrated as black squares. By comparing the results, a signif-

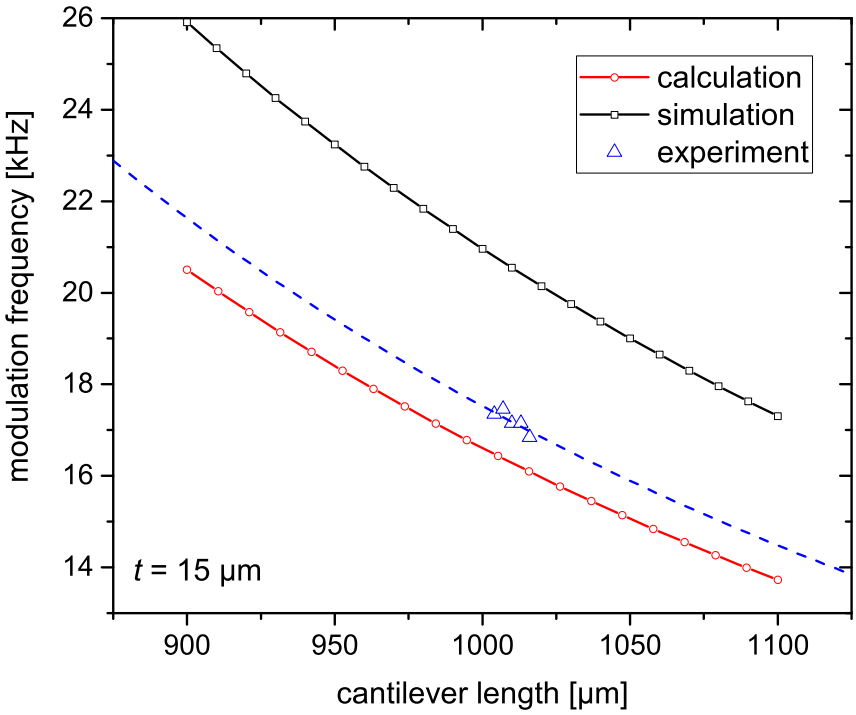

Figure 2.12: Comparison of simulated (black squares), calculated (red circles) and experimental (blue triangles and dashed curve) cantilever eigenfrequencies depending on their length. Fixed dimensions of the beams were 300 µm in width and 15 µm in thickness.

icant discrepancy becomes evident, i.e. the simulated eigenfrequencies are $\sim$ 20 % blue-shifted compared to calculation. Besides, figure 2.12 shows some experimental data resulting from interferometric analysis by means of laser scanning vibrometry. The empirically obtained eigenfrequencies were determined to be underestimated by $\sim$ 5 % in terms of calculation and overestimated by $\sim$ 15 % in terms of simulation. These discrepancies could be further validated regarding cantilevers, which lengths ranged from 1.18 to 1.30 mm. As a consequence of those findings, equation 1.94 can be re-written to

$$f_{\mathrm{C}} = \mathrm{C} \cdot \frac{t}{L^2} \cdot \sqrt{\frac{E}{\rho}} \tag{2.8}$$

where the dimensionless constant C, which varies with the corresponding approach of determination (calculation, simulation or experiment), is specified in table 2.1.

Table 2.1: List of constants for cantilever eigenfrequency based on different approaches, i.e. surface load calculation, point load calculation at the tip, experimentally obtained data and the results of simulation, respectively.

Constant C	Approach of determination
0.12994947	calculation (surface load)
0.07957747	calculation (point load, refer to 1.96)
0.13709669	**experiment**
0.16391519	simulation

In order to most accurately estimate the actual eigenfrequency of fundamental cantilever vibration, it is recommended to apply equation 2.9 with an excess factor of S = 1.055.

$$f = \frac{\mathrm{S}}{2\pi} \cdot \frac{t}{L^2} \cdot \sqrt{\frac{2E}{3\rho}} \tag{2.9}$$

2.4 Mounting position of the detector

Apart from eigenfrequency analysis, the distance between the origin of signal generation and the position of sound detection is of major interest in view of maximum signal amplification.

2.4.1 Acoustic near-field effects

This section is meant to examine different photoacoustic cell designs, i.e. a classical PAC (refer to chapter 4.1), a QEPAS arrangement (refer to chapter 4.3) and a μPAS design (refer to chapter 4.4), with respect to the emergence of acoustic near-field effects. Such phenomena are known as interferences that may appear up to a certain distance of sound propagation, namely within the near-field of the emitter. More precisely, local areas of constructive and destructive interference occur depending on the distance to the emitter, which is due to a 90° phase shift between sound particle velocity and acoustic pressure. It is important to ensure that the detector is not

Table 2.2: List of critical distances of acoustic near-field emergence.

Critical distance r_c	Photoacoustic cell design
1.22 cm	standard PAS
167 µm	QEPAS
458 µm	µPAS

located at a distance of destructive interference, because otherwise the photoacoustic signal might be considerably attenuated. The critical distance r_c of an acoustic near-field solely depends on the wavelength of sound and it is represented by

$$r_c = \frac{\lambda_s}{2\pi} = \frac{c_s}{2\pi f_s} \tag{2.10}$$

while interferences may only appear at distances $r \leq r_c$. Table 2.2 lists the critical distances of different PAC designs.
Considering each of the three designs, the actual distance between the origin of the sound signal, i.e. the opening that is cut into the resonator for sound coupling, and the mounting position of the detector is less than (or similar to) the corresponding critical distance from table 2.2, thus the occurrence of near-field effects has to be investigated more detailed.
From loudspeaker theory, the sound pressure is given by [2]

$$|p(r)| = 2\rho_0 c_s v_s \sin\left(k_s a \frac{\sqrt{\frac{r^2}{a^2}+1} - \frac{r}{a}}{2}\right) \tag{2.11}$$

where c_s is the speed of sound, v_s is the sound particle velocity, k_s is the reciprocal wavelength of sound, a is referred to as the radius of the resonator opening for sound coupling* and r is the distance between this opening and

*Actually, a is the radius of a circular speaker membrane.

the detector. Since v_s is not of interest concerning photoacoustic signals, 2.11 can be normalized to

$$|p(r)|^* = \frac{|p(r)|}{\omega_s \rho_0 a v_s} = \frac{1}{\pi a k_s} \sin\left(k_s a \frac{\sqrt{\frac{r^2}{a^2} + 1} - \frac{r}{a}}{2} \right) \tag{2.12}$$

Again, a MATLAB script was prepared in order to increase the efficiency of calculation. Figure 2.13 illustrates the input parameters, i.e. the speed of sound c_s, the diameter of the opening for sound coupling $2a$ and the sound frequency $\omega_s/(2\pi)$, as well as a representation of the normalized sound pressure $|p(r)|^*$ as a function of the distance r with regard to a hypothetical cell design featuring an exaggerated opening radius of $a = 15$ cm and a resonance frequency of 20 kHz.

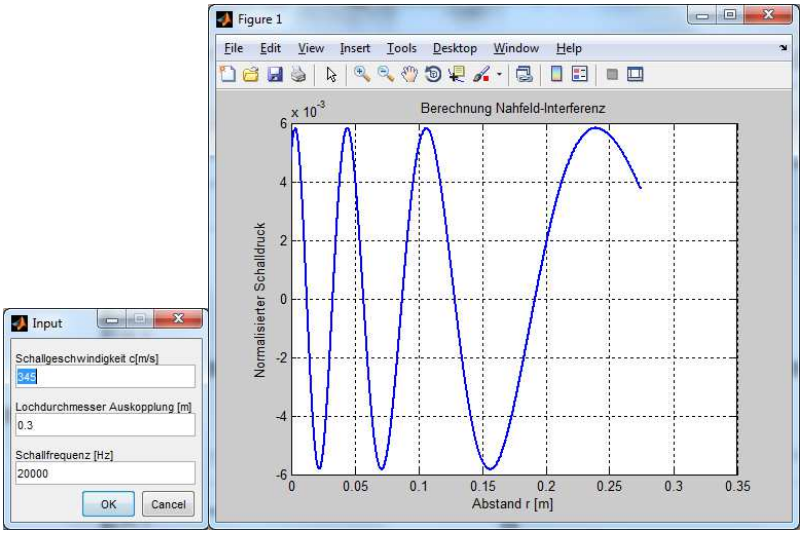

Figure 2.13: Graphical representation of acoustic near-field effects of a hypothetical PAC design. The opening for sound coupling was assumed to be 15 cm in radius and the resonance frequency was arbitrarily specified to 20 kHz.

The graphical representation of the normalized sound pressure clearly indicates the emergence of interferences, thus causing local maxima and minima of the sound pressure amplitude.
Figure 2.14 shows an equivalent presentation with respect to a standard cell design (a), a QEPAS scheme (b) and a µPAS design (c), respectively.

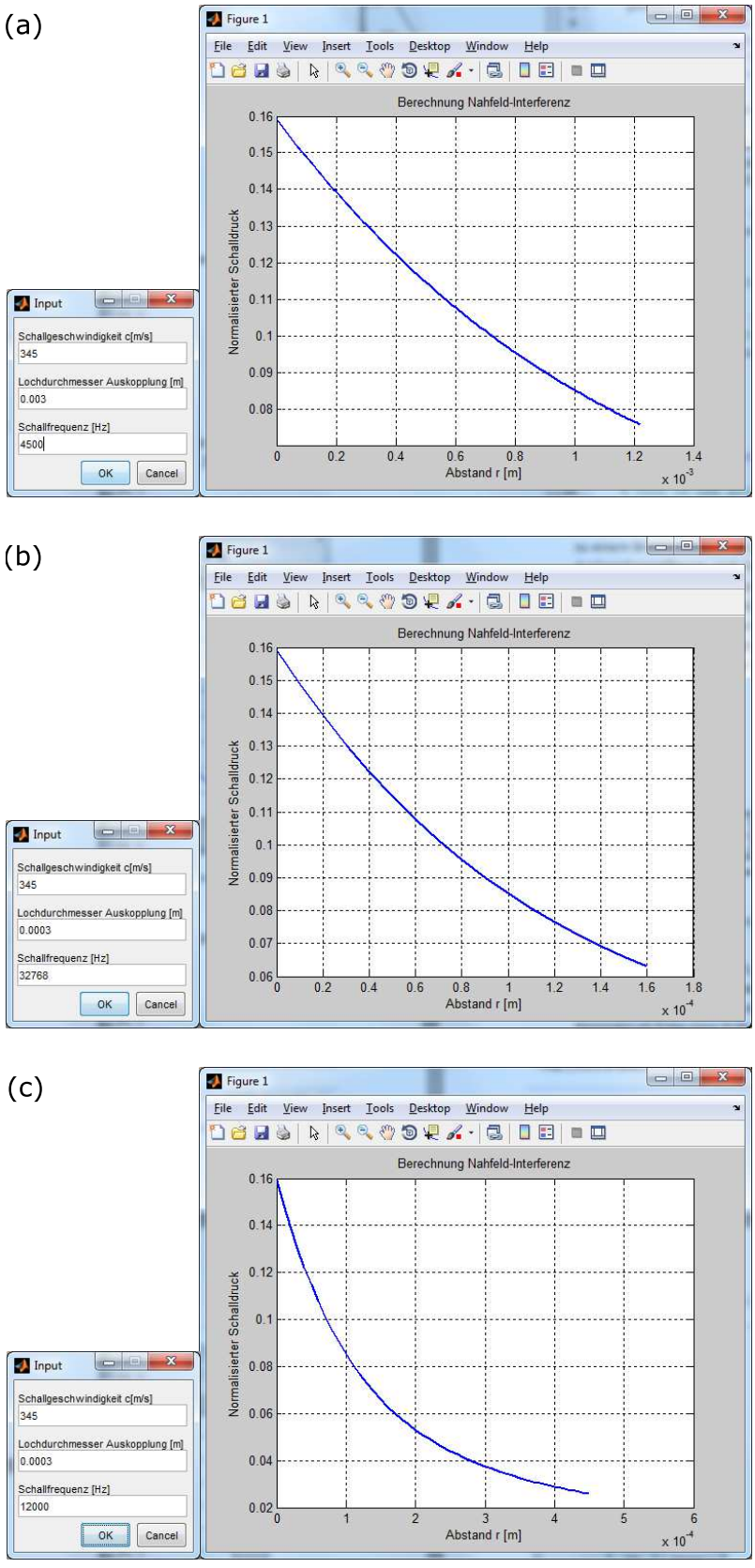

Figure 2.14: Theoretical investigations of near-field effects by plotting the normalized sound pressure depending on the distance from the emitter. (a): standard PAS-, (b): QEPAS- and (c): μPAS-design.

Although each of these three designs was assigned to the critical region $r < r_c$, i.e. the distance between sound generation and detection is less than (or similar to) the wavelength of sound λ_s, none of the PACs revealed the emergence of interferences. This observation is based on the fact that λ_s also exceeds the dimensions of the acoustic source. For comparison, table 2.3 lists the wavelengths of sound and the dimensions of the resonator openings for acoustic coupling with regard to the different cell designs.

Table 2.3: Comparison of wavelength of sound and the dimensions of the resonator opening for acoustic coupling with respect to different PAC designs.

Photoacoustic cell design	Wavelength of sound λ_s [cm]	Diameter of the opening for sound coupling d_{op} [µm]
standard PAS	7.67	1 000
QEPAS	1.05	200
µPAS	2.88	150

Concluding this subsection, no acoustic near-field interferences have to be considered regarding any of the presented photoacoustic cell designs.

2.4.2 Maximum energy transfer

Based on the finding that acoustic near-field effects do not have to be considered, this subsection addresses the sound coupling efficiency to the detector at the example of the µPAS concept. As discussed in the previous subsection, λ_s significantly exceeds the dimensions of the opening for sound coupling. Therefore, the opening can be treated as an acoustic point source, thus spherical wave radiation is assumed.
The following paragraph provides a geometrical derivation in order to quantify the sound coupling efficiency from resonator to cantilever. This efficiency can be considered as the ratio R of a spherical cap surface and the surface of the sound radiation hemisphere*, while the spherical cap represents the remaining part of the hemisphere after cutting it at a distance x, i.e. the plane of cantilever mounting.

*The hemisphere can be considered an isobaric surface.

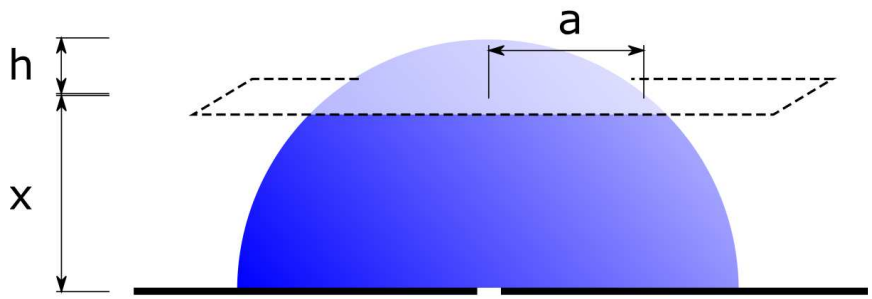

Figure 2.15: Schematic drawing of a geometric consideration concerning the determination of the sound coupling efficiency of the µPAS cell design. x: distance between acoustic resonator and cantilever, h: height of the spherical cap, a: radius of the spherical cap.

Figure 2.15 schematically depicts this geometrical consideration. Therein, the resulting spherical cap is highlighted by an increased transparency and its height and radius are labeled as h and a, respectively.
According to the mathematical definition of the surface A_{sc} and the height of a spherical cap as well as the radius of the sphere r

$$A_{\mathrm{sc}} = \pi r 2h \tag{2.13}$$

$$h = r - \sqrt{r^2 - a^2} \tag{2.14}$$

$$r = x + h \tag{2.15}$$

together with the condition for the effective width q_{c} of a square cantilever*

$$a = \frac{q_{\mathrm{c}}}{2} \tag{2.16}$$

the surface of the cap becomes†

$$A_{\mathrm{sc}} = 2\pi r \left(r - \sqrt{r^2 - \frac{q_{\mathrm{c}}^2}{4}} \right) \tag{2.17}$$

*Equation 2.16 assumes a square cantilever of side length $q_{\mathrm{c}} = (L_{\mathrm{c}} \cdot w_{\mathrm{c}})^{0.5}$ for simplification.
†The geometric consideration further assumes that the center of the cantilever is aligned to the opening without any lateral offset.

Considering the surface of the hemisphere A_{hs}

$$A_{\mathrm{hs}} = 2\pi r^2 \tag{2.18}$$

the ratio R, i.e. the efficiency of sound coupling, can be written as

$$R = \frac{A_{\mathrm{sc}}}{A_{\mathrm{hs}}} = 1 - \frac{\sqrt{r^2 - \frac{q_{\mathrm{c}}^2}{4}}}{r} \tag{2.19}$$

This equation can be solved for the radius of the sphere, thus it follows

$$r = \frac{q_{\mathrm{c}}}{2} \cdot \sqrt{\frac{1}{1-(1-R)^2}} \tag{2.20}$$

Solving 2.15 for x and substituting equations 2.14, 2.16 and 2.20 finally yields to*

$$x = \frac{q_{\mathrm{c}}}{2} \cdot \sqrt{\frac{1}{1-(1-R)^2} - 1} \tag{2.21}$$

Equation 2.21 allows to calculate the distance of resonator and cantilever, which must not be exceeded in order to accomplish a certain sound coupling efficiency for given beam dimensions. Based on a width of 300 µm and a length of 1000 µm, the distance was calculated to ~ 66 µm, when striving for an efficiency of 80 %, for example. Concluding this discussion about the mounting position of the detector, the sound coupling efficiency dependence on the distance x is obtained by solving 2.21 for R. Equation 2.22 and figure 2.16 represent this dependency.

$$R = 1 - \sqrt{1 - \frac{1}{\left(\frac{2x}{q_{\mathrm{c}}}\right)^2 + 1}} \tag{2.22}$$

The µPAS design currently features a distance of $x = 600$ µm, which implicates a coupling efficiency of merely 9 %. Aiming at higher efficiencies, the SOI substrate is intended to be flip-bonded to the glass substrate, i.e. the device layer is directly bonded to the glass wafer. This would result in a

*This derivation was additionally verified by means of an alternative approach using the solid angle Ω.

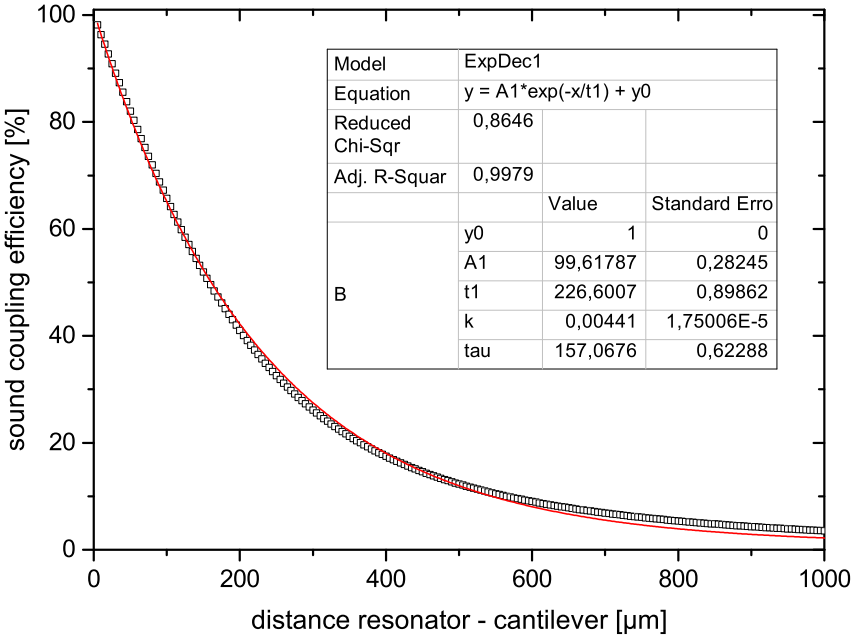

Figure 2.16: Graphical representation of the sound coupling efficiency depending on the distance between acoustic resonator and cantilever, when assuming a cantilever width and length of 300 µm and 1000 µm, respectively.

distance of only $\sim$ 100 µm, thus increasing the efficiency of sound coupling to at least 66 %. With regard to these calculations, it has to be noted that a hypothetical square cantilever was assumed. This simplification causes an error, which increases with the length-to-width ratio of the actual cantilever. Therefore, the calculated coupling efficiency has to be considered a minimum value, as actual coupling might be more efficient. Apart from that, the error caused by this simplification loses weight with increasing the distance between resonator and cantilever. To summarize, the calculated values correspond to reality in good approximation concerning large distances, while actual coupling is even more effective than the calculation with regard to short distances.*

*i.e. the exponential function in figure 2.16 initially decays more slowly.

2.5 Multi-component analysis

The experimental part of this thesis presents a fundamental and comprehensive analysis of the photoacoustic effect as well as an in-depth characterization of a variety of cell designs. All of these investigations were carried out on the basis of NO_2 detection. However, further development aims at a multi-gas sensing device by expanding the current prototype, which is introduced in chapter 4.5. As a preliminary work in view of multi-component detection, this final section of chapter 2 presents a theoretical spectral investigation of suitable absorption peaks regarding different analytes in varying gas compositions (see subsection 2.5.1) and it further shortly addresses a limitation regarding the practical implementation of wavelength modulation (refer to subsection 2.5.2).

2.5.1 Theoretical spectral investigations

All spectral investigations that are discussed in this subsection are based on the HITRAN (high-resolution transmission molecular absorption) database, which can be exploited via [3, 4] for example. Within the first part, several absorption cross sections of the analytes NO, NO_2, CO, CO_2, NH_3 and CH_4 were determined using equation 1.7. The calculations were carried out on the assumption of standard conditions, i.e. 1 atm and 298 K, thus only collision broadening was considered. In order to take into account line width broadening, the HITRAN database provides so called air width broadening factors α, which represent the HWHM values of Lorentz-shaped profiles. Those were substituted in 1.21, while specifying $w_L = 2\alpha$ and $A = 1/2$.
The calculations are illustrated at the example of strong NO_2 absorption ranging from 1 560 to 1 660 cm^{-1}, i.e. 6.41 to 6.02 µm. Figure 2.17 illustrates the line strengths of ro-vibrational transitions, which were extracted from the HITRAN database. As discussed above, these line strengths were converted into the corresponding absorption cross sections σ. Figure 2.18 graphically represents the σ values that were obtained by calculation, while considering the wavenumbers 1 603 (a) and 1 629 cm^{-1} (b), respectively.
All cross sections that were calculated this way are listed in chapter Appendix (see table 7.1). However, it has to be noted that every calculation

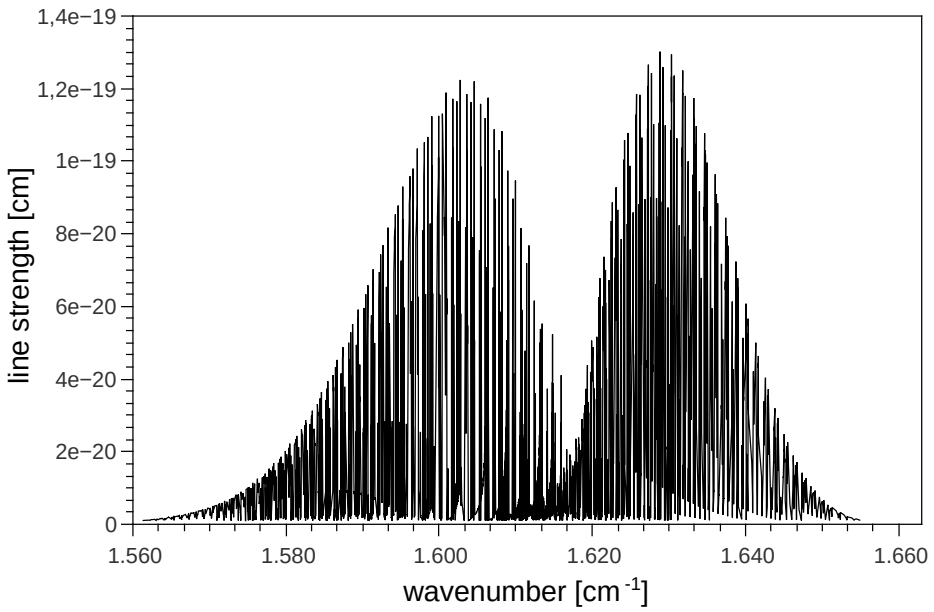

Figure 2.17: Graphical representation of line strengths regarding ro-vibrational transitions of NO_2 in the range of 1 560 to 1 660 cm^{-1} extracted from the HITRAN database.

cycle only reveals the cross section at one particular wavenumber, thus the method is very time consuming. Moreover, this technique does not take into account any cross sensitivities towards other species. For this reason, further simulations were performed using the software MolExplorer v4.01. This software also exploits the HITRAN database, but it is more comfortable in usage, as it supports simultaneous simulation of up to ten compounds in different volume ratios. Doppler- and collision broadening are considered by simply adjusting temperature and pressure. Figure 2.19 shows a screenshot of its user interface, while simulating the absorption coefficients of NO (red spectrum), N_2O (green spectrum) and NO_2 (blue spectrum) in the range between 1 and 6 µm (in each case a volume ratio was specified to 1 ppmV).

The procedure that was followed in terms of simulation is outlined by the example of NO_2 absorption in the region between 1 and 6 µm. For this reason, figure 2.20 again illustrates the data exported from 2.19. In order to demonstrate the importance of taking cross sensitivities into consideration, figure 2.21 illustrates an equivalent simulation, which additionally considers

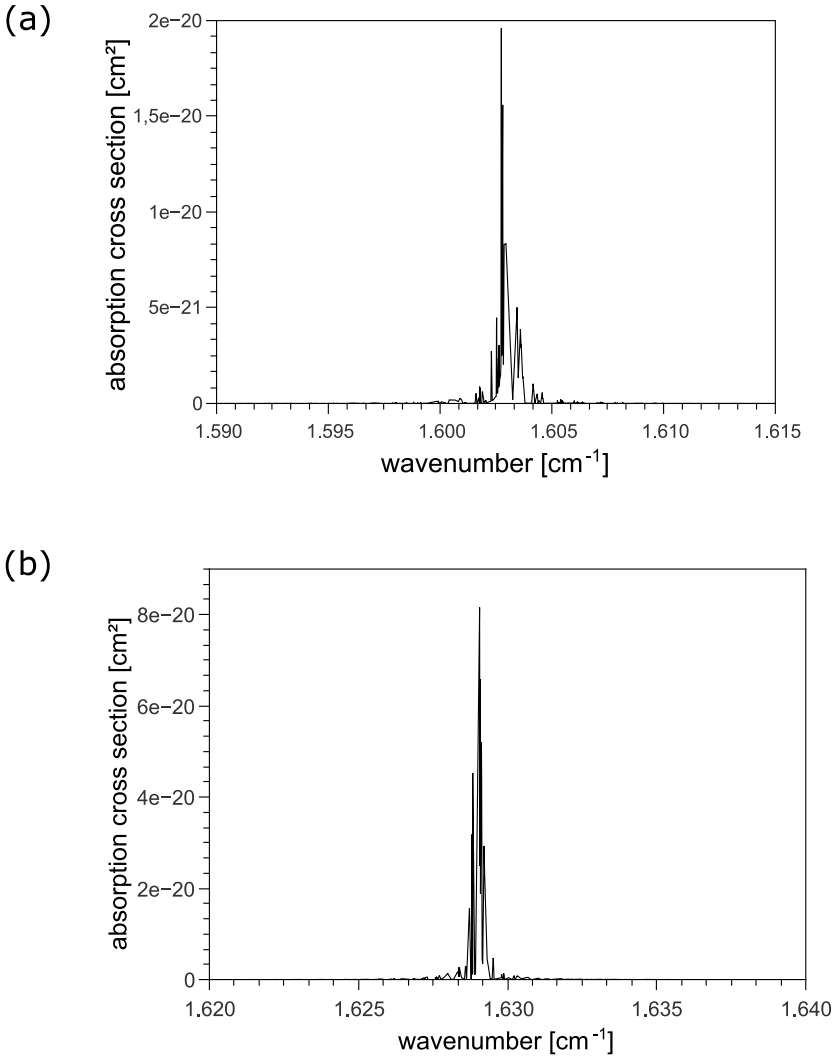

Figure 2.18: Graphical illustration of the calculated absorption cross sections of NO_2 at the wavenumbers 1 603 (a) and 1 629 cm^{-1} (b).

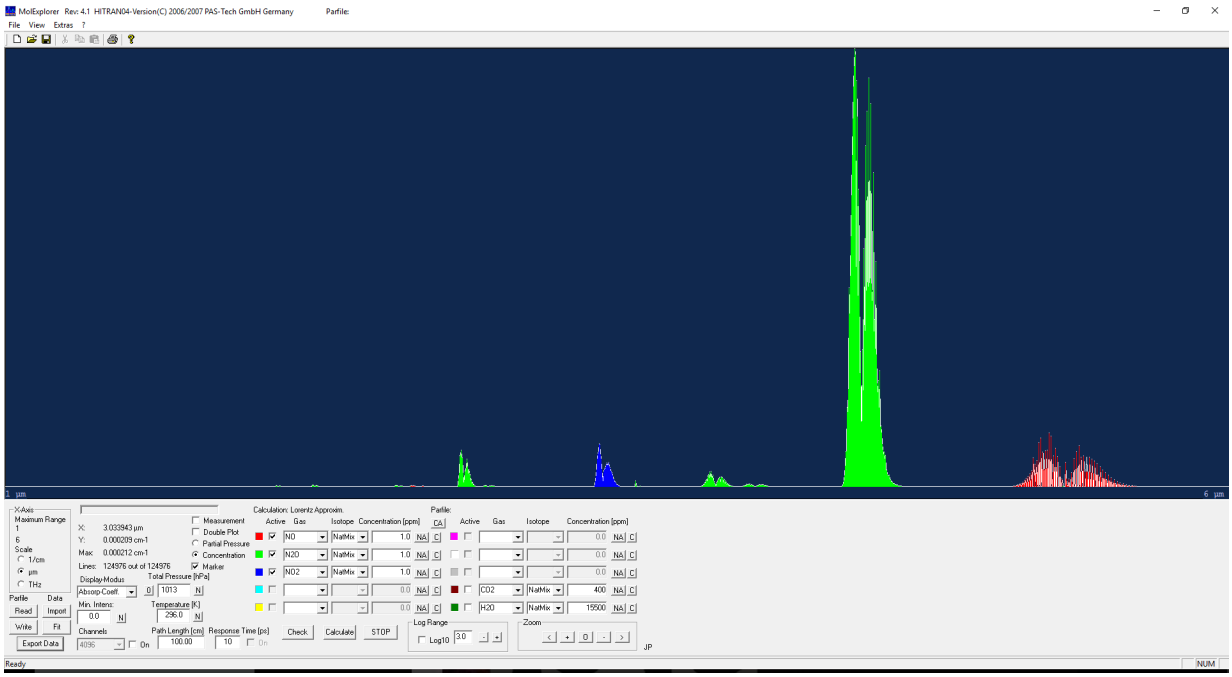

Figure 2.19: Screenshot of the software MolExplorer v4.01 which was used for further multi-component simulations.

400 ppmV CO_2 and 50 %rh (relative humidity)*, i.e. typical ambient air condition. This ambient air simulation reveals that the spectrum is entirely predominated by H_2O and to some extent also by CO_2. In order to identify suitable absorption lines for NO_2 detection anyway, the spectrum has to be investigated in small spectral subdivisions. By analogy with figures 2.20 and 2.21, figures 2.22 and 2.23 illustrate the absorption characteristics ranging from 3.37 and 3.54 µm in dry nitrogen and in humidified air, respectively.

Although the spectrum in figure 2.23 again seems to be entirely predominated by H_2O at first, taking a closer look might indicate some effective NO_2 absorption around wavelengths of 3 430 or 3 465 nm. Finally, this zoom-in procedure hast to be continued to the nanometer scale in order to identify suitable absorption lines.
Figure 2.24 illustrates an absorption profile, that may be suitable in terms of NO_2 detection. The total absorption is represented by a black line, which peaks at a center wavelength of 3 461.43 nm. Except for a minor H_2O ab-

*Assuming a temperature of 25 °C, 50 %rh corresponds to a volume ratio of ∼ 1 550 ppmV.

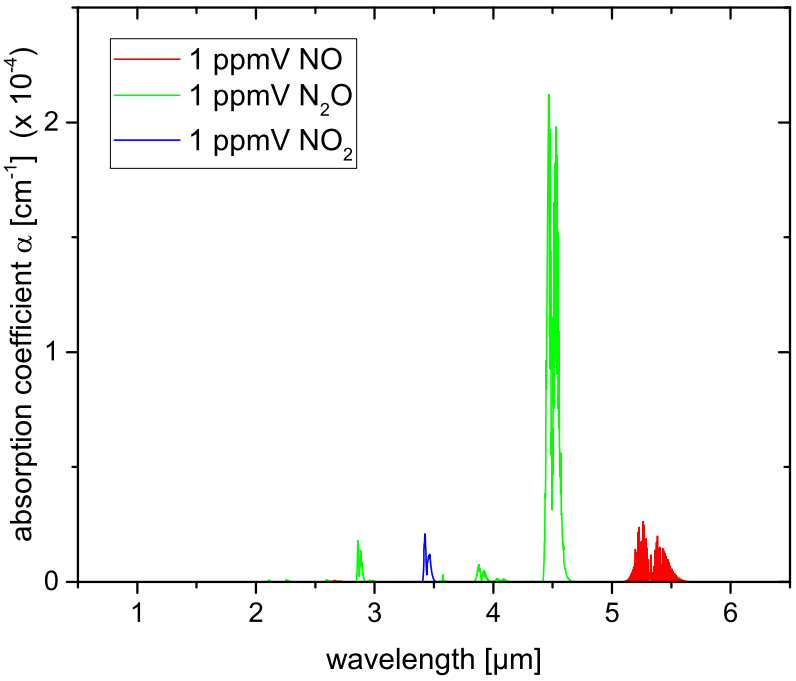

Figure 2.20: Simulated absorption coefficients of NO, N_2O and NO_2 (1 ppmV each) in dry nitrogen in the region between 1 and 6 µm.

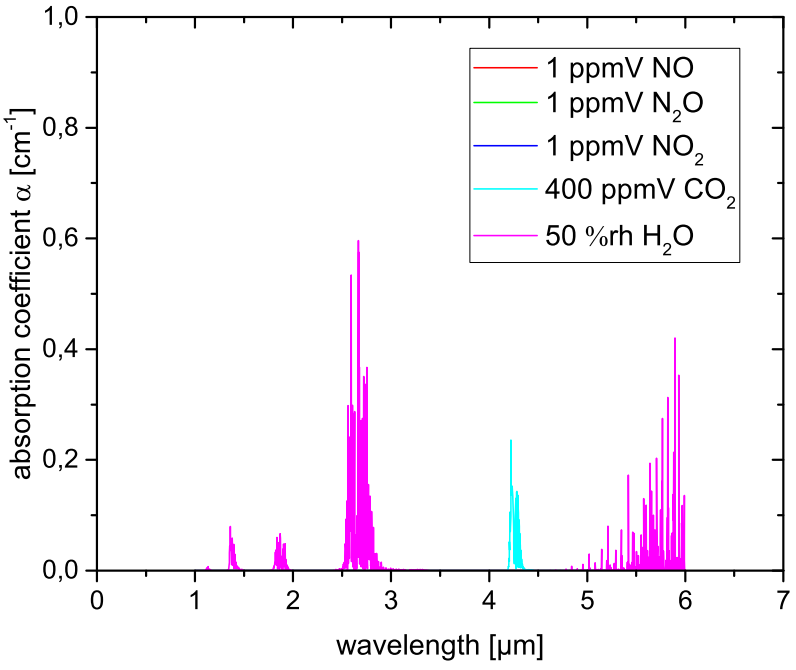

Figure 2.21: Simulated absorption coefficients of NO, N_2O and NO_2 (1 ppmV each) in humidified air in the region between 1 and 6 µm.

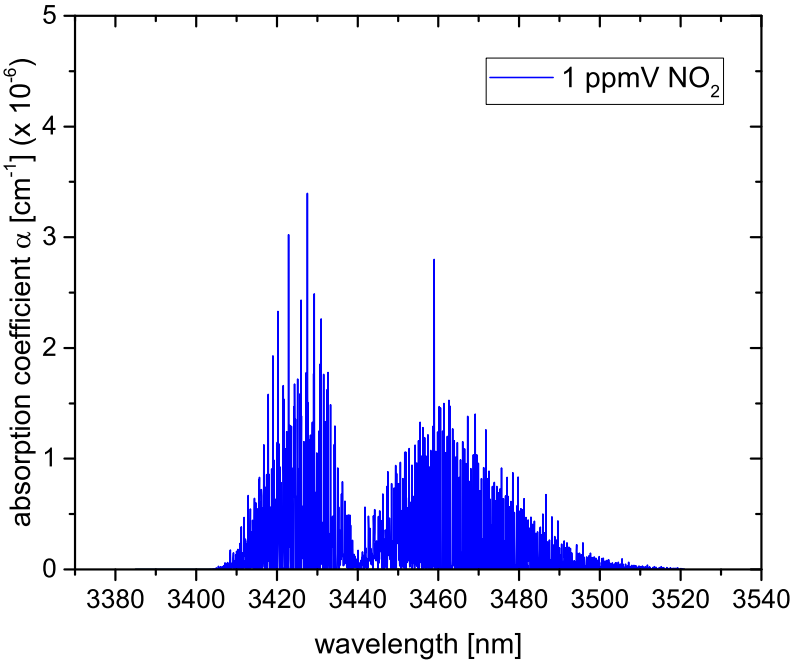

Figure 2.22: Simulated absorption coefficients of 1 ppmV NO_2 in dry nitrogen in the region between 3.37 and 3.54 µm.

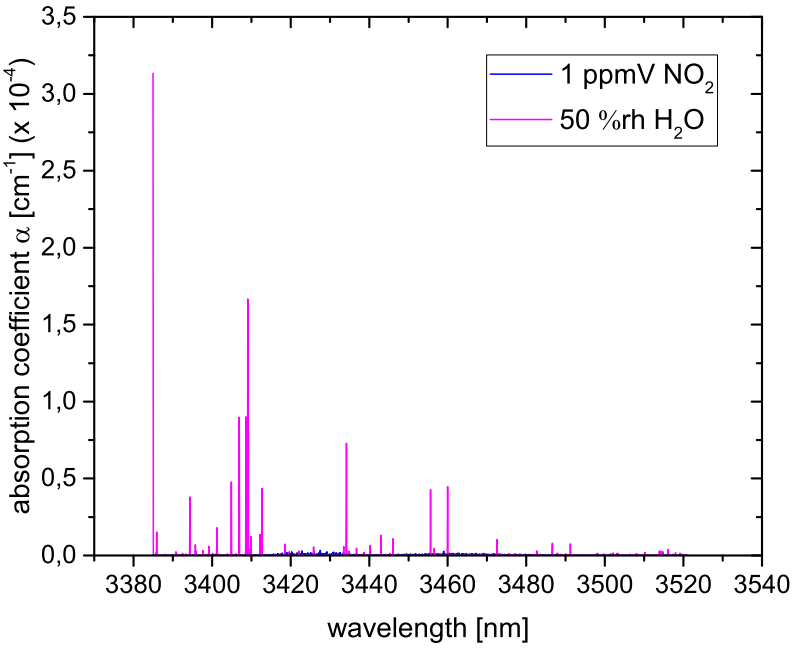

Figure 2.23: Simulated absorption coefficients of 1 ppmV NO_2 in humidified air in the region between 3.37 and 3.54 µm.

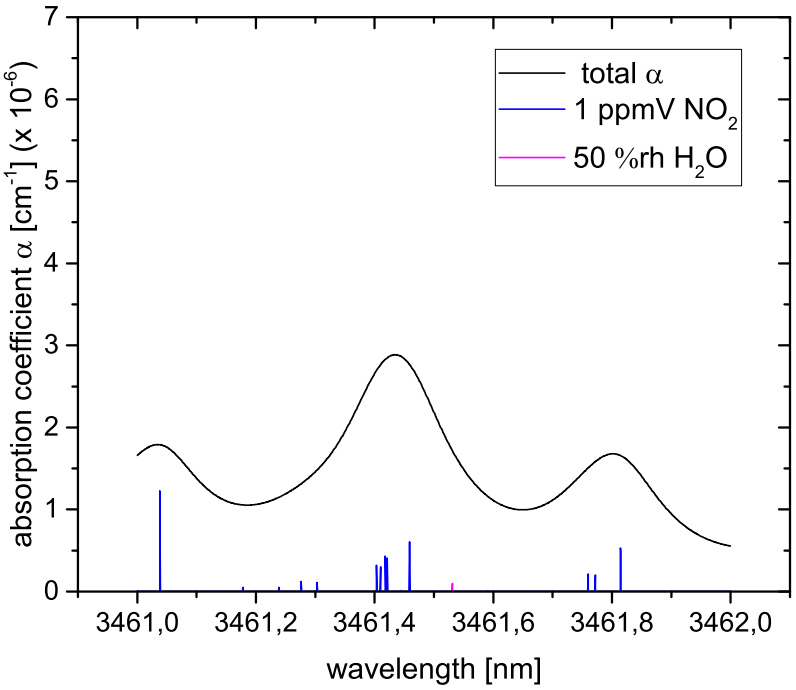

Figure 2.24: Suitable NO_2 absorption profile at 3 461.43 nm obtained by zoom-in simulation of 1 ppmV NO_2 in humidified air.

sorption line at 3 461.53 nm, the total profile comprises six NO_2 transitions, which details are provided in chapter Appendix (refer to figures 7.1 to 7.6).

The absorption cross section σ can be calculated from the volume ratio (1 ppmV) and the absorption coefficient according to equations 1.5 and 1.4. Figure 2.25 illustrates the thus obtained absorption cross section, which reveals a maximum value of $1.16 \cdot 10^{-19}$ cm^2.

The maximum absorption cross section provided by figure 2.25 constitutes about 30 % compared to the absorption of NO_2 at 450 nm, which is utilized with regard to all measurements presented in chapter 4. Concluding this description of the simulation procedure, figure 2.26 demonstrates the changing in total absorption compared to figure 2.24, once the amount of water is increased from 50 %rh to 50 %V (i.e. 50 % volume ratio). Comparing both figures, total absorption is increased by $\sim$ 60 % and besides, the absorption profile is obviously distorted, which further emphasizes the importance of considering cross sensitivities.

Having discussed the methods, the following part provides the starting pa-

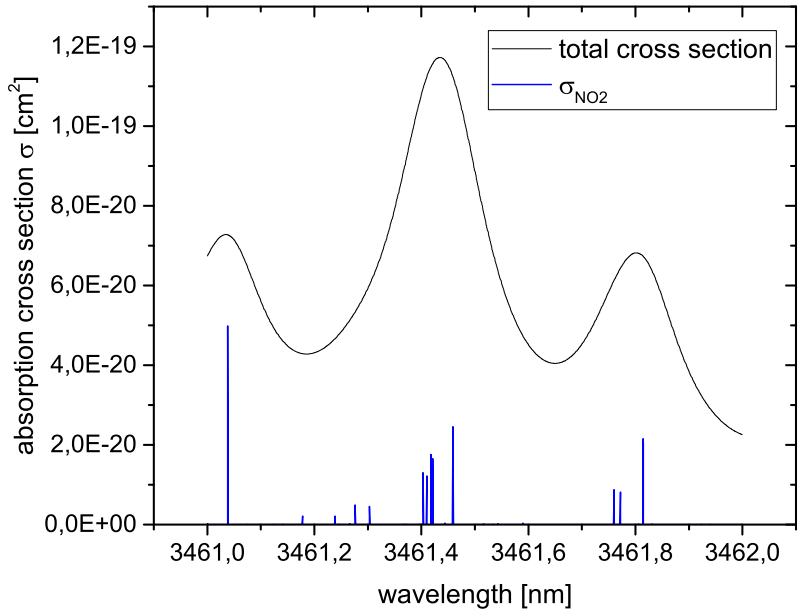

Figure 2.25: Simulated absorption cross section of NO_2 at 3 461.43 nm. The peak value was determined to $1.16 \cdot 10^{-19}$ cm^2.

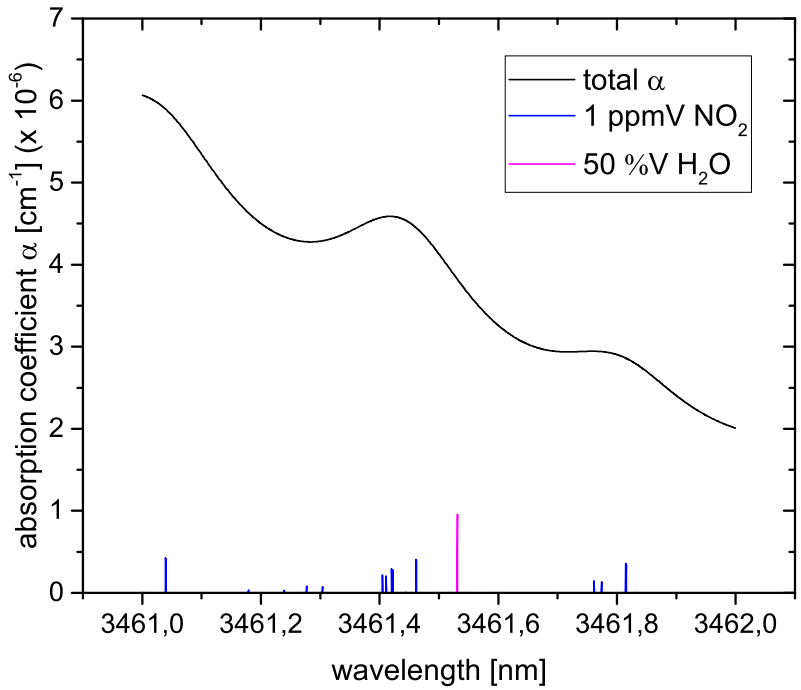

Figure 2.26: NO_2 absorption profile at 3 461.43 nm obtained by zoom-in simulation of 1 ppmV NO_2 in a 50 %V water matrix.

rameter tables and the result matrix of simulation. With respect to photoacoustic multi-component analysis, four different fields of application have been investigated:

i. Ambient air tracing of nitric oxides
ii. Natural gas quality monitoring
iii. Combustion control
iv. Dissolved gas analysis (DGA)

The starting parameter tables include the minimum target concentrations* of the analytes (marked by an ^{a}) as well as the maximum concentrations of other compounds that might lower the sensitivity. If more than one analyte is to be monitored, maximum concentrations are also specified for the other analytes, thus they are considered to possibly cause interferences, too. The spectral region of interest was limited to wavelengths not exceeding 6 µm, as this range is covered by interband cascade lasers (ICLs), which can be provided by the project partner *nanoplus Nanosystems and Technologies GmbH*. In order to counteract collision broadening (refer to chapter 1.1.2), a pressure reduction to 500 mbar was assumed in terms of applications i. and iii. and a further decrease to 250 mbar was considered regarding application iv. The result matrix also specifies detection limits LOD(3σ), which are based on the assumption of wavelength modulation and an optical power of 5 mW. The values were calculated by considering the sensitivity and noise level of a QEPAS setup, which was reported in [5]. However, those LODs are meant to facilitate comparison and to point out trends, rather than to specify absolute and reliable limits.

*For simplicity the volume ratios are referred to as concentrations in this context, which is not correct in an analytical sense.

Table 2.4: i. Ambient air tracing of nitric oxides.

Species	Target concentration [ppmV]	Maximum concentration [ppmV]
NO^a	0.01	100
N_2O^a	0.001	100
$NO_2{}^a$	0.01	100
CH_4		10
CO		1
CO_2		10 000
H_2O		8 000
HNO_3		100

Table 2.5: ii. Natural gas quality monitoring.

Species	Target concentration [ppmV]	Maximum concentration [ppmV]
$CH_4{}^a$	50 000	1 000 000
$C_2H_6{}^a$	1 000	200 000
$C_3H_8{}^a$	500	200 000
CO^a	1	200 000
$CO_2{}^a$	10	150 000
H_2O^a	1	500
H_2S	0.1	5000

Table 2.6: iii. Control of combustion processes.

Species	Target concentration [ppmV]	Maximum concentration [ppmV]
NO^a	0.1	1 000
$NO_2{}^a$	0.1	1 000
$CH_4{}^a$	1 000	100 000
$C_2H_6{}^a$	1 000	100 000
CO^a	1	200 000
$CO_2{}^a$	1 000	150 000
H_2O^a	10	50 000

Table 2.7: iv. Dissolved gas analysis (DGA).

Species	Target concentration [ppmV]	Maximum concentration [ppmV]
$CH_4{}^a$	1	10 000
$C_2H_6{}^a$	1	10 000
$C_2H_4{}^a$	1	10 000
$C_2H_2{}^a$	0.1	1 000
$CO_2{}^a$	1	10 000

Table 2.8: Result matrix of spectral simulation.

Application	Target species	LOD(3σ)[a]	Center wavelength [nm]	Wavelength modulation depth [nm][b]	Source available?
i.[c]	NO	150 ppbV	5 229.9	0.2	–
	N_2O	25 ppbV	4 537.7	0.1	✓
	NO_2	< 1 ppbV	450	n.a.	✓
ii.	CH_4	1 ppmV	3 369	2[d]	✓[e]
	C_2H_6	20 ppmV	3 362.5	1	✓[e]
	C_3H_8	n.a.[f]	3 372.7	n.a.[f]	✓[e]
	CO	100 ppbV[g]	4 633	1	–
	CO_2	150 ppbV	4 281	0.5	–
	H_2O	5 ppmV[h]	940	n.a.	–
iii.[c]	NO	200 ppbV	5 229.9	0.2	–
	NO_2	< 1 ppbV	450	n.a.	✓
	CO	50 ppbV[g]	4 633	1[i]	–
	CO_2	< 1 ppbV	4 281	0.5[i]	–
	CH_4	< 1 ppbV	3 369	2[i]	✓[e]
	C_2H_6	< 1 ppbV	3 362.5	1[i]	✓[e]
	H_2O	20 ppmV[h]	940	n.a.	–
iv.[jk]	CH_4	1 ppmV	3 451.9	0.08	–
	C_2H_6	500 ppbV	3 340.6	0.04	–
	C_2H_4	5 ppmV	3 138.2	0.04	–
	C_2H_2	200 ppbV	3 025.7	0.05	–
	CO	50 ppbV	4 587.6	0.17	–
	CO_2	1.5 ppmV[l]	2 012.7	0.07	–

[a] Unless otherwise stated, the detection limits are estimated for 5 mW optical power and wavelength modulation.
[b] For a definition of the modulation depth $\delta_s \bar{\nu}_{\mathrm{ph}}$ refer to equation 1.25.
[c] A total pressure of 500 mbar was assumed.
[d] An asymmetric demodulation signal containing 4f-signal components has to be expected. The degree of asymmetry depends on the CH_4 concentration.
[e] Single source excitation of CH_4, C_2H_6 and C_3H_8 is intended by means of an ICL, which can be tuned from 3360 to 3374 nm.
[f] Propane is not included in the HITRAN database, thus its center frequency was taken from [6].
[g] The detection may be significantly increased in terms of lower total HC (hydrocarbons) amounts.
[h] Amplitude modulation (AM) has to be applied.
[i] The modulation depth may be smaller due to pressure reduction.
[j] Due to interferences, those wavelengths of prior applications cannot be applied in iv.
[k] A total pressure of 250 mbar was assumed.
[l] An optical power of 100 mW was assumed.

2.5.2 Restriction of wavelength modulation

Concluding chapter 2, this last subsection shortly addresses a limitation of the wavelength modulation technique, which has been discussed in chapter 1.1.4 in detail. Referring to figure 1.3, WM techniques are commonly based on fast sinusoidal modulation superimposed by slow ramp modulation*. While the former actually accounts for the photoacoustic signal (after $2f$ demodulation), the ramp allows to repetitively scan the absorption feature of the analyte. Since signal processing is based on lock-in amplification (refer to chapter 1.3.4), the ramp frequency f_r, however, limits the lock-in time constant τ_LIA and vice versa. Depending on the resolution that is used for ramp signal representation, lock-in integration has to be fast enough to achieve steady state regarding every quantized ramp state. Once the duration of a quantized state, i.e. $T_\mathrm{r}/2^\mathrm{bit}$, is less than the response time τ_{99}, steady state is not achieved, thus the photoacoustic signal is distorted. This condition is represented by

$$\frac{T_\mathrm{r}}{2^\mathrm{bit}} \geq \tau_{99} \tag{2.23}$$

while τ_{99} depends on the lock-in time constant according to

$$\tau_{99} = \tau_\mathrm{LIA} \cdot \mathrm{C}_{99} \tag{2.24}$$

The constant C_{99} that ensures 99.3 % steady state condition was empirically determined to 4.5 (refer to chapter 4.2.5.1). Substituting 2.24 in 2.23 finally yields to

$$f_\mathrm{r} \leq \frac{1}{2^\mathrm{bit} \cdot \tau_\mathrm{LIA} \cdot \mathrm{C}_{99}} \tag{2.25}$$

In order to graphically illustrate this condition, figure 2.27 presents the maximum ramp frequency depending on the lock-in integration time regarding different resolutions for ramp representation, namely 5, 6, 7 and 8 bit.
Considering figure 2.27, the lock-in time constant is limited to values significantly lower than 1 s, even when applying frequencies of several hundred mHz only. In view of implementing wavelength modulation, hence it is

*commonly also referred to as sawtooth modulation

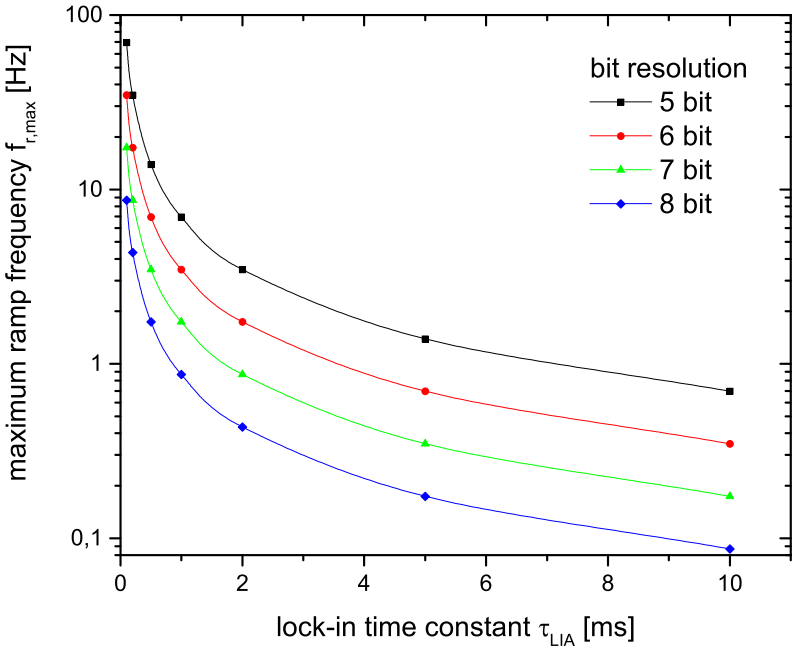

Figure 2.27: Simulation of maximum ramp frequencies for wavelength modulation depending on the lock-in time constant and the resolution for ramp signal representation. The calculation was carried out considering 5 bit (black squares), 6 bit (red points), 7 bit (green triangles) and 8 bit (blue diamonds) resolutions, respectively.

recommended to waive ramp superimposition and to scan the center wavelength along the absorption feature only when it is required instead. This procedure can be considered equivalent to the sweep method that is applied to photoacoustic systems that base upon amplitude modulation.

References

[1] J. Kalkman and H. van Kesteren, Relaxation effects and high sensitivity photoacoustic detection of NO2 with a blue laser diode, *Applied Physics B*, 90(2):197–200 (2008), ISSN 0946-2171, doi:10.1007/s00340-007-2895-0, URL `http://link.springer.com/10.1007/s00340-007-2895-0`.

[2] ARTA, Loudspeaker free field response (application note) (), URL `http://www.artalabs.hr/AppNotes/AP4_FreeField-Rev03eng.pdf`.

[3] HITRANonline (high-resolution transmission molecular absorption database)y (), URL `http://www.hitran.org/lbl/`.

[4] World Data Center for Remote Sensing of the Atmosphere (WDC-RSAT) (), URL `http://wdc.dlr.de/data_products/SPECTRA/spectral_databases/select.php`.

[5] Y. Ma, R. Lewicki, M. Razeghi and F. K. Tittel, QEPAS based ppb-level detection of CO and N2O using a high power CW DFB-QCL., *Optics express*, 21(1):1008–19 (2013), ISSN 1094-4087, doi:10.1364/OE.21.001008, URL `http://www.ncbi.nlm.nih.gov/pubmed/23388995`.

[6] P. Derreumaux, M. Dauchez and G. Vergoten, The structures and vibrational frequencies of a series of alkanes using the SPASIBA force field, *Journal of Molecular Structure*, 295:203–221 (1993), ISSN 0022-2860, doi:http://dx.doi.org/10.1016/0022-2860(93)85021-L, URL `http://www.sciencedirect.com/science/article/pii/002228609385021L`.

Chapter 3

Experimental

3.1 Laboratory setup

This experimental part of the thesis presents a laboratory setup, which was developed to characterize and compare different photoacoustic cell designs and which serves as a reference system for autonomous sensor development. After generally outlining the setup as a whole, detailed information is provided on the gas mixing unit (subsection 3.1.1), on the interconnection of electronic components (subsection 3.1.2) and on the optical parts used for beam guidance (subsection 3.1.3), while the optical path of the OPO (optical parametric oscillator) laser radiation is addressed separately in section 3.2. Besides, experimental details regarding the reference system, i.e. a GC/MS combination (gas chromatograph/mass spectrometer), are presented in chapter 4.6.2. With regard to the development of different cell designs refer to chapters 4.1.3, 4.2.2, 4.3.2, 4.5.2 and 4.4.2, respectively.

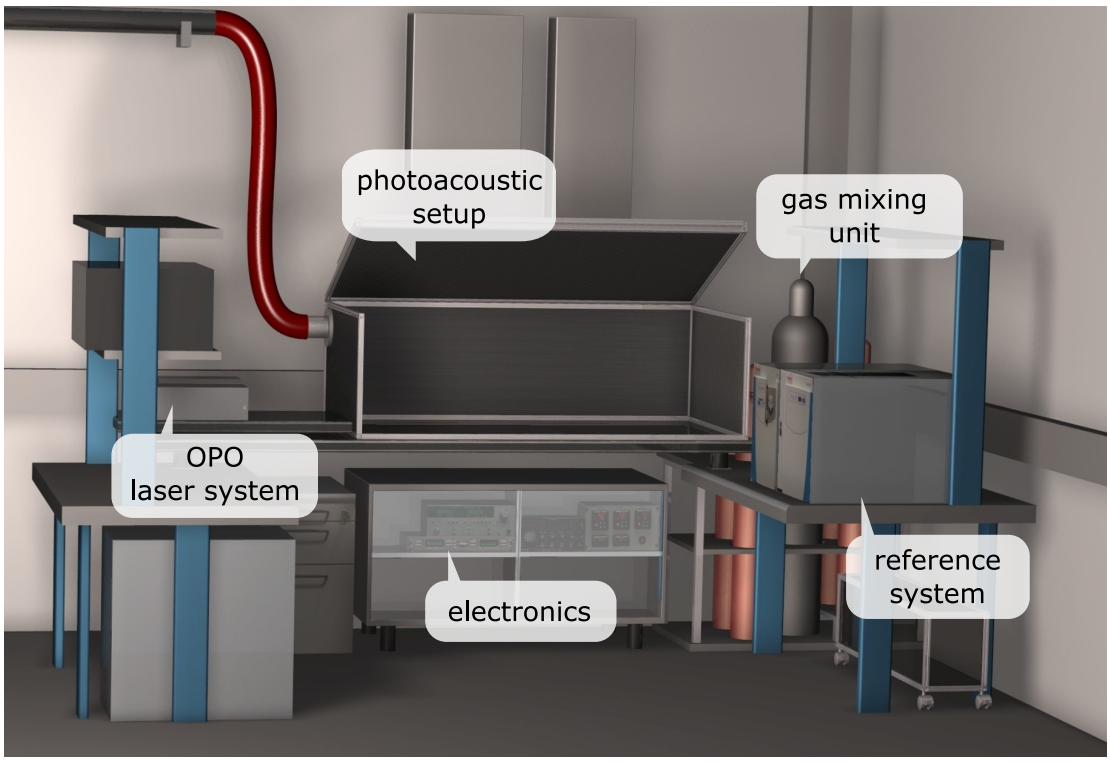

Figure 3.1: Drawing of the laboratory installation, which (from left to right) contains an OPO laser system, the photoacoustic setup installed inside a security box, rack mounted electronic components, a gas mixing unit and a gas chromatograph and mass spectrometer reference system, respectively.

Figure 3.1 shows a drawing of the laboratory installation, where the photoacoustic setup, i.e. the key component of the installation, is centered inside a closable box. This box is also referred to as safety box, as it protects against laser radiation and besides, it ensures continuous aspiration of potential harmful gases, which might leak out due to non-airtight sealing. An OPO laser system is installed to the left of the photoacoustic setup. This laser system provides infrared (IR) radiation, which gets aligned separately before it is coupled into the box by open beam or optical fiber. Underneath the photoacoustic setup, a rack was installed for mounting electronic components, e.g. amplifiers, power supplies, frequency generator. A gas chromatograph and a mass spectrometer, which constitute a reference system for photoacoustic detection, are displayed on the right side of the drawing. The right rear corner of the room finally shows a gas mixing unit.

3.1.1 Gas stream

Figure 3.2 shows a schematic drawing of the gas stream. The left part illustrates the gas mixing unit, which provides the preparation of mixtures containing up to five different test gases, where the latter one usually constitutes the carrier gas, i.e. pure nitrogen or synthetic air (79 %V N_2 and 21 %V O_2). The carrier gas is used to further dilute the test gases in view of photoacoustic trace gas detection. After pressure regulating the gas cylinders, gas mixing is either controlled by F-201CV-500-RBD-11-V mass flow controllers (Bronkhorst, Karmen, Germany) or it is achieved manually by means of needle valves. The carrier gas further can be humidified using an aGEPRO-V4 humidity generator (ADROP Feuchtemeßtechnik GmbH, Fürth, Germany) in order to simulate real ambient air conditions. Following the upper part of the gas stream in figure 3.2, homogeneous mixing is achieved by flowing through a sinter filter. After leaving the mixing unit, the gas is available for photoacoustic analysis or alternatively it can be fed into a reference system that is composed of a Trace GC 1310 gas chromatograph complemented by an ISQ mass spectrometer (Thermo Fisher, Massachusetts, US). With regard to photoacoustic analysis, a distribution panel guarantees flexibility, as it allows to quasi-simultaneously operate up to six devices, e.g. different photoacoustic cells (PACs) or secondary sen-

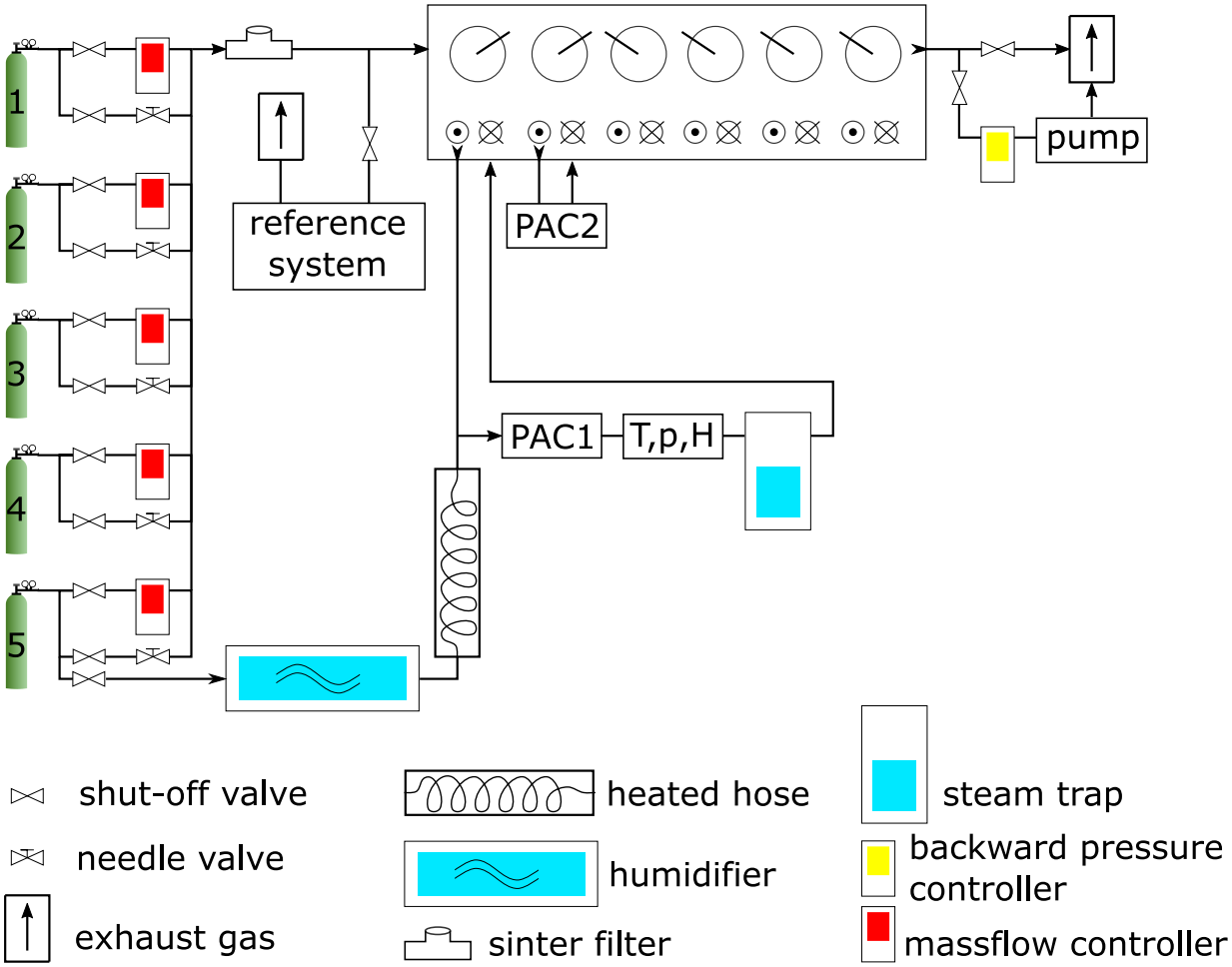

Figure 3.2: Schematic drawing of the gas stream consisting of a gas mixing unit (left part) and a distribution panel (middle upper part).

sors. With a view to figure 3.2, the first two supply lines of the panel are active, while the others are shut. The first line schematically depicts the photoacoustic detection of a humidified gas stream by means of a cell, which is referred to as PAC1. Leaving this PAC, temperature, pressure and humidity of the gas are monitored by a MPL3115A2 (Adafruit Industries, New York, US) and a SHT25 (Sensirion AG, Staefa, Switzerland) sensor, respectively. Afterwards, the test gas is dehumidified by means of an TC-Standard 6111 peltier cooler* (Bühler Technologies GmbH, Ratingen, Germany) and provided to a second photoacoustic cell (referred to as PAC2) through the second supply line of the distribution panel. Downstream of the

*in figure 3.2 referred to as steam trap

panel, the test gas may either directly be fed into an exhaust gas system or drawn through a P-702CV-6K0A-RAD-33-Z backward pressure controller (Bronkhorst), when turning on a TRIVAC D 2,5 E rotary vane vacuum pump (Leybold GmbH, Aschheim, Germany). This configuration allows for generating vacuum down to 200 mbar.

3.1.2 Electronics

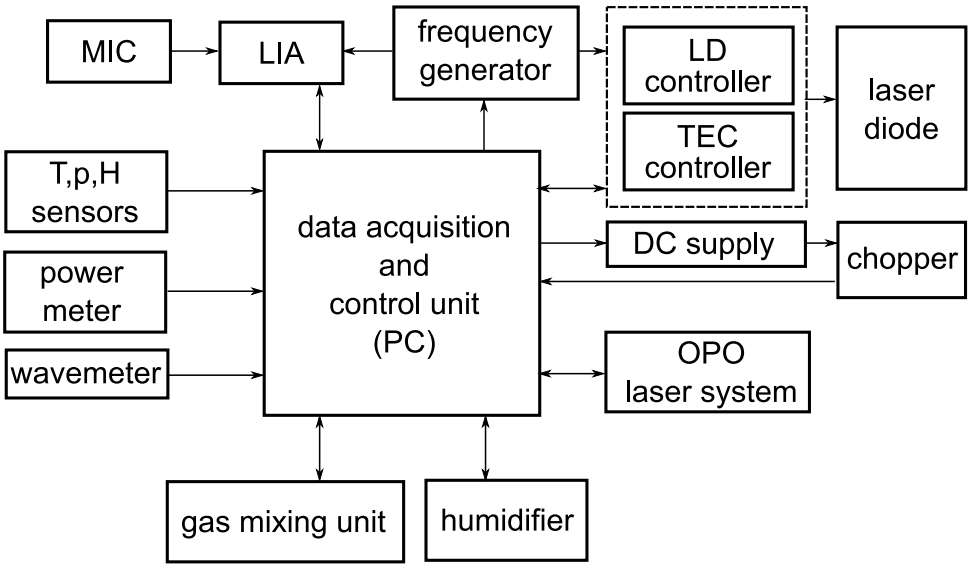

Figure 3.3: Block diagram of electronic components used within the photoacoustic setup. Clockwise description of abbreviations starting in the upper left corner: MIC: microphone, LIA: lock-in amplifier, TEC: Thermoelectric cooler, LD: laser diode, DC: direct current, OPO: optical parametric oscillator, T,p,H: temperature, pressure, humidity.

This subsection addresses the electronic components, which are used within the photoacoustic setup. Figure 3.3 shows a block diagram that illustrates the interconnection of the individual parts. The core element of data acquisition and signal processing is a PC which features a variety of analog and digital interfaces, e.g. Universal Serial Bus (USB), Transmission Control Protocol/Internet Protocol (TCP/IP), RS-232 serial ports and General Purpose Interface Bus (GPIB). All electronic devices are controlled by means of a comprehensive measuring software that was developed in LabVIEW (National Instruments, Austin, Texas, US). The left part in figure 3.3 can be

considered the sensor part, as the data flow mainly is uni-directional towards the control unit. The most essential sensor for photoacoustic detection obviously is a sound transducer. In order to facilitate comparison between different cell designs, an ultra-low noise MEMS microphone (ICS-40720, InvenSense Inc., California, US) was applied regarding all measurements that are presented in chapters 4.1, 4.2 and 4.5. The operating voltage of the microphone is provided by a PL601-P power supply (AimTTi, Cambridgeshire, UK). Apart from monitoring temperature, pressure and humidity, which already has been addressed in section 3.1.1, the sensor part further involves a PM100D power meter equipped with a thermal S302C head (Thorlabs GmbH, Munich, Germany) to monitor the optical power as well as a 621B-IR wavemeter (Acal BFi GmbH, Gröbenzell, Germany) to monitor the wavelength of laser radiation, respectively. The microphone signal is passed on to a 7225 DSP lock-in amplifier (Signal Recovery, Tennessee, US), which is referenced to a certain modulation frequency using a 33500B function generator (Keysight Technologies, California, US). Besides, the modulation signal is provided to a LDC-3744C laser diode controller* (ILX Lightwave, Montana, US), which controls a PL TB450B semiconductor laser (OSRAM Opto Semiconductors, Regensburg, Germany). The diode laser emits at 450 nm with a maximum optical output power of 1.6 W. All photoacoustic measurements presented in chapter 4 are based on amplitude modulating† (AM) this source.‡ Due to their operating principle, diode lasers can be electronically modulated at frequencies that are usually applied in case of photoacoustic detection, i.e. < 50 kHz. In contrast, amplitude modulation of the OPO laser system was realized by a combination of a SCT-Model-310CD mechanical chopping unit and a 300D30 30 slot chopping disc (Scitec Instruments Ltd, Trowbridge, UK). The chopping frequency is controlled by a DC voltage signal that is provided by a E3631A triple output power supply (Agilent Technologies, Santa Clara, California, US).

*which includes a thermoelectric cooler (TEC) for temperature control

†in literature also often referred to as intensity modulation (IM)

‡With the exception of chapter 4.5, where a package is used that contains three of those diode lasers in order to increase the optical output power.

3.1.3 Optical path

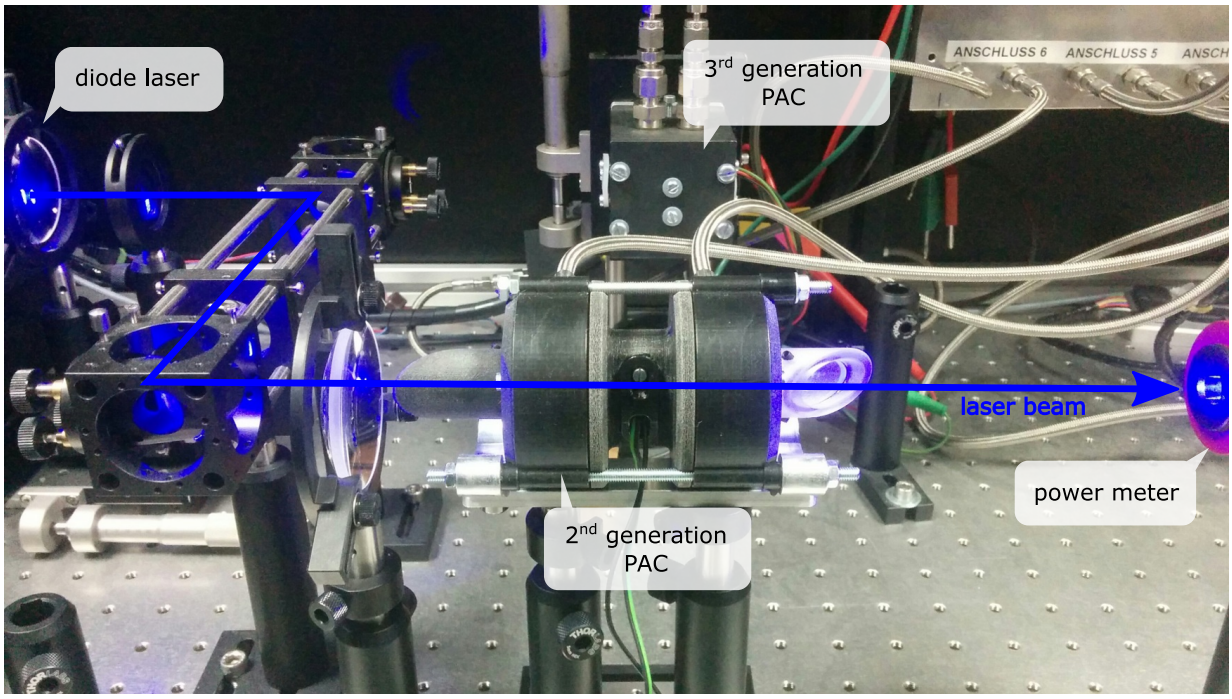

Figure 3.4: Picture of the photoacoustic setup with focus on the optical path, which is highlighted by a blue arrow.

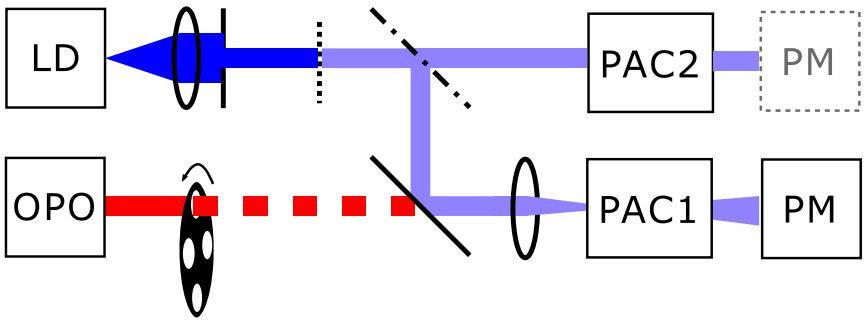

Figure 3.5: Schematic drawing of the optical path. LD: laser diode, OPO: optical parametric oscillator, PAC: photoacoustic cell, PM: power meter.

Concluding section 3.1, figure 3.4 and figure 3.5 show a picture and a schematic drawing of the optical path, respectively. The upper left part of both figures displays a converging lens that is attached immediately in front of the laser diode mount in order to collimate the strongly diverg-

ing laser radiation. Following the optical path, which is highlighted by a blue arrow, the laser beam then passes an iris diaphragm and two mirrors accounting for 90° beam diversion each. The drawing additionally depicts a variable ND filter between diaphragm and mirror, which is used to investigate the effect of optical power reduction on the PA signal (refer to chapter 4.2.5.3). After beam diversion a second converging lens is used to further reduce the beam cross section in order to accurately illuminate the photoacoustic cell. Regarding figure 3.5, this cell is labeled PAC1, while the picture shows the currently mounted 2nd generation cell which is discussed in chapter 4.2 in detail. Having passed the photoacoustic cell, the power of the laser beam is monitored by means of a power meter (PM). By removing the first of those mirrors, i.e. the upper one in both figures, a second cell (PAC2) can be used for photoacoustic detection. Figure 3.4 displays the currently mounted 3rd generation cell, which is characterized in chapter 4.3. In case of PAC2 utilization, the power meter can easily be mounted behind this cell instead. Considering the bottom part in figure 3.5, removal of the second mirror allows for OPO illumination of PAC1.*

3.2 Optical parametric oscillator

The OPO laser system (cwOPO-GIGA, Qioptiq Photonics GmbH, Munich, Germany), which is integrated into the laboratory setup, is an optical parametric oscillator that allows for tunable continuous wave (c/w) emission of wavelengths ranging from 1.4 to 2.0 and 2.3 to 4.3 µm, respectively (refer to figure 3.7). While the optical output power of radiation may exceed 2 W around wavelengths of $\sim$ 1.6 and $\sim$ 3.2 µm, it diminishes to several hundreds of mW when approaching the fringes of OPO emission. Since the laser provides transversal single-mode†, but longitudinal multi-mode radiation, it is specified by a finite but narrow spectral bandwidth of $\Delta\nu < 2$ GHz, i.e. $\Delta\lambda \approx 20$ pm (FWHM) considering an emission of $\lambda = 2$ µm for example. Although this experimental section is not intended to go into detail about

*Obviously the lens in front of PAC1 has to be checked with regard to IR transmission.
†The OPO laser emits in transversal TM00 mode, thus it ensures high focusability.

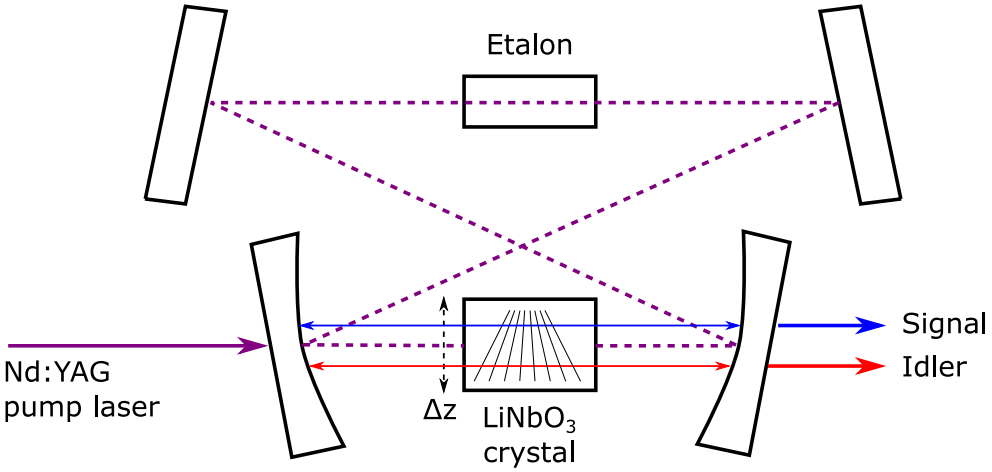

Figure 3.6: Schematic operating principle of an OPO laser system.

OPO theory, figure 3.6 illustrates a schematic overview of the working principle.

A Nd:YAG pump laser,* which emits at 1 064 nm with an output power of $\sim$ 20 W, is fiber coupled to the OPO laser. The core component of the laser is an optical non-linear lithium niobate crystal with an imprinted polarization pattern that is indicated by rake-shaped lines in figure 3.6 (refer to the middle part on the bottom of the drawing). Due to non-linearity, the radiation is divided into a Signal and an Idler beam satisfying the laws of conservation (energy and momentum). As Signal emission is characterized by shorter wavelength compared to Idler emission, they are highlighted by blue and red arrows, respectively. Further resulting from the conservation laws, OPO emission also exhibits a small portion of visible radiation between 580 and 700 nm, which can be useful with regard to optical alignment. The OPO system further utilizes a Fabry-Pérot Etalon which counteracts mode-hopping that may be caused by temperature drift for example. As indicated by the name *optical parametric oscillator*, several parameters are available for wavelength tuning. The following enumeration lists these parameters in descending order regarding their tuning range and in ascending order regarding their tuning resolution, respectively. Thus tuning is provided by variation of the

*neodymium-doped yttrium aluminum garnet; Nd:Y_3Al_5O 12

i. polarization pattern of the $LiNbO_3$ crystal by means of a motorized z-stage (indicated by a dashed double arrow labeled as Δz in figure 3.6),

ii. temperature of the crystal,

iii. temperature of the Etalon,*

iv. wavelength of pump laser radiation (this affects Idler emission only) or

v. resonator length.

Since rough adjustment of the emission wavelength always starts with crystal positioning, figure 7.7 provides a delineation of z-stage starting parameters (refer to chapter Appendix).

⚠ DO NEVER CHANGE Z-STAGE POSITION WHEN PUMP LASER IS ACTIVE

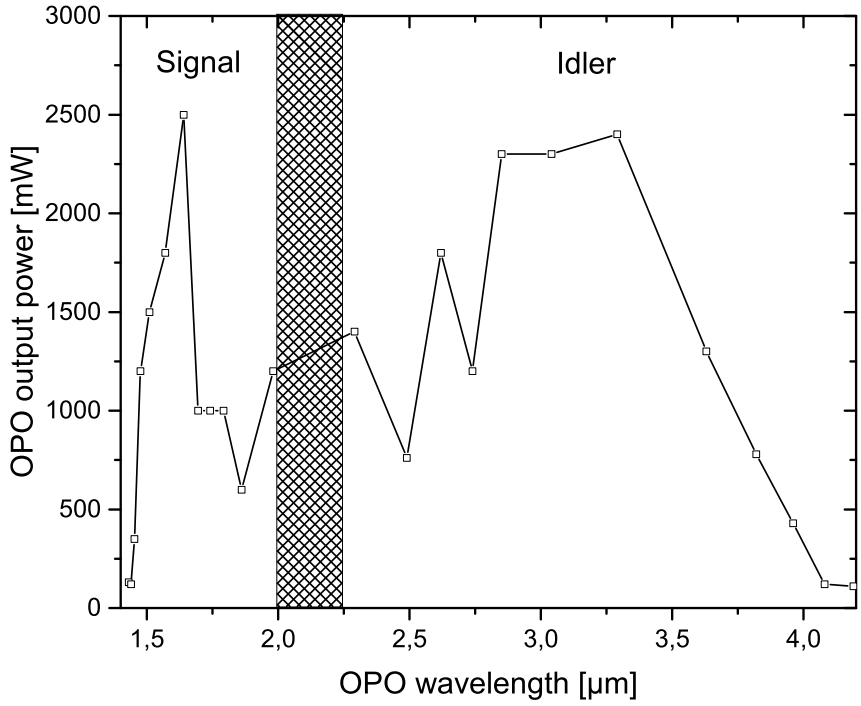

Figure 3.7: Illustration of the optical output power for some specific wavelengths of OPO radiation. Signal and Idler emissions are separated by a crosshatched region that is not available from OPO radiation.

*increasing the temperature causes the emission to red-shift

Concluding this general OPO introduction, figure 3.7 illustrates the optical output power regarding some specific wavelengths of radiation. Therein, Signal and Idler regions are separated by a crosshatched pattern, which visualizes the spectral region that is not available from OPO emission.

3.2.1 Beam alignment

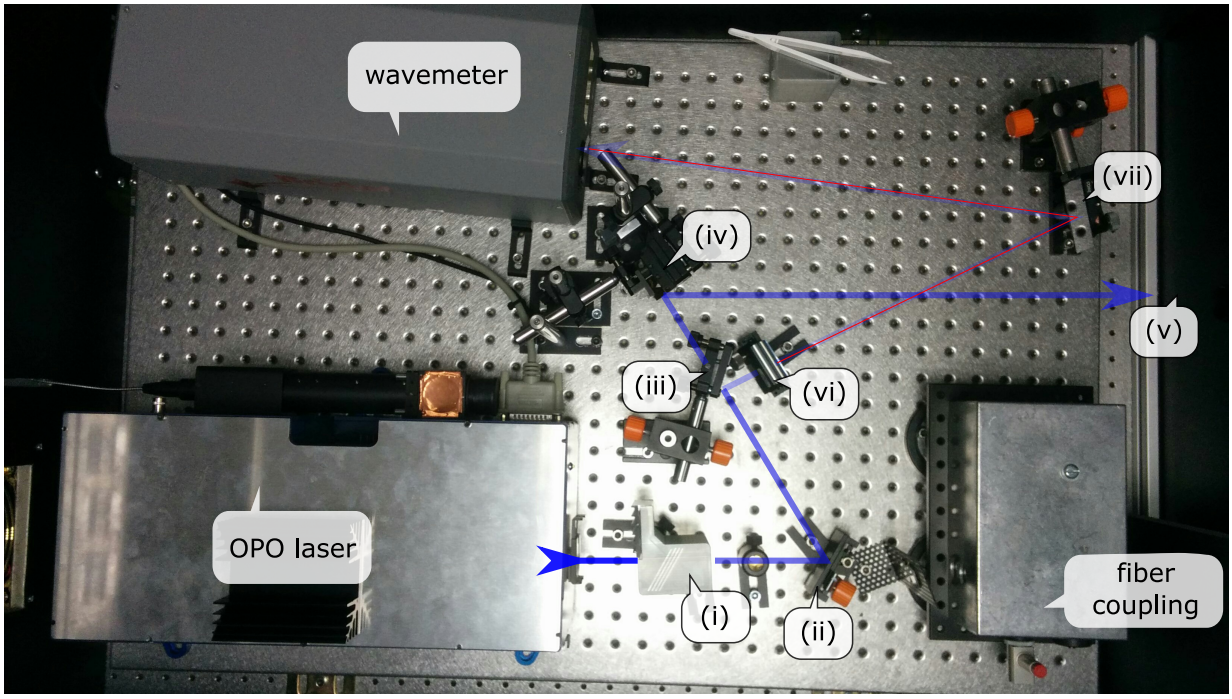

Figure 3.8: Picture of OPO laser beam alignment. (i): neutral density filter array, (ii): mirror, (iii): window, (iv): two gold coated prisms, (v): window facing the photoacoustic setup, (vi): Si-plate, (vii): mirror.

Figure 3.8 shows a picture of the OPO laser system (bottom left side of the picture) and highlights the beam alignment. After being radiated from the laser, the beam passes a neutral density (ND) filter array (i), which was developed to attenuate the optical power in order to facilitate alignment (refer to subsection 3.2.2). Since the picture was taken while open beam configuration, it subsequently is deflected by a mirror (ii), which is to be removed when fiber coupling is required. While the major part of the intensity is transmitted through a window (iii) afterwards, some minor portion is reflected, further attenuated by means of a silicon plate (vi) and

superimposed on an internal reference HeNe laser beam of the wavemeter. Superimposition, which is achieved using another mirror (vii), is required in order to monitor the wavelength of OPO radiation. However, the major part that is transmitted through (iii) is diverted towards a window (v) which was installed in the safety box (refer to section 3.1) for open beam coupling to the photoacoustic setup. This beam diversion is accomplished by means of two gold coated prisms, while one of them was mounted adjustable in height, thus it ca be switched between Signal and Idler excitation.

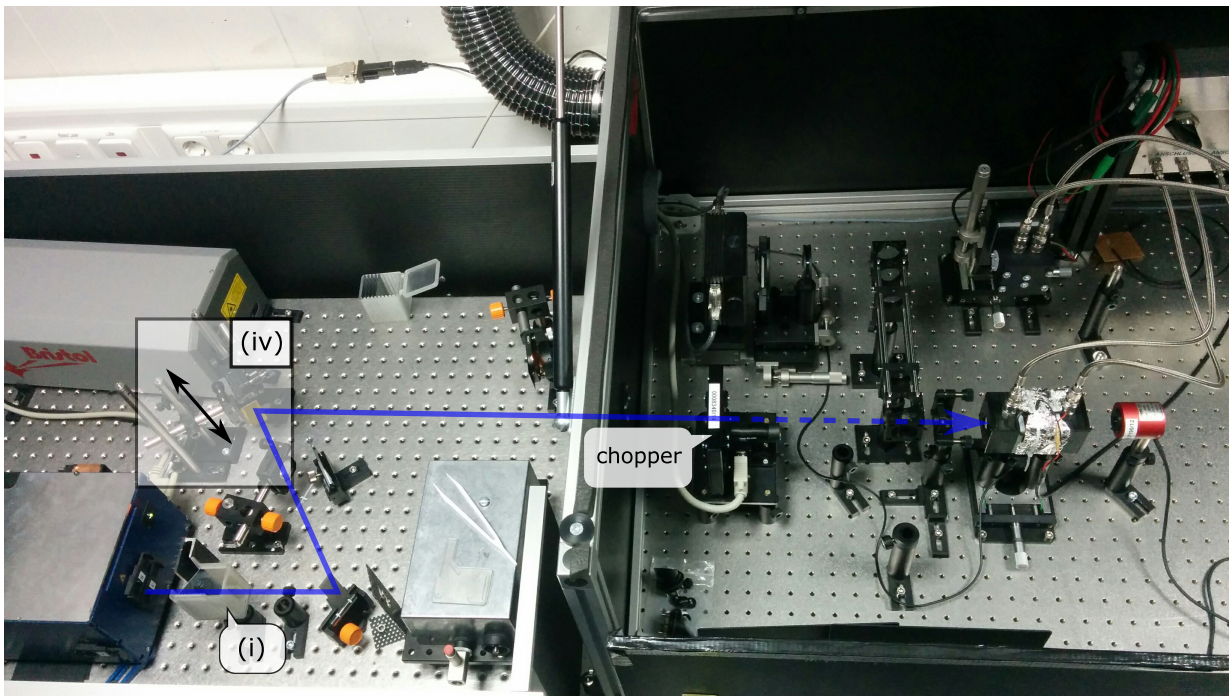

Figure 3.9: Picture of the OPO laser beam path side by side with the photoacoustic setup. The height-adjustable prisms are highlighted by a black double arrow (iv).

Figure 3.9 again shows this optical path, but from another perspective and side by side with the photoacoustic setup. Therein, the height-adjustable gold coated prism (iv) is highlighted by a black double arrow and furthermore, amplitude modulation is visualized to result from mechanical chopping (refer to the photoacoustic setup in the right part of the picture). Besides, the ND filter array is illustrated again after its cover has been removed (i).

3.2.2 Neutral density filter array

A neutral density filter array (NDFA) was developed in order to weaken the optical power, thus facilitating OPO beam alignment. Preliminary material research identified silicon to meet the requirements of optical alleviation, i.e. a linear transmission covering the entire spectral range of OPO emission and a simple practical implementation, respectively. Initially, the optical transmission of a single-side polished (SSP) silicon (Si) wafer was investigated, as those are less expensive than double-side polished (DSP) substrates. However, the non-polished surface of a piece of SSP substrate was determined to cause massive diffuse scattering, as the transmission was specified to 5 % only, although silicon generally is known to feature ~ 55 % transmission.* Regarding a wavelength of 1.65 µm, optical characterization of a DSP plate† revealed a transmission of 56 % and a targeted reflection of 33 % instead. These results agree well with the specifications of various manufacturers. Detailed comparison with these specifications by also taking into consideration the thickness of the material, further determined the remaining 11 % of optical attenuation to mainly result from diffuse scattering, while absorption only accounts for less than 1 %.

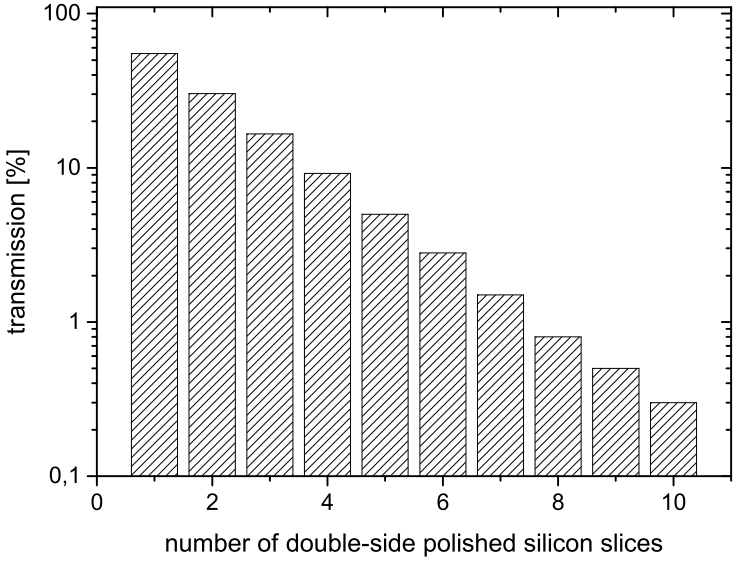

Figure 3.10: Calculated transmission of OPO radiation attenuated by silicon reflectance.

*slightly varying with the substrate width and the wavelength (between 1 and 5 µm)
†300 µm in thickness

Figure 3.10 illustrates the total remaining transmission of OPO radiation that was calculated after passing a certain number of silicon slices. As a result of these calculations, a maximum of ten Si plates was determined to suffice optical alleviation, as only 0.3 % of initial radiation remains. Based on these findings, a filter array concept was designed, which is illustrated in figure 3.11.

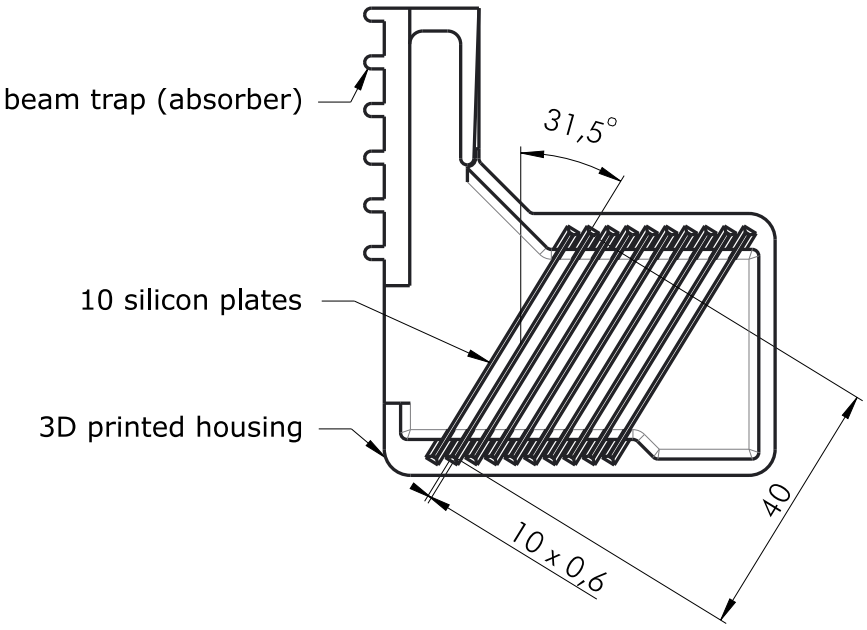

Figure 3.11: Cross section drawing of the ND filter array.

The design of the array provides the mounting of up to ten silicon plates which are tilted towards the incident beam in order to avoid back reflection to the laser. A heat sink consisting of black anodized aluminum was used as a beam trap to defang the radiation that is reflected from the plates. Since the housing was intended to be built by 3D printing, available materials were investigated regarding their resistance to radiation of 1.65 and 3.00 µm in wavelength, respectively.* VWP835 (white color) and DM9895 (black color) were excluded from the list of potential materials, as they were identified to be locally irreversible damaged due to absorption. The material TangoPlus (white and partly transparent) was determined to show only

*All materials that are mentioned in this context are acrylate polymer based mixtures, which are compounded of several different substances. For further details refer to the supplier specifications (Stratasys, Minnesota, US).

slightly less absorption, but it appeared to provide better thermal conduction, as heat input by radiation rather caused widespread turbidity than local burn damages. Anyway, the material had to be excluded for its high elasticity as well. Finally, VeroClear (white and partly transparent) was identified to be the most suitable one for housing, as it suffers from absorption the least, still it ensures the required mechanical stability. In order to definitely avoid material damage, the distance between the Si reflectors was defined sufficiently low, thus multiple reflections were calculated to only deliver radiation in the single-digit mW range to the inner walls of the filter array.

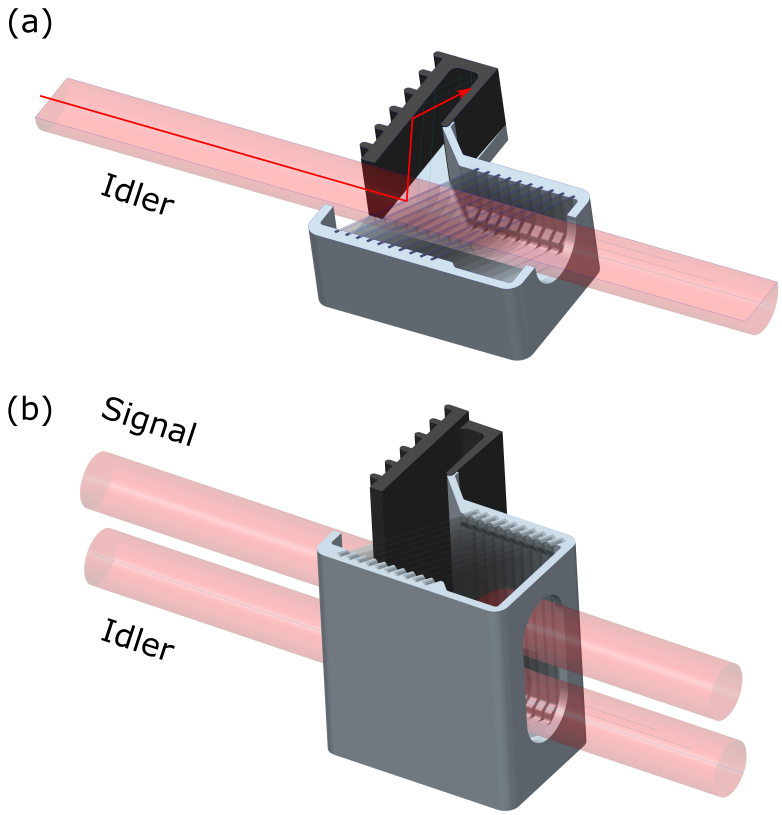

Figure 3.12: 3D drawings of the ND filter array. (a): Cross section drawing with highlighted Idler beam reflection at the first Si plate (red arrow), (b): Full drawing of the filter array (top cover removed) that displays simultaneous Signal and Idler beam illumination.

Figure 3.12 shows two three-dimensional drawings of the filter array. Part (a) illustrates a cross section drawing that only displays Idler beam illumi-

nation, but additionally highlights the reflection at the first silicon slice (red arrow). Figure 3.12 (b) further shows a drawing of the entire filter array without its top cover, thus illustrating simultaneous Signal and Idler beam attenuation.

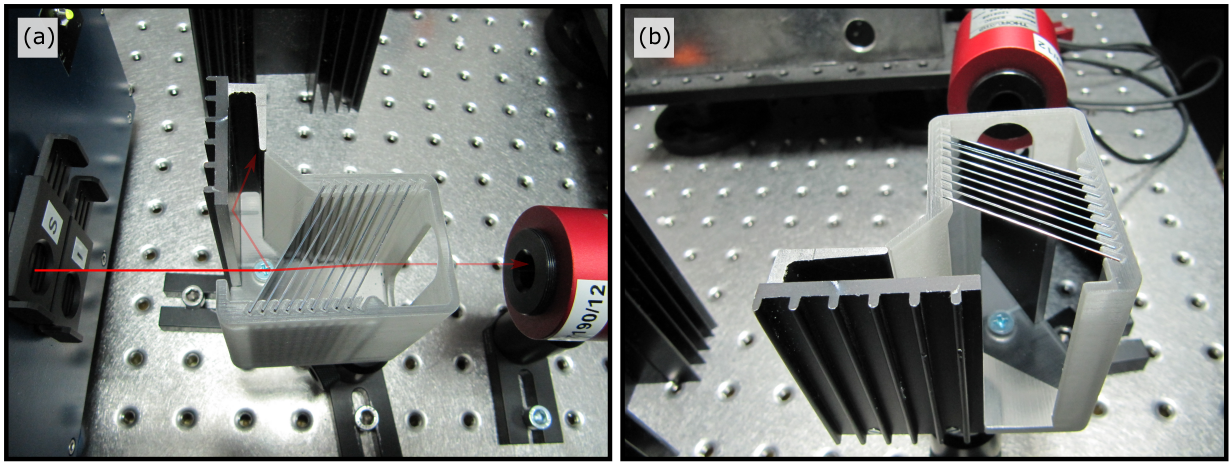

Figure 3.13: Two pictures of the ND filter array. (a): Visualization of Idler beam reflection at the first Si plate with highlighting of attenuation and beam offset (red arrow), (b): front view of the array.

Figure 3.13 finally displays two pictures of the neutral density filter array from a bird's-eye perspective (a) and in front view (b), respectively. By analogy with figure 3.12 (a), figure 3.13 (a) again highlights the OPO emission being reflected at the first silicon plate. Furthermore, it illustrates a certain lateral offset of the laser beam that results from tilting the reflectors. Without going into the details of derivation, equation 3.1 provides an expression in order to calculate the offset per Si plate h depending on the tilt angle α, the thickness of the silicon substrate d and the refractive indices of air n_1 and silicon n_2, respectively.

$$h = \frac{d}{\cos\left(\arcsin\left(\frac{n_1}{n_2}\cdot\sin\alpha\right)\right)}\cdot\sin\left(\alpha-\arcsin\left(\frac{n_1}{n_2}\cdot\sin\alpha\right)\right) \tag{3.1}$$

Based on the values $d = 525$ µm, $\alpha = 31.5°$, $n_1 = 1$ and $n_2 = 3.44$, the offset h thus is calculated to ~ 200 µm per Si plate, i.e. a maximum offset of ~ 2 mm when exploiting the capacity of ten plates.

Chapter 4

Results and discussion

Synopsis
Chapter 4 (Results and discussion) is subdivided into six sections. Sections 4.1 to 4.3 represent detailed characterizations of three different photoacoustic cell designs (PACs). The results of characterization were already published or submitted for publication (refer to pages xi to xv) and constitute the main part of this chapter. Sections 4.4 and 4.5 shortly introduce a further stage of developing a miniaturized photoacoustic sensor chip on the basis of MEMS technology and the realization of a portable photoacoustic NO_2 detection system which utilizes a standard PAC, respectively. Concluding this chapter, section 4.6 deals with the integration and characterization of a reference system, i.e. the assembly of a modified gas chromatograph and a quadrupole mass spectrometer.

4.1 Development and characterization of a laboratory setup for photoacoustic NO_2 determination based on the excitation of electronic $^2B_2$ and $^2B_1$ states using a low cost diode laser

4.1.1 Introduction

Photoacoustic spectroscopy (PAS) is known as a suitable method for trace gas sensing applications, e.g. environmental pollution monitoring [1–4], life science [5–9] and exhaust emission monitoring [10–14]. In each of these fields of application nitrogen dioxide is an analyte of great interest. Especially the automobile exhaust monitoring of NO_2 aroused great public interest by the end of 2015, when Thiruvengadam et al. [15] published research results which finally led to the Volkswagen emission scandal. NO_2 is classified as an extremely hazardous substance as chronic human exposure to concentrations above 100 ppmV can cause pulmonary edema leading to death [16, 17].
The most obvious way to quantify nitrogen dioxide using any vibrational spectroscopic technique is to excite the antisymmetric stretching vibration ν_{as} of NO_2. This fundamental oscillation is strongly absorbing at wave-

Major parts of section 4.1 are adapted from [P1] (refer to page xi).

lengths around 6.2 µm, whereas bending vibrations require significantly lower-frequency excitation. Bernegger and Sigrist [18] and Pushkarsky et al. [19] published photoacoustic NO_2 detection exciting this ν_{as} oscillation using a carbon monoxide laser and a quantum cascade laser (QCL) operating in an external grating cavity configuration, respectively. They reported detection limits (LOD) of 0.9 ppbV [18] and 0.5 ppbV (1σ) [19]. Unlike most other analytes, NO_2 provides the opportunity of electronic $^2B_2$ and $^2B_1$ excitation instead of directly exciting vibrational states in order to generate a photoacoustic signal. Slezak [20] and Angus et al. [21] already described this electronic excitation for photoacoustic NO_2 detection. However, in spite of using cost-intensive bulk tunable visible dye laser, they only achieved LODs of 30 ppbV (3σ) and 10 ppbV (3σ), respectively. Besides, Santiago et al. [22] applied low-cost light emitting diodes (LEDs) for electronic excitation and PC-based audio detection and determined detection limits of 5 ppmV (3σ) and 50 ppbV (2σ) [23], respectively. Saarela [24] also used LEDs and achieved a detection limit of 10 ppbV (0.75σ).
In contrast to the concepts above [18–21] we used a low-cost semiconductor laser for electronic excitation. The work of this publication provides the installation and the characterization of a laboratory photoacoustic setup which is meant to serve as a reference system for future development steps towards a portable photoacoustic trace gas monitoring device. In view of cost and size of this device, the components mounted into the reference system for the photoacoustic signal generation and signal detection are micromachined standard parts. The electronic excitation of NO_2 was achieved via semiconductor lasers which are mass-produced for use in laser projectors. In terms of signal detection, standard microphones were used, which are commonly built into smartphones or hearing aids.

4.1.2 Electronic excitation of NO_2

In terms of photoacoustic signal generation an PL TB450B semiconductor laser (OSRAM Opto Semiconductors, Regensburg, Germany), which emits at 450 nm with a maximum optical output power of 1.6 W, was amplitude modulated (AM) with a duty cycle of 50 %. NO_2 shows a broad chaotic absorption spectrum in the visible range from 250 nm to 650 nm with an

absorption cross section of $4 \cdot 10^{-19}$ cm^2 at 450 nm [25, 26]. The strongest absorption exhibits a cross section of $8 \cdot 10^{-19}$ cm^2 at 410 nm. By further increasing the energy of the incident light, the ONO bond angle decreases to 102° before the molecule finally photolytic dissociates at wavelengths below 398 nm [27, 28]. This broad absorption spectrum of NO_2 corresponds to electronic $^2B_2 \leftarrow X^2A_1$ and $^2B_1 \leftarrow X^2A_1$ transitions. The high line density and the complexity of the spectrum is based on strong vibronic interactions between the vibrational levels of the first electronically excited state A^2B_2 and the highly exited isoenergetic vibronic levels of the electronic ground state $^2A_1$ [28–30]. Unlike most other analyte species, the electronic excitation of NO_2 can be used in order to generate a photoacoustic signal. The special feature of NO_2 is that the VT relaxation rate of the excited states and the vibration-vibration energy transfer rate between different vibro-electronic states is much faster than the long radiative lifetime of the excited states [20]. The density of vibro-electronic levels supports the successive vibronic relaxation from the excited $^2B_2$ and $^2B_1$ states. Therefore, the ratio of radiating relaxation is much less than that calculated from the electronic oscillator strength [31] and the efficiency of heat production due to light absorption is at least 90% [32].

4.1.3 Photoacoustic cell design

The photoacoustic cell presented in this work is a bulky corpus made of stainless steel containing movable window mounts in order to adjust the buffer volumes (acoustic filter volumes) next to an open ended cylindrical acoustic resonator. Figure 4.1 shows a cross section drawing of the cell. The laser beam, which illuminates the acoustic resonator (b), is illustrated by a blue arrow and the microphone (MIC) is mounted at the bottom site of the cell. The microphone is located at a distance of 19 mm from the resonator. The acoustic resonator is 40 mm in length and 8 mm in diameter. The acoustic filter length can be adjusted by varying the position of the window mounts (a). The diameter of the buffer volumes and the maximum buffer volume length are 55 mm each.
In addition, the upper part of the drawing shows a second acoustic resonator (c) with two drilled channels for a second microphone and a speaker for

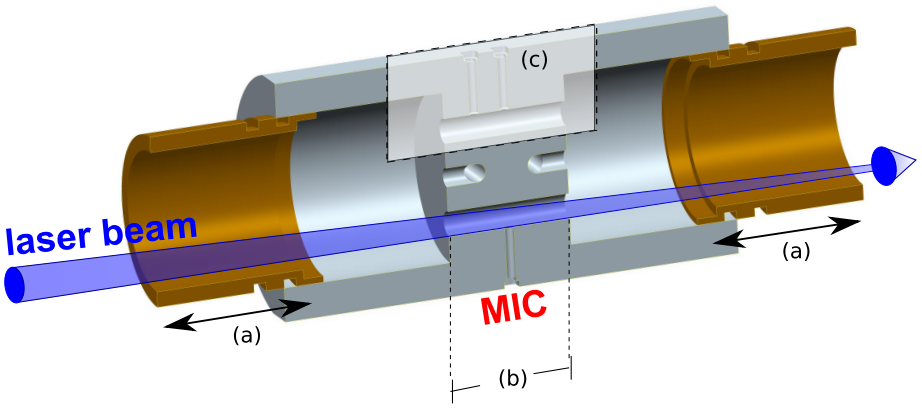

Figure 4.1: Cross section drawing of the photoacoustic cell. The double arrows (a) depict the movable window mountings for buffer length variation. The laser beam illuminating the acoustic resonator (b) is illustrated by a blue arrow. The upper part of the drawing (c) shows a second resonator for differential measurements.

differential acoustic noise reduction measurements and acoustic resonance characterization, respectively. Former investigations, however, identified no improvements using this differential measuring technique [33] and therefore, only the acoustic resonator highlighted in the bottom part of 4.1 was used with regard to the following measurements.

4.1.4 Acoustic resonance analysis

The acoustic resonance profile of the cell is recorded photoacoustically by sweeping the laser modulation frequency whilst test gas continuously flows through the cell. The acoustic resonance measurement was repeated at seven different buffer volume lengths, i.e. 15.5, 19.5, 25.0, 30.0, 35.0, 40.0 and 41.9 mm, respectively. The correlation between the length l of a both-side open-ended cylindrical resonator pipe and the length λ of standing longitudinal sound waves generated within this pipe is $l = \mathrm{n} \cdot \lambda_\mathrm{n}/2$ [34]. This work aims at the excitation of the longitudinal acoustic mode of 1st order, i.e. $\mathrm{n} = 1$. Due to non-ideal conditions, e.g. the finiteness of the buffer volumes and the resonator opening for microphone mounting, the results show complex frequency spectra instead of ideal Gaussian peak profiles.
Figure 4.2 (a) shows the acoustic resonance profiles in the range from 3.9 to 5.5 kHz, which is assumed to include the ideally calculated 1st longitudinal

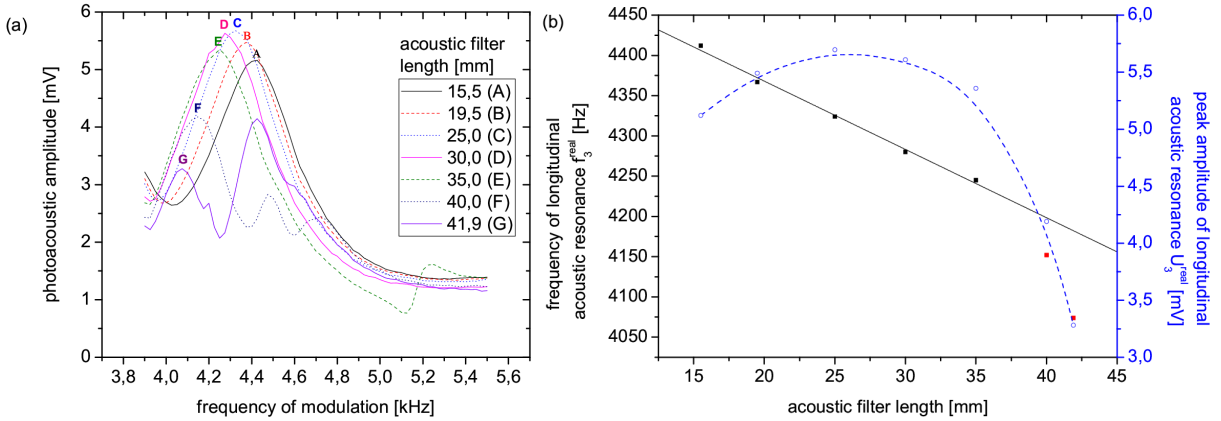

Figure 4.2: Analysis of the acoustic resonance X_3^{real}.(a) Resonance profile of the cell at modulation frequencies from 3.9 to 5.5 kHz and at seven different buffer lengths.(b) Frequency- and amplitude-shift as a function of the buffer lengths.

mode $f_{1st} = 4331$ Hz (at T = 25 °C). Figure 4.2 (b) shows the shifting of the observed peak maxima in frequency f_3^{real} and in amplitude U_3^{real} whilst increasing the buffer lengths from A to G. The frequencies show a linear dependency up to a buffer length of 35 mm and another linear dependency with an increased slope is assumed exceeding this value. The amplitudes show a parabolic dependency covering the entire range. The buffer lengths at the maximum of the parabola roughly are of the order of $\lambda/4$. However, the amplitude considerably decreases once the length of the filter volumes approach the acoustic resonator length. With an acoustic filter length of 35 mm and longer, Figure 4.2 (a) indicates the emergence of another peak that is blue-shifted. Although the origin of this peak cannot be finally resolved, it is assumed to be related to non-symmetrical conditions, e.g. slightly differing filter lengths or the fact that the resonator openings are not mounted centrally in the axis of rotation of the cylindrical filter volumes.

Figure 4.3 (a) shows the shifting of a second resonance profile with buffer length in the frequency range from 2.6 to 4.0 kHz. Figure 4.3 (b) again shows the shifting of these peak maxima in frequency f_2^{real} and in amplitude U_2^{real} whilst increasing the buffer lengths. The peak maxima again are moving towards lower frequencies by increasing the filter lengths. At lengths of 40 mm and above, the frequencies are assumed to not be affected by the acoustic filter length anymore. The amplitudes U_2^{real} show an exponential

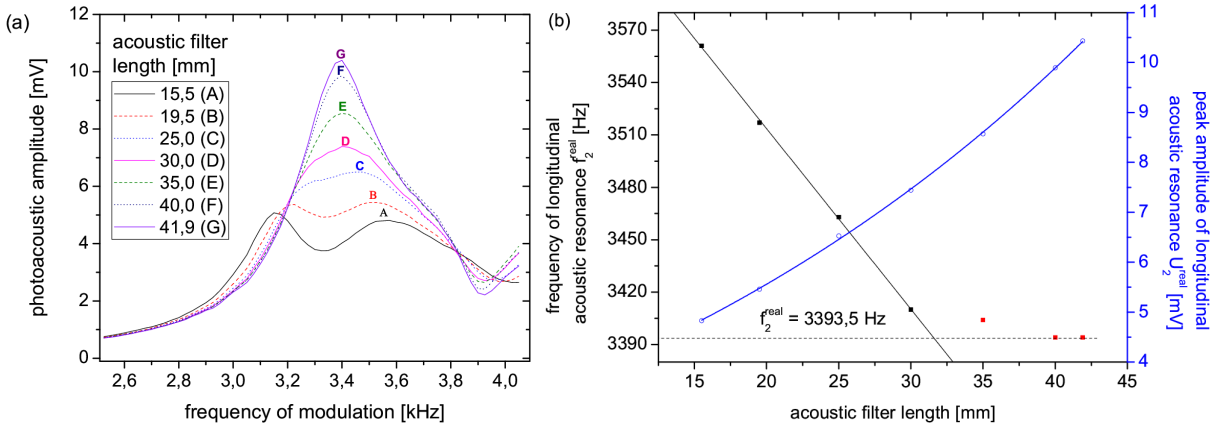

Figure 4.3: Analysis of the acoustic resonance X_2^{real}.(a) Resonance profile of the cell at modulation frequencies from 2.6 to 4.0 kHz and at seven different buffer lengths.(b) Frequency- and amplitude-shift as a function of the buffer lengths.

growth behavior with increasing buffer lengths. The lengths of the acoustic buffer volumes are known to shift the nodes of the standing acoustic wave from the resonator openings into the buffer volumes once the buffer lengths increase. This causes the resonance frequencies to red-shift [35]. With respect to buffer lengths ranging from 15 to 30 mm, this frequency shifting was determined to linearly relate to the filter lengths. The red-shifting was specified to be in the order of 10 Hz when increasing the buffer lengths by 1 mm (see Figure 4.2b and Figure 4.3b).
Since this second peak at $f_2^{\text{real}} = 3393.5$ Hz exhibits a stronger resonance amplification than the first one at f_3^{real}, this modulation frequency was chosen for further experiments. Figure 4.4 illustrates the resonance profile of this chosen modulation frequency again, showing the amplitude and the phase information of the photoacoustic signal, respectively.

The measurement was recorded at a buffer length of 41.9 mm. The mid-frequency of maximal amplification and the resonance quality factor Q, which is defined as the ratio of the mid-frequency and the full with half maximum (FWHM) [36], were identified to be 3395 Hz and 7.9 respectively. The 1.5 Hz deviation from the resonance frequency recorded above might be due to temperature effects, since neither the photoacoustic cell nor the gas flow is designed to be temperature controlled.
On the lines of Figure 4.2 (a), the generation of red-shifted peaks in Fig-

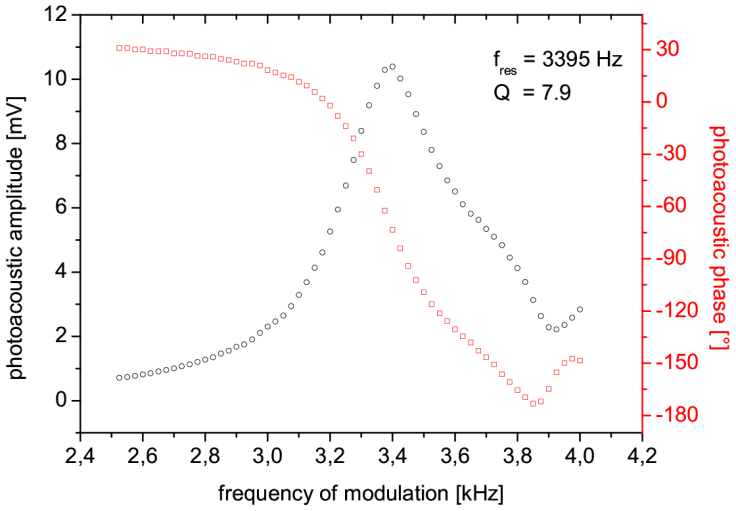

Figure 4.4: Resonance profile of the f_2^{real} peak. It shows the photoacoustic amplitude and phase at different modulation frequencies and a filter length of 41.9 mm.

ure 4.3 (a) (at filter lengths A and B) as well as the partly overlapped blue-shifted peak in Figure 4.4 are supposed to result from non-symmetric conditions and/or standing wave formation between the microphone and the actual acoustic resonator. The generation of this blue-shifted peak in Figure 4.4 contributes to the low Q value compared to other photoacoustic cell designs described in literature [37–39].

4.1.5 Signal-to-noise ratio (SNR) and noise composition

This part of the work deals with the impact of the gas flow rate, the optical power of the source and the lock-in time constant on the noise behavior of the photoacoustic signal. Unless otherwise specified, all measurement points plotted within this work represent the mean values of 100 raw data points and every noise analysis bases on the standard deviation σ of these 100 raw data points. The results are discussed at the end of this chapter.
Figure 4.5 shows the results of a series of photoacoustic experiments at a test gas concentration of 20 ppmV NO_2. Given a fixed τ_{LIA}, the standard deviations obviously do not systematically change with the flow rate. Only the mean values of the signal amplitudes slightly decrease with increasing flow rates. The mean values also do not show a systematical dependency on the lock-in time constant. However, the σ values of course depend on

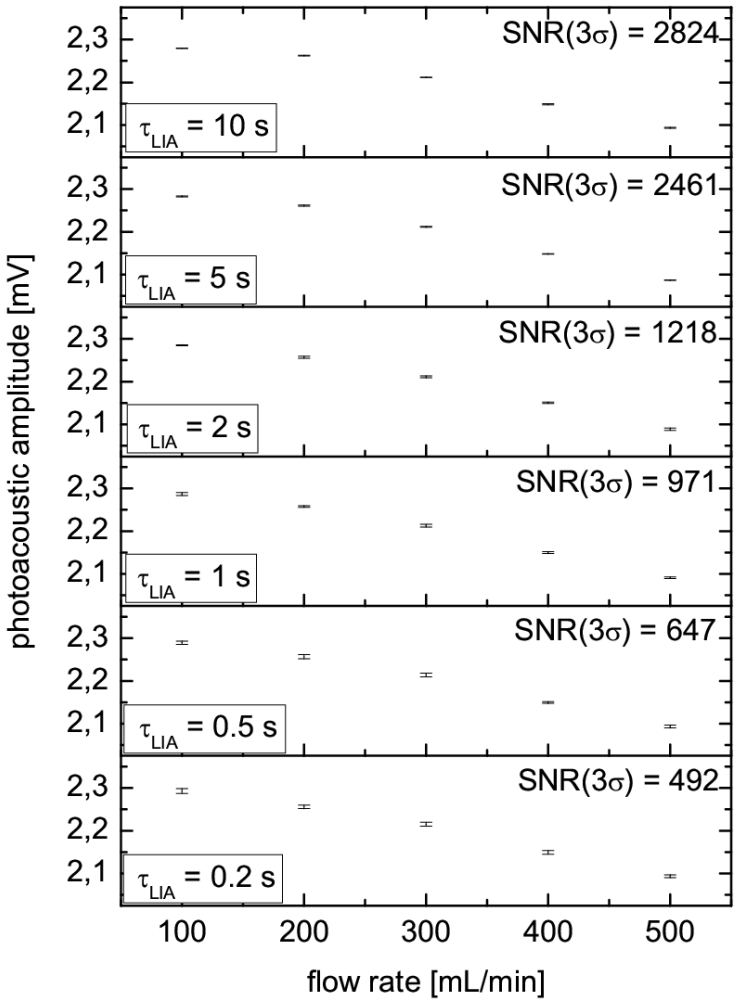

Figure 4.5: Characterization of the signal-to-noise ratio (SNR). All measurements base on a NO_2 concentration of 20 ppmV in N_2 and a mean optical power of 500 mW. The photoacoustic amplitude is illustrated at gas flow rates of 100, 200, 300, 400 and 500 mL/min and lock-in time constants of 0.2, 0.5, 1.0, 2.0, 5.0 and 10.0 seconds, respectively.

τ_{LIA}. For this reason, the chart also specifies the SNR values averaged over the results measured at different flow rates. The selection of the optimum lock-in time constant is always a trade-off between precision and measuring time. The SNR in Figure 4.5 is continuously increasing within the range of $0.2 \leq \tau_{\mathrm{LIA}}$ [s] ≤ 10 at a NO_2 concentration of 20 ppmV. However, the SNR shows an exponential decay dependency on the lock-in time constant. As the optimum lock-in time constant of the system has to be determined with regard to a NO_2 trace gas sensing application, its choice will be discussed at

the end of this chapter taking into account the background-signal at pure nitrogen flow instead of the signal at 20 ppmV NO_2 (see Figure 4.6).
As a result of the experiments, the flow rate shows no systematical dependency on the SNR, as long as it does not exceed the limit of the critical Reynolds number. Remaining below this critical number avoids the generation of turbulences inside the resonator pipe affecting the sound wave generation. The critical Reynolds number R_c is defined as [40]

$$R_c = \frac{\rho \nu d}{\eta} \tag{4.1}$$

where ρ and η are the density and the dynamic viscosity of the medium, ν and d are the mean velocity through the pipe and its diameter, respectively. In literature, the critical Reynolds number is stated to be $R_c \sim 2000$ [41], which corresponds to a maximal flow rate of 10.8 L/min through the acoustic resonator. The lower limit of the flow rate setting almost exclusively affects the measuring time of the device. Unless otherwise specified, all of the following measurements were carried out at a flow rate of 0.5 L/min.
Unlike the flow rate, the lock-in time constant is significantly affecting the noise level of the measuring system. In order to identify the optimum lock-in time constant for trace gas detection, Figure 4.6 shows the impact of the lock-in time constant on the standard deviation of the background signal. This background signal results from window and wall absorption at pure N_2 flow.
The graph indicates an exponential decay dependency and it reveals almost no improvement to the precision of the system using lock-in time constants exceeding 5 s. As a compromise between measuring time and precision, the time constant was set to 2 s in terms of the following measurements unless otherwise specified.
However, especially in terms of trace gas detection, once the analyte concentration converges to the detection limit of the system, it is recommended to increase the lock-in integration time to 5 s. Under ideal conditions, e.g. no ambient noise, further increasing τ_{LIA} does not positively affect the SNR.
By analogy with the flow rate, decreasing the optical power of the source does not reduce the noise level of the offset signal. As this noise level restricts the limit of detection (LOD) of the measuring system, its com-

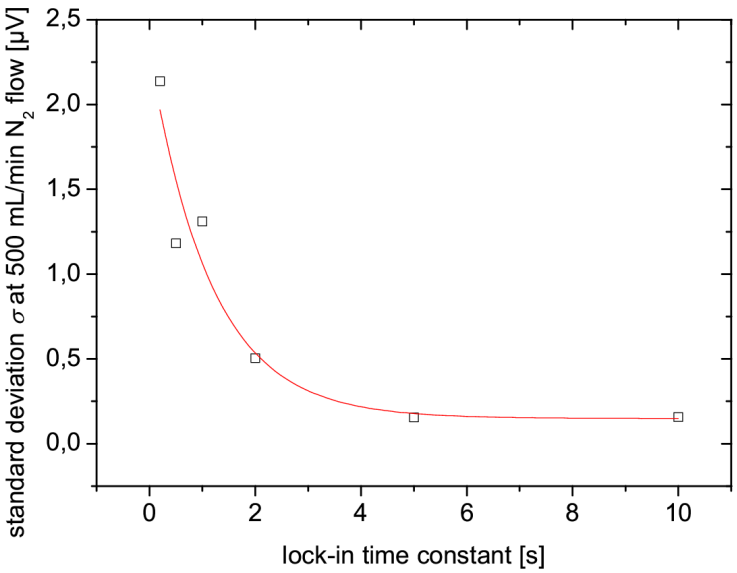

Figure 4.6: Impact of the lock-in time constant on the standard deviation of the background signal. The measurement was carried out at a 500 mL/min nitrogen flow and a mean optical power of 500 mW.

position was investigated and specified to 51 % electronic noise for lack of electromagnetic shielding and 49 % gas flow noise resulting from the test gas flowing through the acoustic resonator.

4.1.6 Calibration characteristics

Figure 4.7 illustrates the NO_2 calibration characteristics of the photoacoustic measuring system in the range of 300 ppbV to 100 ppmV.
The coefficient of determination $R^2 = 0.99992$ specifies the linear dependency of the photoacoustic amplitude on the NO_2 concentration. The sensitivity of the measuring system is 110 µV/ppmV and the maximum concentration error due to calibration was calculated to ± 0.8 % by taking $\pm\ 3\sigma$ and $\pm\ 3\sigma_m$ into account, which corresponds to the standard deviations of the raw data points and the standard deviation of the slope of the linear regression, respectively. The LOD (3σ) of the measuring system was calculated to 2.0 ppbV, which is comparable to previously reported data based on infrared excitation using a CO-laser [18] and an external cavity QCL [19], respectively.

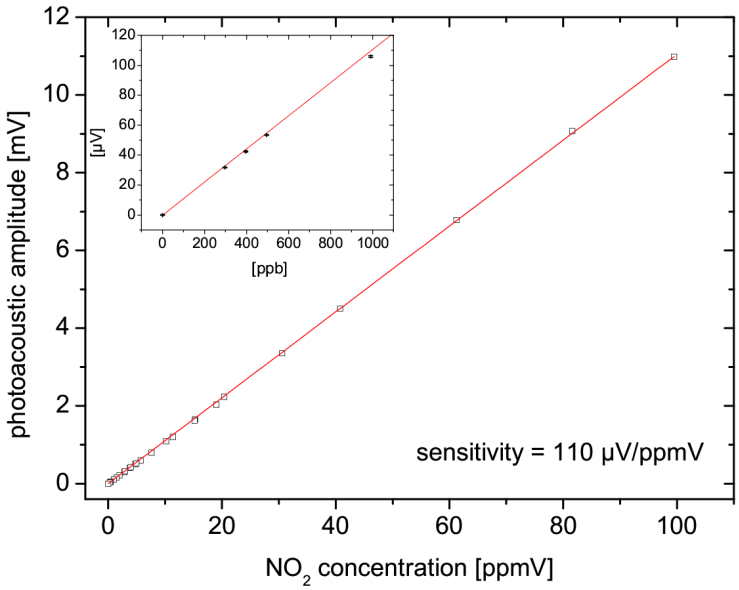

Figure 4.7: Calibration characteristics. The calibration characteristics of the photoacoustic system are illustrated in the concentration range from 300 ppbV to 100 ppmV.

4.1.7 Long-term stability

The graphical representations within this chapter show the photoacoustic amplitude with varying NO_2 concentrations recorded over a measuring period of about four hours. Furthermore, the impact of ambient noise on the photoacoustic signal was studied. The analyte concentrations within Figure 4.7 describe the nominal concentrations used for MFC control and the percentage values specify the accuracy, i.e. the discrepancy between these nominal concentrations and the respective calculated concentrations using the calibration curve. The calibration curve was recorded three days prior to this experiment.

Figure 4.8 shows the typical response behavior of the photoacoustic amplitude for changing concentrations of nitrogen dioxide. The nominal concentrations of 30 ppmV and 90 ppmV were rerun, respectively. The two dotted horizontal lines together with the hardly altering accuracy values validate the stability of the signal. The response time τ_{90} of the photoacoustic signal in terms of the NO_2 concentration increasing from 70 ppmV to 90 ppmV (at a measuring time of 65 minutes in Figure 4.8) was determined to 58 s. Another experiment was carried out in order to investigate the signal drift

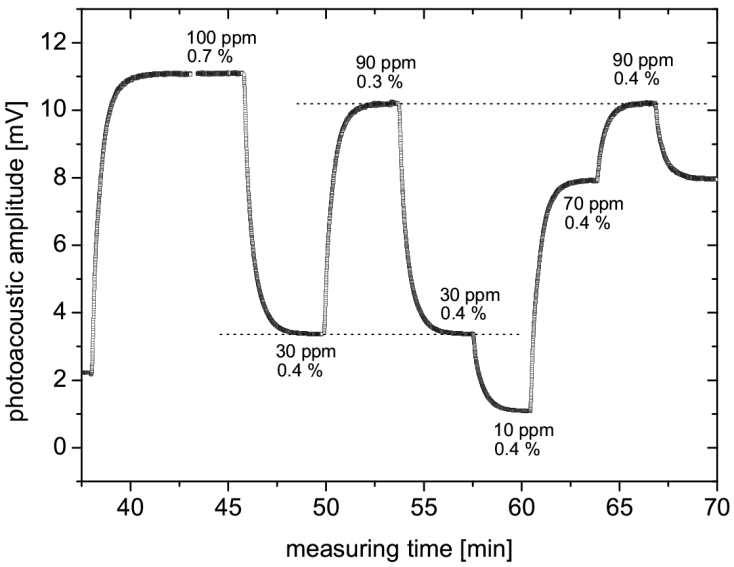

Figure 4.8: Signal stability. Investigation of the stability of the photoacoustic signal in a measuring time range from minute 35 to minute 70.

behavior. For this purpose, the NO_2 concentration was set to 20 ppmV and 1 ppmV, respectively, and the photoacoustic signal was monitored for about half an hour. Both measurements identified the photoacoustic amplitude to drift less than 1 % within this measuring period. Given the fact that neither the gas flow nor the photoacoustic cell is temperature controlled, these results again prove the stability of the photoacoustic signal.

Figure 4.9 again shows the nominal NO_2 concentrations together with the respective deviations after changing the test gas cylinders. The fact that the accuracy of the system is not adversely affected by changing the cylinders of the gas mixing unit proves a good quasi-reproducibility of the system.
Furthermore, some first test series were carried out in order to evaluate the influence of ambient noise on the photoacoustic signal. For this purpose, an audio file reproducing traffic noise and a diesel engine was played and the sound pressure level next to the photoacoustic detector was recorded using a sound level meter. The acoustic pressure was specified to be in the range of 85 dB, which corresponds to noise resulting from high volume road traffic [42, 43]. As a result of this ambient noise simulation, the standard deviation increased from 1.6 µV to 7.2 µV. By increasing the lock-in time constant from 2 s to 10 s the standard deviation decreased to 1.7 µV even

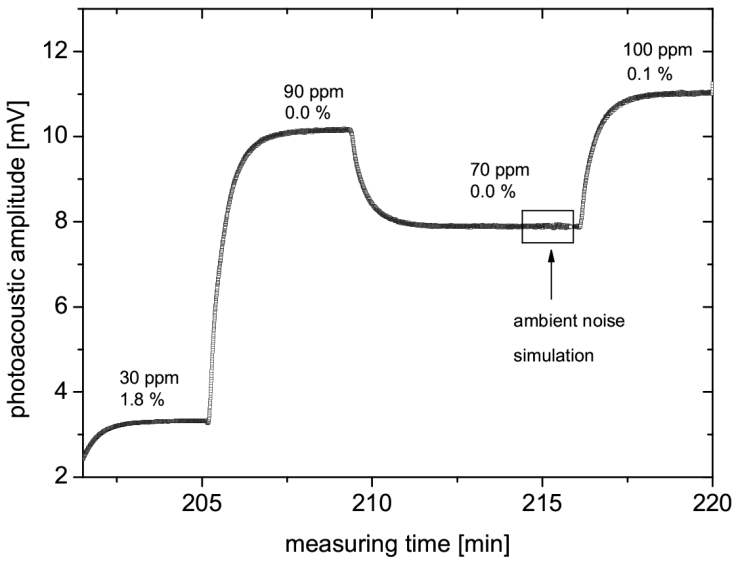

Figure 4.9: Influence of acoustic noise. Investigation of ambient noise affecting the precision of the photoacoustic measurement. The measuring time ranges from minute 202 to minute 220 and the ambient noise was simulated at minute 215.

whilst ambient noise simulation. Reducing the integration time of the LIA to 0.2 s caused σ to further increase to 17.7 µV. Since audio files only feature a limited sample rate, the impact of ambient noise on the SNR has to be further investigated.

4.1.8 Conclusion

The linearity of the photoacoustic signal dependency on the analyte concentration was verified from 300 ppbV to 100 ppmV NO_2 with a coefficient of determination $R^2 = 0.99992$. The results show that the presented photoacoustic measuring system is suitable for highly accurate trace gas quantification with a detection limit of 2.0 ppbV NO_2. Using a low-cost semiconductor laser for electronic excitation of the analyte together with a standard MEMS microphone for signal recording pave the way from a laboratory setup to a downscaled portable application.
An acoustic resonator was used for signal amplification and a frequency analysis was performed. The results show that the design of the buffer volumes and the diameter of the resonator have to be considered in view of dimensioning the photoacoustic cell. The highest signal amplification was

achieved at buffer lengths equaling the resonator length or longer. The frequency of this resonance peak turned out to be red-shifted. The optimum lock-in time constant was identified to 2 s for analyte concentrations ranging from 300 ppbV to 100 ppmV. In case of ambient noise τ_{LIA} was determined to 10 s in order to preserve the SNR. However, these ambient noise simulations were performed using an audio file playing back recorded street traffic. Since audio files have limited sample rates, these results must be treated with some reservation and are solely meant to illustrate the general tendency of ambient noise affecting the photoacoustic signal.
A general noise analysis of the photoacoustic measuring system identified the electronic noise to account for 51 % and the gas flow noise for 49 % of the total noise level. Therefore, there is still a potential for improving, as optimal shielding the detection unit as well as improving the gas flow design of the photoacoustic cell might improve the detection limit of the measuring system. Table 4.1 sums up the characteristics of the photoacoustic measuring system for the determined optimum operating parameters, i.e. a LIA time constant of 2 s, a mean optical power of 500 mW and a flow rate of 500 mL/min.

Table 4.1: Characterization of the photoacoustic measuring system for NO_2 detection. f_{res}: frequency of modulation, Q: quality factor of acoustic resonance, LOD: limit of detection, maximum error of calibration, signal drift, sensitivity, response time.

f_{res}	Q	LOD(3σ)	max. error[a]	signal drift[b]	sensitivity	τ_{90}
3395 Hz	7.9	2.0 ppbV	$\pm$ 0.8 %	$\leq \pm$ 1 %	110 µV/ppmV	58 s

[a]The maximum error takes into account three times the standard deviation of 100 raw data points and three times the standard deviation of the linear regression of the calibration curve.
[b]Signal drift within a measuring period of 30 minutes.

References

[1] H. Huszar, A. Pogany, Z. Bozoki, A. Mohacsi, L. Horvath and G. Szabo, Ammonia monitoring at ppb level using photoacoustic spectroscopy for environmental application, *Sensors and Actuators, B: Chemical*, 134(2):1027–1033 (2008), ISSN 09254005, doi:10.1016/j.snb.2008.05.013.

[2] P. L. Meyer and M. W. Sigrist, Atmospheric pollution monitoring using CO2-laser photoacoustic spectroscopy and other techniques, *Review of Scientific Instruments*, 61(7):1779–1807 (1990), ISSN 00346748, doi:10.1063/1.1141097.

[3] H. A. Beck, *Anwendung der Photoakustischen Spektroskopie in der Prozess- und Umweltanalytik*, Ph.D. thesis, TU München (2003).

[4] F. J. Harren, G. Cotti, J. Oomens and S. t. L. Hekkert, Photoacoustic Spectroscopy in Trace Gas Monitoring, in *Encyclopedia of Analytical Chemistry*, pages 2203–2226 (John Wiley and Sons, Ltd, Chichester, UK, 2000), ISBN 0471976709, doi:10.1002/9780470027318.a0718, URL `http://doi.wiley.com/10.1002/9780470027318.a0718`.

[5] F. Keppler, J. T. Hamilton, M. Bra and T. Rockmann, Methane emissions from terrestrial plants under aerobic conditions, *Nature*, 439(January):187–191 (2006), ISSN 0028-0836, doi:10.1038/nature04420.

[6] M. M. J. W. Van Herpen, A. K. Y. Ngai, S. E. Bisson, J. H. P. Hackstein, E. J. Woltering and F. J. M. Harren, Optical parametric oscillator-based photoacoustic detection of CO2 at 4.23 um allows real-time monitoring of the respiration of small insects, *Applied Physics B: Lasers and Optics*, 82(4):665–669 (2006), ISSN 09462171, doi:10.1007/s00340-005-2119-4.

[7] A. K. Y. Ngai, S. T. Persijn, G. Von Basum and F. J. M. Harren, Automatically tunable continuous-wave optical parametric oscillator for high-resolution spectroscopy and sensitive trace-gas detection, *Applied Physics B: Lasers and Optics*, 85(2-3):173–180 (2006), ISSN 09462171, doi:10.1007/s00340-006-2362-3.

[8] P. M. V. Bodegom, T. Groot, B. V. D. Hout, P. A. Leffelaar and J. Goudriaan, Diffusive gas transport through flooded rice systems, *Journal of Geophysical Research*, 106:20,861–20,873 (2001).

[9] F. Müller, A. Popp, S. Schiller and F. Kühnemann, Cw-OPO based photoacoustic spectrometer for highly sensitive detection of ethane and other volatile organic compounds, *Photons Plus Ultrasound: Imaging and Sensing*, 49(0):138–144 (2004), ISSN 16057422, doi:10.1117/12.532706, URL `http://proceedings.spiedigitallibrary.org/proceeding.aspx?articleid=1321668`.

[10] W. Schindler, C. Haisch, H. a. Beck, R. Niessner, E. Jacob and D. Rothe, A Photoacoustic Sensor System for Time Resolved Quantification of Diesel Soot Emissions, *Sae 2004-01-0968*, 2004(724) (2004), doi:10.4271/2004-01-0968.

[11] J. Cihelka, V. Horka and S. Civis, Diode laser photoacoustic detection of automobile exhaust emissions, in *Proceedings of 2005 7th International Conference on Transparent Optical Networks, ICTON 2005*, volume 1, pages 349–354 (2005), ISBN 0780392361, doi: 10.1109/ICTON.2005.1505820.

[12] H. A. Beck, R. Niessner and C. Haisch, Development and characterization of a mobile photoacoustic sensor for on-line soot emission monitoring in diesel exhaust gas, *Analytical and Bioanalytical Chemistry*, 375(8):1136–1143 (2003), ISSN 16182642, doi:10.1007/s00216-003-1810-8.

[13] W. P. Arnott, J. W. Walker, H. Moosmüller, R. A. Elleman, H. H. Jonsson, G. Buzorius, W. C. Conant, R. C. Flagan and J. H. Seinfeld, Photoacoustic insight for aerosol light absorption aloft from meteorological aircraft and comparison with particle soot absorption photometer measurements: DOE Southern Great Plains climate research facility and the coastal stratocumulus imposed perturbat, *Journal of Geophysical Research Atmospheres*, 111(5):1–16 (2006), ISSN 01480227, doi:10.1029/2005JD005964.

[14] S. M. Japar and A. N. N. C. Szkarlat, Measurement of Diesel Vehicle Exhaust Particulate Using Photoacoustic Spectroscopy, *Combustion Science and Technology*, 24(5-6):215–219 (1980), ISSN 0010-2202, doi:10.1080/00102208008952440, URL `http://www.tandfonline.com/doi/abs/10.1080/00102208008952440`.

[15] A. Thiruvengadam, M. C. Besch, P. Thiruvengadam, S. Pradhan, D. Carder, H. Kappanna, M. Gautam, A. Oshinuga, H. Hogo and M. Miyasato, Emission rates of regulated pollutants from current technology heavy-duty diesel and natural gas goods movement vehicles, *Environmental Science and Technology*, 49(8):5236–5244 (2015), ISSN 15205851, doi: 10.1021/acs.est.5b00943.

[16] U.S. EPA, Integrated Science Assessment for Oxides of Nitrogen - Health Criteria (Final Report), (EPA/600/R-15/068) (2016), URL `https://cfpub.epa.gov/ncea/risk/recordisplay.cfm?deid=310879&inclCol=hhra`.

[17] U.S. Department of Health and Human Services: Agency for Toxic Substances and Disease Registry, Nitrogen Oxides (NO, NO2 and others) CAS 10102-43-9 ; UN 1660 (NO) CAS 10102-44-0 ; UN 1067 NO2) UN 1975 (Mixture), *Agency for Toxic Substances and Disease Registry (ATSDR)*, 1660(2):1–20 (1975), URL `http://www.atsdr.cdc.gov/MHMI/mmg175.pdf`.

[18] S. Bernegger and M. Sigrist, *CO-laser photoacoustic spectrocopy of gases and vapors for trace gas analysis*, Phd thesis, ETH Zürich (1988).

[19] M. Pushkarsky, A. Tsekoun, I. G. Dunayevskiy, R. Go and C. K. N. Patel, Sub-parts-per-billion level detection of NO2 using room-temperature quantum cascade lasers., *Proceedings of the National Academy of Sciences of the United States of America*, 103(29):10846–9 (2006), ISSN 0027-8424, doi:10.1073/pnas.0604238103, URL `http://www.pnas.org/content/103/29/10846.full`.

[20] V. Slezak, High-precision pulsed photoacoustic spectroscopy in NO2 - N2, *Applied Physics B: Lasers and Optics*, 73(7):751–755 (2001), ISSN 0946-2171, doi:10.1007/s003400100686, URL http://www.springerlink.com/openurl.asp?genre=article&id=doi:10.1007/s003400100686.

[21] A. M. Angus, E. E. Marinero and M. J. Colles, Opto-acoustic spectroscopy with a visible CW dye laser, *Optics Communications*, 14(2):223–225 (1975), ISSN 00304018, doi:10.1016/0030-4018(75)90218-7.

[22] G. D. Santiago, M. G. Gonzalez, A. L. Peuriot, F. Gonzalez and V. B. Slezak, Blue light-emitting diode-based, enhanced resonant excitation of longitudinal acoustic modes in a closed pipe with application to NO2, *Review of Scientific Instruments*, 77(2):2004–2007 (2006), ISSN 00346748, doi:10.1063/1.2173031.

[23] G. Santiago, V. Slezak and A. L. Peuriot, Resonant photoacoustic gas sensing by PC-based audio detection, *Applied Physics B: Lasers and Optics*, 77(4):463–465 (2003), ISSN 09462171, doi:10.1007/s00340-003-1263-y.

[24] J. Saarela, *Gas-Phase Photoacoustic Spectroscopy Advanced Methods for Photoacoustic Detection and Signal Processing* (2011), ISBN 9789521526763.

[25] K. Bogumil, J. Orphal, T. Homann, S. Voigt, P. Spietz, O. Fleischmann, A. Vogel, M. Hartmann, H. Kromminga, H. Bovensmann, J. Frerick and J. Burrows, Measurements of molecular absorption spectra with the SCIAMACHY pre-flight model: instrument characterization and reference data for atmospheric remote-sensing in the 230-2380 nm region, *Journal of Photochemistry and Photobiology A: Chemistry*, 157(2-3):167–184 (2003), ISSN 10106030, doi:10.1016/S1010-6030(03)00062-5, URL http://linkinghub.elsevier.com/retrieve/pii/S1010603003000625.

[26] A. Vandaele, C. Hermans, P. Simon, M. Carleer, R. Colin, S. Fally, M. Mérienne, A. Jenouvrier and B. Coquart, Measurements of the NO2 absorption cross-section from 42 000 cm-1 to 10 000 cm-1 (238-1000 nm) at 220 K and 294 K, *Journal of Quantitative Spectroscopy and Radiative Transfer*, 59(3-5):171–184 (1998), ISSN 00224073, doi:10.1016/S0022-4073(97)00168-4, URL http://www.sciencedirect.com/science/article/pii/S0022407397001684.

[27] T. Obernhuber, *Aufbau einer Velocity-Map Ion-Imaging Apparatur und Messungen zur Photodissoziation von Nitrosobenzol und t-Butylnitrit*, Ph.D. thesis (2003), URL http://epub.uni-regensburg.de/10218/.

[28] R. Jost, J. Nygård, A. Pasinski and A. Delon, The photodissociation threshold of NO2 : Precise determination of its energy and density of states, *The Journal of Chemical Physics*, 105(3):1287–1290 (1996), ISSN 0021-9606, doi:10.1063/1.471992, URL http://aip.scitation.org/doi/10.1063/1.471992.

[29] K. K. Lehmann and S. L. Coy, Microwave detected, microwave-optical double resonance spectra of NO2: A test of Hardwick's ergodicity conjecture, *The Journal of Chemical Physics*, 83(7):3290–3296 (1985), ISSN 0021-9606, doi:10.1063/1.449188, URL http://aip.scitation.org/doi/10.1063/1.449188.

[30] V. N. Serov, V. B. Sovkov, V. S. Ivanov and O. Atabek, Split operator method for the nonadiabatic (J=0) bound states and (A¡-X) absorption spectrum of NO2, *The Journal of Chemical Physics*, 115(14):6450–6458 (2001), ISSN 0021-9606, doi:10.1063/1.1396854, URL http://aip.scitation.org/doi/10.1063/1.1396854.

[31] V. M. Donnelly and F. Kaufman, Fluorescence lifetime studies of NO2. I. Excitation of the perturbed 2B2 state near 600 nm, *The Journal of Chemical Physics*, 66(9):4100–4110 (1977), doi:10.1063/1.434483, URL http://dx.doi.org/10.1063/1.434483.

[32] J. Saarela, *Gas-Phase Photoacoustic Spectroscopy: Advanced Methods for Photoacoustic Detection and Signal Processing*, Ph.D. thesis, Tampere University of Technology, Tampere (2011).

[33] T. Rück, *Photoakustische Detektion von NO2 und Einflussanalyse physikalischer Parameter*, Diploma thesis, University of Regensburg (2010).

[34] M. Saul, *Physik und Musik*, State examination, Johannes Gutenberg-Universität Mainz (2007).

[35] J. Ulrich, Schallausbreitung in Rohren, *Hörakustik*, pages 86–88 (2005).

[36] M. B. Pushkarsky, M. E. Webber, O. Baghdassarian, L. R. Narasimhan and C. K. N. Patel, Laser-based photoacoustic ammonia sensors for industrial applications, *Applied Physics B: Lasers and Optics*, 75(2-3):391–396 (2002), ISSN 09462171, doi:10.1007/s00340-002-0967-8.

[37] J.-p. Besson, *Photoacoustic spectroscopy for multi-gas sensing using near infrared lasers*, Phd thesis, University of Lausanne (2006).

[38] A. Miklós, P. Hess and Z. Bozóki, Application of acoustic resonators in photoacoustic trace gas analysis and metrology, *Review of Scientific Instruments*, 72(4):1937–1955 (2001), ISSN 00346748, doi:10.1063/1.1353198.

[39] J. Breguet, J. Pellaux and N. Gisin, Photoacoustic detection of trace gases with an optical microphone, *Sensors and Actuators A: Physical*, 48(1):29–35 (1995), ISSN 09244247, doi:10.1016/0924-4247(95)00848-9, URL http://linkinghub.elsevier.com/retrieve/pii/0924424795008489.

[40] G. K. Batchelor, *An Introduction to Fluid Dynamics* (1967), ISBN 0521663962, doi:10.1063/1.3060769.

[41] D. Meschede, *Gerthsen Physik* (Springer Berlin / Heidelberg, 2006), 23. auflag edition, ISBN 9783540254218.

[42] Umwelt-Bildungs-Zentrum Steiermark, Lärmtabelle (2008).

[43] Bundesministeriums der Justiz und für Verbraucherschutz, Sechzehnte Verordnung zur Durchführung des Bundes-Immissionsschutzgesetzes (Verkehrslärmschutzverordnung-16.BImSchV) (2014), URL https://www.gesetze-im-internet.de/bundesrecht/bimschv_16/gesamt.pdf.

4.2 Low-cost photoacoustic NO_2 trace gas monitoring at the pptV-level

4.2.1 Introduction

Within the last few decades, photoacoustic spectroscopy (PAS) was more and more frequently used in trace gas monitoring applications. This increased utilization of the photoacoustic technique is primarily due to the constantly growing availability of short-, mid- and long-wavelength infrared semiconductor lasers [1]. Current major applications are environmental ones, e.g. stack gas emissions, car exhaust emissions and ambient air monitoring, and biological and medical applications, respectively, e.g. post-harvest and general plant physiology, microbiology, human health analysis and entomology [2]. In some of these fields, different analytes were already monitored down to the pptV-level. When using continuous wave optical parametric oscillator (c/w OPO) laser systems, for example, some detection limits (LOD) are reported to be 65 pptV (1σ) [3] for methane, 110 pptV (3σ) [4] and 25 pptV (3σ) [5] for ethane and 190 pptV (1σ) [3] for hydrogen cyanide. Nägele and Sigrist [6] published detection limits (3σ) of 70 pptV ethylene, 200 pptV methanol and 500 pptV ethanol and Pushkarsky et al. [7] specified the minimum detectable ammonia concentration to 220 pptV (1σ) using a CO_2 laser. The utilization of the photoacoustic technique for nitrogen dioxide trace gas detection has already been described in literature as well. In this context Bernegger and Sigrist [8] and Pushkarsky et al. [9] published NO_2 detection limits of 900 pptV and 500 pptV (1σ) using a CO laser and a QCL laser with external grating, respectively. All of those references base on the direct excitation of molecular vibrations of the analyte using infrared radiation. Unlike most other analytes, nitrogen dioxide also provides the opportunity of electronic excitation in the visible range. It shows a broad absorption spectrum from 250 nm to 650 nm with an absorption cross section of $4 \cdot 10^{-19}$ cm^2 at 450 nm [10, 11]. The special feature of NO_2 is that the VT relaxation rate of the excited states and the vibration–vibration energy transfer rate between different vibro-electronic states is much faster than the long radiative lifetime of the excited states

Section 4.2 is adapted from [P2] (refer to page xiii).

[12]. For this reason the electronic energy is entirely converted into vibronic energy and contributes to the generation of the photoacoustic signal. Using tunable dye- or argon-ion-lasers for electronic excitation, Slezak [12], Angus et al. [13] and Santiago et al. [14] already specified NO_2 detection limits of 30 ppbV (3σ), 10 ppbV (3σ) and 50 ppbV (2σ), respectively. However, in 2006 Santiago et al. [15] also applied low-cost light emitting diodes (LEDs) for photoacoustic NO_2 detection and they determined the LOD to 5 ppmV (3σ). Five years later Saarela et al. [16] reported an improved photoacoustic LED setup and specified the limit of NO_2 detection to 10 ppbV (0.75σ)*. Kalkman and Van Kesteren [17] were the first† to use a GaN based diode laser emitting at 444 nm for photoacoustic NO_2 detection, that is based on electronic excitation. They achieved a detection limit of 200 pptV (1σ). Yi et al. [18] subsequently exploited electronic excitation of NO_2 using a diode laser emitting at 450 nm and reported a detection limit of 18 ppbV (1σ). Using a 4.7 W laser emitting at 532 nm and extending the measuring time to 120 s, Peltola et al. [19] determined the NO_2 detection limit to 55 pptV (1σ). Yin et al. [20] most recently published the noise equivalent NO_2 detection limit (1σ) to 54 pptV using a 3.5 W cw multimode diode laser emitting at 447 nm. Summing up these results, the utilization of semiconductor laser diodes is expected to meet the demands for photoacoustic environmental NO_2 monitoring in terms of sensitivity. In order to protect people and environment, the EU Directive 2008/50/EG provides a limit value of 40 $\mu g/m^3$ for the annual mean NO_2 concentration in air. Considering air as an ideal gas at standard ambient temperature and pressure (SATP), this emission limit equals a volume concentration of about 21 ppbV. Commissioned by the NGO Greenpeace, the NO_2 street traffic emissions were monitored in twelve German cities over a period of about one month. The results showed that 64 % of the averaged NO_2 concentration readings in all stationary measurement locations exceeded this limit.

On the lines of the concepts in [17, 18] we used a low-cost high power semiconductor laser for electronic excitation. With a view to the future implementation of the photoacoustic setup into a portable NO_2 trace gas sensing device, we also took care of selecting low-cost components relating

*i.e. the root mean square (RMS) of white noise.

†to the best of the authors knowledge

the measuring cell and the detector of the setup. This publication provides the characterization of an improved photoacoustic measuring cell in terms of acoustic resonance analysis (4.2.3), determination of optimal operating parameters (4.2.4) and performance characteristics (4.2.5). Furthermore, the influence of the interference components H_2O and CO_2 on the photoacoustic signal was investigated (4.2.6).

4.2.2 Photoacoustic cell design

The photoacoustic cell (PAC) presented in this work is made using a 3D printer. The applied material is an acrylate polymer which is compounded of twelve different substances. Only in terms of acoustic resonance amplification a tube consisting of stainless steel was mounted into the cell. The length of the tube is L = 38.7 mm and its diameter is d = 3.95 mm.

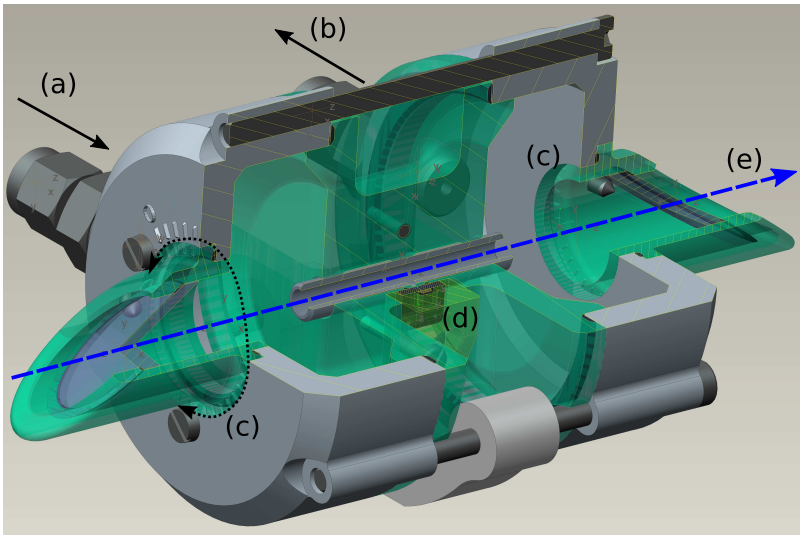

Figure 4.10: Cross section drawing of the photoacoustic cell (PAC). Gas inlet (a) and outlet (b), rotatable Brewster window mounts (c), socket for mounting various detectors (d) and laser beam (e).

Figure 4.10 shows a cross section drawing of the photoacoustic measuring cell. The gas inlet and outlet (a) are mounted at the rear of the corpus. The laser beam (d), which is illustrated by a dashed blue arrow passes a rotatable mounted Brewster window (b), illuminates the acoustic resonator and again leaves the cell passing through a second rotatable mounted Brewster

window. There is a hole drilled into the resonator tube at L/2 with 1 200 µm in diameter in order to release some of the acoustic energy. Next to this hole there is a socket for acoustic signal detection (c). The design of the socket allows the integration of different adapters in order to use different acoustic detectors. The buffer volumes next to the open ended resonator tube are of cylindrical shape with a diameter of 50 mm and 20 mm in length. Another volume is generated at the outer rim of the buffer volumes due to the rotatable Brewster window mountings. The mountings are 16.3 mm in diameter and the windows are uncoated UV Fused Silica Brewster windows (Thorlabs GmbH, München, Germany). The rotatable mounting of the windows allows to adjust the angle of incidence towards the polarization plane of the laser beam. The transmission of radiation through the measuring cell reaches its maximum at the Brewster angle, i.e. 55°32'.

4.2.3 Acoustic resonance analysis

In order to determine the resonance profile of the acoustic resonator, the modulation frequency of the laser was swept in a frequency range of 3 to 5 kHz whilst test gas of 10 ppmV NO_2 in N_2 was continuously flowing through the measuring cell with a mass flow of $Q_{\text{gas}} = 500$ mL/min. The integration time of the lock-in amplifier was set to $\tau_{\text{LIA}} = 1$ s.

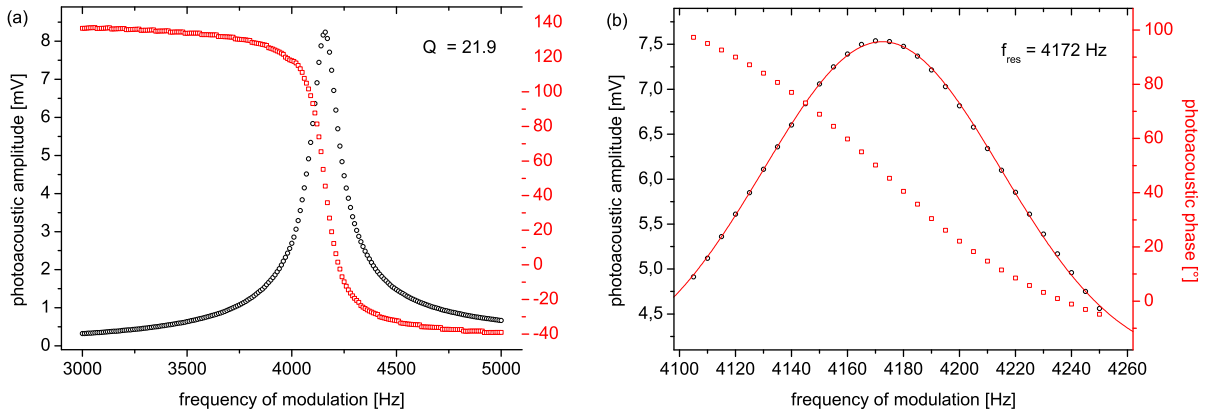

Figure 4.11: Resonance profile of the photoacoustic measuring cell. (a) Frequency range 3 to 5 kHz; increment 10 Hz. (b) Close-up of the resonance profile; increment 5 Hz.

Figure 4.11 (a) shows the resonance profile of the photoacoustic measuring cell with an increment of 10 Hz, i.e. 200 measuring points. Except

for those illustrations showing the photoacoustic signal as a function of the measuring time, i.e. 4.12, 4.15 and 4.17, every measuring point within the respective plots represents the mean value of 100 raw data points gathered with a sample rate of 5 Hz. The quality factor of the cell was determined to $Q = 21.9$. To identify the resonance frequency more precisely, figure 4.11 (b) illustrates another set of measuring points in a frequency range of 4 105 Hz to 4 250 Hz with an increment of 5 Hz. The data was fitted to the Gaussian function and the coefficient of determination was $R^2 = 0.99958$. The resonance frequency was identified to $f_{res} = 4\,172$ Hz at 24.86 °C. We were able to improve the quality of resonant amplification by a factor 3 compared to our 1st generation photoacoustic cell published in [21]. This increase is assumed to be mainly attributed to a higher symmetry of the PAC. The symmetry was increased as prior investigations revealed complex PAC geometries to cause superimposed acoustic resonance spectra, thus lowering the quality of resonant amplification. Consequently, we forewent a differential design and mounted the microphone flush with the inner wall of the resonator.

The effective length of an acoustic resonator tube L_{eff} is known to exceed its real dimensions since the nodes of the standing acoustic wave are shifted into the buffer volumes. This causes the ideally calculated resonance frequency of the longitudinal oscillation to red-shift. Previous investigations of our group determined this node shifting phenomenon to gain weight with increasing buffer lengths [21]. Once the length of the volumes is in the order of the resonator tube, the effective tube length does not increase any further. However, those previous investigations revealed complex spectra due to minor symmetry of the PAC. Since the shape of the PAC in figure 4.10 shows upper symmetry, the resonance profile in figure 4.11 can be fitted to a simple Gaussian function and the effective length of the tube is stated to depend on its radius* r_{res} and the radius of the hole r_{hole}, which serves for coupling acoustic energy to the detector.

$$L_{eff} = L_{real} + 2r_{res} - r_{hole} \tag{4.2}$$

*not the effective diameter as in [21]

Previous simulations of our group concerning differently shaped resonator geometries support this hypothesis of L_{eff} also depending on the size of the hole. This effect partly compensates the red-shifting phenomenon of f_{res} which is described above. The compensation gains influence by increasing the size of the hole. The calculation of the resonance frequency basing on 1.73 and applying 1.61 and 4.2 resulted in 4 176 Hz, which deviates only 0.8 ‰ from the empirical data. Besides its geometry, the resonance behavior of the PAC also gets affected by the composition of the sample. This shifting-dependency of f_{res} is further discussed by the example of H_2O and CO_2 in chapter 4.2.6.

4.2.4 Determination of optimal operating parameters

With the integration of Brewster windows into the PAC (see chapter 4.2.2), the photoacoustic background signal due to window absorption was reduced by 67 %. Decreasing this blank value offers two benefits: It increases the dynamic range of the application and it allows to more easily attributing the shifting of the photoacoustic phase to potential interferences, e.g. acoustic noise or cross-sensitivities to other absorbing species within the sample. However, the latter benefit can also be achieved by offset-correcting the data in vector space whilst taking into account the phase information of the photoacoustic signal. Moreover, the benefit of increasing the dynamic range by applying Brewster windows does not come into noticeable effect in view of the photoacoustic cell design presented in Figure 2. This is because the acoustic offset pressure within the PAC, which is partly due to window absorption, is only 0.134 ‰ of the maximum sound pressure level (SPL) of the microphone. Therefore, the dynamic range of the setup allows the quantification of NO_2 concentrations ranging from 100 pptV to 1 400 ppmV, i.e. a dynamic range of more than 7 orders of magnitude. Further increasing this dynamic range by reducing the background signal due to Brewster window integration is not enough to be worth the engineering effort. However, their utilization obviously increases the intensity of irradiation that is available for the generation of the photoacoustic signal. Rotating the windows to the Brewster angle led to an increase of transmission passing through the PAC by 10 %. With the results presented in chapter 4.2.5.3, this increase

in irradiation means an enhancement of the detection limit (LOD) of the system by 9 %. Nonetheless, the integration of Brewster windows is deemed accountable for delaying the response time of the PAC due to poorly flushed dead volumes (see chapter 4.2.5.1).
Another important characteristic of a photoacoustic system is the noise ($\pm 3\sigma$), as it directly determines its detection limit. This noise is mainly attributed to electronic noise for lack of electromagnetic shielding and noise resulting from the gas flow, respectively. In order to minimize the total noise, the optimal operating parameters for the time constant of the lock-in amplifier τ_{LIA} and for the mass flow through the PAC Q_{gas} were investigated. The results reveal an exponential decay dependency of the noise on τ_{LIA}. Increasing τ_{LIA} from 2 s to 5 s hardly improves the signal-to-noise ratio (SNR) and further prolonging τ_{LIA} is not considered appropriate as it unnecessarily slows down the response behavior of the system. For this reason, a time constant of 5 s was only used in case of low analyte concentrations, i.e. $N_{\mathrm{NO2}} < 1$ ppmV (see chapter 4.2.5.2). For NO_2 concentrations exceeding 1 ppmV, the time constant was set to 2 s, unless otherwise specified.
As already discussed in [21], in terms of relatively small mass flow rates, the noise does hardly depend on the mass flow. However, once the mean velocity of the flow within the resonator tube exceeds a critical value, an exponential growth dependency was determined. This critical velocity was identified to $v_{\mathrm{c}} = 0.340$ m/s, which corresponds to one-tenth of the critical Reynolds flow v_{R} calculated using the critical Reynolds number $\mathrm{R_c} = 2\,000$ [22].

$$\mathrm{R_c} = \frac{\rho v_{\mathrm{R}} d}{\eta} \tag{4.3}$$

The quantities ρ and η are the density and the dynamic viscosity of the medium and d is the diameter of the resonator pipe. Considering this diameter, the mass flow was set to the critical value of 250 mL/min in terms of all measurements, except for the analysis of the acoustic resonance (chapter 4.2.3) and the response behavior (chapter 4.2.5.1). On the basis of $\tau_{\mathrm{LIA}} = 5$ s and $Q_{\mathrm{gas}} = 250$ mL/min the noise level of the blank value at pure nitrogen flow was determined to $3\sigma = 0.08$ µV. This noise level

means an improvement by a factor 3 compared to our 1st generation PAC, although the corresponding mean velocity of the flow through the acoustic resonator exceeds the one in [21] by a factor greater 4. Since the lock-in time constant and the entire electronic configuration remained the same, the improvement is assumed to be mainly attributed to the sophisticated design of the PAC in terms of its flow characteristics. More precisely, we applied rounded edges, wherever they could be realized. In fact, the 3D-printing technique offers more freedom with respect to the details of design. Especially regarding the edges of the resonator tube itself (which is not 3D printed though), we emphasized avoiding sharp edges. Moreover, the microphone was mounted flush with the inner walls of the tube, which might counteract turbulences next to the microphone as well. The polymer material that is used for printing, however, is not assumed to contribute to noise reduction to a large extend. Prior investigations of our group actually identified the material to drastically lower the Q factor due to attenuation effects, if the acoustic resonator itself is 3D printed, too. For this reason, we utilized a stainless steel tube in view of resonance amplification instead.

4.2.5 Performance characteristics

4.2.5.1 Response behavior

The response behavior of a photoacoustic system mainly depends on the integration time of the lock-in amplifier τ_{LIA}, the mass flow Q_{gas} through the PAC and the dimensions and the shape of the buffer volumes, respectively, which the sample has to pass through before it enters the acoustic resonator. The optimal operating parameters for τ_{LIA} and Q_{gas} were specified to 2 s and 250 mL/min (see chapter 4.2.4). Even though the corresponding mean flow velocity through the resonator is 4 times faster than in case of our 1st generation PAC [21], the measured response time $\tau_{90} = 19$ s is only improved by a factor 3.* By comparing both PACs, the gas exchange within the buffer volumes of the one illustrated in figure 4.10 should be about as fast as in terms of [21], since the latter one is about twice in volume but the flow rate as well is twice as fast. Therefore, the shape of the buffer volumes

*The response time was recorded while the analyte concentration was increased from 70 to 90 ppmV.

is assumed to be accountable for delaying the gas exchange. This delay may be related to the formation of poorly flushed dead volumes due to Brewster window integration.
The following section is meant to discuss and to quantify the limits regarding the fastest possible response time of a photoacoustic setup. Therefore, turning on the laser radiation was used as a quasi-Heaviside step function. The step response to this unit step function can be used in order to calculate the theoretical fastest possible response time of an idealized photoacoustic system, i.e. an infinitely fast gas exchange within the PAC. This hypothetical response time only depends on the lock-in time constant.

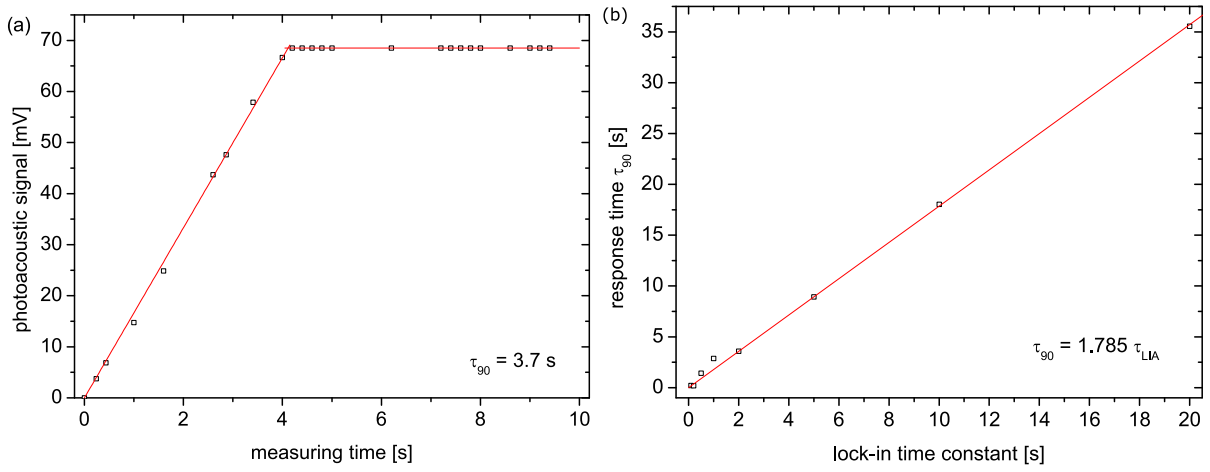

Figure 4.12: Response behavior of an idealized photoacoustic system. Turning on the laser irradiation was used as a quasi-Heaviside step function. The NO_2 concentration was set to 90 ppmV and the mass flow to 250 mL/min. (a) Step response for $\tau_{\mathrm{LIA}} = 2$ s. (b) The response time dependence on τ_{LIA}.

Figure 4.12 (a) illustrates the step response to the unit step function at a lock-in time constant of 2 s. The response time was calculated to $\tau_{90} = 3.7$ s. Furthermore, Figure 4.12 (b) specifies the linear response time dependency on τ_{LIA}.

4.2.5.2 Calibration characteristics

Figure 4.13 illustrates the calibration characteristics of the photoacoustic setup in the concentration range from 200 ppbV to 100 ppmV NO_2.

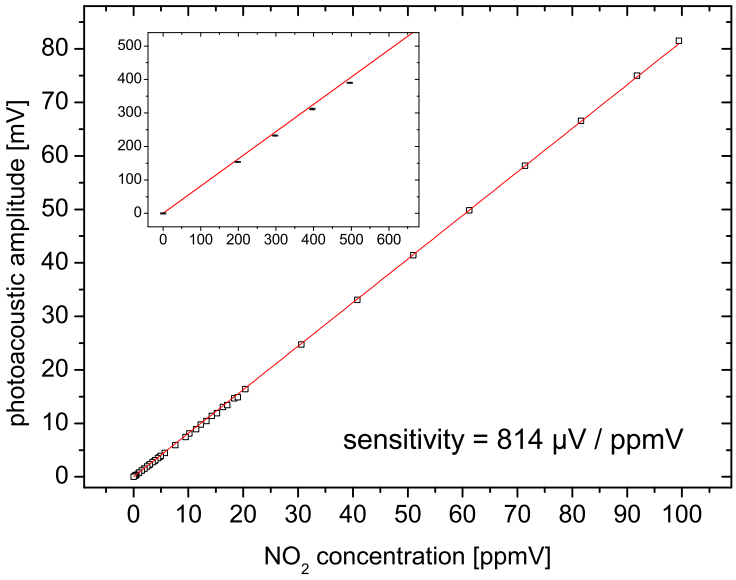

Figure 4.13: The calibration characteristics of the system ranging from 200 ppbV to 100 ppmV NO_2 diluted in N_2.

The measuring points regarding concentrations below 0.5 ppmV NO_2 are plotted separately (picture-in-picture) for better visualization. The hardly recognizable error bars mark ± 3 times the standard deviation σ of 100 raw data points. The coefficient of $R^2 = 0.99997$ specifies the linear dependency of the photoacoustic amplitude on the analyte concentration. The sensitivity of the system was determined to 814 µV per ppmV NO_2, which means an improvement by a factor 7 compared to our 1st generation PAC published in [21]. However, a combination of several factors is assumed to be accountable for this sensitivity enhancement. The major impact has to be attributed to an increase of the resonance quality factor, which was discussed in chapter 4.2.3. In addition, the resonator tube is only half in diameter compared to [21], which yields to an increase in length-to-volume ratio by a factor 4. Taking into account equation 1.85, the L/V ratio of the tube directly affects the photoacoustic signal. Besides, the smaller cross section of the PAC might also support effective light-to-sound coupling (refer to the product of coupling integral and acoustic mode in equation 1.85), since the cross section of the collimated beam remained unchanged compared to our investigations presented in [21].
The LOD (1σ) of the system was calculated to 33 pptV. Considering a

lock-in time constant of 5 s and a roll-off of 6 dB/octave, the manufacturer of the lock-in amplifier specifies an equivalent noise bandwidth (ENBW) of 50 mHz. By further taking into account the absorption cross section of NO_2 at 450 nm ($\sigma_\nu = 4 \cdot 10^{-19}$ cm^2) and a mean optical power of 480 mW, the normalized noise equivalent absorption coefficient (NNEA) was calculated* to $7.0 \cdot 10^{-10}$ W cm^{-1} Hz$^{-1/2}$. The improvement of the detection limit by a factor 20 towards our 1st generation PAC results from the product of sensitivity (discussed above) and noise improvement (refer to chapter 4.2.5), respectively.

4.2.5.3 Optical performance

Improving the sensitivity and the offset signal noise of a photoacoustic system directly affects its limit of detection. Considering moderate intensities of illumination, the photoacoustic signal correlates linearly with the intensity (see equations 1.87 and 1.40), while the noise level is hardly affected by the optical power that is used for signal generation. Thus, improving the optical performance directly yields to an enhancement of the detection limit of the system.

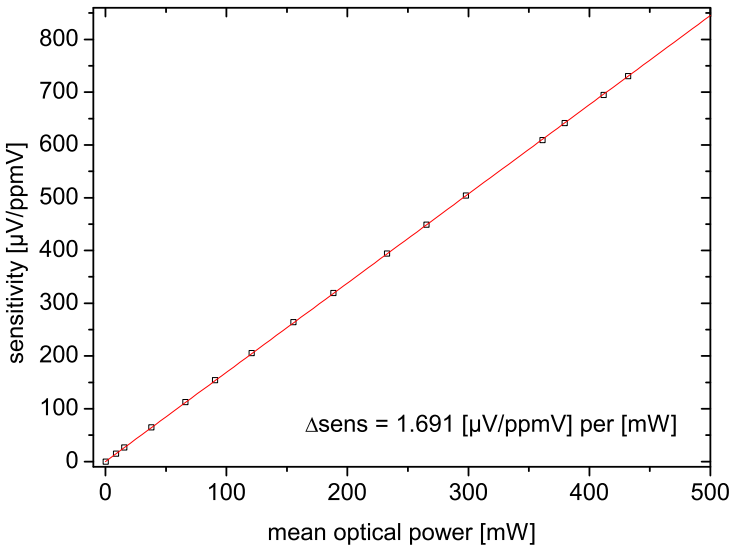

Figure 4.14: The dependency of the sensitivity on the mean power of irradiation. The measuring parameters were $\tau_{LIA} = 2$ s, $N_{NO2} = 20$ ppmV and $Q_{gas} = 250$ mL/min.

*Regarding details about the calculation refer to chapter 7 (page 257).

Figure 4.14 specifies the optical performance of irradiation improving the sensitivity of the system. The irradiation was attenuated by means of a variable ND filter. The coefficient of determination $R^2 = 0.99999$ clearly identifies a linear dependency.

4.2.5.4 Signal stability

This section aims at analyzing the stability of the photoacoustic signal. Figure 4.15 shows the typical response behavior of the photoacoustic signal with regard to changing NO_2 concentrations. The concentrations of 20 ppmV, 14 ppmV and 0 ppmV, i.e. pure nitrogen flow, were rerun in order to investigate the stability of the signal.

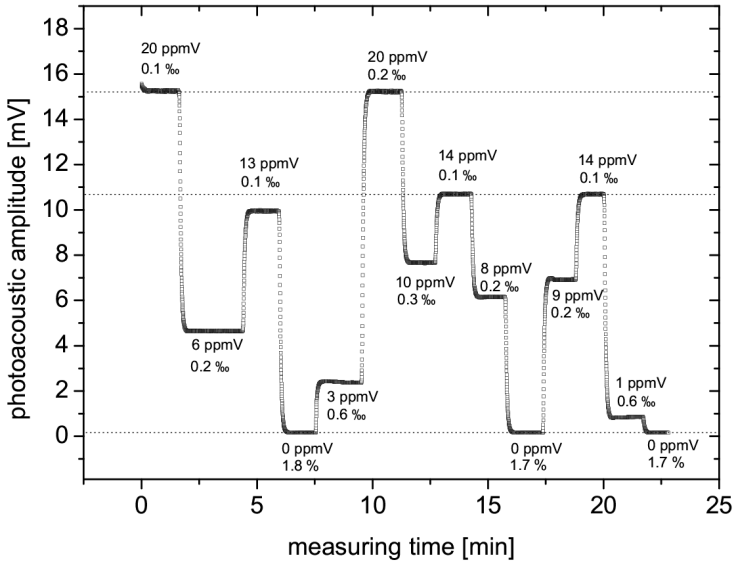

Figure 4.15: Signal stability. Photoacoustic signal at different NO_2 concentrations diluted in N_2 ranging from 0 to 20 ppmV. The precision of the system is represented by relative standard deviations.

The dotted horizontal lines in Figure 4.15 visualize this signal stability. Although, neither the PAC nor the gas flow is designed to be temperature controlled, no drifting effects are recognized, which proves the stability of the signal. Besides the respective NO_2 concentrations, the plot contains the relative standard deviations at those NO_2 concentration levels. While excluding the measurements at pure nitrogen flow, i.e. 0 ppmV, the mean relative standard deviation was calculated to 0.3 ‰, which validates the

good precision of the system. Furthermore, the photoacoustic signal at 20 ppmV NO_2 in N_2 was monitored for 35 minutes in order to investigate the long-term stability of the system. While the temperature stability of the PAC was ensured, we still observed a slightly drifting of the optical power and the humidity of the sample, respectively. After mathematically compensating those drifts, the photoacoustic signal could be considered drift-free.

4.2.6 Interference components

This section is meant to discuss the systems cross-sensitivity towards typical air components, i.e. H_2O and CO_2, respectively. The maximal H_2O concentration, a sensor system for environmental analysis has to be able to handle in our (Northern European) latitude, is approximated to 80 % relative humidity (%rh) at 30 °C. This corresponds to a mass concentration of about 24.3 g/m^3 and assuming water vapor as an ideal gas, the volume concentration is calculated to 3.2 %V. Concerning the amount of atmospheric CO_2, the Federal Ministry for Environment, Nature Conservation and Nuclear Safety of Germany stated its annual mean concentration to be 400 ppmV in 2014.

4.2.6.1 Humidity

Regarding the interference analysis of the photoacoustic system towards H_2O, a humidity generator was used. In order to avoid water condensation within the PAC due to a missing option of heating the cell, the maximal H_2O concentration was set to 25 %rh, which at the given temperature corresponds to a volume concentration of about 0.77 %V. Figure 4.16 shows the photoacoustic signal for NO_2 concentrations of 15, 30, 50 and 70 ppmV, respectively. The black squares correspond to a relative humidity of about 5 %rh and the red triangles to 25 %rh. The averaged difference in H_2O concentration was calculated to 5 669 ppmV.
The relative signal deviation due to increasing the humidity does not depend on the NO_2 concentration and it was averaged to 1.6 %. Addressing the cause of this small deviation, the shifting of the resonance frequency due to

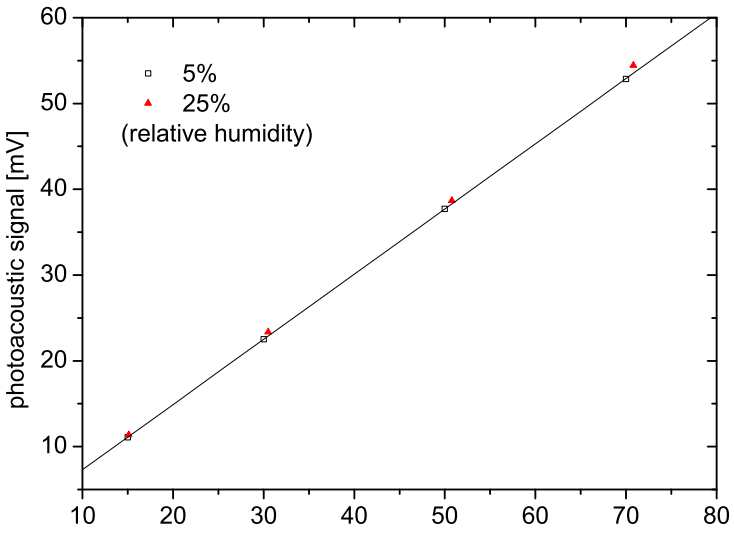

Figure 4.16: Cross-sensitivity towards H_2O. The signal dependency on the H_2O concentration was studied in a concentration range from 15 ppmV to 70 ppmV NO_2.

increased water content in the sample was investigated. In this regard, the resonance profile was recorded at 2.63 %rh and 9.04 %rh, which corresponds to H_2O volume concentrations of 800 ppmV and 2 769 ppmV, respectively. The respective theoretical resonance frequencies were calculated to 4 167 Hz and 4 170 Hz and the actual frequencies were experimentally determined to 4 169 Hz and 4 171 Hz. These theoretical and experimental data are in good accordance and the deviations are in the range of the measurement error. Since the data in figure 4.16 was recorded at a constant frequency of modulation, the 1.6 % signal deviation is assumed to partly result from a change in the speed of sound c, which subsequently causes this resonance shifting (see equation 1.61). By adding water to the gas mixture, the heat capacity ratio γ and the mean molecular mass M increases. Although both reversely affect the speed of sound, c still increases by 1 m/s. The deviations due to humidification of the sample up to 0.77 %V H_2O was identified to result from slightly detuning, which can be compensated by adjusting the modulation frequency of the laser. The fact that no further significant signal change occurred by subsequently adding H_2O to the buffer gas, hence revealed a 100 % VT relaxation efficiency of NO_2. Photoacoustic signal losses due to slow VT relaxation have been reported several times and H_2O

is well known to support the relaxation rates of various compounds [23–25]. However, in terms of NO_2 detection in pure nitrogen, a relaxation rate of 2 µs was reported [17], thus the criterion $f_{\mathrm{mod}} << 1/\tau_{\mathrm{VT}}$ is satisfied and the absorbed energy is entirely released as heat into the system. Indeed, the situation may be different considering other buffer gas compositions. Yin et al. [20] for example determined a 15 % increase in signal by adding 0.3 % of water to a mixture of 100 ppbV NO_2 diluted in synthetic air. Exceeding this amount of H_2O was presented to not further affect the PA signal. These findings can be interpreted to result from intermolecular VV energy transfer to O_2, which is known to exhibit long VT lifetimes, e.g. 1.6 ms in terms of self-quenching and 2.5 ms considering collisions with N_2 [26]. Therefore, VV energy exchange to O_2 might cause significant signal loss. The results of Yin et al. [20] are in good agreement with Kalkman and Van Kesteren [17], who studied the influence of O_2 content up to an amount of 50 %. Actually, we performed similar investigations together with a comprehensive interference analysis towards acoustical noise, which are recently submitted elsewhere.

4.2.6.2 Carbon dioxide

In order to investigate the cross-sensitivity of the photoacoustic signal towards carbon dioxide, 4 %V CO_2 were added to a binary gas mixture containing 50 ppmV NO_2 diluted in N_2. Although this CO_2 concentration corresponds to approximately 100 times the mean atmospheric CO_2 level, a higher dilution could not be achieved due to setup restrictions.
Figure 4.17 shows the amplitude (black line at the bottom) and the phase (red line at the top) of the photoacoustic signal. The initial signal at $t = 0$ results from a gas mixture of 50 ppmV NO_2 diluted in N_2. The frequency of modulation was set to 4 165 Hz. After about 1 minute, 4 %V CO_2 were added to the gas mixture, which caused an amplitude drop by 15 %. At a measuring time of 3.5 minutes, acoustic detuning due to CO_2 was compensated by adjusting the modulation frequency to 4 130 Hz. After detuning compensation the signal drop remained to 1.5 %. At $t = 5.8$ minutes the CO_2 was removed from the gas mixture, which again caused the signal amplitude to decrease due to resonance detuning. After 8 minutes of measuring time, the initial parameters were restored by re-adjusting f_{res} to

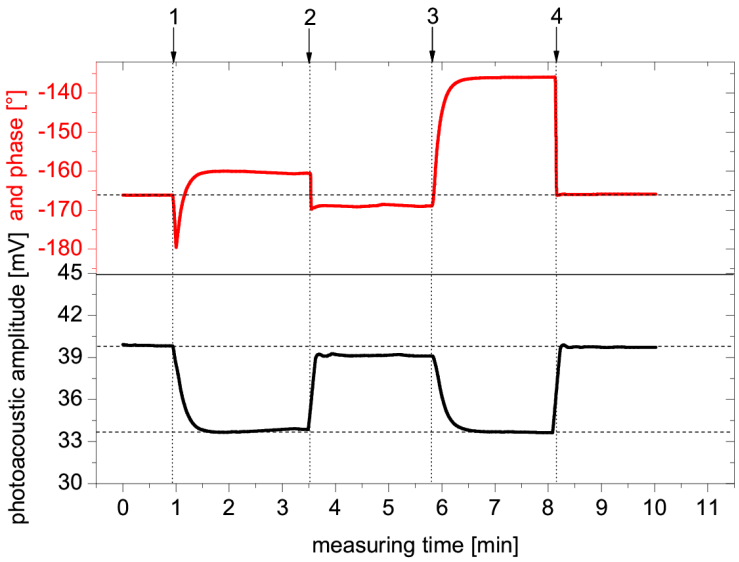

Figure 4.17: Cross-sensitivity of phase (top) and amplitude (bottom) of the PA signal towards CO_2. Initial parameters: 50 ppmV NO_2 diluted in N_2 and f_{res} = 4 165 Hz → 1: 4 %V CO_2 were added to a gas mixture → 2: Frequency detuning was compensated by adjusting f_{res} to 4 130 Hz → 3: CO_2 was removed → 4: Initial parameters were restored by re-adjusting f_{res} to 4 165 Hz.

4 165 Hz again and the photoacoustic signal was reproduced in amplitude and in phase. The signal drop which remained after detuning compensation ($3.5 < t$ [min] < 5.5) is supposed to result from acoustic attenuation. However, this attenuation is also not assumed to be solely attributed to classical acoustic attenuation effects (refer to chapter 1.4.1), since those gain influence not until frequencies above 10 or even 100 kHz [27]. Relating to additional effects contributing to the overall acoustic attenuation, Ejakov et al. [28] pointed out the attenuation due to excitation and relaxation of rotational and vibrational molecular energy levels of CO_2 at lower frequencies. Basing on their data, the overall acoustic attenuation of the gas mixture was estimated to $\alpha = 0.047$ m^{-1}. Considering this value of total attenuation, a sound signal would have to pass a distance of 32 cm to be attenuated by 1.5 %. As this calculation bases on linear sound propagation, the signal drop in figure 4.17 is assumed to result from acoustic attenuation effects, which are amplified by standing sound wave generation within the acoustic resonator. Once this calculated distance of linear sound propagation is divided by the factor of resonance amplification, the distance

remains to 1.46 cm, which is in the order of the resonator dimensions. Although the results of CO_2 interference analysis are in good accordance with empirically and theoretically obtained data relating molecular based sound attenuation effects [28], no references were found that report about acoustic attenuation whilst photoacoustic detection, resulting from CO_2. Literature search either yielded CO_2 containing gas compositions, where carbon dioxide was considered a trace gas component, i.e. the analyte that was to be quantified, or CO_2 was dosed as an additive in order to simulate ambient air conditions. No references were found, where CO_2 was added to the buffer gas to an amount that is comparable to this study.

4.2.7 Conclusion

We developed a photoacoustic system for NO_2 trace gas detection, which is mainly based on the integration of low-cost components, e.g. a mass-fabricated diode laser and a standard MEMS microphone. Furthermore, we designed a photoacoustic measuring cell (PAC) which enables Brewster window mounting. The PAC was 3D printed in order to avoid long production times and further reduce the costs of the system. In spite of keeping in view the costs, the photoacoustic system was shown to have an outstanding sensitivity. The detection limit was determined to LOD (1σ) = 33 pptV NO_2. The optimum lock-in time constant was identified to 2 s, but only in terms of small analyte concentrations less than 1 ppmV increasing τ_{LIA} to 5 s is recommended. The optimum gas flow rate was determined to Q_{gas} = 250 mL/min. Increasing this flow rate means exceeding a critical value which leads to an increase of the acoustical noise level. This critical mean velocity of the gas flow was calculated to 0.34 m/s. Basing upon these optimal operating parameters τ_{LIA} and Q_{gas}, the noise of the offset signal was determined and the response time of the system was investigated. Furthermore, the idealized response time towards a unit step function was specified to $\tau_{90,\mathrm{id}} = 3.7$ s which can be considered as a limit in view of future sensor development. The improvement of integrating Brewster windows was investigated and identified to reduce the photoacoustic offset signal by 67 %. The utilization was discussed to generally improve the dynamic range of the system which, however, is of minor effect in view

of the photoacoustic setup presented in this work. Therefore, the only real benefit of integrating Brewster windows in this context was to increase the intensity of irradiation transmitted through the PAC by 10 %. Increasing the intensity of irradiation by 1 mW was specified to cause a boost in sensitivity by 1.691 µV/ppmV. Due to the high symmetry of the PAC, its resonant profile showed no complex overlapping in frequency domain. The corrected length of the resonator tube was stated to take into account its diameter as well as the effective diameter of the hole, which was drilled into the tube for microphone coupling. Moreover, the photoacoustic signal was identified to be stable in time and its cross-sensitivity towards H_2O and CO_2 was investigated, respectively. A humidification of the test gas up to 25 %rh at a temperature of 25 °C was identified to hardly affect the photoacoustic signal. Adding H_2O was shown to only cause minor detuning, which can be compensated by adjusting the frequency of modulation. In view of developing a portable NO_2 trace gas sensing device, the integration of a low-cost sensor like the SHT25 is recommended in order to monitor temperature and water content of the gas sample. Once a detuning of the acoustic resonator is assumed, the modulation frequency of the laser can be corrected theoretically using equations 1.73 and 1.61. Besides humidification, atmospheric fluctuations of the CO_2 level were identified to hardly affect the photoacoustic signal, as well. Typical fluctuations of the atmospheric CO_2 level are stated to be in the range of 370 to 400 ppmV [29]. Even in terms of heavy street traffic monitoring, the CO_2 level is not expected to exceed 1 500 ppmV. In view of developing a portable device for outdoor air-quality NO_2 monitoring, the calibration gas is suggested to contain 500 ppmV CO_2. Based on the results discussed in chapter 4.2.6.2, the influence of an increase of the CO_2 concentration from 500 ppmV to 1 500 ppmV can be calculated to 0.8 Hz detuning and 1.5 ‰ signal drop due to acoustic attenuation. Both effects are negligible and, therefore, separate CO_2 monitoring and calibration is determined to not be crucial in terms of standard atmospheric NO_2 detection.

Table 4.2: Characterization of the photoacoustic measuring system for NO_2 detection. f_{res}: frequency of modulation, Q: quality factor of acoustic resonance, LOD: limit of detection, maximum error of calibration, signal drift, sensitivity, response time.

f_{res}	Q	LOD(1σ)	max. error[a]	signal drift[b]	sensitivity	τ_{90}
4 172 Hz	21.9	33 pptV	± 0.6 %	none	814 µV/ppmV	19 s

[a]The maximum error takes into account three times the standard deviation of 100 raw data points and three times the standard deviation of the linear regression of the calibration curve.
[b]Signal drift within a measuring period of 30 minutes.

References

[1] A. Elia, P. M. Lugarà, C. di Franco and V. Spagnolo, Photoacoustic techniques for trace gas sensing based on semiconductor laser sources, *Sensors*, 9(12):9616–9628 (2009), ISSN 14248220, doi:10.3390/s91209616.

[2] F. J. Harren, G. Cotti, J. Oomens and S. t. L. Hekkert, Photoacoustic Spectroscopy in Trace Gas Monitoring, in *Encyclopedia of Analytical Chemistry*, pages 2203–2226 (John Wiley and Sons, Ltd, Chichester, UK, 2000), ISBN 0471976709, doi:10.1002/9780470027318.a0718, URL `http://doi.wiley.com/10.1002/9780470027318.a0718`.

[3] J. Peltola, M. Vainio, T. Hieta, J. Uotila, S. Sinisalo, M. Siltanen and L. Halonen, High sensitivity trace gas detection by cantilever- enhanced photoacoustic spectroscopy using a mid-infrared continuous-wave optical parametric oscillator, *Optics Express*, 21(8):2103–2109 (2013), ISSN 1094-4087, doi:10.1364/OE.21.010240.

[4] F. Müller, A. Popp, F. Kühnemann and S. Schiller, Transportable, highly sensitive photoacoustic spectrometer based on a continuous-wave dualcavity optical parametric oscillator, *Optics express*, 11(22):2820–2825 (2003), ISSN 1094-4087, doi:10.1364/OE.11.002820.

[5] F. Müller, A. Popp, S. Schiller and F. Kühnemann, Cw-OPO based photoacoustic spectrometer for highly sensitive detection of ethane and other volatile organic compounds, *Photons Plus Ultrasound: Imaging and Sensing*, 49(0):138–144 (2004), ISSN 16057422, doi:10.1117/12.532706, URL `http://proceedings.spiedigitallibrary.org/proceeding.aspx?articleid=1321668`.

[6] M. Nägele and M. W. Sigrist, Mobile laser spectrometer with novel resonant multipass photoacoustic cell for trace-gas sensing, *Applied Physics B: Lasers and Optics*, 70:895–901 (2000), ISSN 0946-2171, doi:10.1007/PL00021151.

[7] M. B. Pushkarsky, M. E. Webber, O. Baghdassarian, L. R. Narasimhan and C. K. N. Patel, Laser-based photoacoustic ammonia sensors for industrial applications, *Applied Physics B: Lasers and Optics*, 75(2-3):391–396 (2002), ISSN 09462171, doi:10.1007/s00340-002-0967-8.

[8] S. Bernegger and M. Sigrist, *CO-laser photoacoustic spectrocopy of gases and vapors for trace gas analysis*, Phd thesis, ETH Zürich (1988).

[9] M. Pushkarsky, A. Tsekoun, I. G. Dunayevskiy, R. Go and C. K. N. Patel, Sub-parts-per-billion level detection of NO2 using room-temperature quantum cascade lasers., *Proceedings of the National Academy of Sciences of the United States of America*, 103(29):10846–9 (2006), ISSN 0027-8424, doi:10.1073/pnas.0604238103, URL `http://www.pnas.org/content/103/29/10846.full`.

[10] K. Bogumil, J. Orphal, T. Homann, S. Voigt, P. Spietz, O. Fleischmann, A. Vogel, M. Hartmann, H. Kromminga, H. Bovensmann, J. Frerick and J. Burrows, Measurements of molecular absorption spectra with the SCIAMACHY pre-flight model: instrument characterization and reference data for atmospheric remote-sensing in the 230-2380 nm region, *Journal of Photochemistry and Photobiology A: Chemistry*, 157(2-3):167–184 (2003), ISSN 10106030, doi:10.1016/S1010-6030(03)00062-5, URL `http://linkinghub.elsevier.com/retrieve/pii/S1010603003000625`.

[11] A. Vandaele, C. Hermans, P. Simon, M. Carleer, R. Colin, S. Fally, M. Mérienne, A. Jenouvrier and B. Coquart, Measurements of the NO2 absorption cross-section from 42 000 cm-1 to 10 000 cm-1 (238-1000 nm) at 220 K and 294 K, *Journal of Quantitative Spectroscopy and Radiative Transfer*, 59(3-5):171–184 (1998), ISSN 00224073, doi:10.1016/S0022-4073(97)00168-4, URL `http://www.sciencedirect.com/science/article/pii/S0022407397001684`.

[12] V. Slezak, High-precision pulsed photoacoustic spectroscopy in NO2 - N2, *Applied Physics B: Lasers and Optics*, 73(7):751–755 (2001), ISSN 0946-2171, doi:10.1007/s003400100686, URL `http://www.springerlink.com/openurl.asp?genre=article&id=doi:10.1007/s003400100686`.

[13] A. M. Angus, E. E. Marinero and M. J. Colles, Opto-acoustic spectroscopy with a visible CW dye laser, *Optics Communications*, 14(2):223–225 (1975), ISSN 00304018, doi:10.1016/0030-4018(75)90218-7.

[14] G. Santiago, V. Slezak and A. L. Peuriot, Resonant photoacoustic gas sensing by PC-based audio detection, *Applied Physics B: Lasers and Optics*, 77(4):463–465 (2003), ISSN 09462171, doi:10.1007/s00340-003-1263-y.

[15] G. D. Santiago, M. G. González, A. L. Peuriot, F. González and V. B. Slezak, Blue light-emitting diode-based, enhanced resonant excitation of longitudinal acoustic modes in a closed pipe with application to NO2, *Review of Scientific Instruments*, 77(2):2004–2007 (2006), ISSN 00346748, doi:10.1063/1.2173031.

[16] J. Saarela, T. Sorvajärvi, T. Laurila and J. Toivonen, Phase-sensitive method for background-compensated photoacoustic detection of NO2 using high-power LEDs, *Optics express*, 19 Suppl 4(2):A725–A732 (2011), ISSN 1094-4087, doi:10.1364/OE.19.00A725.

[17] J. Kalkman and H. W. Van Kesteren, Relaxation effects and high sensitivity photoacoustic detection of NO2 with a blue laser diode, *Applied Physics B: Lasers and Optics*, 90(2):197–200 (2008), ISSN 09462171, doi:10.1007/s00340-007-2895-0.

[18] H. Yi, K. Liu, W. Chen, T. Tan, L. Wang and X. Gao, Application of a broadband blue laser diode to trace NO2 detection using off-beam quartz-enhanced photoacoustic spectroscopy., *Optics letters*, 36(4):481–483 (2011), ISSN 0146-9592, doi:10.1364/OL.36.000481.

[19] J. Peltola, T. Hieta and M. Vainio, Parts-per-trillion-level detection of nitrogen dioxide by cantilever-enhanced photo-acoustic spectroscopy, *Opt Lett*, 40(13):2933–2936 (2015), ISSN 0146-9592, doi:10.1364/OL.40.002933, URL `http://www.ncbi.nlm.nih.gov/pubmed/26125335`.

[20] X. Yin, L. Dong, H. Wu, H. Zheng, W. Ma, L. Zhang, W. Yin, S. Jia and F. K. Tittel, Sub-ppb nitrogen dioxide detection with a large linear dynamic range by use of a differential photoacoustic cell and a 3.5 W blue multimode diode laser, *Sensors and Actuators B: Chemical*, 247:329–335 (2017), ISSN 09254005, doi:10.1016/j.snb.2017.03.058, URL `http://linkinghub.elsevier.com/retrieve/pii/S0925400517304756`.

[21] T. Rück, R. Bierl and F.-M. Matysik, Development and characterization of a laboratory setup for photoacoustic NO2 determination based on the excitation of electronic 2B2 and 2B1 states using a low-cost semiconductor laser, *Sensors and Actuators A: Physical*, 258:193–200 (2017), ISSN 09244247, doi:10.1016/j.sna.2017.03.024, URL `http://linkinghub.elsevier.com/retrieve/pii/S0924424716310433`.

[22] G. K. Batchelor, *An Introduction to Fluid Dynamics* (1967), ISBN 0521663962, doi:10.1063/1.3060769.

[23] A. A. Kosterev, Y. A. Bakhirkin and F. K. Tittel, Ultrasensitive gas detection by quartz-enhanced photoacoustic spectroscopy in the fundamental molecular absorption bands region, *Applied Physics B*, 80(1):133–138 (2005), ISSN 0946-2171, doi:10.1007/s00340-004-1619-y.

[24] L. Dong, R. Lewicki, K. Liu, P. R. Buerki, M. J. Weida and F. K. Tittel, Ultra-sensitive carbon monoxide detection by using EC-QCL based quartz-enhanced photoacoustic spectroscopy, *Applied Physics B: Lasers and Optics*, 107(2):275–283 (2012), ISSN 09462171, doi:10.1007/s00340-012-4949-1.

[25] L. Dong, A. A. Kosterev, D. Thomazy and F. K. Tittel, Compact portable QEPAS multi-gas sensor, in M. Razeghi, R. Sudharsanan and G. J. Brown (editors), *Proc. SPIE 2011*, volume 7945, page 79450R (2011), ISBN 9780819484826, ISSN 0277786X, doi:10.1117/12.875108, URL `http://proceedings.spiedigitallibrary.org/proceeding.aspx?articleid=722094`.

[26] P. L. Meyer and M. W. Sigrist, Atmospheric pollution monitoring using CO2-laser photoacoustic spectroscopy and other techniques, *Review of Scientific Instruments*, 61(7):1779–1807 (1990), ISSN 00346748, doi:10.1063/1.1141097.

[27] Y. Dain and R. M. Lueptow, Acoustic attenuation in three-component gas mixtures–theory., *The Journal of the Acoustical Society of America*, 109(5 Pt 1):1955–1964 (2001), ISSN 00014966, doi:10.1121/1.1352087.

[28] S. G. Ejakov, S. Phillips, Y. Dain, R. M. Lueptow and J. H. Visser, Acoustic attenuation in gas mixtures with nitrogen: experimental data and calculations, *J Acoust Soc Am*, 113(4 Pt 1):1871–1879 (2003), ISSN 00014966, doi:10.1121/1.1559177, URL `http://www.ncbi.nlm.nih.gov/pubmed/12703699`.

[29] M. Forkel, N. Carvalhais, C. Rödenbeck, R. Keeling, M. Heimann, K. Thonicke, S. Zaehle and M. Reichstein, Enhanced seasonal CO2 exchange caused by amplified plant productivity in northern ecosystems, *Science*, 351(6274):696–699 (2016), doi:10.1126/science.aac4971.

4.3 NO_2 trace gas monitoring in air using off-beam quartz enhanced photoacoustic spectroscopy (QEPAS) and interference studies towards CO_2, H_2O and acoustic noise

4.3.1 Introduction

The concept of photoacoustic (PA) spectroscopy gained more and more attention of the scientific community in the last decades. This growing interest in investigating the photoacoustic technique was mainly due to the constantly growing availability of short-, mid- and long-wavelength infrared emitters. Previous investigations yielded several publications which identified PA spectroscopy to be a promising technique in terms of highly accurate trace gas monitoring down to the pptV-level [1]. In synergy with the growing availability of a variety of small-sized semiconductor lasers [2], these results in turn aroused great interest of industry. However, in view of commercializing the technique, there are two main drawbacks of standard PA setups combining acoustic resonator tubes and microphones. They are restricted in terms of downscaling and susceptible to ambient noise. Both disadvantages ceased, when Kosterev et al. [3] used quartz tuning forks (QTF) for PA signal detection for the first time in 2002. QTFs are clock generators featuring high resonance quality factors, i.e. $Q \approx 100\,000$ in vacuum and 10 000 under standard conditions, respectively. The measuring scheme utilizing QTFs in photoacoustic applications is abbreviated as QEPAS (quartz enhanced photoacoustic spectroscopy). In terms of the QEPAS technique, the irradiation used for photoacoustic signal generation is focused between the tines of the tuning fork. Using this scheme, Kosterev and Tittel [4] specified the detection limit of NH_3 to LOD (1σ) = 650 ppbV. Horstjann et al. [5] applied the QEPAS technique to formaldehyde monitoring and published a detection limit (1σ) of 600 ppbV for H_2CO and Wysocki et al. [6] determined the detection limit (1σ) of CO_2 to 110 ppmV.
In 2005, Kosterev et al. [7] were able to further enhance the sensitivity of the QEPAS technique by combining QTFs with acoustic resonator tubes. Ar-

Section 4.3 is adapted from [P3] (refer to page xv).

ranging the tubes in front and behind the QTF causes double-resonant amplification [8]. This measuring scheme is abbreviated as on-beam QEPAS, which is the most commonly used QEPAS scheme to date. By applying the on-beam QEPAS arrangement, Kosterev et al. [9] determined detection limits (1σ) of 4 ppbV for N_2O and 80 ppbV for CO, 155 ppbV for HCN [10], 100 ppbV for NH_3, 125 ppbV for HCN and 30 ppbV for C_2H_2 [11] and 10 ppmV for H_2S, 270 ppmV for CO_2 and 1.5 ppmV for CH_4, respectively [12]. To mention only further LODs at sub-ppmV level, other references reported detection limits of 300 ppbV (3σ) for C_2H_4 [13], 15 ppbV (1σ) for NO [14], 4.9 ppbV for NO [15], 2 ppbV (1σ) for CO [16], 100 ppbV (1σ) for SO_2 [17], 100 ppbV (1σ) for CH_4 [18] and 240 pptV (1σ) for CO and 4 ppbV (1σ) for N_2O, respectively [19]. It has to be noted that the above authors use different criterion for determination of the detection limit. Therefore, the noise amplitude, which was used for LOD calculation, was indicated in brackets.

However, this work is based on the so-called off-beam QEPAS scheme, which for the first time was reported by Liu et al. [20] in 2009. The off-beam QEPAS arrangement resembles PA standard setups, as the QTF is mounted outside an acoustic resonator, but still gains double-resonant amplification. This spatial separation of resonator and QTF facilitates optical alignment, as the laser beam does not have to be focused between the tines of the tuning fork. As a drawback compared to on-beam QEPAS, the coupling of acoustic energy from resonator to QTF is weaker in terms of the off-beam arrangement. Nevertheless, Liu et al. [21] identified these coupling losses to be mainly compensated by higher quality resonance amplification and determined a detection limit (1σ) of 260 ppbV for H_2O. Besides easier optical alignment, this setup also lowers the demands on the beam quality. Consequently, Böttger et al. [22] used light emitting diodes (LEDs) for illumination and achieved a minimum detectable O_3 concentration of 1.27 ppmV (1σ). Apart from this LED off-beam QEPAS arrangement, all of the above references are based upon wavelength modulation (WM) in combination with $2f$-signal-demodulation. The WM technique is performed by modulating a sine wave on the DC working current of a laser diode and thus periodically scanning the absorption peak of the analyte (refer to chapter

1.1.4). In comparison, amplitude modulation (AM) is achieved using modulation depths from threshold to working current and thus turning on and off radiation. Although the photoacoustic amplitudes generated by WM are smaller than in terms of AM, WM offers upper immunity towards changing absorption background, e.g. caused by varying composition of the sample. However, WM cannot be applied in order to spectroscopically monitor NO_2 at 450 nm, as this absorption peak ranges from 250 to 650 nm [23, 24], which exceeds feasible modulation depths of common laser sources. Therefore, this work is based on the common principle of amplitude modulation. Literature provides two references presenting photoacoustic NO_2 detection using QEPAS techniques. Zheng et al. [25] applied AM on-beam QEPAS and specified a detection limit (1σ) of 1.3 ppbV for NO_2. Although they repetitively mention the utilization of LEDs, due to matching part number (OSRAM opto-semiconductor PLTB 450), optical power, beam profile and beam divergence angles, we assume they applied the same laser source that we are using. However, they additionally had to utilize the E-MOCAM (electrical modulation cancellation) technique in order to suppress background noise resulting from direct illumination of the QTF. In order to avoid direct illumination, Yi et al. [26] used the AM off-beam QEPAS scheme and reported a detection limit of LOD (1σ) = 4.4 ppbV for NO_2 without active modulation cancellation.
All measurements presented within this work base upon AM off-beam QEPAS as well. As with [26], due to off-beam arrangement no modulation cancellation had to be utilized. Despite of diluting the NO_2 samples with synthetic air instead of N_2, which causes a 15 % signal decrease, we specified the LOD to be $\sim$ 7 times lower than in [26], although using the same averaging time of 20 s. The improvement might be primarily due to higher optical power and increased lock-in time constant of 10 s, which, however, does not slow down the response time of the system using an averaging time of 20 s. Concerning details of the variety of QEPAS schemes, Patmisco et al. [27] provided a comprehensive comparison pointing out the advantages and disadvantages of different QEPAS arrangements.

4.3.2 Experimental

Figure 4.18 shows a schematic drawing of the experimental setup. The gas-mixing unit consists of 100 ppmV and 5 ppmV NO_2 test gases in nitrogen (6.0) and in synthetic air, respectively. Synthetic air is composed of 79 %V N_2 and 21 %V O_2. For cross-sensitivity investigations, another test gas containing 1 %V CO_2 in synthetic air as well as an aGEPRO-V4 humidity generator (ADROP Feuchtemeßtechnik GmbH, Fürth, Germany) were installed in order to simulate real ambient air conditions. All test gases were supplied by Westfalen AG, Germany. The gases can be further diluted with pure nitrogen (6.0) or synthetic air using F-201CV-500-RBD-11-V mass flow controllers (Bronkhorst, Karmen, Germany). After passing the photoacoustic cell (PAC) the gas mixture can be analyzed with regard to temperature, pressure and humidity by means of a MPL3115A2 (Adafruit Industries, New York, US) and a SHT25 (Sensirion AG, Staefa, Switzerland) sensor, respectively.
In terms of photoacoustic signal generation a PL TB450B semiconductor laser (OSRAM Opto Semiconductors, Regensburg, Germany), which emits at 450 nm with a maximum optical output power of 1.6 W, was amplitude modulated (AM) with a duty cycle of 50 %. The laser diode is controlled by a LDC-3744C laser diode controller (ILX Lightwave, Montana, US) and a 33500B function generator (Keysight Technologies, California, US). The laser beam is shaped and aligned by means of a collimator and an iris diaphragm. The power of incident light used for photoacoustic signal generation is monitored by a PM100D power meter equipped with a thermal S302C head (Thorlabs GmbH, München, Germany). The data acquisition and signal processing is managed by means of a measuring software tool developed in LabVIEW.
The middle part of the drawing shows the photoacoustic cell in off-beam QEPAS arrangement. The acoustic resonator (mR) was cut from a hypodermic needle and an opening slit was wire-cut in order to couple acoustic energy to the sensor element. The resonator is 4.66 mm in length, its inner diameter is 1.6 mm and the wall thickness is 0.2 mm. The opening slit is 890 µm in height and 134 µm in width. The sensor element is a quartz clock generator, which is shaped like a tuning fork (FOXElectronics,

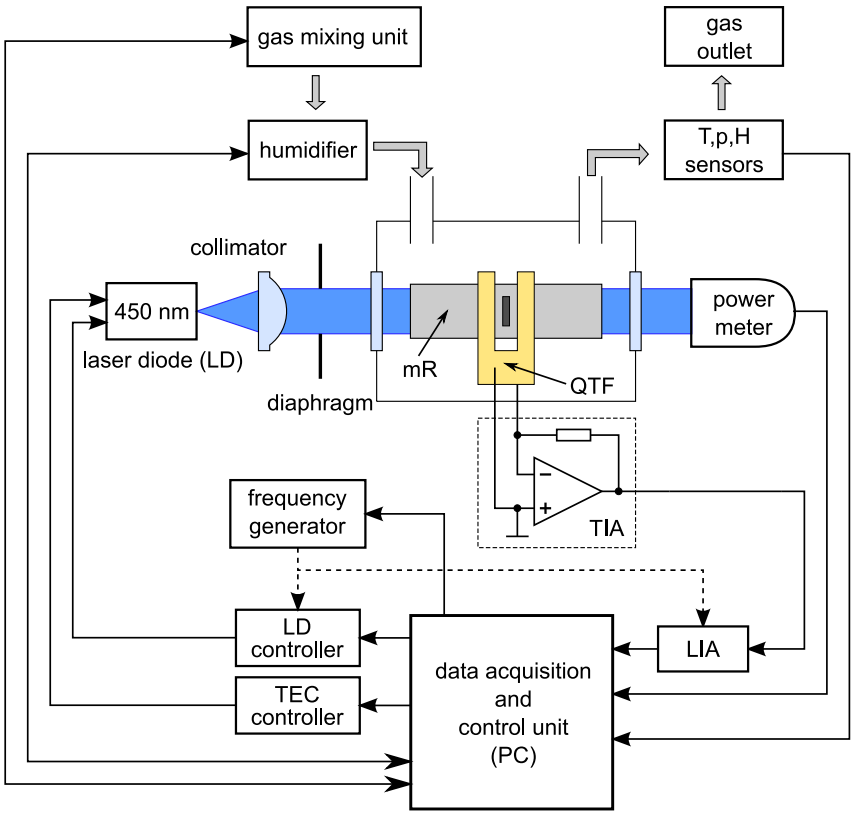

Figure 4.18: Schematic drawing of the experimental setup. The photoacoustic cell (PAC) consists of an acoustic resonator (mR) and a quartz tuning fork (QTF). T,p,H: temperature, pressure, humidity, TIA: transimpedance amplifier, LIA: lock-in amplifier.

Florida, US). By disregarding its footing, the tines of the quartz tuning fork (QTF) are 3.7 mm in length, 600 µm in width and 270 µm thick. The spacing between the tines is 300 µm. In terms of optimal aligning QTF and mR [3, 20, 21, 27], the QTF spacing was horizontally centered on the opening slit of the resonator. In view of vertical alignment, the distance between the QTF opening (top site of the QTF) and the center of mR opening was adjusted to approximately 1 mm. The distance between the tines and the resonator was adjusted to 125 µm. The piezoelectric current resulting from QTF oscillation was converted and amplified using a transimpedance amplifier with a 1 MΩ feedback resistor and further processed using a 7225 DSP lock-in amplifier (Signal Recovery, Tennessee, US).
In order to investigate the system with respect to ambient noise (refer to chapter 4.3.5.3), we installed a test setup for acoustic noise simulation. The

setup included a bunch of keys that were set into motion by means of a V201 permanent magnetic shaker and a type 4138 pressure-field reference microphone, which was used for acoustic noise monitoring (Brüel and Kjaer, Denmark). This configuration allowed us to simulate similar noise levels at 4 kHz and 32 kHz in order to be able to compare the noise susceptibility of the QEPAS scheme with the standard microphone-based PAC presented in [28]. The reference microphone is specified to have a linear frequency response between 3 and 33 kHz.

4.3.3 Resonance analysis

The off-beam QEPAS scheme is a feedback-free double-resonant system. The acoustic pressure of the photoacoustic signal, which is generated within the mR tube, is amplified by standing acoustic wave interference. In ideal case, the nodes of acoustic pressure form at the resonator openings, thus the length of the standing acoustic wave is twice the length of the mR. However, tubes with finite diameter are known to cause the acoustic pressure nodes to red-shift off the mR openings [29]. Therefore, the actual length L_{res} of the mR has to be smaller than the ideally calculated one $L_{\mathrm{res,id}}$. Literature provides different approaches in order to quantify this length correction depending on the mR diameter $2r_{\mathrm{res}}$ and the opening for QTF coupling r_{slit}, respectively [29, 30]. However, none of these approaches was capable of mathematically quantifying previous results concerning the frequency analysis of a variety of acoustic resonators. Therefore, we define an empiric, tube specific excess factor s_{tube} in order to relate to this node-shifting phenomenon.

$$L_{\mathrm{res,id}} = L_{\mathrm{res}} + 2s_{\mathrm{tube}}r_{\mathrm{res}} - s_{\mathrm{tube}}r_{\mathrm{slit}} \tag{4.4}$$

After acoustic amplification, the sound signal couples to the QTF through an opening slit centered at the mR tubes length. Proper alignment of the QTF forces the tines of the fork to oscillate in opposite directions. The tines can be interpreted as two clamped cantilevers. Neglecting damping effects, the eigenfrequency of the first flexural mode of cantilever oscillation, i.e.

the first in-plane vibration, can be deviated from theory of driven harmonic oscillators considering a surface load forcing oscillation (refer to chapter 1.3.2). Since mR and QTF constitute a feedback-free double-resonant system, i.e. no feedback from QTF oscillation to standing wave generation within the mR, the resonance frequency f_{off} of the off-beam QEPAS scheme fairly matches f_{QTF}.

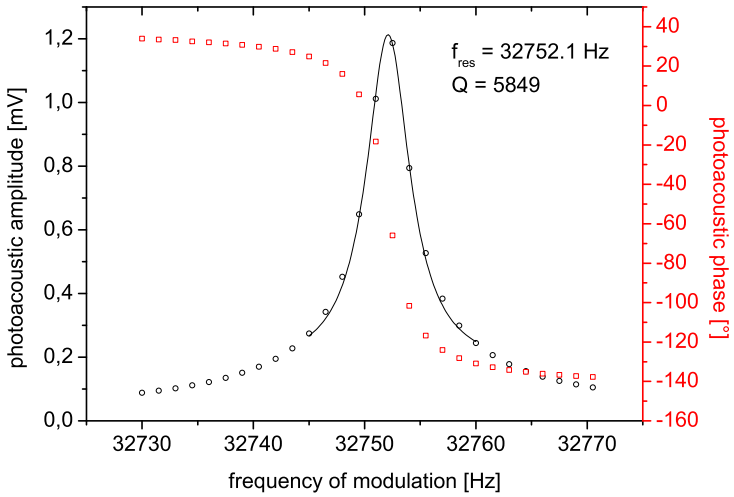

Figure 4.19: Resonance profile of the off-beam QEPAS scheme. Photoacoustic amplitude (black circles) and phase (red squares) in a frequency range from 32 730 to 32 770 Hz; increment 1.5 Hz.

Figure 4.19 shows the resonance profile of the off-beam QEPAS scheme. The profile was recorded at a constant flow of 10 ppmV NO_2. Unless otherwise specified, the analyte was diluted with synthetic air in terms of all measurements presented in this work. The photoacoustic amplitude (black circles) and phase (red squares) were recorded in a frequency range from 32 730 Hz to 32 770 Hz. The resonance frequency was specified to 32 752.1 Hz. The quality factor, which is determined by f_{off} divided by FWHM (full width half maximum), was calculated to $Q_{\text{off}} = 5\,849$.
Figure 4.20 illustrates the combination of the individual mR and QTF spectra. In order to determine the QTF profile (red dashed line), an AC voltage was applied to one of the electrodes and a frequency sweep was performed. The thus induced piezoelectric current was accessed from the counter electrode and processed by means of a transimpedance and a lock-in amplifier, respectively. The combined off-beam QEPAS spectrum (blue dots) cor-

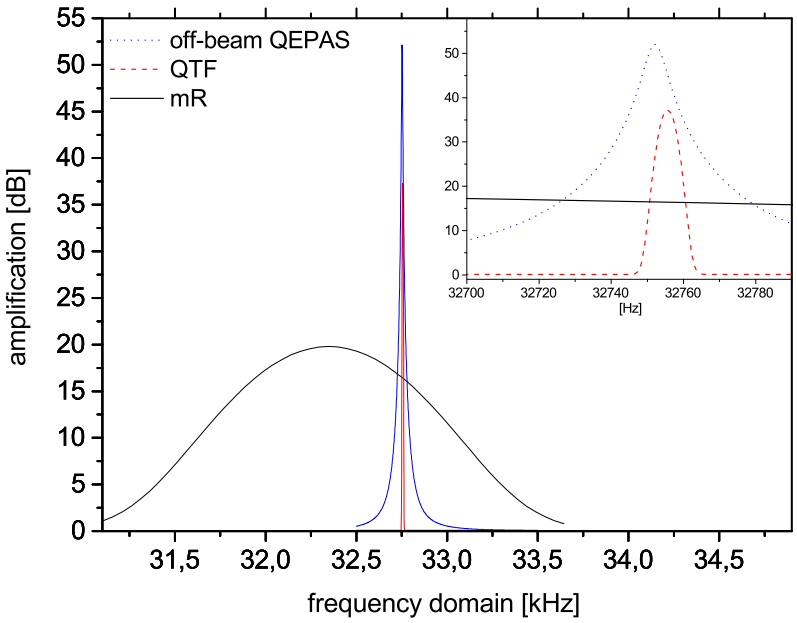

Figure 4.20: Combination of the individual acoustic resonator (mR) and quartz tuning fork (QTF) spectra. Resonance amplification of mR (black line), QTF (red dashed line) and off-beam QEPAS arrangement (blue dots) in a frequency range from 31 to 35 kHz; detailed view from 32 700 to 32 790 Hz.

responds to figure 4.19. Due to assembly restrictions, the mR spectrum (black line) cannot be accessed separately. Therefore, it was reproduced by varying the speed of sound while monitoring the amplitude of the double-resonant system. Considering equation 1.73, increasing the speed of sound causes the mR spectrum in figure 4.20 to shift to the right, i.e. towards higher frequencies, whereas the frequency of the QTF resonance does not get affected, (refer to equation 1.94). This leads to an increase in off-beam QEPAS amplitude. The amplitude culminates once the mR peak maximum correlates with the QTF peak maximum. Further increasing the speed of sound causes the off-beam QEPAS signal to decrease again. Since the PAC is not designed to be temperature controlled, changing the speed of sound was realized by changing the composition of the sample (for details refer to chapter 4.3.5.2). Figure 4.20 indicates the mR and QTF profiles to not perfectly match up at the given conditions, i.e. temperature, pressure and composition of the sample. This mismatch of about 470 Hz is because the PAC was designed for dilution with N_2 instead of synthetic air. The dis-

crepancy causes a decrease in signal of about 30 %. In order to optimize amplification, the PAC needs to be either temperature controlled (which cannot be realized using this PAC due to setup limitations) or the geometry of the resonator tube has to be adapted. However, reproducing the mR spectrum allowed us to calculate the empirical and PAC-specific node-shifting excess factor to $s_{\text{tube}} = 0.49$ (for details refer to chapter 4.3.5.2). The overall amplification of the system was specified to 52 dB, i.e. 15 dB mR amplification plus 37 dB QTF amplification.

4.3.4 Performance Characteristics

4.3.4.1 NO_2 calibration characteristics in synthetic air

The calibration characteristics of the off-beam QEPAS setup in the concentration range from 200 ppbV to 100 ppmV NO_2 in synthetic air is displayed in figure 4.21. For visualization purposes, the measuring points regarding concentrations below 2 ppmV NO_2 are plotted separately (picture-in-picture). The error bars mark $\pm$ 3 times the standard deviation σ of 100 raw data points. The sample rate of raw data was set to 5 Hz in terms of all measurements presented in this work. The linear dependency of the photoacoustic amplitude on the analyte concentration is determined to $R^2 = 0.9996$. The sensitivity of the system was specified to 127 μV per ppmV NO_2, which implies an improvement by 15 % compared to the microphone-based PAC reported in [28].
The measurement was carried out at a constant flow of 300 mL/min through the PAC and the mean optical power was measured to 672.5 mW. The background signal was monitored in the absence of NO_2. In order to calculate the detection limit of the system, we took into account three times the standard deviation of the background signal, i.e. LOD (3σ). In terms of background signal determination, the time constant and the roll-off of the lock-in amplifier was set to $\tau_{\text{LIA}} = 10$ s and $\Delta L = 6$ dB/octave, respectively, and the averaging time was $\tau_{\text{av}} = 20$ s (100 raw data points with a data acquisition rate of 5 Hz). Using these parameters, the detection limit of NO_2 was specified to LOD (3σ) = 1.8 ppbV, which is about the same range as the microphone-based PA setup presented in [28]. These 1.8 ppbV

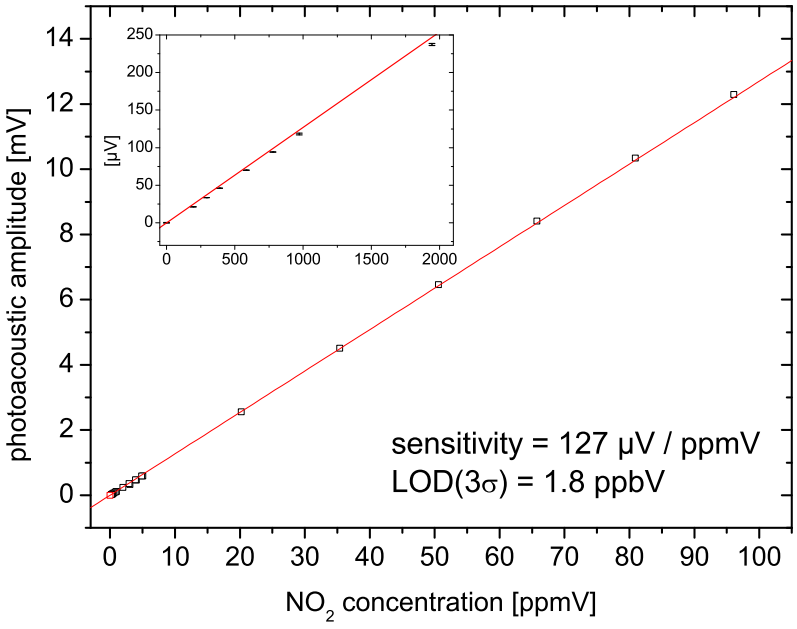

Figure 4.21: Calibration characteristics of the system ranging from 200 ppbV to 100 ppmV NO_2 in synthetic air.

correspond to a detection limit of LOD (1σ) = 600 pptV. To the best of the authors knowledge, this is the lowest detection limit for NO_2 that was specified by means of a QEPAS technique so far [25, 26].

4.3.4.2 Signal stability

Subject of the following chapter are stability studies of the off-beam QEPAS signal. The typical response behavior of the signal with regard to changing NO_2 concentrations is displayed in figure 4.22. By reproducing the concentrations of 60 ppmV, 42 ppmV and 0 ppmV, i.e. pure synthetic air, the stability of the signal was verified.

The dotted horizontal lines in figure 4.22 visualize this signal stability in 5-minute range. The stability of the signal is proved, as nearly no drifting effects were identified within this measuring period, even though neither the PAC nor the gas flow is designed to be temperature controlled. Aside from the corresponding NO_2 concentrations, Figure 4.22 further contains the relative standard deviations of 100 raw data points. Closing out the measurements at 0 ppmV NO_2, the mean relative standard deviation was

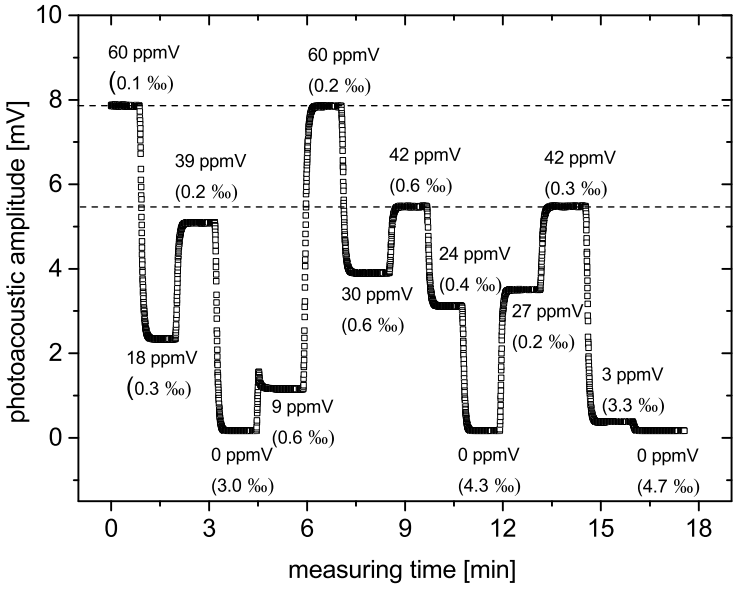

Figure 4.22: Signal stability and precision. Photoacoustic signal at different NO_2 concentrations ranging from 0 to 60 ppmV nitrogen dioxide in synthetic air. The precision of the system is represented by relative standard deviations.

0.6 ‰, which validates the good precision of the system. For analyzing the long-term stability of the system the off-beam QEPAS signal at 90 ppmV NO_2 in synthetic air was observed for 40 minutes. After optical power compensation, we identified the signal to slightly drift by 1.4 ‰ within this period, which was traced back to a continuous increase in PAC temperature.

4.3.4.3 Response time vs. detection limit

In general, the photoacoustic technique is well suitable for trace gas analysis. However, depending on the demands of the specific measuring situation, the measuring parameters have to be adjusted in order to achieve optimum results. Besides the fundamental choice of the most suitable PAS scheme, photoacoustic techniques are always a trade-off between precision and response time. The most critical parameters affecting this trade-off are the lock-in time constant τ_{LIA}, the signal averaging time τ_{av} and the flow rate Q. However, unlike some conventional microphone-based measuring schemes [31], the precision of the presented off-beam QEPAS arrangement was identified to virtually not depend on the flow rate up to 500 mL/min.

Nevertheless, we took the loss of slower response times and retained the flow to 300 mL/min concerning the following measurements in order to facilitate comparison with previous investigations.

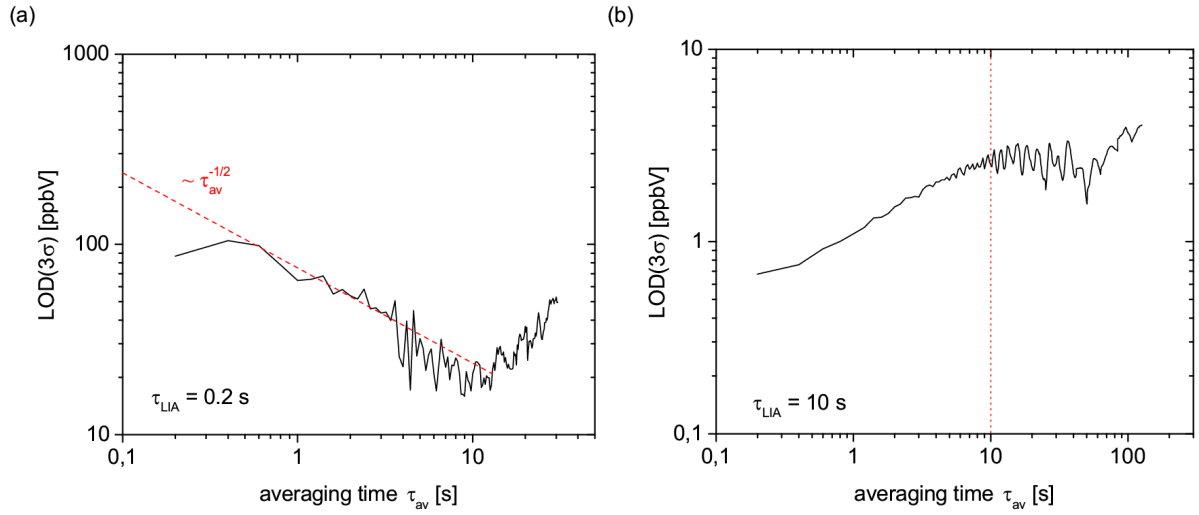

Figure 4.23: LOD dependency on the averaging time τ_{av} derived from Allan deviation analysis. a) $\tau_{\mathrm{LIA}} = 200$ ms; b) $\tau_{\mathrm{LIA}} = 10$ s.

In order to examine the critical parameters τ_{LIA} and τ_{av}, figure 4.23 shows the LOD dependency on the averaging time with regard to different lock-in time constants, i.e. $\tau_{\mathrm{LIA}} = 200$ ms (a) and $\tau_{\mathrm{LIA}} = 10$ s (b), respectively. The data is based on Allan deviation (σ_{AD}) analysis at pure synthetic air flow [32]. As for short averaging times, figure 4.23 (a) shows $\sim \tau_{\mathrm{av}}^{-0.5}$ decay characteristic, which typifies QEPAS schemes due to Johnson noise domination [7, 11, 12, 19, 26, 27, 33]. However, after an averaging period of 10 s, the noise already starts to increase. This poor noise-reduction-by-averaging performance is attributed to drifting effects for lack of temperature controlling the PAC. Figure 4.23 (b) again shows an Allan deviation analysis, but with a lock-in time constant of 10 s and a period of data acquisition of about 100 s. It is obvious that longer lock-in integration generally improves the precision of the system. Moreover, the extended lock-in time constant increases the inertia of the system why it cannot follow the fast random walk noise up to 10 s. Between 10 and 50 s the plot indicates minor noise improvement due to averaging before the noise again starts to increase due to drifting effects. According to results shown in figure 4.23, setting τ_{LIA}

to 10 s is recommended in view of trace gas detection by means of this off-beam QEPAS scheme, but exceeding an averaging time of 20 s is not appropriate, as minor noise improvement does not justify increasing response times. Concluding this chapter, figure 4.24 shows the response time τ_{90} (black circles) and the detection limit LOD (3σ) (red dots) for three different lock-in time constants, namely 200 ms, 2 s and 10 s. In terms of these measurements, the flow through the PAC was set to 300 mL/min and the signals were averaged over 20 s.

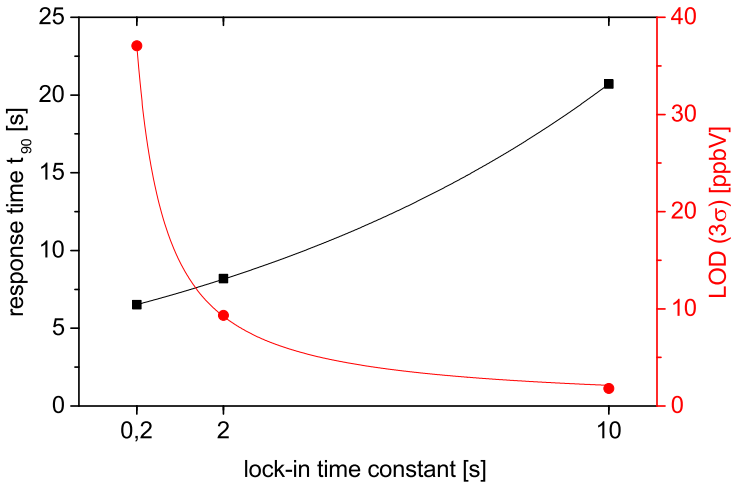

Figure 4.24: Response time (black squares) vs. detection limit (red dots). Response time τ_{90} and LOD (3σ) for $\tau_{\mathrm{LIA}} = 0.2$, 2 and 10 s, respectively. $Q = 300$ mL/min, $\tau_{\mathrm{av}} = 20$ s.

In terms of trace gas detection, i.e. analyte concentrations less than 500 ppbV, setting τ_{LIA} to 10 s results in a response time $\tau_{90} = 21$ s and a detection limit of 1.8 ppbV NO_2, respectively. However, at higher analyte concentrations adjusting τ_{LIA} to 2 s is suggested to satisfy the demands of the measuring situation. This decrease of τ_{LIA} from 10 s to 2 s results in increasing the LOD to 9 ppbV, but fastens the response time to 8 s.

4.3.5 Interference studies

4.3.5.1 Cross-sensitivities towards O_2 and CO_2

This section is meant to discuss the cross-sensitivity of the system towards typical air components, i.e. O_2 and CO_2. In order to determine the interference towards oxygen, we carried out several measurements where NO_2 was

firstly diluted with pure N_2 and repeated them with dilution in synthetic air. As a result, we observed a signal decrease in air of about 31 % regardless of the NO_2 concentration. About half of this decrease was attributed to detuning of the photoacoustic resonator (refer to chapter 4.3.3). The remaining 15 % were assumed to be attributed to vibrational-vibrational relaxation of NO_2 to O_2. Kalkman and van Kesteren [34] already observed this energy loss due to VV relaxation during photoacoustic NO_2 measurements. They provide a model coinciding with their empirical data, which quantifies this energy transfer depending on the O_2 concentration. Our findings are in good agreement with this model as well.
Moreover, we carried out an interference studies towards CO_2, which contributes approximately 400 ppmV to lower atmosphere composition. Therefore, we investigated several mixtures containing varying amounts of NO_2, i.e. 0.5, 1.5, 2.5, 3.5 and 4.5 ppmV, diluted with synthetic air and repeated the measurement after adding 400 ppmV CO_2. Regardless of the NO_2 concentration, the PA signal was identified to slightly decrease by 1 % once CO_2 was added. This signal drop is assumed to depend on acoustic attenuation effects rather than resonance detuning, as 400 ppmV CO_2 only cause minor shifting of the mR spectrum by -2.3 Hz. Relating to Ejakov et al. [35], CO_2 shows molecular relaxation at lower frequencies with its maximum approximately matching the modulation frequency used for QEPAS measurements. Exciting these vibrational and rotational energy levels is supposed to cause acoustic attenuation which increases by resonant amplification and accounts for the 1 % signal drop.
However, neither interferences towards O_2 nor CO_2 were identified to bar the way to utilizing the off-beam QEPAS scheme for air monitoring applications. As these air components are not subject to major fluctuations, calibration is suggested to satisfy the demands on a trace-gas air-quality monitoring application. A separate detection of O_2 and CO_2 combined with active adjustment of operating parameters can be abandoned. Spectral interferences were not observed at all.

4.3.5.2 Cross-sensitivity towards H_2O

In view of developing an air-quality monitoring device, H_2O might be the most critical interference component as the humidity level is subject to major variations. Therefore, a sensor system for environmental analysis might be able to handle about 80 % relative humidity (%rh) at 30 °C, i.e. a mass concentration of 24.3 g/m^3. Assuming water vapor as an ideal gas, this corresponds to 3.2 %V. In order to investigate if the off-beam QEPAS NO_2 measurement gets affected by humidity, we monitored the PA signal resulting from 10 ppmV NO_2 in synthetic air while adding up to 80 %rh to the gas flow (see Figure 4.25a).

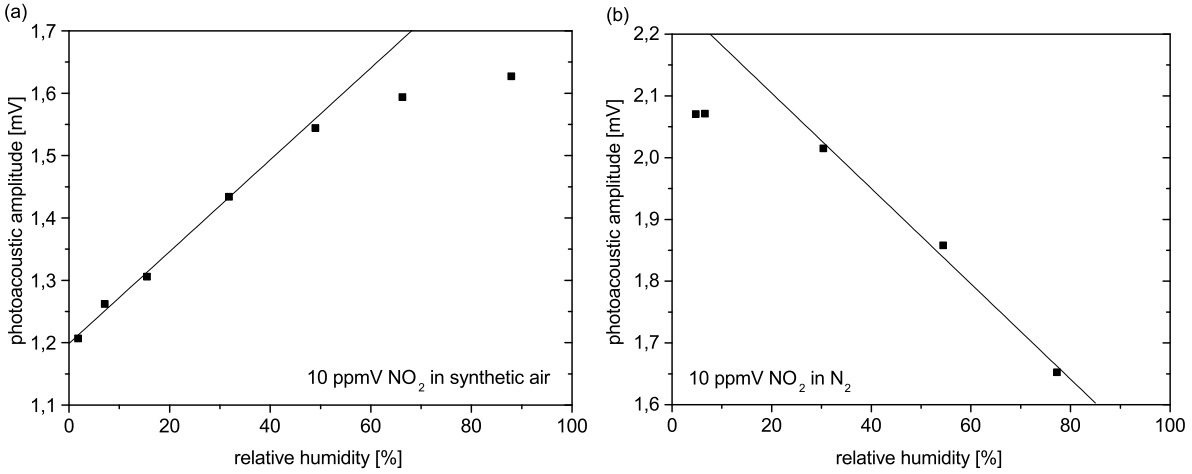

Figure 4.25: Interference studies of NO_2 detection towards H_2O. Addition of up to 80 % relative humidity to a 10 ppmV NO_2 containing sample in synthetic air (figure (a) left) and in N_2 (figure (b) right), respectively.

Figure 4.25 (a) clearly indicates the water concentration affecting the PA signal. Up to approximately 50 %rh, there seems to be a linear growth dependency and at higher humidity levels, the effect weakens. As one possible interpretation of these results, it could be expected that H_2O might act as a promoter and thus fasten the effective VT relaxation time of NO_2. Such phenomena of signal increase by enhancing the VT relaxation rate due to H_2O have already been reported several times in terms of CO, CO_2, HCN and CH_4 detection, respectively [6, 10, 16, 36, 37]. However, Kalkman and van Kesteren [34] reported a relaxation rate of $\tau_{VT} \approx 2$ µs for NO_2 in N_2 mixtures. While the condition for complete VT relaxation in literature is

mostly approximated by $\tau_{VT} << 1/f_{mod}$, previous calculations of our group give a more accurate condition, i.e. $\tau_{VT} \leq 1/(10 f_{mod})$. With regard to QEPAS measurement, the term $1/(10 f_{mod})$ was calculated to ~ 3 µs. Thus, the above condition is met and the process of NO_2 relaxation is assumed to run completely even in absence of H_2O.
In order to further investigate the observed dependency on H_2O, we repeated the measurement with synthetic air replaced by N_2. The results are plotted in figure 4.25 (b). In contrast to figure 4.25 (a), the plot shows a decay dependency that can be considered linear exceeding a humidity level of about 30 %rh. This decay obviously proofs the assumption that the H_2O dependency is not based on VT relaxation effects. Considering these two delineations, we assumed the signal dependency on H_2O to result from changes in speed of sound and, therefore, shifting the acoustic resonance profile of the mR towards the profile of the QTF (refer to figure 4.20). Consequently, we calculated the speed of sound for every measuring point within figure 4.25 (a) and (b) with respect to temperature and composition of the gas mixture and summarized the results in figure 4.26. More precisely, prior to plotting figure 4.26, two further steps towards reproducing the resonance spectrum of the mR have already been considered:

i. The 15 % signal drop due to $VV_{NO2\text{-}O2}$ relaxation was taken into account and the amplitudes gathered from measurements carried out in pure N_2 atmosphere were accordingly compensated (see chapter 4.3.5.1).
ii. All amplitudes were divided by the sole QTF amplification factor, which was specified to 76.

The thus obtained values were fitted using the Gaussian-Amplitude function and the coefficient of determination was calculated to $R^2 = 0.97$. From the speed of sound $c_{res,id}$ at the peak maximum and the frequency used for modulation, i.e. 3 2751.5 Hz, we calculated $\lambda_{res,id}$ to $10.73 \cdot 10^{-3}$ m. This is the length of those sound waves, which get maximal amplified within the resonator tube. By knowing the actual length of the tube together with $\lambda_{res,id}$, we calculated the node-shifting excess factor s_{tube} to 0.49 using equation 4.4. In order to finally reproduce the individual mR profile, two more calculations have to be performed:

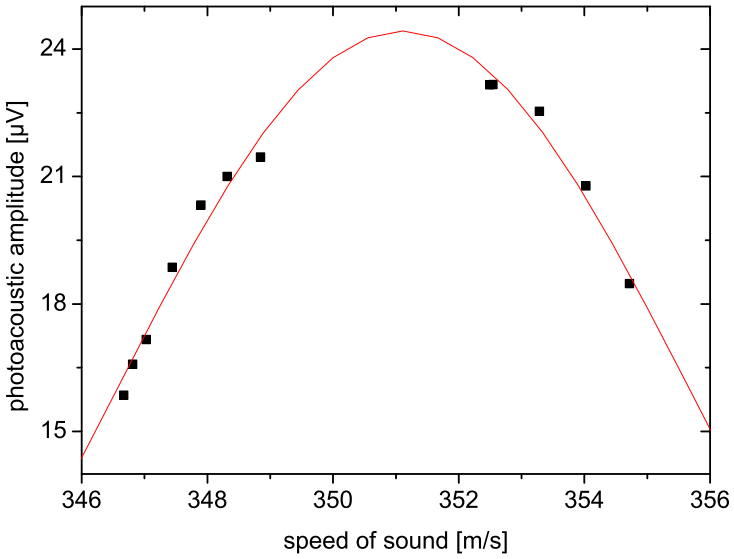

Figure 4.26: Replication of the individual mR resonance profile. The speed of sound was varied by altering the composition of the sample.

iii. The peak profile from figure 4.26 has to be shifted by $\Delta c = c_{\text{meas}} - c_{\text{res,id}}$, where c_{meas} is the speed of sound which prevailed while recording the double resonance profile of the off-beam QEPAS scheme.

iv. The thus obtained values for c_i have to be converted into the correspondent frequencies using $\lambda_{\text{res,id}}$ and equation 1.73.

These calculations finally allowed us to reproduce the individual mR spectrum, which is shown in figure 4.20. Concluding the results of this chapter, H_2O obviously does have an effect on off-beam QEPAS NO_2 detection. The dependency was identified to result from acoustic detuning. Moreover, double-resonant QEPAS schemes were identified to suffer from a significant disadvantage compared to common microphone-based PA setups. The double-resonance feature negatively amplifies signal decreases due to acoustic detuning and besides, they obliterate to compensate acoustic detuning by re-adjusting the modulation frequency. Therefore, humidity has to be measured separately in view of developing a double-resonant QEPAS air monitoring application. Knowing the H_2O concentration, either different calibration curves have to be applied or the temperature has to be adjusted in order to compensate detuning.

4.3.5.3 Acoustic noise interference

Besides interference studies towards the main components of air, it is obviously necessary to investigate photoacoustic-based applications with respect to ambient noise. For this purpose, we installed a test setup for acoustic noise simulation, which was described in chapter 4.3.2. By putting the setup into operation, we increased the standard laboratory noise level by almost 40 dB, which is tantamount to heavy street traffic.

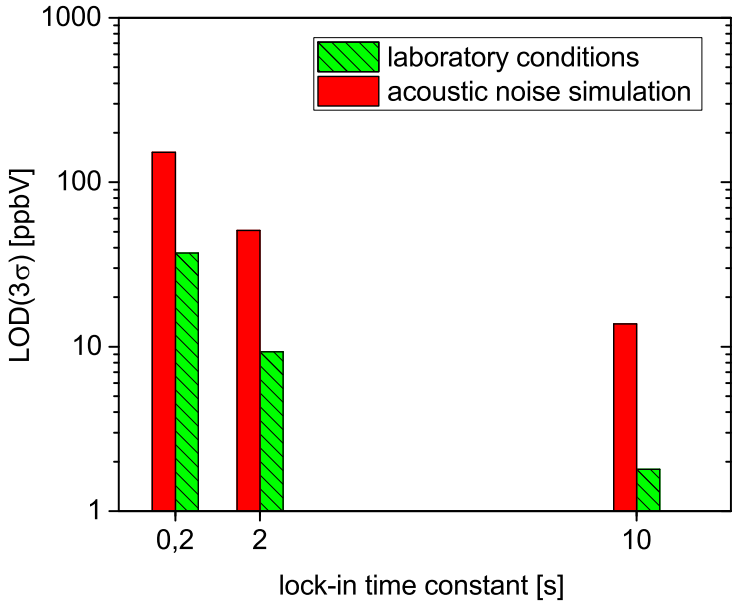

Figure 4.27: Ambient noise simulation. LOD dependency on acoustic noise using different lock-in time constants, i.e. 200 ms, 2 s and 10 s, respectively. LODs specified at standard laboratory noise level are marked by green patterned columns, LODs determined while acoustic noise simulation are shown as red columns.

Figure 4.27 illustrates the LOD dependency on acoustic noise using lock-in amplifier time constants of 200 ms, 2 s and 10 s, respectively, and an averaging time of 20 s. In terms of trace gas analysis and $\tau_{\mathrm{LIA}} = 10$ s, the limit of detection increases to 14 ppbV, which means almost a deterioration factor of 8. Still, this noise susceptibility of the QEPAS setup is very low compared to microphone-based PACs. For comparison, while using a standard PA setup [28], the same noise level caused the LOD to deteriorate to 0.74 ppmV, which is a factor of 370. There are two reasons why QTFs show improved acoustic noise immunity. Firstly, only noise within the frequency

range of OTF resonance affects its oscillation to an appreciable degree. Besides, QTFs show acoustic quadrupole characteristics [38]. Based on a simplified quadrupole model, only one single-point noise source between the QTF tines or two symmetrically placed single-point sources next to the tines might affect the QTF oscillation. For this reason, ambient noise affecting the QTF as quasi plane wave fronts ideally does not affect flexural mode oscillation. Summing up, it is highly recommended to utilize tuning fork based detection schemes rather than standard microphone-based PA setups in view of developing real-life trace gas monitoring applications, which are exposed to ambient noise.

4.3.6 Summary of key characteristics

Table 4.3: Key parameters of the off-beam QEPAS setup for NO_2 detection. Dilution medium, f_{res}: frequency of modulation, Q: quality factor of acoustic resonance, L_p: resonance amplification factor, LOD: limit of detection, LOD_{noise}: LOD while heavy street traffic simulation, maximum error of calibration, signal drift, sensitivity, response time.

	f_{res} [Hz]	Q	L_p [dB]	LOD (3σ) [ppbV]	LOD_{noise} (3σ) [ppbV]	max. error[a] [%]	signal drift[b]	sensitivity [µV/ppmV]	τ_{90}[c] [s]
Air	32 752	5 849	52	1.8	14	± 1.4	1 ‰	127	8 s
N_2	32 755	5 132	53	1.2	9.3	n.a.[d]	n.a.[d]	185	n.a.[d]

[a]The maximum error takes into account three times the standard deviation of 100 raw data points and three times the standard deviation of the linear regression of the calibration curve.
[b]Signal drift within a measuring period of 30 minutes.
[c]Lock-in time constant: 2 s, increase in analyte concentration: 20 ppmV.
[d]No data available, but mo difference to measurements in synthetic air is expected.

For short but clear presentation of key parameters of the off-beam QEPAS scheme, table 4.3 sums up the most crucial characteristics of NO_2 detection in synthetic air. To facilitate comparability with a standard PA setup, which was characterized in [28], some key characteristics were additionally specified in NO_2/N_2 mixtures.

4.3.7 Conclusion

Concluding the results of characterization, the off-beam QEPAS scheme is highly suitable for NO_2 trace gas detection in view of developing an air-quality monitoring application. The corresponding detection limit, response time, precision, signal stability and the immunity towards ambient noise are suggested to meet the demands on such an application. We identified a mismatch of mR- and QTF-resonance that can be eliminated, e.g. by adjusting the length of the resonator tube, to further increase the sensitivity of the system by $\sim$ 2 dB, i.e. 26 %. The gas flow rate may be increased to 500 mL/min in order to improve the response behavior of the system, as no increase in noise level due to turbulences was observed. Cross-sensitivity investigations towards N_2, CO_2 and H_2O showed no interferences other than detuning, but O_2 was identified to additionally cause signal decrease due to $VV_{NO2\text{-}O2}$ relaxation. Monitoring the speed of sound and compensating matrix variations by temperature controlling the PAC is recommended. Besides re-adjusting the mR resonance, temperature controlling the PAC is also assumed to allow noise reduction by averaging. Acoustic noise interference revealed the detection limit to downgrade by a factor 8 in terms of heavy street traffic simulation, which is 46 times less compared to standard microphone-based PA setups [28].
However, although this QEPAS setup was generally determined to meet the requirements of a NO_2 trace gas monitoring application, the choice of the most appropriate PA setup and the choice of operating parameters always depends on the application scenario. This article is meant to reveal the advantages and disadvantages of the technique and thus to assist making that choice. The following key questions have to be raised prior to choosing the appropriate PA arrangement.

Do I have to expect changes in the composition of the sample apart from the analyte?
Changes in composition cause detuning of the resonator. Common PA setups can compensate these changes by adjusting the modulation frequency. In view of double resonant systems, those changes have to be monitored separately. Compensation has to be done actively by adjusting the temper-

ature or passively by relying on appropriate calibration curves.

Do I have to expect ambient noise?
Common PA setups are much more susceptible towards ambient noise.

Do I plan to miniaturize the sensor element, e.g. to fasten the response time or to reduce energy consumption?
Common PA setups are limited with regard to miniaturization.

Providing that double-resonant QEPAS arrangement was answered to be most suitable, figure 4.24 assists choosing the optimum lock-in time constant in view of response time and precision of the system. However, with respect to most other analyte species than NO_2, direct excitation of vibrational states has to be applied using infrared emitters. Moreover, wavelength modulation may be given priority to amplitude modulation in order to reduce spectral interferences. To avoid analyte-specific signal losses due to slow VT-relaxation, we recommend to use customized sensor elements allowing for slower modulation [30, 39].

References

[1] F. J. Harren, G. Cotti, J. Oomens and S. t. L. Hekkert, Photoacoustic Spectroscopy in Trace Gas Monitoring, in *Encyclopedia of Analytical Chemistry*, pages 2203–2226 (John Wiley and Sons, Ltd, Chichester, UK, 2000), ISBN 0471976709, doi:10.1002/9780470027318.a0718, URL `http://doi.wiley.com/10.1002/9780470027318.a0718`.

[2] A. Elia, P. M. Lugarà, C. di Franco and V. Spagnolo, Photoacoustic techniques for trace gas sensing based on semiconductor laser sources, *Sensors*, 9(12):9616–9628 (2009), ISSN 14248220, doi:10.3390/s91209616.

[3] A. A. Kosterev, Y. A. Bakhirkin, R. F. Curl and F. K. Tittel, Quartz-enhanced photoacoustic spectroscopy., *Optics letters*, 27(21):1902–1904 (2002), ISSN 0146-9592, doi:10.1364/OL.27.001902.

[4] A. A. Kosterev and F. K. Tittel, Ammonia detection by use of quartz-enhanced photoacoustic spectroscopy with a near-IR telecommunication diode laser., *Applied optics*, 43(33):6213–6217 (2004), ISSN 0003-6935, doi:10.1364/AO.43.006213.

[5] M. Horstjann, Y. Bakhirkin, A. Kosterev, R. Curl, F. Tittel, C. Wong, C. Hill and R. Yang, Formaldehyde sensor using interband cascade laser based quartz-enhanced photoacous-

tic spectroscopy, *Applied Physics B*, 79(7):799–803 (2004), ISSN 0946-2171, doi:10.1007/s00340-004-1659-3, URL http://link.springer.com/10.1007/s00340-004-1659-3.

[6] G. Wysocki, A. A. Kosterev and F. K. Tittel, Influence of molecular relaxation dynamics on quartz-enhanced photoacoustic detection of CO2 at 2um, *Applied Physics B: Lasers and Optics*, 85(2-3):301–306 (2006), ISSN 09462171, doi:10.1007/s00340-006-2369-9.

[7] A. A. Kosterev, F. K. Tittel, D. V. Serebryakov, A. L. Malinovsky and I. V. Morozov, Applications of quartz tuning forks in spectroscopic gas sensing, *Review of Scientific Instruments*, 76(4):1–9 (2005), ISSN 00346748, doi:10.1063/1.1884196.

[8] A. A. Kosterev, L. Dong, D. Thomazy, F. K. Tittel and S. Overby, QEPAS for chemical analysis of multi-component gas mixtures, *Applied Physics B: Lasers and Optics*, 101(3):649–659 (2010), ISSN 09462171, doi:10.1007/s00340-010-4183-7.

[9] A. A. Kosterev, Y. A. Bakhirkin and F. K. Tittel, Ultrasensitive gas detection by quartz-enhanced photoacoustic spectroscopy in the fundamental molecular absorption bands region, *Applied Physics B*, 80(1):133–138 (2005), ISSN 0946-2171, doi:10.1007/s00340-004-1619-y.

[10] A. A. Kosterev, T. S. Mosely and F. K. Tittel, Impact of humidity on quartz-enhanced photoacoustic spectroscopy based detection of HCN, *Applied Physics B: Lasers and Optics*, 85(2-3):295–300 (2006), ISSN 09462171, doi:10.1007/s00340-006-2355-2.

[11] A. A. Kosterev, F. K. Tittel and G. Bearman, Advanced Quartz-Enhanced Photoacoustic Trace Gas Sensor for Early Fire Detection, *SAE International Journal of Aerospace*, 1(1):2008–01–2091 (2008), ISSN 1946-3901, doi:10.4271/2008-01-2091, URL http://www.sae.org/technical/papers/2008-01-2091.

[12] N. Weppenaar, A. Kosterev, L. Dong, D. Tomazy and F. Tittel, SS: Advances in Flexible Riser Technology: Fiberoptic Gas Monitoring Of Flexible Risers, in *Offshore Technology Conference*, December, pages 73–74 (Offshore Technology Conference, 2009), ISBN 9781555632441, ISSN 01492136, doi:10.4043/19901-MS, URL http://www.onepetro.org/doi/10.4043/19901-MS.

[13] S. Schilt, A. A. Kosterev and F. K. Tittel, Performance evaluation of a near infrared QEPAS based ethylene sensor, *Applied Physics B: Lasers and Optics*, 95(4):813–824 (2009), ISSN 09462171, doi:10.1007/s00340-008-3306-x.

[14] V. Spagnolo, A. A. Kosterev, L. Dong, R. Lewicki and F. K. Tittel, NO trace gas sensor based on quartz-enhanced photoacoustic spectroscopy and external cavity quantum cascade laser, *Applied Physics B-Lasers and Optics*, 100(1):125–130 (2010), ISSN 0946-2171, doi:10.1007/s00340-010-3984-z.

[15] L. Dong, V. Spagnolo, R. Lewicki and F. K. Tittel, Ppb-level detection of nitric oxide using an external cavity quantum cascade laser based QEPAS sensor, *Optics Express*, 19(24):24037 (2011), ISSN 1094-4087, doi:10.1364/OE.19.024037.

[16] L. Dong, R. Lewicki, K. Liu, P. R. Buerki, M. J. Weida and F. K. Tittel, Ultra-sensitive carbon monoxide detection by using EC-QCL based quartz-enhanced photoacoustic spectroscopy, *Applied Physics B: Lasers and Optics*, 107(2):275–283 (2012), ISSN 09462171, doi:10.1007/s00340-012-4949-1.

[17] J. Waclawek, R. Lewicki, M. Jahjah, Y. Ma, E. Chrysostom, B. Lendl and F. K. Tittel, A sensitive CW DFB quantum cascade laser based QEPAS sensor for detection of SO2, in *Conference on Lasers and Electro-Optics 2012*, volume 1, page CW3B.4 (OSA, Washington, D.C., 2012).

[18] M. Jahjah, S. Belahsene, L. Nahle, M. Fischer, J. Koeth, Y. Rouillard and A. Vicet, Quartz enhanced photoacoustic spectroscopy with a 3.38 mum antimonide distributed feedback laser., *Optics letters*, 37(13):2502–2504 (2012), ISSN 1539-4794 (Electronic).

[19] Y. Ma, R. Lewicki, M. Razeghi and F. K. Tittel, QEPAS based ppb-level detection of CO and N2O using a high power CW DFB-QCL., *Optics express*, 21(1):1008–19 (2013), ISSN 1094-4087, doi:10.1364/OE.21.001008, URL `http://www.ncbi.nlm.nih.gov/pubmed/23388995`.

[20] K. Liu, X. Guo, H. Yi, W. Chen, W. Zhang and X. Gao, Off-beam quartz-enhanced photoacoustic spectroscopy, *Opt. Lett.*, 34(10):1594–1596 (2009), doi:10.1364/OL.34.001594, URL `http://ol.osa.org/abstract.cfm?URI=ol-34-10-1594`.

[21] K. Liu, H. Yi, A. A. Kosterev, W. Chen, L. Dong, L. Wang, T. Tan, W. Zhang, F. K. Tittel and X. Gao, Trace gas detection based on off-beam quartz enhanced photoacoustic spectroscopy: Optimization and performance evaluation, *Review of Scientific Instruments*, 81(10):3–8 (2010), ISSN 00346748, doi:10.1063/1.3480553.

[22] S. Böttger, M. Köhring, U. Willer and W. Schade, Off-beam quartz-enhanced photoacoustic spectroscopy with LEDs, *Applied Physics B*, 113(2):227–232 (2013), ISSN 0946-2171, doi:10.1007/s00340-013-5462-x, URL `http://dx.doi.org/10.1007/s00340-013-5462-x`.

[23] K. Bogumil, J. Orphal, T. Homann, S. Voigt, P. Spietz, O. Fleischmann, A. Vogel, M. Hartmann, H. Kromminga, H. Bovensmann, J. Frerick and J. Burrows, Measurements of molecular absorption spectra with the SCIAMACHY pre-flight model: instrument characterization and reference data for atmospheric remote-sensing in the 230-2380 nm region, *Journal of Photochemistry and Photobiology A: Chemistry*, 157(2-3):167–184 (2003), ISSN 10106030, doi:10.1016/S1010-6030(03)00062-5, URL `http://linkinghub.elsevier.com/retrieve/pii/S1010603003000625`.

[24] A. Vandaele, C. Hermans, P. Simon, M. Carleer, R. Colin, S. Fally, M. Mérienne, A. Jenouvrier and B. Coquart, Measurements of the NO2 absorption cross-section from 42 000 cm-1 to 10 000 cm-1 (238-1000 nm) at 220 K and 294 K, *Journal of Quantitative Spectroscopy and Radiative Transfer*, 59(3-5):171–184 (1998), ISSN 00224073, doi:10.1016/S0022-4073(97)00168-4, URL `http://www.sciencedirect.com/science/article/pii/S0022407397001684`.

[25] H. Zheng, L. Dong, X. Yin, X. Liu, H. Wu, L. Zhang, W. Ma, W. Yin and S. Jia, Ppb-level QEPAS NO2 sensor by use of electrical modulation cancellation method with a high power

blue LED, *Sensors and Actuators, B: Chemical*, 208(2):173–179 (2015), ISSN 09254005, doi:10.1016/j.snb.2014.11.015, URL http://dx.doi.org/10.1016/j.snb.2014.11.015.

[26] H. Yi, K. Liu, W. Chen, T. Tan, L. Wang and X. Gao, Application of a broadband blue laser diode to trace NO2 detection using off-beam quartz-enhanced photoacoustic spectroscopy., *Optics letters*, 36(4):481–483 (2011), ISSN 0146-9592, doi:10.1364/OL.36.000481.

[27] P. Patmisco, G. Scamarcio, F. K. Tittel and V. Spagnolo, Quartz-enhanced photoacoustic spectroscopy: a review, *Sensors (Basel, Switzerland)*, 14(4):6165–6206 (2014), ISSN 14248220, doi:10.3390/s140406165.

[28] T. Rück, R. Bierl and F.-M. Matysik, Development and characterization of a laboratory setup for photoacoustic NO2 determination based on the excitation of electronic 2B2 and 2B1 states using a low-cost semiconductor laser, *Sensors and Actuators A: Physical*, 258:193–200 (2017), ISSN 09244247, doi:10.1016/j.sna.2017.03.024, URL http://linkinghub.elsevier.com/retrieve/pii/S0924424716310433.

[29] A. Miklos, P. Hess and Z. Bozoki, Application of acoustic resonators in photoacoustic trace gas analysis and metrology, *Review of Scientific Instruments*, 72(4):1937–1955 (2001), ISSN 00346748, doi:10.1063/1.1353198.

[30] M. Giglio, A. Sampaolo, P. Patimisco, H. Zheng, H. Wu, L. Dong, F. K. Tittel and V. Spagnolo, Single-tube on beam quartz-enhanced photoacoustic spectrophones exploiting a custom quartz tuning fork operating in the overtone mode, volume 10111, page 1011107 (2017), doi:10.1117/12.2252368, URL http://proceedings.spiedigitallibrary.org/proceeding.aspx?doi=10.1117/12.2252368.

[31] A. Schmohl, A. Miklós and P. Hess, Detection of ammonia by photoacoustic spectroscopy with semiconductor lasers., *Applied optics*, 41(2):1815–1823 (2002), ISSN 0003-6935, doi:10.1364/AO.41.001815.

[32] M. Marinov and Z. Petrov, Allan Variance Analysis on Error Characters of Low-Cost MEMS Accelerometer MMA8451Q, in *INTERNATIONAL CONFERENCE of SCIENTIFIC PAPER, AFASES 2014* (2014).

[33] L. Dong, J. Wright, B. Peters, B. A. Ferguson, F. K. Tittel and S. McWhorter, Compact QEPAS sensor for trace methane and ammonia detection in impure hydrogen, *Applied Physics B: Lasers and Optics*, 107(2):459–467 (2012), ISSN 0946-2171, doi:10.1007/s00340-012-4908-x.

[34] J. Kalkman and H. van Kesteren, Relaxation effects and high sensitivity photoacoustic detection of NO2 with a blue laser diode, *Applied Physics B*, 90(2):197–200 (2008), ISSN 0946-2171, doi:10.1007/s00340-007-2895-0, URL http://link.springer.com/10.1007/s00340-007-2895-0.

[35] S. G. Ejakov, S. Phillips, Y. Dain, R. M. Lueptow and J. H. Visser, Acoustic attenuation in gas mixtures with nitrogen: experimental data and calculations, *J Acoust Soc Am*, 113(4 Pt 1):1871–1879 (2003), ISSN 00014966, doi:10.1121/1.1559177, URL http://www.ncbi.nlm.nih.gov/pubmed/12703699.

[36] A. A. Kosterev, Y. A. Bakhirkin, F. K. Tittel, S. McWhorter and B. Ashcraft, QEPAS methane sensor performance for humidified gases, *Applied Physics B: Lasers and Optics*, 92(1):103–109 (2008), ISSN 09462171, doi:10.1007/s00340-008-3056-9.

[37] R. Lewicki, G. Wysocki, A. A. Kosterev and F. K. Tittel, Carbon dioxide and ammonia detection using 2 mu m diode laser based quartz-enhanced photoacoustic spectroscopy, *Applied Physics B-Lasers and Optics*, 87(1):157–162 (2007), ISSN 0946-2171, doi:10.1007/s00340-006-2474-9.

[38] D. A. Russell, On the sound field radiated by a tuning fork, *American Journal of Physics*, 68(June 1999):1139 (2000), ISSN 00029505, doi:10.1119/1.1286661.

[39] H. Wu, A. Sampaolo, L. Dong, P. Patimisco, X. Liu, H. Zheng, X. Yin, W. Ma, L. Zhang, W. Yin, V. Spagnolo, S. Jia and F. K. Tittel, Quartz enhanced photoacoustic H2S gas sensor based on a fiber-amplifier source and a custom tuning fork with large prong spacing, *Applied Physics Letters*, 107(11):22–26 (2015), ISSN 00036951, doi:10.1063/1.4930995.

4.4 Miniaturized sensor element μPAS

4.4.1 Introduction

In comparison to common absorption spectroscopy, photoacoustic spectroscopy offers the advantage of miniaturization, as the signal amplitude correlates with the reciprocal cross section* (refer to equation 1.85), rather than with the length of the measuring cell (refer to equation 1.3). The characterization of a PAC, which already takes advantage of miniaturization (namely an off-beam QEPAS cell design) was discussed in chapter 4.3 in detail. This section introduces a further step of miniaturization and integration, which yielded a PA cell design that is referred to as μPAS (miniaturized photoacoustic sensor chip). This cell design is based on a MEMS sensor module, thus all steps of process development were carried out within the clean room facilities of the *Ostbayerische Technische Hochschule (OTH) Regensburg*. With regard to this sensor chip, sound conversion is realized by means of a resonant cantilever beam.
Conventional photoacoustic applications that utilize cantilevers for sound conversion are referred to as cantilever enhanced photoacoustic spectroscopic (CEPAS) devices. However, most cantilever based photoacoustic systems do not operate at resonant conditions [1–9]†. There are only two resonant CEPAS systems presented in literature so far,‡ i.e. a piezoelectric cantilever microphone operating at 20 Hz [10] and an AFM (atomic force microscopy) cantilever operating at $\sim$5.3 kHz [11], respectively.
The concept of μPAS on the contrary combines an acoustic resonator with a mechanically resonant cantilever as acoustic transducer, thus constituting a double resonant system. To the best of the authors knowledge, such a double-resonant CEPAS system has not been reported so far.

*assuming a tube shaped design

†These references are all based on the same system, which was developed at the institutes of Prof. Kauppinen (Aalto University of Helsinki, Finland) and Prof. Tittonen (University of Turku, Finland). The system is based on interferometric read-out, thus it is also referred to as an optical microphone.

‡to the best of the authors knowledge

4.4.2 Experimental

As mentioned in subsection 4.4.1, double resonance amplification of the sensor chip is achieved by combining an acoustic resonator with a mechanically resonant cantilever beam for sound conversion. More precisely, acoustic resonance was achieved by etching a resonator tube into a borofloat glass substrate through a multi-wafer process.

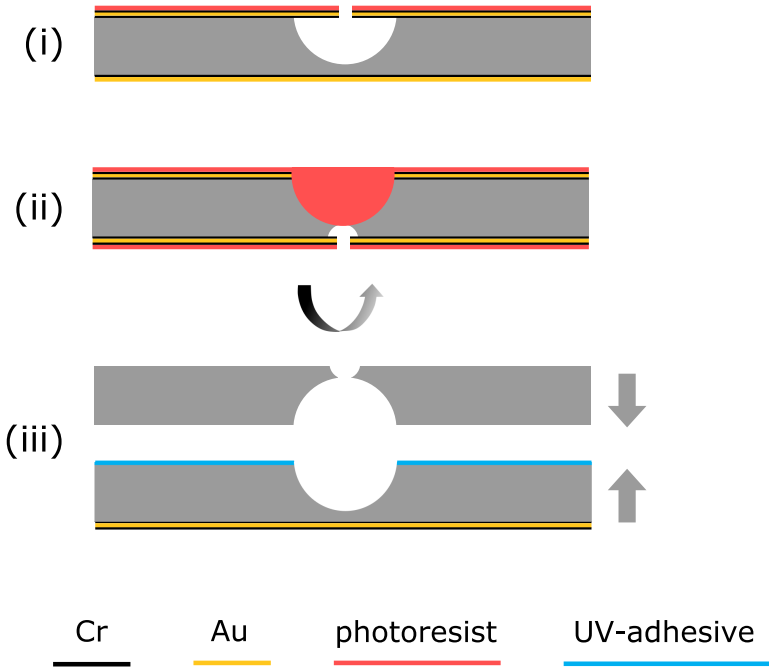

Figure 4.28: Flowchart of micro-resonator fabrication. SiO_2: silicon dioxide, Cr: chromium, Au: gold.

Figure 4.28 illustrates a flowchart that represents the process of micro-resonator (mR) fabrication. First of all, the substrate is top and bottom coated by means of in-situ electron beam evaporation with a 8 nm layer of chromium acting as adhesion promoter for a 100 nm gold coating. This coating in turn serves as stop layer for wet-chemical hydrogen fluoride etching. Another 30 nm Cr layer is top coated onto the substrate in order to promote spin coating of the photoresist. Afterwards, the photoresist is structured by exposure (lithography) and a half-pipe shaped trench is etched into the substrate (i). These steps of fabrication are applied to two wafers, while

one of them is further subjected to bottom side treatment. Therefore, the substrate again is protected by photoresist and a lower share of material is subsequently removed from the bottom side (according to the processes used for top side treatment), which later on constitutes a hole for acoustic coupling to the cantilever (ii). Finally, both wafers are flip-bonded by means of an UV-adhesive (iii), thus constituting the acoustic micro-resonator tube.

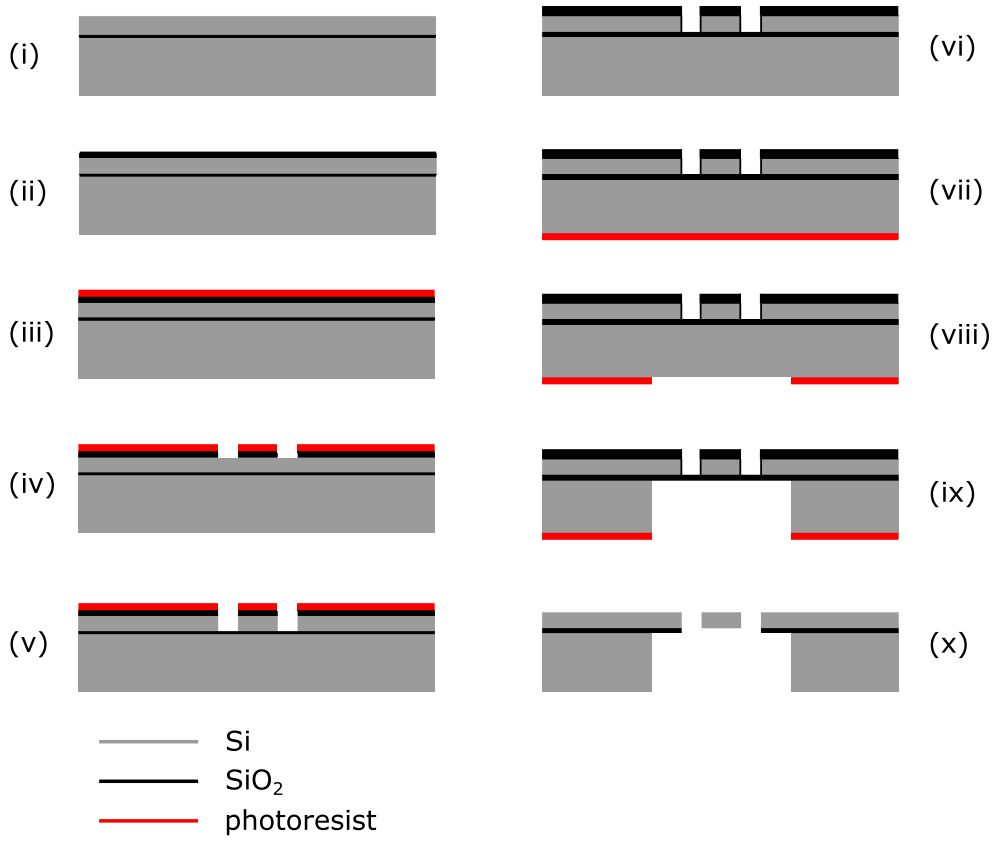

Figure 4.29: Flowchart of cantilever fabrication.

In accordance with figure 4.28, figure 4.29 shows a flowchart that illustrates the process of cantilever fabrication. Previous investigations, which were based on pure silicon substrates, yielded inconsistent cantilever thicknesses, thus causing a significant variation of eigenfrequencies. Therefore, silicon on insulator (SOI) wafer, which feature a SiO_2 etch-stop layer and a Si layer of defined thickness, are currently used instead (i).* Those substrates first are coated with SiO_2 by means of plasma enhanced chemical vapor deposition

*In terms of cantilever development 15 μm SOI substrates were utilized.

(PECVD) (ii) as well as spin-coated with photoresist (iii) and subsequently structured by means of lithography. Afterwards SiO_2 and silicon substrate are dry etched based on the reactive ion etching (RIE) technique (iv,v). After that, the photoresist is removed and further SiO_2 is deposited in order to protect the verticals of the cantilever beam in preparation for bottom treatment of the wafer (vi). In this context photoresist is applied to the bottom side (vii) and structured by exposure (viii). The silicon substrate again is removed by RIE (ix).* Subsequent removal of SiO_2 and photoresist finally leads to the freestanding beam that is displayed in figure 4.29 (x).

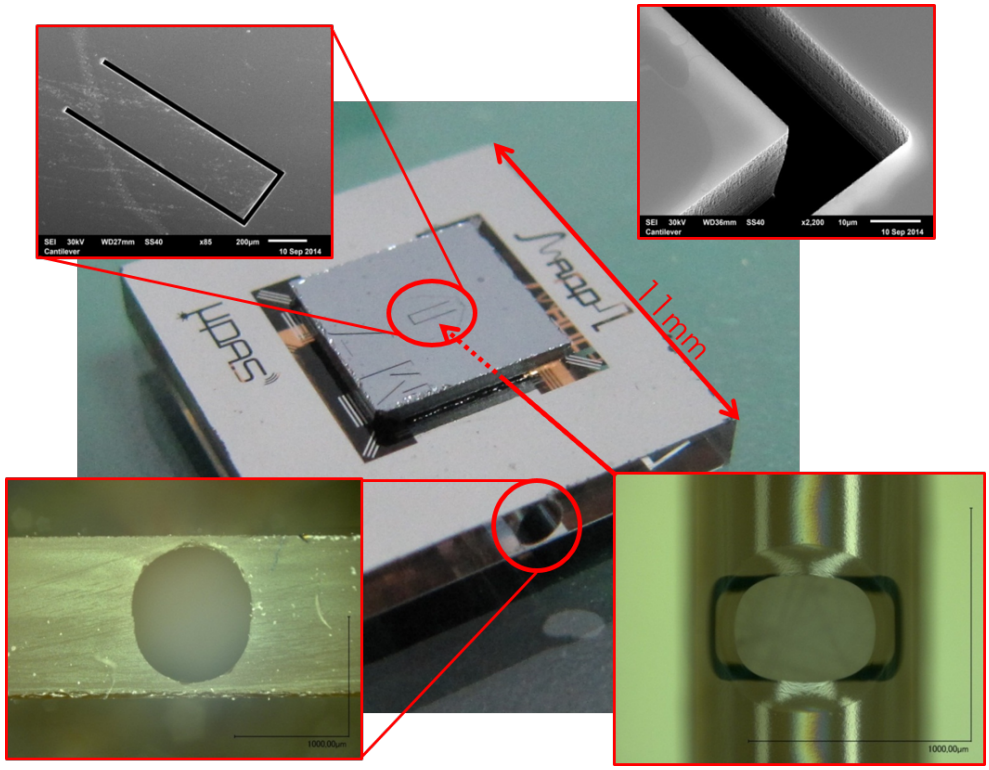

Figure 4.30: Picture of the µPAS sensor chip (center) with four close-ups, i.e. two raster electron microscopic images of the cantilever (top left and top right) as well as two microscopic images of the acoustic micro-resonator (bottom left and bottom right).

The center of figure 4.30 displays a picture of a finalized µPAS sensor chip, which overall dimensions roughly are about 11 x 10 x 2 mm. The figure additionally shows four close-ups, i.e. two top view raster electron microscopic

*The SiO_2 insulator layer is hardly corroded by RIE, as the etching rate is much less than in case of Si.

images highlighting the complete cantilever (top left) and a detailed view of an edge (top right), respectively, as well as two microscopic images, that display the cross section (bottom left) and the coupling hole (bottom right) of the micro-resonator. Currently used micro-resonators are 11 mm in length and 1.2 mm in diameter, while their openings for acoustic coupling to the cantilever beam are approximately 300 μm in diameter. The cantilevers in turn are 1 250 μm x 300 μm x 15 μm (length x width x thickness).
Besides double resonant amplification, the μPAS setup offers a further advantage compared to common CEPAS arrangements, i.e. bottom-up illumination of the sensor chip. This method of illumination is considered a special feature as it significantly facilitates optical alignment and increases the mechanical robustness of the system.

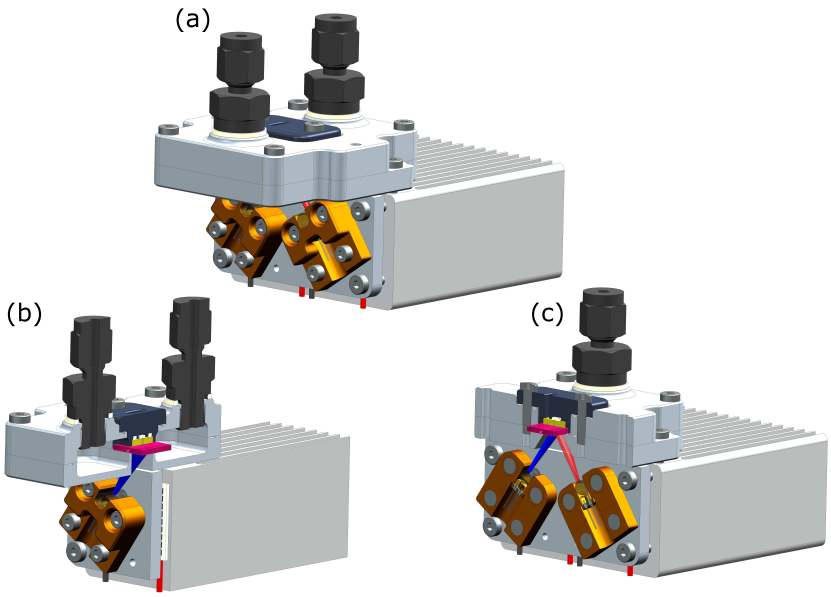

Figure 4.31: Drawing of a manifold for μPAS sensor chip characterization in overall view (a) and two vertical plane cross sections (b) and (c), respectively.

Figure 4.31 illustrates an overall drawing (a) as well as two vertical plane cross section drawings of a manifold (b and c), which was developed for μPAS sensor chip characterization. This manifold comprises two mountings (gold) for a blue and a red diode laser, respectively, which are in contact with a peltier element that in turn is connected to a heat sink (silver) for thermal dissipation. Figure 4.31 further displays a gas inlet and a gas outlet on top

of the device (black) as well as a modular chip mounting adapter in between (dark blue). The modular design of this adapter ensures the mounting of chips that differ in size and it additionally allows for integrating ultra-low noise MEMS microphones (ICS-40720, InvenSense Inc., California, US) for individual mR characterization. It further features the integration of a tilted window, which facilitates cantilever monitoring by utilizing a PSV-400 laser vibrometer (Polytec GmbH, Waldbronn, Germany), hence this adapter is referred to as manifold. All photoacoustic double resonant μPAS investigations that are presented in section 4.4.3 rely on interferometric signal conversion.

4.4.3 Results and discussion

Figure 4.32 illustrates the individual resonance characteristics of a cantilever (a) and a micro-resonator (b), respectively. The cantilever vibration was recorded by feeding a chirp signal to a loudspeaker and monitoring the velocity of beam deflection by means of laser scanning vibrometry. On the contrary, individual acoustic resonance amplification was investigated photoacoustically by utilizing a ICS-40720 MEMS microphone.

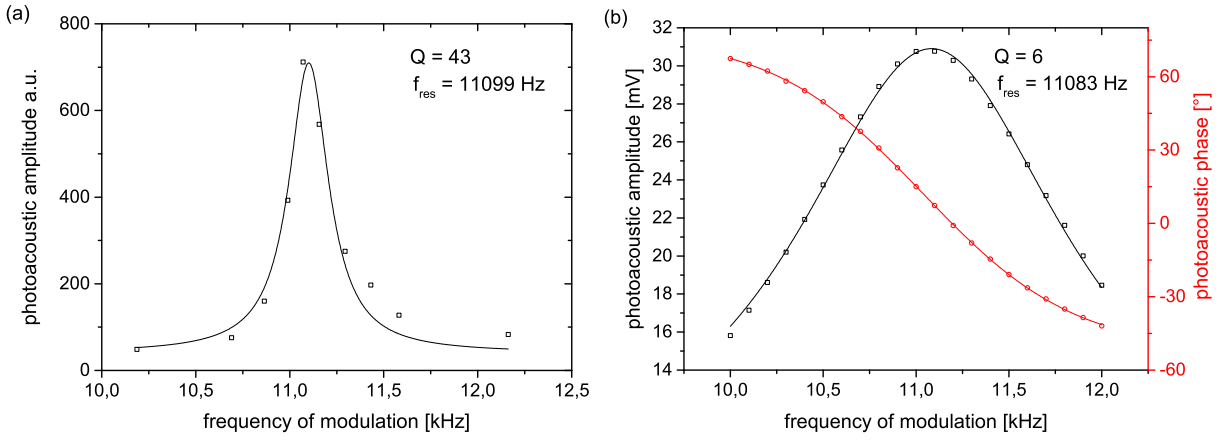

Figure 4.32: Individual resonance characteristics of a cantilever beam (a) and a micro-resonator (b).

Although the cantilever profile seems to be slightly distorted, a simple Lorentzian fit function (refer to equation 1.21) was suggested to satisfy the requirements of cantilever and microphone characterization. Thus, the

quality factors and eigenfrequencies were specified to 43 and 11 099 Hz in terms of resonant cantilever vibration and to 6 and 11 083 Hz with regard to acoustic amplification. Considering the peak and baseline magnitudes of the individual profiles, these values correspond to an amplification by the factors of 18 and 5, respectively. Figure 4.33 finally depicts the photoacoustically determined double resonance profile resulting from the combination of the individual parts.

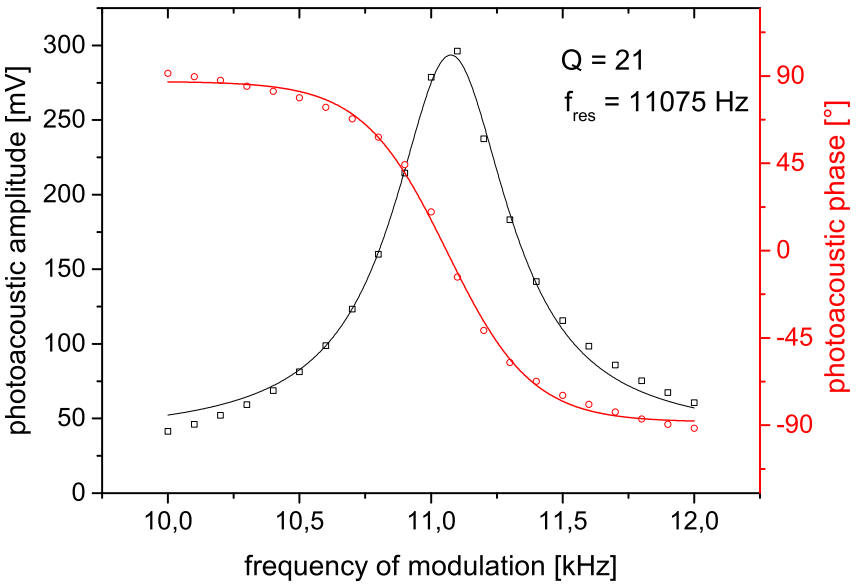

Figure 4.33: Double resonance characteristics of a μPAS sensor chip.

While the resonance frequency of the system is in the range of the individual eigenfrequencies, the determined quality factor of 21 as well as the overall amplification by a factor of 8 are surprisingly less than 50 % compared to exclusive cantilever vibration. These findings might be assumed to result from the cantilever oscillation affecting the standing wave generation within the micro-resonator, thus constituting a coupled system. However, further investigations revealed the resonance frequencies of sensor chips, which were assembled by individual parts with strongly differing eigenfrequencies, to largely correspond to the individual cantilever frequencies. The individual resonator eigenfrequency on the contrary was determined to hardly influence such double resonant systems. Since coupled systems are expected to be affected from both individual parts, feedback is not held accountable for the observed deterioration. Acoustic detuning is also excluded, since

double resonance amplification either way would have to exceed individual cantilever amplification. The method of bottom-up illumination constitutes the major difference in measuring conditions comparing figure 4.32 (a) and figure 4.33. Direct illumination of the beam hence may cause heating, which is however supposed to offset-shift the entire resonance profile, rather than to lower the quality of resonance amplification. Heating may only be considered responsible for a decrease in amplification, when going beyond the linear range of sensor characteristics, yet it is questionable whether illuminating the cantilever has such a strong impact. Anyway, this Q factor deterioration cannot finally be solved within this context, but has to be further investigated. Besides, the above considerations have to be interpreted with caution, as the applied method of interferometric cantilever readout was identified to react very sensitive to the positioning of the laser scanning focus point on the cantilever.

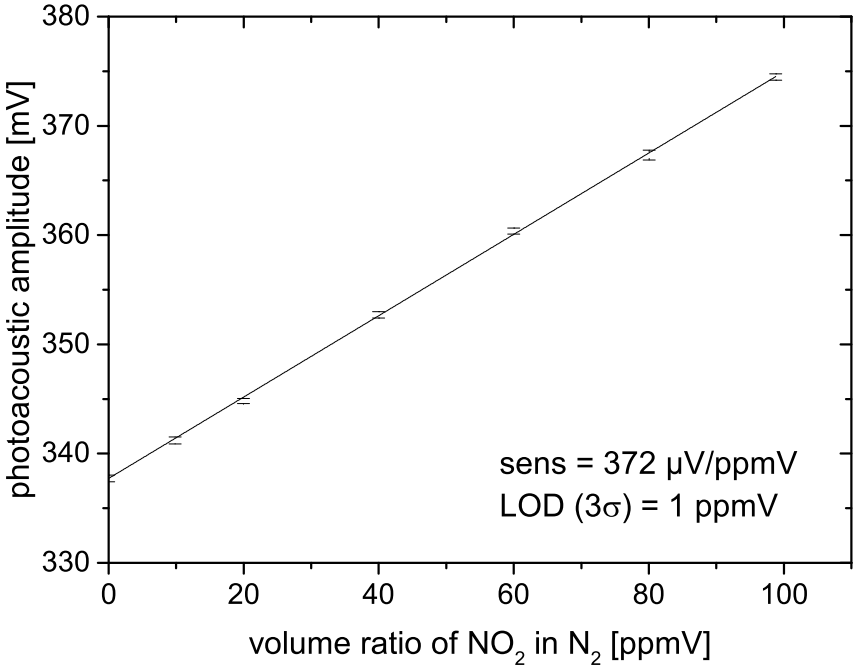

Figure 4.34: Calibration characteristics of a µPAS sensor chip based on bottom-up illumination and interferometric readout.

Figure 4.34 illustrates the calibration characteristics of a µPAS sensor chip based on bottom-up illumination and interferometric readout. While the sensitivity of the sensor was determined to be three times the sensitivity

of a double resonant QEPAS system (refer to chapter 4.3.4.1), the μPAS arrangement still suffers from two further drawbacks. Since these disadvantages significantly affect the resolution and the detection limit of the system, respectively, they are further discussed in the following section.

4.4.4 Conclusion

Whether or not cantilever illumination is accountable for quality factor deterioration, it definitely constitutes an offset shift of the photoacoustic signal. This offset shift implies a ~ 90 % loss in resolution capacity. An approach in order to counteract photoacoustic background signal generation is referred to as modulation cancellation method (MOCAM) [12]. Without going into detail about the theory or its practical implementation, MOCAM was applied by means of a second diode laser, which is displayed in figure 4.31 (c), yet it was identified to only cause minor improvement. A second major drawback of the μPAS arrangement is a very high noise level, which exceeds the one of common photoacoustic applications about three orders of magnitude. Still, it only makes limited sense to try to locate the noise source at this stage of development, as an interferometric readout is not intended to be applied in the end. The intention of applying laser scanning vibrometry was to get an idea about the dimension of cantilever deflection, while subsequently applied detection schemes might show completely different noise characteristics. In view of future development, various approaches of sound conversion are currently investigated, i.e. cantilevers coated with piezoelectric lead zirconate titanate, capacitive cantilevers, resonant capacitive membranes and cantilever based optical readout techniques, respectively. In order to effectively counteract background signal generation due to illumination, it is intended to investigate a special technique of background signal suppression. This approach is known as electrical modulation cancellation method (E–MOCAM), which for the first time was reported by Zheng et al. [13] in 2015.

References

[1] P. Sievilä, V.-P. Rytkönen, O. Hahtela, N. Chekurov, J. Kauppinen and I. Tittonen, Fabrication and characterization of an ultrasensitive acousto-optical cantilever, *Journal*

of Micromechanics and Microengineering, 17(5):852–859 (2007), ISSN 0960-1317, doi: 10.1088/0960-1317/17/5/002, URL http://stacks.iop.org/0960-1317/17/i=5/a=002?key=crossref.565a923b56a4f9fd65a01f3f41c7d152.

[2] R. E. Lindley, A. M. Parkes, K. A. Keen, E. D. McNaghten and A. J. Orr-Ewing, A sensitivity comparison of three photoacoustic cells containing a single microphone, a differential dual microphone or a cantilever pressure sensor, *Applied Physics B: Lasers and Optics*, 86(4):707–713 (2007), ISSN 09462171, doi:10.1007/s00340-006-2543-0.

[3] V. Koskinen, J. Fonsen, K. Roth and J. Kauppinen, Progress in cantilever enhanced photoacoustic spectroscopy, *Vibrational Spectroscopy*, 48(1):16–21 (2008), ISSN 09242031, doi: 10.1016/j.vibspec.2008.01.013.

[4] J. Uotila, *Use Of The Optical Cantilever Microphone In Photoacoustic Spectroscopy* (2009), ISBN 9789512939114.

[5] J. Y. Tan, F. X. Li, D. Wu, Y. L. Luo and X. X. Yang, *Association of the C3 gene polymorphisms with susceptibility to adult asthma*, Ph.D. thesis, Aalto university, Helsinki, Finnland (2011), doi:10.3760/cma.j.issn.1003-9406.2011.02.018.

[6] C. Project and T. Theisen, Miniaturised photoacoustic gas sensor based on patented interferometric readout and novel photonic integration technologies (MINIGAS), Technical report, Summary report of an European joint project (2011).

[7] J. Peltola, M. Vainio, T. Hieta, J. Uotila, S. Sinisalo, M. Siltanen and L. Halonen, High sensitivity trace gas detection by cantilever- enhanced photoacoustic spectroscopy using a mid-infrared continuous-wave optical parametric oscillator, *Optics Express*, 21(8):2103–2109 (2013), ISSN 1094-4087, doi:10.1364/OE.21.010240.

[8] C. B. Hirschmann, S. Sinisalo, J. Uotila, S. Ojala and R. L. Keiski, Trace gas detection of benzene, toluene, p-, m- and o-xylene with a compact measurement system using cantilever enhanced photoacoustic spectroscopy and optical parametric oscillator, *Vibrational Spectroscopy*, 68:170–176 (2013), ISSN 09242031, doi:10.1016/j.vibspec.2013.07.004, URL http://dx.doi.org/10.1016/j.vibspec.2013.07.004.

[9] J. Peltola, T. Hieta and M. Vainio, Parts-per-trillion-level detection of nitrogen dioxide by cantilever-enhanced photo-acoustic spectroscopy, *Opt Lett*, 40(13):2933–2936 (2015), ISSN 0146-9592, doi:10.1364/OL.40.002933, URL http://www.ncbi.nlm.nih.gov/pubmed/26125335.

[10] N. Ledermann, P. Muralt, J. Baborowski, M. Forster and J.-P. Pellaux, Piezoelectric Pb(Zr x , Ti 1-x)O3 thin film cantilever and bridge acoustic sensors for miniaturized photoacoustic gas detectors, *Journal of Micromechanics and Microengineering*, 14(12):1650–1658 (2004), ISSN 0960-1317, doi:10.1088/0960-1317/14/12/008, URL http://stacks.iop.org/0960-1317/14/i=12/a=008?key=crossref.4381152431a8f97385e0da3cab3330a3.

[11] B. D. Adamson, J. E. Sader and E. J. Bieske, Photoacoustic detection of gases using microcantilevers, *Journal of Applied Physics*, 106(11):2–5 (2009), ISSN 00218979, doi: 10.1063/1.3271157.

[12] V. Spagnolo, L. Dong, A. A. Kosterev, D. Thomazy, J. H. Doty and F. K. Tittel, Modulation cancellation method in laser spectroscopy, *Applied Physics B: Lasers and Optics*, 103(3):735–742 (2011), ISSN 09462171, doi:10.1007/s00340-011-4494-3.

[13] H. Zheng, L. Dong, X. Yin, X. Liu, H. Wu, L. Zhang, W. Ma, W. Yin and S. Jia, Ppb-level QEPAS NO2 sensor by use of electrical modulation cancellation method with a high power blue LED, *Sensors and Actuators, B: Chemical*, 208(2):173–179 (2015), ISSN 09254005, doi:10.1016/j.snb.2014.11.015, URL `http://dx.doi.org/10.1016/j.snb.2014.11.015`.

4.5 Portable NO_2 measuring device

4.5.1 Introduction

Detection systems that are based on photoacoustic spectroscopy offer the advantage of miniaturization. To fully unleash this potential of the technique, it is obvious to envisage portable measuring devices instead of solely utilize it for research purposes. With regard to recent events like the Volkswagen emission scandal in 2015 [1], in particular the development of portable NO_2 trace gas detection systems gains more and more in importance. Common measuring techniques that are applied for NO_2 monitoring base upon absorption spectroscopy (AS) or chemiluminescence. The advantages of PAS over AS were already discussed on page 27. Although chemiluminescence detectors (CLD) are widely used for NO_x trace gas detection, they still suffer from two drawbacks. Since the actual analyte in terms of CLDs is NO, NO_2 detection is based on chemical reduction of all nitrous components by means of catalytic conversion. NO_2 quantification then is achieved by comparing the resulting signal to the signal that is monitored without conversion [2]. Besides the disadvantage of being an indirect measuring technique, a further drawback of CLDs represents the fact that ozone has to be provided to the apparatus. Hence, the system has to be extended by a gas cylinder or an ozone generator.
Striving for alternative measuring instruments, this chapter deals with the transfer and downscaling of a laboratory photoacoustic setup to a portable demonstrator for NO_2 monitoring at the trace gas level. The demands on this portable device contain autonomous operation, intuitive usability and a detection limit in the single-digit ppbV domain, respectively.

4.5.2 Experimental

Besides technical requirements, the portable device was further assumed to be visually appealing and to exhibit a base area in the ballpark of a DIN A4 page ($\sim 30\,\mathrm{x}\,20$ cm). Figure 4.35 shows a concept drawing (a) as well as a picture (b) of the device, which project title was designated *black demon*.

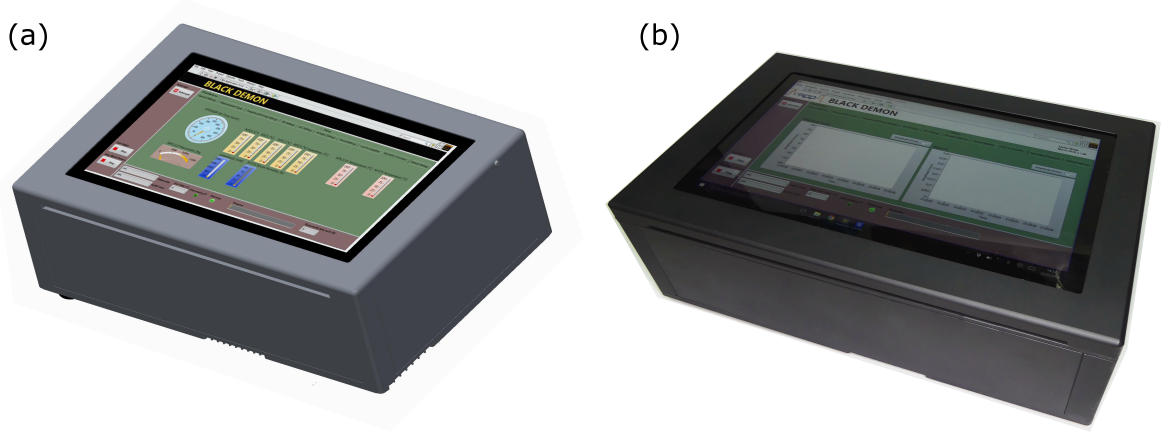

Figure 4.35: Comparison of a previous concept drawing (a) and a picture (b) of a portable NO_2 monitoring device.

The housing of the apparatus is made of black anodized aluminum and user interaction is provided by a full screen user interface (UI), as a touch sensitive 10.8-inch tablet is mounted on top of the device.* Besides tablet hardware, a second central processing unit (CPU) is located inside the demonstrator, i.e. the core element of a myRIO 1900 (National Instruments, Austin, Texas, US). All program routines are written in LabVIEW, but they are separated into a signal processing part running on the myRIO CPU and an UI part, which is executed directly on the tablet. Since the tablet is only secured magnetically and connected to the myRIO via wifi, it can easily be removed during measurement and the device can be controlled from another room in case of dangerous laboratory conditions, for example. Figure 4.36 additionally displays the interior of the device, while again the left side (a) illustrates a previous concept drawing and the right side (b) shows a picture of the completed apparatus. The measuring device comprises two gas inlets, one for non-corrosive gas compositions, e.g. air quality monitoring or known laboratory conditions, as well as an external inlet for unknown gas matrices. While unknown mixtures have to be fed by slight overpressure, non-corrosive compositions are aspirated by means of a pump (ii). Both inlets are directly connected to a filter (iv), while switching the gas stream is realized by a controllable valve (i). Whereas the external inlet is only connected to the photoacoustic cell (viii), known mixtures are pre-

*Dell Venue 11 Pro

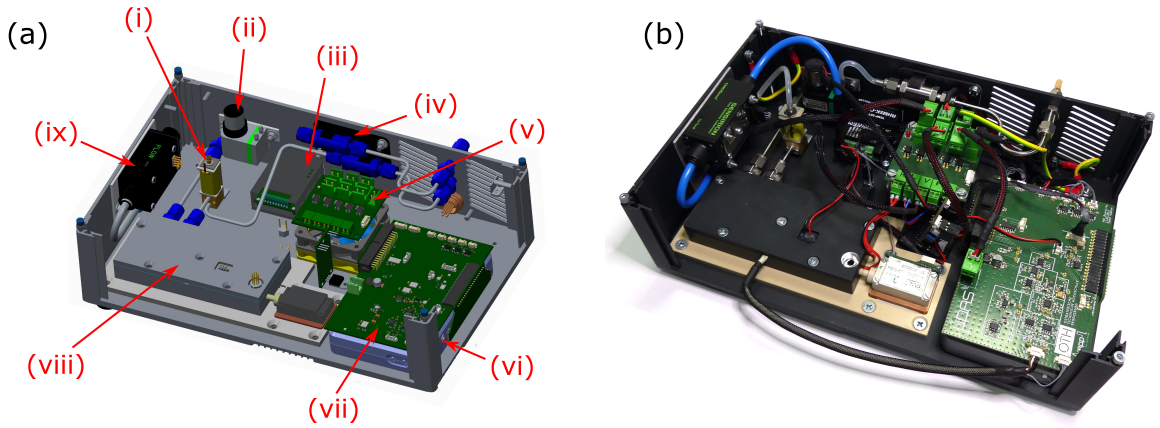

Figure 4.36: Concept drawing (a) and picture (b) of the interior of the device. (i): valve, (ii): pump, (iii): peltier controller, (iv): filter, (v): voltage supply unit, (vi): myRIO 1900, (vii): main circuit, (viii): photoacoustic cell, (ix): flow meter.

viously analyzed with regard to temperature, pressure, humidity and mass flow (ix). In either case the gas is finally supplied to an outlet after photoacoustic detection. Figure 4.36 further displays a voltage supply unit (v), a peltier controller (iii) and the myRIO (vi), which is located beneath a main circuit board (vii).

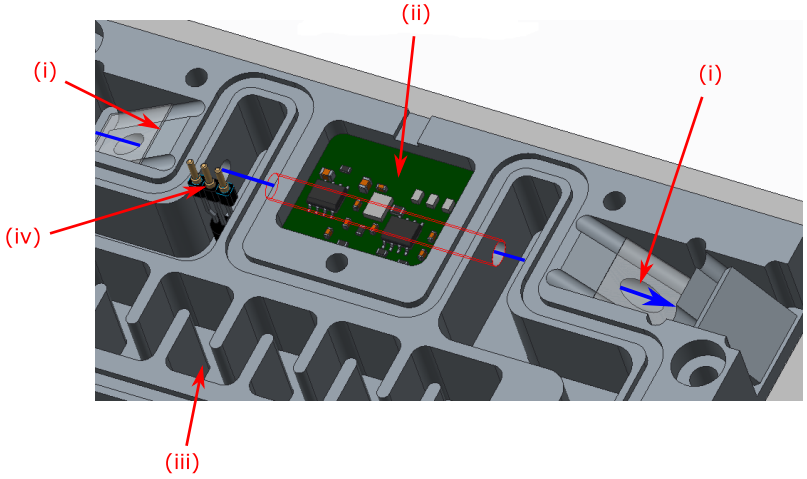

Figure 4.37: Close-up drawing of the photoacoustic measuring cell. (i): Brewster windows, (ii): preamplifier circuit board, (iii): meander structured heating zone, (iv): temperature sensor.

Figure 4.37 shows a close-up drawing of the photoacoustic measuring cell without cover. Therein, the laser beam, which is represented by a blue

arrow, from left to right passes a Brewster window (i), the resonator tube (highlighted by a red cylinder) and a second Brewster window before it is absorbed by means of a beam trap. The drawing additionally depicts a meander structured heating zone (iii) in order to ensure temperature stabilization of the gas, a temperature sensor (iv) and a preamplifier board (ii), which is located directly on top of the resonator tube. The tube is 38 mm in length and 4 mm in diameter, while the hole for acoustic coupling to the microphone is 1 mm in diameter.* The buffer volumes next to the resonator are 14 x 8 x 22 mm (height x width x length).

4.5.3 Results and discussion

As already discussed in chapter 1.3.4, lock-in amplification (LIA) has to be considered the key component of photoacoustic signal processing. With regard to the laboratory photoacoustic setup (refer to chapter 3.1), a 7225 Dual Phase DSP lock-in amplifier is utilized. In terms of transferring the setup to a portable device, software-based lock-in amplification was implemented on a field programmable gate array (FPGA) [3], which is placed at the disposal of the myRIO. More precisely, two LIA algorithms that rely on moving average (MA) and an exponential weighted moving average (EWMA) filtering [4], respectively, were compared with the reference 7225 amplifier.

Figure 4.38 provides a comparison of those lock-in approaches with regard to the particular response (a) and noise (b) characteristics. The different methods are highlighted in black (DSP 7225), red (EWMA) and blue (MA) colors. While the response times of both software implementations were found to hardly differ from the DSP lock-in, the steady state magnitudes slightly exceed the one of the reference LIA by ~ 3 %, as further signal amplification was interposed prior to digitization and processing by means of the myRIO. The mean standard deviations of the software-based LIAs were specified to $\bar{\sigma}_{\mathrm{EWMA}} = 207\ \mathrm{nV_{rms}}$ and $\bar{\sigma}_{\mathrm{MA}} = 210\ \mathrm{nV_{rms}}$. Although these values exceed the standard deviation of the reference LIA to some extend, they are still very small and therefore considered acceptable. Although MA and EWMA show comparable characteristics, MA was identified to

*For comparability an ICS-40720 MEMS microphone was utilized (refer to chapters 4.1.3 and 4.2.2).

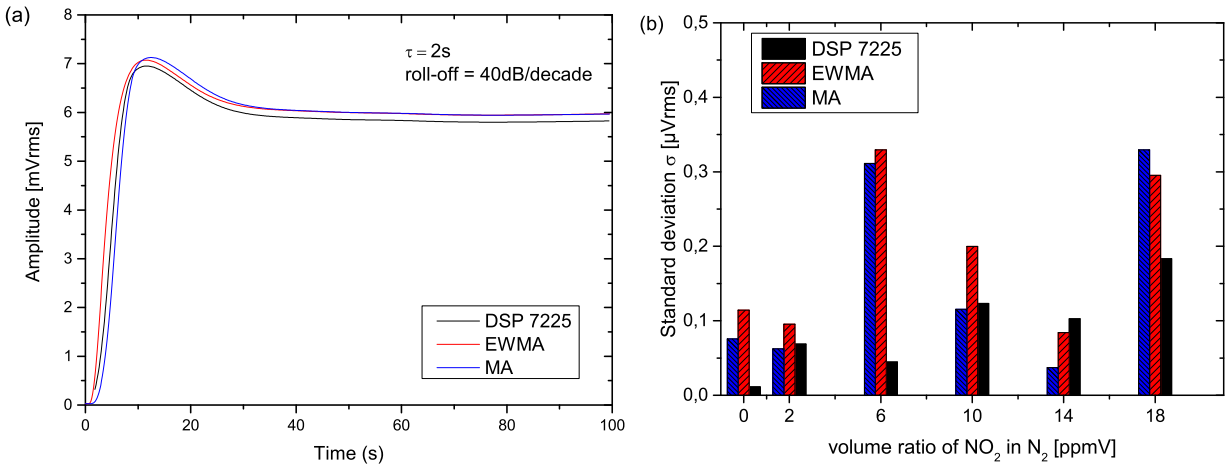

Figure 4.38: Comparison of a standalone DSP lock-in amplifier (black) with two software-based implementations that use moving average (MA, blue) and exponentially weighted moving average (EWMA, red) filter algorithms, respectively. The three approaches were compared with regard to response (a) and noise (b) characteristics.

exhibit slightly higher resource consumption. Therefore, EWMA was used for further experiments.

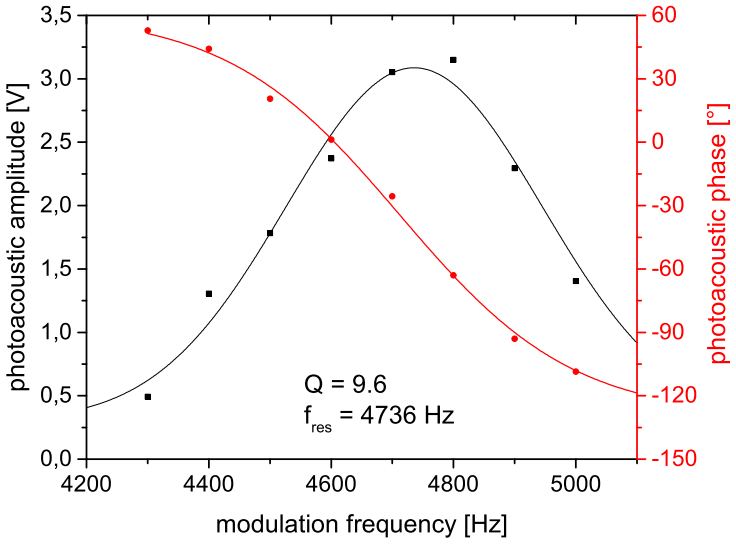

Figure 4.39: Characteristics of acoustic resonance amplification. The amplitude and the phase of the photoacoustic signal are illustrated by black squares and red diamonds, respectively.

Figure 4.39 depicts the characteristics of acoustic resonance amplification. The amplitude and the phase of the photoacoustic signal are illustrated

by black squares and red diamonds, respectively. Resonance amplification was identified to peak at a modulation frequency of 4 736 Hz,* exhibiting a quality factor of $Q = 9.6$.

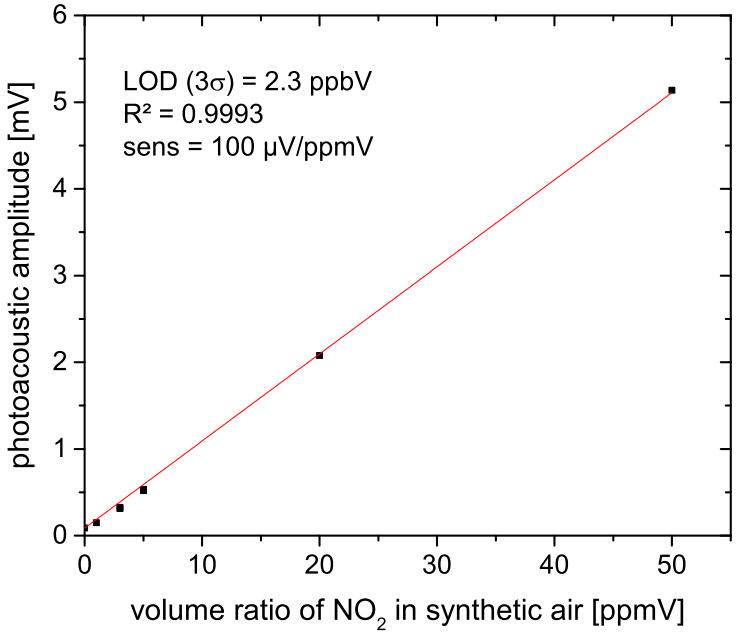

Figure 4.40: Calibration characteristics of the portable NO_2 monitoring device *black demon*.

Figure 4.40 illustrates the calibration characteristics of the portable NO_2 trace gas monitoring device *black demon*. The coefficient of determination $R^2 = 0.9993$ specifies the linear dependency of the photoacoustic amplitude on the analyte concentration. The sensitivity of the system is 100 µV/ppmV and the detection limit was determined to LOD(3σ) = 2.3 ppbV. The presented limit of detection is based on a lock-in time constant of 10 s, a roll-off of 6 dB/octave and a data acquisition averaging time of 20 s.†
Although this LOD already meets the demands on the system, which were specified in section 4.5.1, figure 4.41 additionally points out the potential of enhancement by further increasing the lock-in time constant. Thus, sub-ppbV detection is achieved by increasing the lock-in time constant to 20 s. Besides extending the lock-in integration time, increasing the optical power

*Actually, the resonance profile is obviously distorted to a certain extent. Thus detailed scanning the peak region determined the exact resonance frequency rather to be 4 765 Hz.
†This corresponds to 1 875 raw data points, as the output rate of the LIA was ∼ 93 Hz.

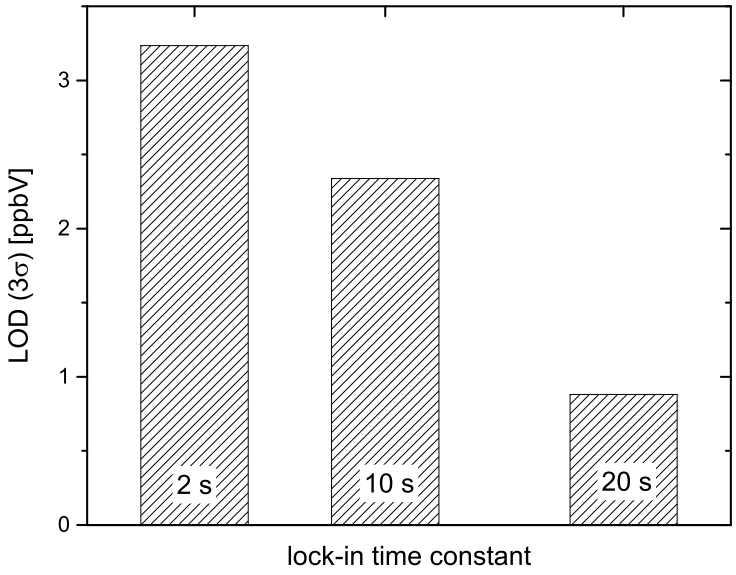

Figure 4.41: Graphical illustration of LOD enhancement by increasing the time constant of lock-in amplification.

also improves the sensitivity and in consequence the detection limit of the system. Indeed, the laser device that was installed to the apparatus incorporates three diodes of identical type, while only two of them were powered concerning the presented measurements due to heat dissipation issues. Further operating the third diode was identified to cause a sensitivity enhancement to 165 µm/ppmV, thus improving the detection limit to 1.4 ppmV (when using a lock-in time constant of 10 s).

4.5.4 Conclusion

Summing up the results of demonstrator development, photoacoustic spectroscopy was determined to be highly suitable for autonomous NO_2 trace gas monitoring within a portable device. However, the presented measuring system was meant to demonstrate the potential of downscaling, rather than to built a marketable prototype. Indeed, a second version of the device is currently being developed, which targets simultaneous monitoring of N_2O, NO_2, CH_4, C_2H_6 and C_3H_8. To this end, the existent diode laser is supplemented with a quantum cascade laser (QCL) and an interband cascade laser (ICL), which are emitting at 4.536 µm and from 3.360 µm to 3.374 µm with

an optical output power of 50 mW and 6 mW, respectively. This further development results from direct cooperation with the project partner *AVL Emission and Test Systems GmbH* (Gaggenau, Germany) and is assumed to yield further LOD improvement due to noise reduction by applying optimized electronics. Moreover, the next version of the apparatus is based on a quartz enhanced detection scheme, as this additionally provides improved immunity towards ambient noise (refer to chapter 4.3.5.3). Except for NO_2, the analytes besides are quantified by means of wavelength modulation (refer to chapter 1.1.4) in order to counteract spectral interferences to other components within the gas matrix.

References

[1] A. Thiruvengadam, M. C. Besch, P. Thiruvengadam, S. Pradhan, D. Carder, H. Kappanna, M. Gautam, A. Oshinuga, H. Hogo and M. Miyasato, Emission rates of regulated pollutants from current technology heavy-duty diesel and natural gas goods movement vehicles, *Environmental Science and Technology*, 49(8):5236–5244 (2015), ISSN 15205851, doi: 10.1021/acs.est.5b00943.

[2] J. Schmitt, *Aufbau und Erprobung eines in-situ NO/NOy-Mess-Systems am Höhenforschungsflugzeug*, Ph.D. thesis, Ludwig-Maximilians-Universität München (2003).

[3] A. Sikora, *Programmierbare Logikbauelemente: Architekturen und Anwendungen; mit 31 Tabellen* (Hanser, 2001), ISBN 9783446216075, URL `https://books.google.de/books?id=zwDxPQAACAAJ`.

[4] R. Lyons, *Understanding digital signal processing*, volume 6 (2010), ISBN 9780137027415.

4.6 Reference monitoring by mass spectrometry

4.6.1 Introduction

The development and characterization of trace component detection systems obviously requires exact knowledge about the composition of the calibration substances. Concerning the particular case of NO_2 trace gas analysis, for example, suppliers provide a minimum analyte concentration of 100 ppbV diluted in N_2 or synthetic air, while they specify a concentration tolerance of ± 10 %. Further dilution of these test gases is achieved by means of mass flow controllers (MFCs), which cause additional uncertainties regarding the final analyte concentrations.* Therefore, it is highly recommended to utilize analysis systems for reference monitoring. Aiming at gas samples of complex or unknown compositions a fortiori necessitates the use of reference systems. Since photoacoustic sensor development is to be expanded to various target components rather than only NO_2, the reference system is required to ensure trace gas quantification of a wide range of analytes. For this reason, the decision was made in favor of a gas chromatograph (GC) in tandem with a quadrupole mass spectrometer (MS).
Applying mass spectrometry for continuous trace gas analysis has already been introduced in the early 1990s, when the technique was identified to feature detection limits of just a few ppbV regarding various volatile organic compounds (VOCs) in human breath, e.g. propanol as a marker for cirrhosis of liver [1] or acetone as a marker for diabetes [2]. While the techniques were evolved in subsequent years and expanded to indoor air quality monitoring, exhaust emission monitoring, petrol vapor analysis as well as food and flavor research, they can basically be separated into two methods, which are referred to as PTR-MS (proton transfer reaction MS) [1, 3, 4] and SIFT-MS (selected ion flow tube MS) [2, 5, 6], respectively. De Gouw et al. [7] further applied preconnected separation by means of gas chromatography, thus they achieved detection limits of less than 100 pptV in spite of complex gas compositions.

*Errors resulting from F-201CV-500-RBD-11-V (Bronkhorst, Karmen, Germany) MFC usage are specified to take into account 0.8 % of the reading value and 0.2 % of the maximum value, respectively.

4.6.2 Experimental

Although PTR-MS and SIFT-MS are reported to probably be the best choice with regard to continuous trace gas reference quantification by means of mass spectrometry, a standard GC/quadrupole-MS, which is based on electron ionization, was installed to the photoacoustic laboratory setup. This decision was founded on cost and complexity reasons as well as on the fact that the manufacturer specified a detection limit (SNR = 3) of 35 ppbV NO_2 in N_2, which was assumed to meet the requirements of photoacoustic sensor referencing. More precisely, the reference system combines a Trace GC-1310 gas chromatograph and a Voyager quadrupole mass spectrometer (Thermo Fisher Scientific, Waltham, Massachusetts, US), which were modified and adapted for continuous trace gas monitoring (S+H Analytik GmbH, Mönchengladbach, Germany).

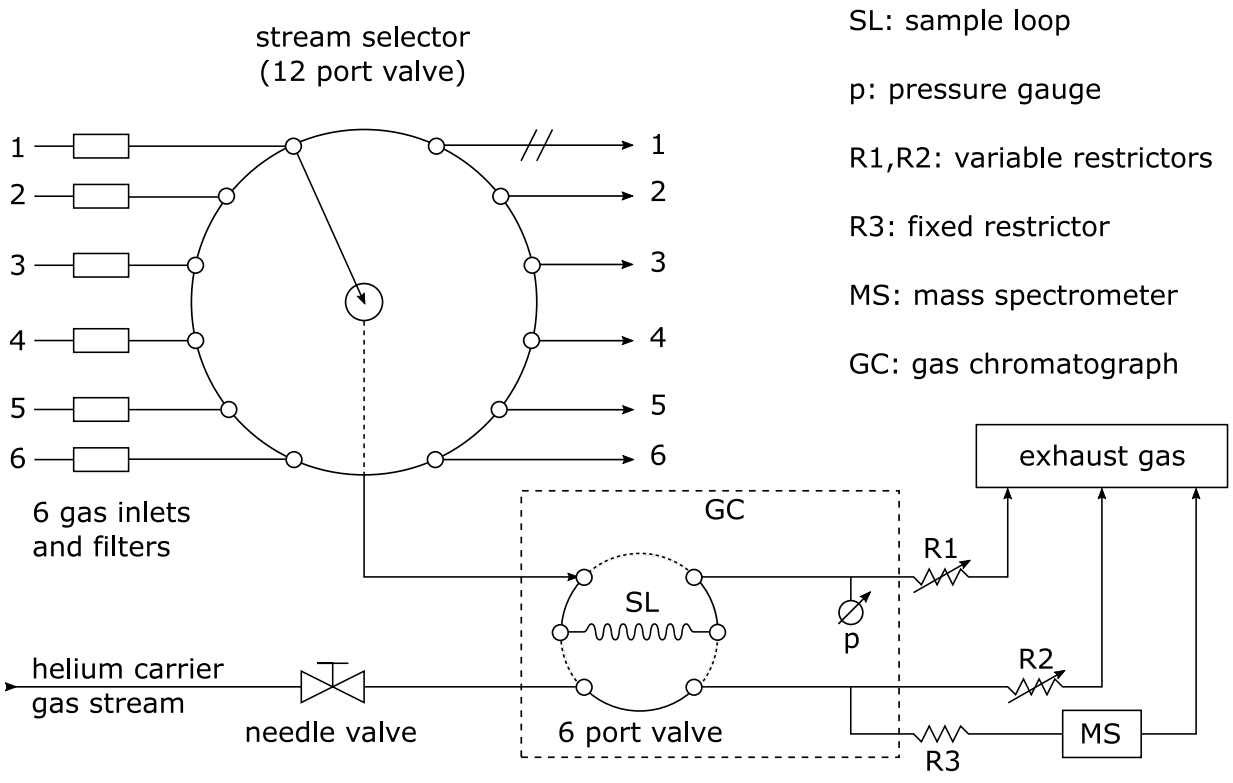

Figure 4.42: Schematic drawing that illustrates the operating principle of an installation, which combines a modified and adapted gas chromatograph and a quadrupole mass spectrometer.

Figure 4.42 displays a block diagram which illustrates the operating principle of the adapted GC/MS system. The top left of the drawing shows a twelve port valve (referred to as stream selector), which features six inlet and seven outlet ports. While one of the inlets can be linked to the seventh outlet (i.e. vertically led out at the bottom of the stream selector drawing), which in turn is connected to a six port valve, all other inputs of the stream selector are directly linked to their respective outputs. In figure 4.42, inlet stream 1, which is supplied by a gas mixing unit (refer to figure 3.2 on page 136), is linked to the six port valve, while the other inlets are provided for later implementation of calibration gases, for example. The six port valve, that is connected to the stream selector, is mounted inside the gas chromatograph for temperature control (the GC is illustrated by a dashed rectangle). This valve offers two positions which are highlighted by solid and dashed lines, respectively. The current valve position in figure 4.42, i.e. idle mode position, depicts the gas stream passing a sample loop (SL) and an adjustable restrictor R1* before it is fed into an exhaust stream. The sample loop, which has a defined volume of 2 mL, is temperature controlled by the GC, too. The pressure within the SL can be variably regulated by adjusting R1 and monitored by a pressure gauge p. During idle mode position, a second gas stream is supplied to the six port valve, namely a helium (He) carrier gas stream, which is usually set to a flow rate of 1.5 mL/min by means of a needle valve. While part of the carrier stream is directly fed into an exhaust stream, the remaining part previously enters a mass spectrometer. The split ratio of the amount, which is supplied to the MS, is defined by the ratio R2/R3 and results from R2 adjustment only, since R3 is a fixed restrictor, i.e. a heated transfer capillary of 1.1 m in length and 0.1 mm in diameter.† Thus, the amount that is fed to the MS can be reduced in terms of high analyte concentrations.
Once a measurement is started, the six port valve is switched (refer to the dashed connections) and the gas sample within the SL, that is to be analyzed, is shoved to the MS by means of the carrier gas stream. Actually, the switching time of the valve (typically $\sim 20-60$ s) has to be set with regard to the flow rate of the carrier stream, as the SL must not be completely

*represented by a mass flow controller
†inner diameter

drained. Otherwise, mixing of the sample and the carrier gas would gain influence, which in turn would cause peak distortion of the chromatogram.

4.6.3 Results and discussion

Two different program modes of the mass spectrometer software have been utilized in terms of the following studies, i.e. tune mode and selected ion monitoring mode (SIM). While tune mode allows for continuously comparing up to four different mass-to-charge (m/z) ratios, SIM mode is actually used for analyte quantification. The following two figures demonstrate tune mode operation for functional testing of the MS. These tests were carried out each time the device was put into operation.

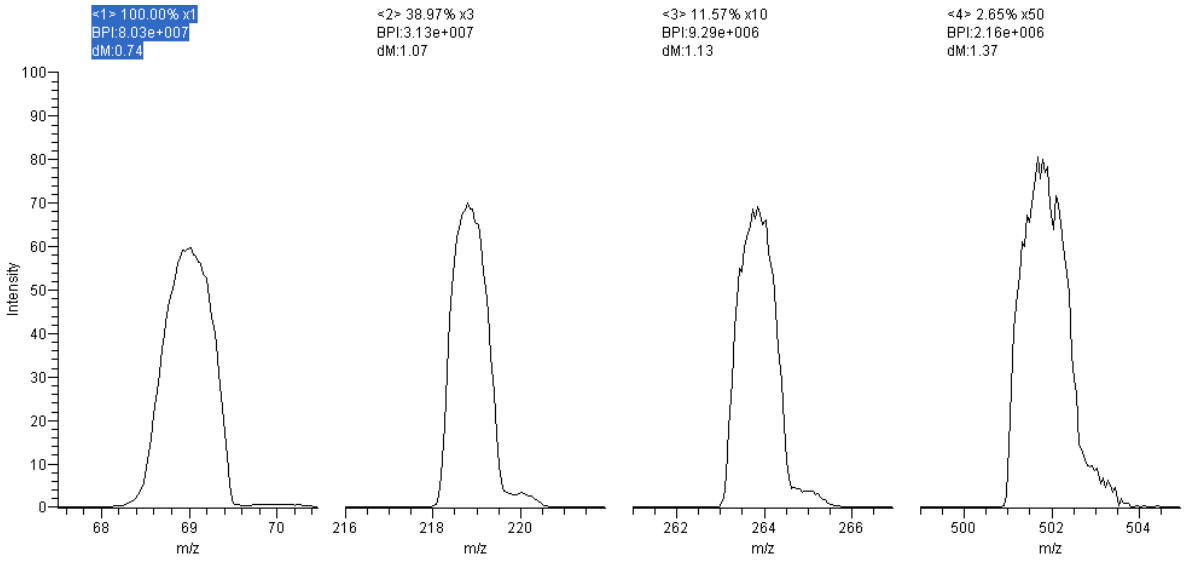

Figure 4.43: Screenshot of the MS tune mode while mass calibration testing by using the calibration substance perfluorotributylamine (PFTBA). The major peak at m/z = 69 is highlighted by a blue colored background. BPI: base peak intensity, m/z: mass-to-charge ratio.

Figure 4.43 displays a screenshot of the tune mode while checking the mass calibration of the system. For this purpose, an internal calibration substance, namely perfluorotributylamine (PFTBA)*, was supplied to the MS. PFTBA is used as a reference, because it is known to decompose in a highly repeatable pattern. In order to check mass calibration, the detector signals

*sometimes also referred to as FC43

emerging at m/z: 69, 219, 264 and 502 are compared to each other. Mass calibration is considered valid, if the peak value at 219 is about one-half as large as the peak value at 69 and if the one at 502 is about 2-5 % of the peak value at 69, respectively [8]. Regarding figure 4.43, the corresponding ratios were calculated from the given base peak intensities (BPI). These calculations yielded values of 0.39 for m/z(219) : m/z(69) and of 0.03 for m/z(502) : m/z(69), which were assumed to satisfy proper mass calibration.

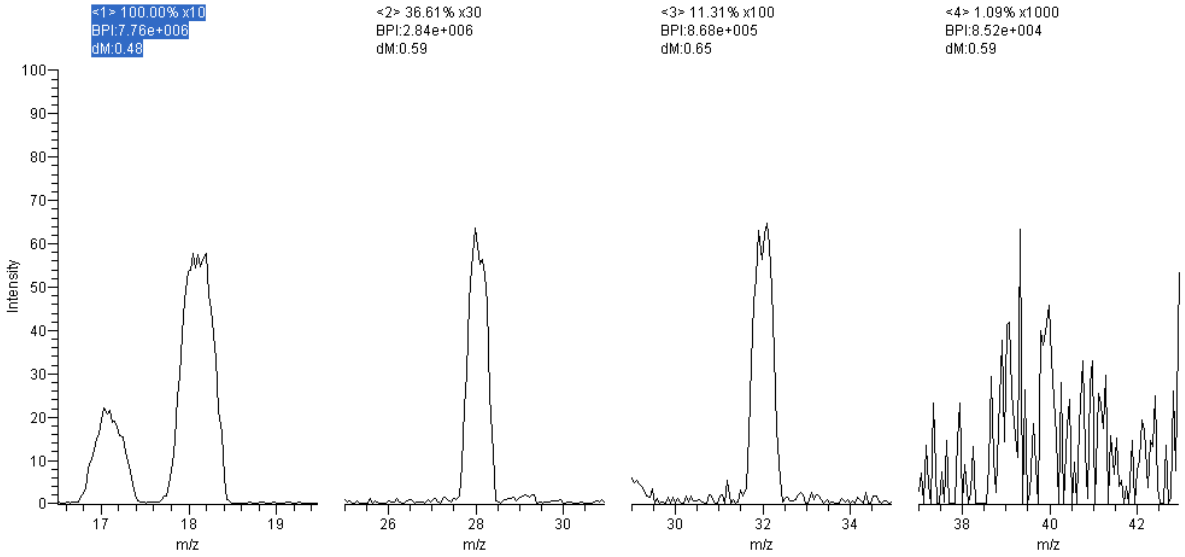

Figure 4.44: Screenshot of the MS tune mode while leak testing by comparing m/z: 18 (H_2O), 28 (N_2), 32 (O_2) and 40 (Ar). The major peak at m/z = 18 is highlighted by a blue colored background. BPI: base peak intensity, m/z: mass-to-charge ratio.

Figure 4.44 again shows a tune mode screenshot while comparing m/z: 18 (H_2O), 28 (N_2), 32 (O_2) and 40 (Ar) in terms of leak testing. As long as the peak value of H_2O exceeds (or at least is on same scale as) the peak value resulting from nitrogen, the system can be stated leak-free. With regard to figure 4.44, the H_2O peak was calculated to be 2.7 times as large as the N_2 peak, thus the system is considered free from air leaks.
Since early quantitative measurements in SIM mode indicated a significantly inferior performance than specified by the manufacturer, the method of LOD calculation, that was applied by *S+H Anlaytik GmbH*, was repeated. In this context a calibration gas containing 20 ppmV NO_2 in synthetic air

(79 % N_2, 21 % O_2) was supplied to the system, while the m/z-range was monitored from 45.5 to 46.5.*

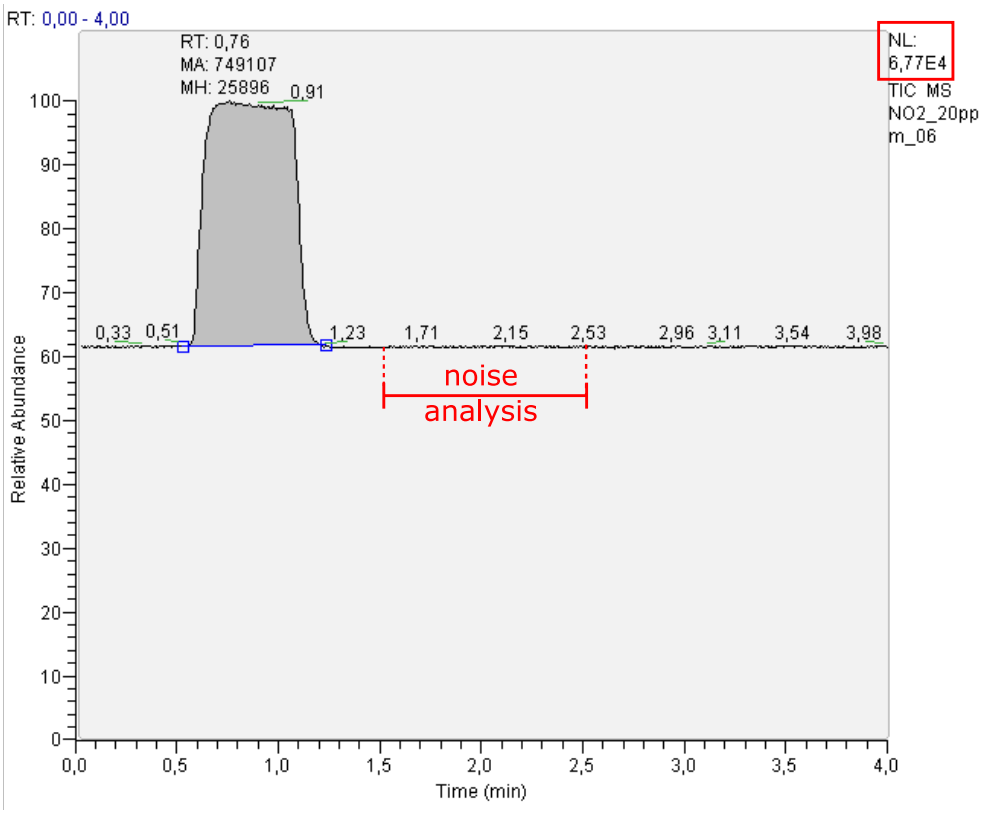

Figure 4.45: Screenshot of a chromatogram resulting from SIM mode operation. The signal peak emerging at a retention time (RT) of 0.51 min corresponds to 20 ppmV NO_2 in synthetic air. MA: manually integrated peak area, MH: manually integrated peak height, NL: normalization level, TIC: total ion current.

Figure 4.45 depicts the resulting chromatogram with a signal peak emerging at a retention time (RT) of 0.51 min, while the width of the peak corresponds to the switching time of the valve. More precisely, the abscissa of the chromatogram shows the relative abundance that is normalized to the maximum total ion current (TIC) of the signal peak. The corresponding normalization level (NL), which is framed by a red rectangle (top right), was specified to $6.77 \cdot 10^{-4}$. The drawing further depicts a red horizontal line (center) which highlights the time window for noise analysis.

*Pressure and temperature of the sample loop were set to 500 mbar and 80 °C, while the switching time of the six port valve (refer to figure 4.42) was adjusted to 43 s.

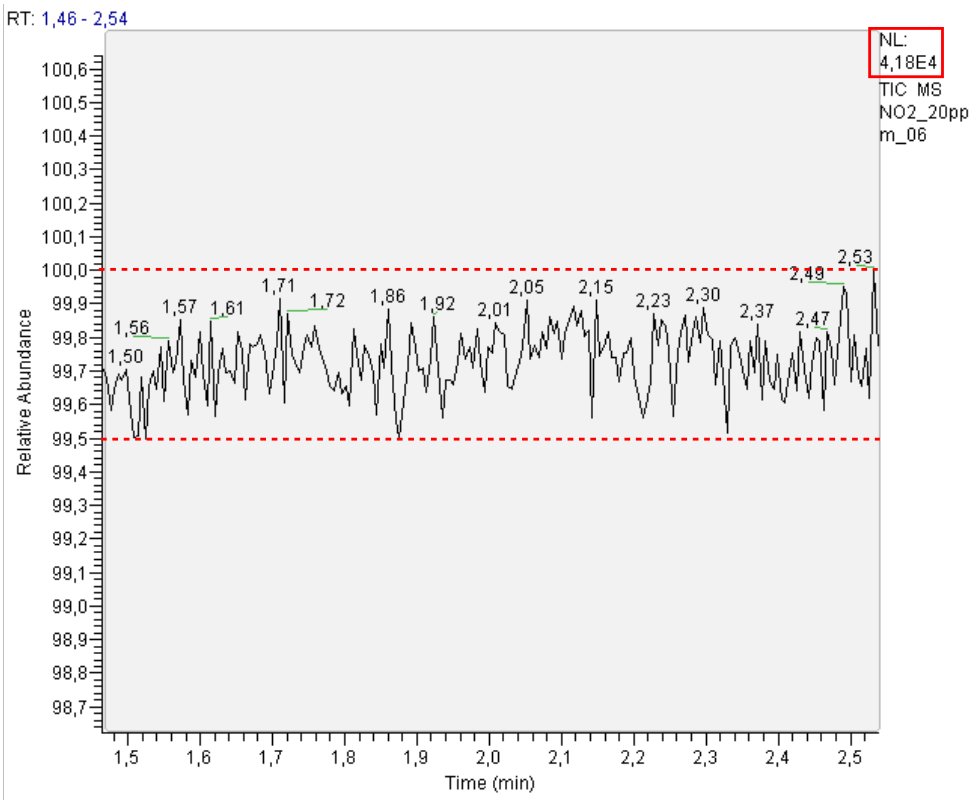

Figure 4.46: Close-up of the chromatogram represented by figure 4.45 for background noise analysis within a retention time window ranging from ∼ 1.5 to 2.5 min.

Figure 4.46 shows a close-up of the baseline within a retention time window ranging from ∼ 1.5 to 2.5 min. While the normalization level is highlighted by a red rectangle again, the dashed horizontal lines visualize the total noise amplitude, which was identified to constitute ∼ 0.5 % of the NL. Thus the signal-to-noise ratio was calculated to

$$\mathrm{SNR} = \frac{6.77 \cdot 10^4}{0.005 \cdot 4.18 \cdot 10^4} = 324 \tag{4.5}$$

which results in a hypothetical detection limit (SNR = 3) of 185 ppbV for NO_2 diluted in synthetic air. The worsening by a factor of ∼ 5 compared to the detection limit specified by the manufacturer might be due to using synthetic air instead of N_2 as dilution medium or due to differing system parameters. However, further experiments revealed signal peaks resulting from pure synthetic air to be comparable to the one that is observed for a gas composition of 20 ppmV NO_2 in synthetic air (refer to figure 4.45).

Actually, the above presented method of detection limit determination, that was performed on the lines of the manufacturer specifications, simply has to be considered wrong from an analytical point of view. Since equation 4.5 is related to the noise level of the He carrier gas stream only, the calculated detection limit is assumed to specify the minimum detectable concentration of synthetic air* in He rather than of NO_2 in synthetic air. This findings were validated by investigating several NO_x species in tune mode, namely m/z = 30 (NO), 44 (N_2O), 46 (NO_2) and 92 (N_2O_4), while 200 ppmV NO_2 in synthetic air were supplied to the MS.

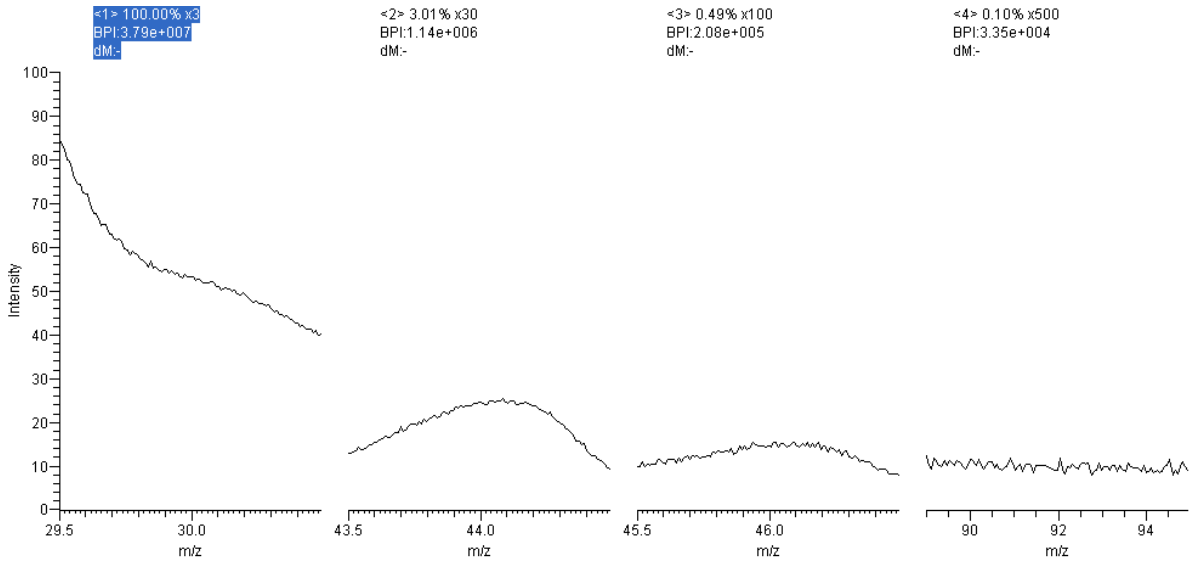

Figure 4.47: Screenshot of the MS tune mode while NO_x examination by comparing m/z: 30 (NO), 44 (N_2), 46 (NO_2O) and 92 (N_2O_4). The major peak at m/z = 30 is highlighted by a blue colored background. BPI: base peak intensity, m/z: mass-to-charge ratio.

Without going into detail about other peak emergences, the actual molecule peak of the analyte species NO_2 was identified to hardly stand out against the background signal. Moreover, a similar experiment was repeated on the basis of a test gas containing 100 ppmV NO_2 in N_2, which revealed no peak emergence at m/z = 46 at all.
In order to nevertheless determine the actual limits of the system, an optimized method of data acquisition and signal processing was established. For this purpose, a second m/z-window was monitored simultaneously whilst

*containing a relative volume ratio of 20 ppmV NO_2

SIM mode quantification of the analyte. This reference m/z should, in the ideal case, have the same background level as the analyte peak, still the background level must not depend on the analyte concentration. In terms of signal processing, the peak emergence resulting from reference monitoring can be subtracted from the actual signal peak, thus yielding a background compensated chromatogram. With regard to NO_2 detection, mass-to-charge ratios of 46 and 47 were selected for analyte and reference monitoring, respectively, while the monitoring window was set to $\Delta m/z = \pm 0.4$ in both cases. Each measuring cycle was repeated five times, while the first two peaks were disregarded in terms of quantification in order to ensure steady-state analyte concentration within the transfer capillary. The switching time of the six port valve (refer to figure 4.42) was set to 30 s.

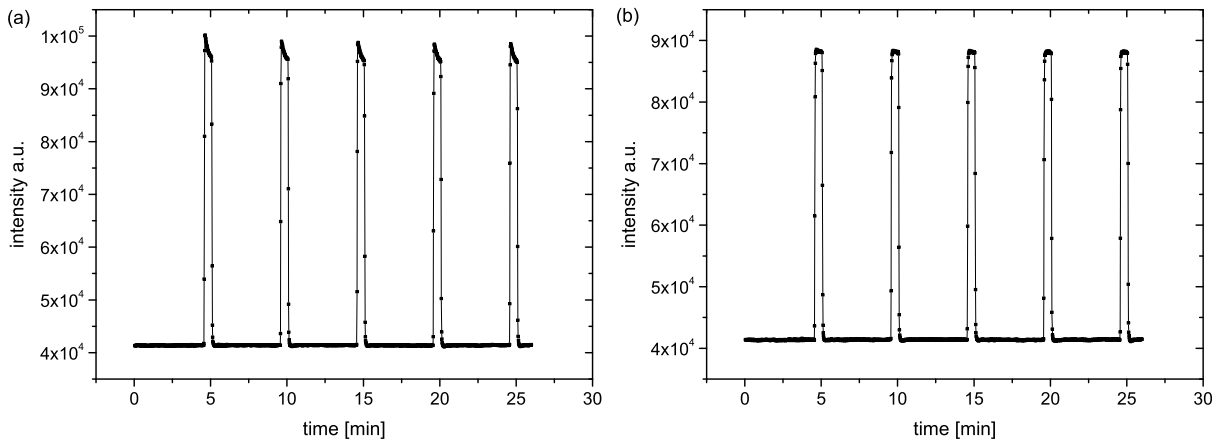

Figure 4.48: Raw data chromatograms prior to peak area subtraction at the example of 20 ppmV NO_2 in N_2 (a) and pure nitrogen (b), respectively.

Figure 4.48 depicts the raw data signals of 20 ppmV NO_2 containing samples (a) and pure nitrogen (b) prior to peak area subtraction. In both cases the overall baseline whilst carrier gas flow was identified to $4.2 \cdot 10^4$ and the peak heights were determined to $1.0 \cdot 10^5$ and $8.8 \cdot 10^4$ in the presence and in the absence of the analyte, respectively.
Figure 4.49 finally represents the signal peaks that remain after peak area subtraction. This background compensated chromatogram obviously reveals overcompensation regarding the first two values and the last two values of every signal peak, which may be caused by slightly differing retention times of the raw data signals. This overcompensation could easily be

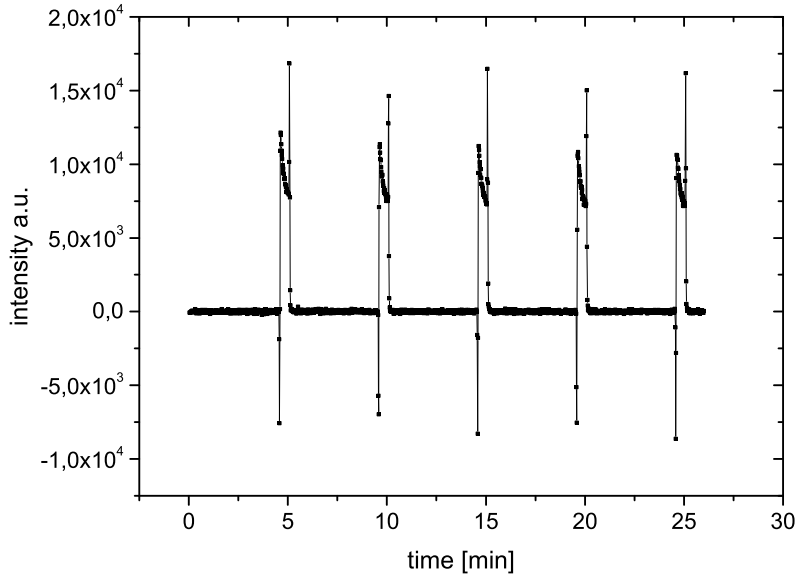

Figure 4.49: Background compensated chromatogram. The peak emergences result from 20 ppmV NO_2.

remedied by disregarding the concerning measuring points. However, over-compensation was not considered in terms of further evaluation, as it only affects the peak heights, while the peak areas were used for LOD calculation.

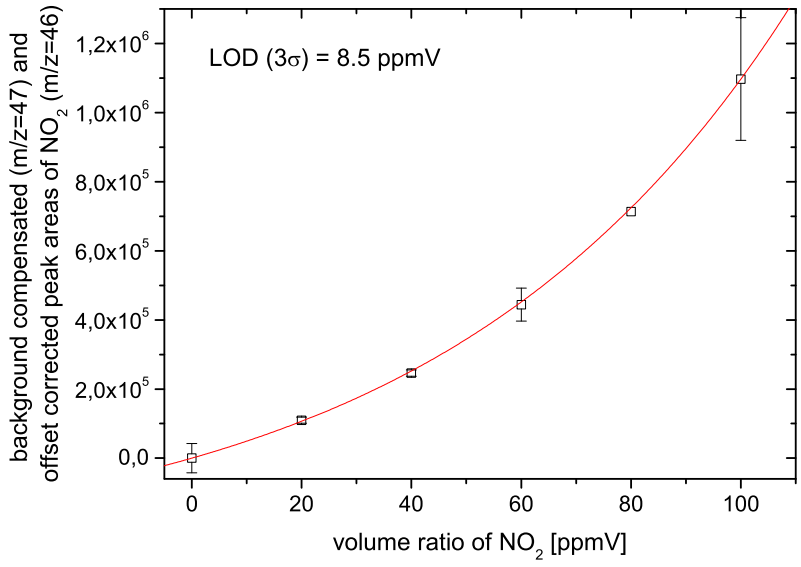

Figure 4.50: Calibration characteristics of an optimized method for the detection of NO_2 in N_2 by means of mass spectrometry.

Figure 4.50 displays the calibration characteristics of an optimized method for the detection of NO_2 in N_2 by means of mass spectrometry. Besides N_2 compensation, the measuring points were offset corrected with respect to pure nitrogen, thus the fit curve was fixed to the origin of the coordinate system. While the error bars depict $\pm 3\sigma$, the measuring point at 80 ppmV NO_2 represents a single measurement, as two of three signals in the chromatogram had to be regarded as outliers. The concentration series reveals an exponential growth dependency and the detection limit (3σ) was determined to 8.5 ppmV NO_2 in N_2.
Besides NO_2 detection, similar studies were performed with regard to the quantification of CO_2 in synthetic air. In this context mass-to-charge ratios of 44 and 46 were selected for analyte and reference monitoring, respectively, while the monitoring window was reduced to $\Delta m/z = \pm 0.2$ in both cases. The test gas was specified to contain a volume ratio of 9 700 ppmV CO_2.

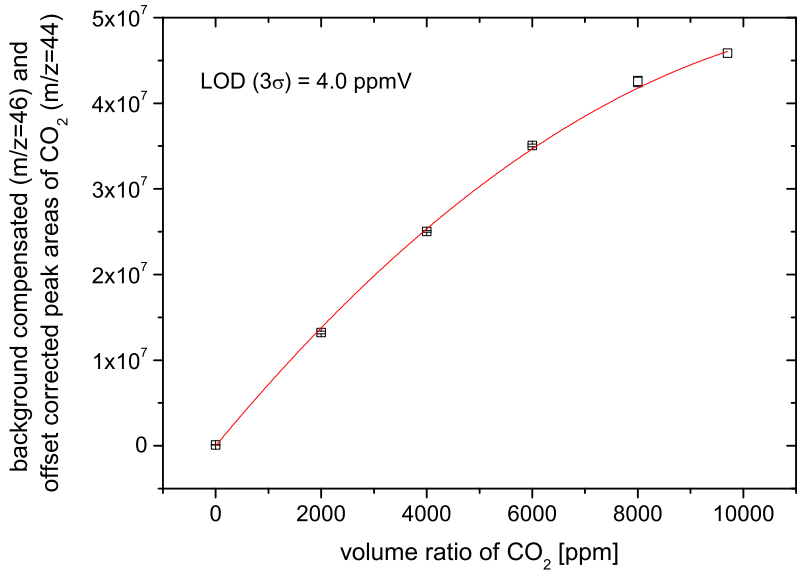

Figure 4.51: Calibration characteristics of an optimized method for the detection of CO_2 in synthetic air by means of mass spectrometry.

By analogy with figure 4.50, figure 4.51 shows the calibration characteristics of CO_2 quantification. The detection limit (3σ) was specified to 4.0 ppmV CO_2 in synthetic air. The signal dependency on the analyte concentration was again determined to be non-linear, but inversely to NO_2 detection.

4.6.4 Conclusion

The non-linearities regarding figures 4.50 and 4.51 are assumed to result from background compensation rather than from intrinsic characteristics of the MS system. However, both non-linearities should be interpreted with caution, as completely different concentration ranges were investigated. These concentration ranges or, more precisely, the corresponding signal ranges also have to be considered in order to avoid putative misinterpretation of better accuracy in terms of CO_2 detection compared to NO_2 detection. In fact, 11 % of the measuring points had to be regarded as outliers in terms of NO_2 detection and 30 % with regard to CO_2 quantification. Although optimization yielded an enhancement of the detection limit by a factor of ~ 20, the GC/MS system does not meet the requirements of trace gas referencing, as the detection limits of photoacoustic applications were determined still to be 3–4 orders of magnitude lower (refer to figures 4.7, 4.13, 4.21 and 4.40). Moreover, recording one measuring point for a given analyte concentration takes almost thirty minutes followed by signal processing, thus the presented method can hardly be referred to as continuous. In view of developing photoacoustic multi-component sensors, however, the GC/MS system is considered a comprehensive tool in order to investigate interferences and cross-sensitivities.

References

[1] W. Lindinger, J. Hirber and H. Paretzke, An ion/molecule-reaction mass spectrometer used for on-line trace gas analysis, *International Journal of Mass Spectrometry and Ion Processes*, 129(C):79–88 (1993), ISSN 01681176, doi:10.1016/0168-1176(93)87031-M.

[2] D. Smith and P. Spanel, The novel selected-ion flow tube approach to trace gas analysis of air and breath, *Rapid Communications in Mass Spectrometry*, 10(10):1183–1198 (1996), ISSN 09514198, doi:10.1002/(SICI)1097-0231(19960731)10:10⟨1183::AID-RCM641⟩3.0.CO;2-3.

[3] A. Hansel, W. Lindinger and A. Jordan, Proton transfer reaction mass spectrometry: on-line trace gas analysis at the ppb level, *Chemical Society Reviews*, 27(5):347–354 (1998).

[4] W. Lindinger, A. Hansel and A. Jordan, Proton-transfer-reaction mass spectrometry (PTR-MS): on-line monitoring of volatile organic compounds at pptv levels, *Chemical Society Reviews*, 27:347–375 (1998), ISSN 0306-0012, doi:10.1039/a827347z.

[5] D. Smith and P. Spanel, Selected ion flow tube mass spectrometry (SIFT-MS) for on-line trace gas analysis, *Mass Spectrometry Reviews*, 24(5):661–700 (2005), ISSN 02777037, doi: 10.1002/mas.20033.

[6] P. Španěl, K. Dryahina and D. Smith, A general method for the calculation of absolute trace gas concentrations in air and breath from selected ion flow tube mass spectrometry data, *International Journal of Mass Spectrometry*, 249-250:230–239 (2006), ISSN 13873806, doi:10.1016/j.ijms.2005.12.024.

[7] J. De Gouw, C. Warneke, T. Karl, G. Eerdekens, C. Van der Veen and R. Fall, Sensitivity and specificity of atmospheric trace gas detection by proton-transfer-reaction mass spectrometry, *International Journal of Mass Spectrometry*, 223-224:365–382 (2003), ISSN 13873806, doi: 10.1016/S1387-3806(02)00926-0.

[8] M. C. McMaster, *GC/MS: A Practical User's Guide: Second Edition* (2007), ISBN 9780470101636, doi:10.1002/9780470228357.

Chapter 5

Summary

This thesis provides a detailed theoretical discussion about common absorption spectroscopy (AS) and, in particular, about photoacoustic spectroscopy (PAS). The physical concepts of signal generation are illustrated in view of amplitude modulation (AM) and wavelength modulation (WM). Furthermore the advantages and disadvantages of the techniques are presented. As a result, PAS was identified to outclass AS, thus it turned out to be the method of choice in view of developing a miniaturized trace gas sensing application. The theoretical part of this work further outlines various approaches of signal enhancement, e.g. by acoustic and/or mechanical resonance amplification. Besides, several phenomena of signal attenuation are addressed, e.g. acoustic detuning, vibrational-translational (VT) relaxation and vibrational-vibrational (VV) energy transfer processes, which have to be considered with regard to the individual measuring conditions. Simulation and experimental chapters illustrate the pre-development and the practical implementation of a laboratory photoacoustic setup, a portable trace gas monitoring device and various photoacoustic cell (PAC) designs. These include a conventional bulky design, an optimized low-cost 3D printed PAC, a miniaturized quartz enhanced photoacoustic spectroscopic (QEPAS) scheme and a further integrated microelectromechanical system (MEMS) based sensor chip, respectively. Although several parts of this thesis also provide preparatory work for multi-component analysis, nitrogen dioxide (NO_2) was used as primary analyte in order to characterize the above mentioned photoacoustic cell designs. This involves acoustic resonance and noise analysis, determination of optimal operating parameters (e.g. gas flow rate

and lock-in time constant), performance evaluation (e.g. response behavior, optical performance, calibration characteristics and long-term signal stability) as well as interference studies towards oxygen (O_2), carbon dioxide (CO_2), humidity (H_2O) and acoustic noise. In conclusion, NO_2 detection by means of the low-cost 3D printed PAC and the QEPAS configuration even revealed two world record detection limits (1σ) of 33 pptV and 600 pptV, respectively.

Chapter 6

Zusammenfassung in deutscher Sprache

Die vorliegende Arbeit präsentiert eine detaillierte Beschreibung des Messprinzips der Absorptionsspektroskopie (AS) und im Speziellen der photoakustischen Spektroskopie (PAS). Die Vor- und Nachteile beider Prinzipien werden sowohl auf Grundlage der Amplitudenmodulation (AM) als auch der Wellenlängenmodulation (WM) herausgearbeitet. Darüber hinaus werden mögliche Ansätze zur Signaloptimierung (z. B. durch akustische oder mechanische Resonanzverstärkung) sowie Ursachen potentieller Signalverluste erörtert. Letztere beruhen auf akustischer Resonanzverschiebung auf Grund von Änderungen der Schallgeschwindigkeit, langsamen Vibrations–Translations (VT) Relaxationszeiten oder Vibrations–Vibrations (VV) Energietransferprozessen, wodurch dem System ein Teil der Energie entzogen wird und auf andere Molekülspezies übertragen wird. Im Hinblick auf die Implementierung einiger Konzepte (z. B. Messzellengeometrien) wurden verschiedene Entwicklungschritte bereits im Vorfeld berechnet bzw. simuliert. Die praktische Umsetzung wird dem Leser im jeweiligen experimentellen Teil der Arbeit erläutert. Diese beinhalten zum einen die Entwicklung eines photoakustischen Labormessplatzes inklusive der entsprechenden Einzelkomponenten (z. B. durchstimmbares Lasersystem, Gasmischanlage, photoakustischer Aufbau, Referenzsystem) und behandeln zum anderen auch Details zur sukzessiven Weiterentwicklung von vier unterschiedlichen photoakustischen Meszellentypen. Die optimalen Dimensionen und Betriebsparameter wurden auf Grundlage einer klassischen, aus

massivem Edelstahl gefertigten Messzelle evaluiert und in einer zweiten, optimierten Version umgesetzt. Zur Miniaturisierung des Gesamtsystems wurden zwei weitere Messzellendesigns konstruiert, wovon das erste auf der bekannten QEPAS (quartz enhanced photoacoustic spectroscopy) Messanordnung beruht. Die Weiterentwicklung hingegen wurde eigens konzipiert und zeichnet sich durch einen hohen Grad an Integration aus, da sie auf Basis von MEMS (microelectromechanical system) Prozesstechnologien auf Chip-Ebene realisiert wird. Obwohl in verschiedenen Kapiteln bereits vorbereitende Arbeitsschritte für eine zukünftige Multikomponentenmessung vorgestellt werden, wird für die Charakterisierung aller oben genannter Messzellentypen ausschließlich der Analyt Stickstoffdioxid (NO_2) genutzt. Im Rahmen entsprechender Messreihen erfolgte die Evaluation von akustischer Resonanzverstärkung, Zusammensetzung des Rauschpegels, einigen optimalen Betriebsparametern (z. B. Massendurchfluss, Lock-In Zeitkonstante), systemspezifischen Leistungscharakteristika (Ansprechverhalten, Einfluss der Lichtleistung, Kalibrierkurven, Langzeitstabilität) sowie Querempfindlichkeiten gegenüber Sauerstoff (O_2), Kohlenstoffdioxid (CO_2), Feuchte (H_2O) und Störgeräuschen in der Umgebung. Als Resultat dieser umfangreichen Studien konnten die Detektionslimits (1σ) zu 33 pptV für das optmierte klassische Messzellendesign und zu 600 pptV hinsichtlich der QEPAS Messanordnung bestimmt werden. Diese Ergebnisse übertreffen sowohl in Bezug auf klassische als auch in Bezug auf miniaturisierte photoakustische NO_2 Quantifizierung alle bisher publizierten Detektionslimits.

Chapter 7

Appendix

Table 7.1: List of several absorption cross sections σ regarding the analytes NO, NO_2, CO, CO_2, NH_3 and CH_4. The σ values were calculated from the HITRAN database.

Analyte species	Wavenumber [cm^{-1}]	Wavelength [μm]	Absorption cross section [cm^2]
NO	5 516	1.813	$1.73 \cdot 10^{-24}$
	5 568	1.796	$4.41 \cdot 10^{-24}$
NO_2	1 603	6.24	$1.96 \cdot 10^{-20}$
	1 629	6.13	$8.16 \cdot 10^{-20}$
CO	2 116	4.726	$2.61 \cdot 10^{-20}$
	2 171	4.606	$1.37 \cdot 10^{-21}$
	4 232	2.363	$2.62 \cdot 10^{-22}$
	4 288	2.332	$3.77 \cdot 10^{-22}$
CO_2	2 336	4.280	$3.25 \cdot 10^{-18}$
	2 361	4.240	$1.85 \cdot 10^{-18}$
	3 272	3.065	$5.58 \cdot 10^{-20}$
	4 865	2.055	$1.18 \cdot 10^{-22}$
	4 964	2.015	$5.07 \cdot 10^{-23}$
	4 989	2.004	$1.26 \cdot 10^{-22}$
	5 087	1.966	$1.65 \cdot 10^{-23}$
	5 111	1.957	$5.69 \cdot 10^{-23}$
	6 360	1.572	$3.15 \cdot 10^{-23}$
	6 958	1.437	$3.26 \cdot 10^{-23}$
	6 983	1.432	$1.22 \cdot 10^{-22}$
NH_3	1 041	9.606	$1.73 \cdot 10^{-21}$
	1 650	6.061	$4.15 \cdot 10^{-21}$
	3 361	2.975	$7.33 \cdot 10^{-23}$
	4 382	2.282	$6.63 \cdot 10^{-22}$
	4 485	2.230	$9.95 \cdot 10^{-22}$
	5 094	1.963	$9.58 \cdot 10^{-21}$
CH_4	2 980	3.356	$1.27 \cdot 10^{-21}$
	3 018	3.313	$3.61 \cdot 10^{-20}$
	3 067	3.261	$4.04 \cdot 10^{-20}$

```
Original HITRAN04(R) Database values for the selected spectral line
-------------------------------------------------------------------
Database line:                504960
Molecule number:              10   (NO2)
Isotopologue number:          1    (646)
Natural abundance:            99.16160000%     Molecular weight: 45.99290400 g/mol
Transition frequency:         2889.003759      [cm-1]
Line intensity (S):           3.170e-021       [cm/molecule] @296K
Einstein A-coefficient:       2.680e+001       [s-1]
Air broadened width:          0.0766           [cm-1 atm-1] Half width @ 296K
Self broadened width:         0.0950           [cm-1 atm-1] Half width @ 296K
Lower state energy:           235.5508         [cm-1]
T dependence of air width:    0.73
Pressure shift:               -0.002390        [cm-1 atm-1] @296K
Upper vibrational quanta :              1 0 1
Lower vibrational quanta:               0 0 0
Upper local quanta:            15  4 11 15.5+
Lower local quanta:            16  4 12 16.5+
Error codes:                  465233
Reference codes:              11 7 3 2 2 1.
Flag for line mixing:
Upper statistical weight:     32.0
Lower statistical weight:     34.0
```

Figure 7.1: Absorption line 1/6 that constitutes the NO_2 absorption profile at 3 461.43 nm.

```
Original HITRAN04(R) Database values for the selected spectral line
-------------------------------------------------------------------
Database line:                504958
Molecule number:              10   (NO2)
Isotopologue number:          1    (646)
Natural abundance:            99.16160000%     Molecular weight: 45.99290400 g/mol
Transition frequency:         2888.998401      [cm-1]
Line intensity (S):           2.975e-021       [cm/molecule] @296K
Einstein A-coefficient:       2.682e+001       [s-1]
Air broadened width:          0.0766           [cm-1 atm-1] Half width @ 296K
Self broadened width:         0.0950           [cm-1 atm-1] Half width @ 296K
Lower state energy:           235.4183         [cm-1]
T dependence of air width:    0.73
Pressure shift:               -0.002390        [cm-1 atm-1] @296K
Upper vibrational quanta :              1 0 1
Lower vibrational quanta:               0 0 0
Upper local quanta:            15  4 11 14.5-
Lower local quanta:            16  4 12 15.5-
Error codes:                  465233
Reference codes:              11 7 3 2 2 1.
Flag for line mixing:
Upper statistical weight:     30.0
Lower statistical weight:     32.0
```

Figure 7.2: Absorption line 2/6 that constitutes the NO_2 absorption profile at 3 461.43 nm.

```
Original HITRAN04(R) Database values for the selected spectral line
-------------------------------------------------------------------
Database line:                504956
Molecule number:              10   (NO2)
Isotopologue number:          1    (646)
Natural abundance:            99.16160000%     Molecular weight: 45.99290400 g/mol
Transition frequency:         2888.992311      [cm-1]
Line intensity (S):           4.187e-021       [cm/molecule] @296K
Einstein A-coefficient:       2.766e+001       [s-1]
Air broadened width:          0.0751           [cm-1 atm-1] Half width @ 296K
Self broadened width:         0.0950           [cm-1 atm-1] Half width @ 296K
Lower state energy:           197.2414         [cm-1]
T dependence of air width:    0.73
Pressure shift:               -0.003190        [cm-1 atm-1] @296K
Upper vibrational quanta :              1 0 1
Lower vibrational quanta:               0 0 0
Upper local quanta:            16   3 14 16.5+
Lower local quanta:            17   3 15 17.5+
Error codes:                  465233
Reference codes:              11 7 3 2 2 1.
Flag for line mixing:
Upper statistical weight:     34.0
Lower statistical weight:     36.0
```

Figure 7.3: Absorption line 3/6 that constitutes the NO_2 absorption profile at 3 461.43 nm.

```
Original HITRAN04(R) Database values for the selected spectral line
-------------------------------------------------------------------
Database line:                504955
Molecule number:              10   (NO2)
Isotopologue number:          1    (646)
Natural abundance:            99.16160000%     Molecular weight: 45.99290400 g/mol
Transition frequency:         2888.989925      [cm-1]
Line intensity (S):           3.945e-021       [cm/molecule] @296K
Einstein A-coefficient:       2.768e+001       [s-1]
Air broadened width:          0.0751           [cm-1 atm-1] Half width @ 296K
Self broadened width:         0.0950           [cm-1 atm-1] Half width @ 296K
Lower state energy:           197.1834         [cm-1]
T dependence of air width:    0.73
Pressure shift:               -0.003190        [cm-1 atm-1] @296K
Upper vibrational quanta :              1 0 1
Lower vibrational quanta:               0 0 0
Upper local quanta:            16   3 14 15.5-
Lower local quanta:            17   3 15 16.5-
Error codes:                  465233
Reference codes:              11 7 3 2 2 1.
Flag for line mixing:
Upper statistical weight:     32.0
Lower statistical weight:     34.0
```

Figure 7.4: Absorption line 4/6 that constitutes the NO_2 absorption profile at 3 461.43 nm.

```
Original HITRAN04(R) Database values for the selected spectral line
-------------------------------------------------------------------
Database line:                504949
Molecule number:              10   (NO2)
Isotopologue number:          1    (646)
Natural abundance:            99.16160000%     Molecular weight: 45.99290400 g/mol
Transition frequency:         2888.959118      [cm-1]
Line intensity (S):           5.674e-021       [cm/molecule] @296K
Einstein A-coefficient:       2.866e+001       [s-1]
Air broadened width:          0.0729           [cm-1 atm-1] Half width @ 296K
Self broadened width:         0.0950           [cm-1 atm-1] Half width @ 296K
Lower state energy:           153.8158         [cm-1]
T dependence of air width:    0.73
Pressure shift:               -0.004080        [cm-1 atm-1] @296K
Upper vibrational quanta :              1 0 1
Lower vibrational quanta:               0 0 0
Upper local quanta:            17  1 16 17.5+
Lower local quanta:            18  1 17 18.5+
Error codes:                  465233
Reference codes:              11 7 3 2 2 1.
Flag for line mixing:
Upper statistical weight:     36.0
Lower statistical weight:     38.0
```

Figure 7.5: Absorption line 5/6 that constitutes the NO_2 absorption profile at 3 461.43 nm.

```
Original HITRAN04(R) Database values for the selected spectral line
-------------------------------------------------------------------
Database line:                504948
Molecule number:              10   (NO2)
Isotopologue number:          1    (646)
Natural abundance:            99.16160000%     Molecular weight: 45.99290400 g/mol
Transition frequency:         2888.958697      [cm-1]
Line intensity (S):           5.367e-021       [cm/molecule] @296K
Einstein A-coefficient:       2.871e+001       [s-1]
Air broadened width:          0.0729           [cm-1 atm-1] Half width @ 296K
Self broadened width:         0.0950           [cm-1 atm-1] Half width @ 296K
Lower state energy:           153.8192         [cm-1]
T dependence of air width:    0.73
Pressure shift:               -0.004080        [cm-1 atm-1] @296K
Upper vibrational quanta :              1 0 1
Lower vibrational quanta:               0 0 0
Upper local quanta:            17  1 16 16.5-
Lower local quanta:            18  1 17 17.5-
Error codes:                  465233
Reference codes:              11 7 3 2 2 1.
Flag for line mixing:
Upper statistical weight:     34.0
Lower statistical weight:     36.0
```

Figure 7.6: Absorption line 6/6 that constitutes the NO_2 absorption profile at 3 461.43 nm.

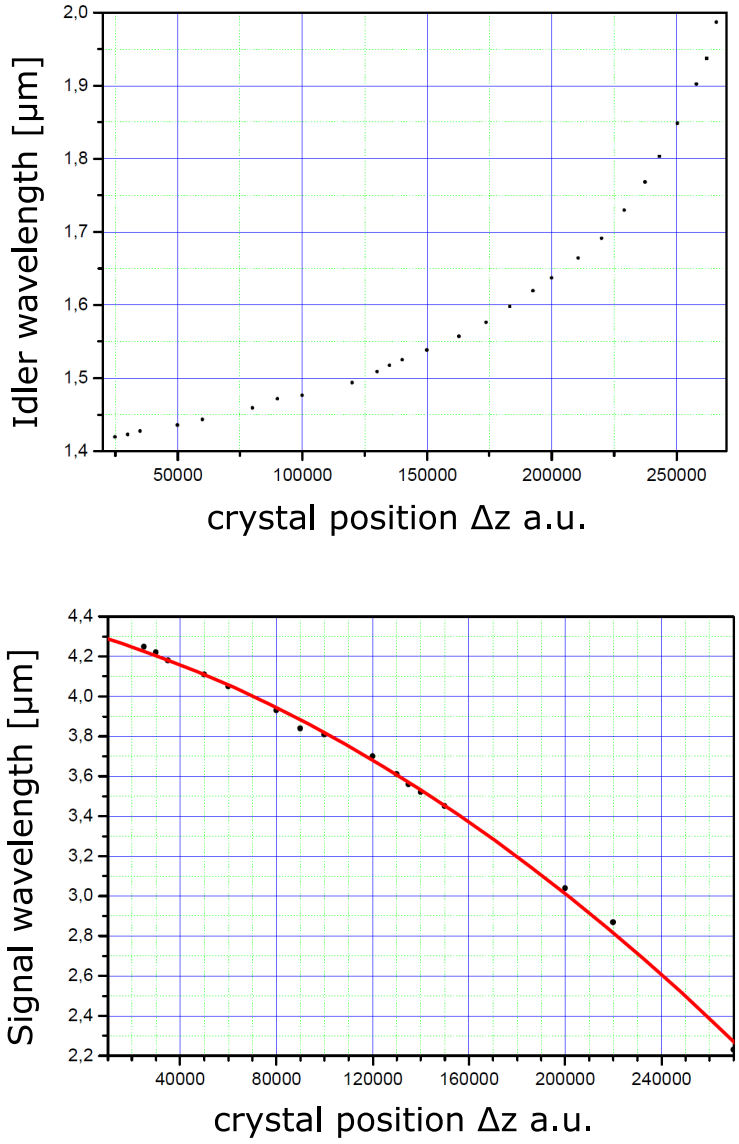

Figure 7.7: Values of z-stage positioning for OPO wavelength adjustment.
⚠ DO NEVER CHANGE Z-STAGE POSITION WHEN PUMP LASER IS ACTIVE

Normalized noise equivalent absorption coefficient (NNEA)

The normalized noise equivalent absorption coefficient (NNEA) [$\mathrm{Wcm^{-1}Hz^{-0.5}}$] is an uniform way to express the performance of a photoacoustic setup. It takes into account*

- ☑ the minimum detectable volume ratio N_i (i.e. the detection limit) for a given signal-to-noise ratio (SNR),
- ☑ the absorption cross-section of the analyte at a given wavelength $\sigma(\lambda)$ [$\mathrm{cm^2}$],
- ☑ the mean power of the light source P_0 [W] and
- ☑ the equivalent noise bandwidth (ENBW) Δf [Hz], which depends on the lock-in time constant as well as on the filter roll-off.

$$\mathrm{NNEA} = \frac{\alpha_\mathrm{min} \cdot P_0}{\sqrt{\Delta f}} = \frac{\rho_{i,\mathrm{min}} \cdot \sigma(\lambda) \cdot P_0}{\mathrm{SNR} \cdot \sqrt{\Delta f}} = \frac{N_{i,\mathrm{min}} \cdot \mathrm{N_A} \cdot \sigma(\lambda) \cdot P_0}{\mathrm{SNR} \cdot \sqrt{\Delta f} \cdot V_\mathrm{mol}} \tag{7.1}$$

Therein the Avogadro constant is $\mathrm{N_A} = 6.022 \cdot 10^{23}$ [$\mathrm{mol^{-1}}$] and the molar volume is defined as $V_\mathrm{mol} = 24.47 \cdot 10^3$ [$\mathrm{cm^3 \cdot mol^{-1}}$] at standard conditions. The SNR is the multiple of the standard deviation that was considered in terms of LOD calculation.† The ENBW either has to be directly measured from the lock-in amplifier or looked up in the manufacturer specifications. For this purpose, figure 7.8 presents the ENBW depending on the lock-in time constant and the filter roll-off with regard to the lock-in amplifier, which was utilized in chapters 4.1, 4.2, 4.3 and 4.5. Figure 7.9 furthers provides a general correlation between ENBW, f_3dB‡ and filter roll-off.
However, it has finally to be noted that NNEA does not imply completely uniform performance characterization, as it does not take into account

- ☐ the period of raw data averaging.

*assuming ideal gas behavior
†If N_i was specified as LOD (1σ), SNR equals 1 in equation 7.1.
‡3 dB cutoff frequency

Time Constant	Equivalent Noise Bandwidth (Hz) at Filter Slope			
	6dB/octave	12dB/octave	18dB/octave	24dB/octave
5 ms	50	37.5	31.25	27.35
10 ms	25	17.2	14.15	12.35
20 ms	12.5	8.3375	6.875	5.9875
50 ms	5	3.335	2.75	2.395
100 ms	2.5	1.6675	1.375	1.1975
200 ms	1.25	0.83375	0.6875	0.59875
500 ms	0.5	0.3335	0.275	0.2395
1 s	0.25	0.16675	0.1375	0.11975
2 s	0.125	0.083375	0.06875	0.059875
5 s	0.05	0.03335	0.0275	0.02395
10 s	0.025	0.016675	0.01375	0.011975

Figure 7.8: ENBW dependency on lock-in time constant and filter roll-off taken from the manufacturer specifications.

Number of poles	Rolloff dB/Decade	Equivalent Noise Bandwidth Δf
1	-20	1.57 f_{3dB}
2	-40	1.22 f_{3dB}
3	-60	1.15 f_{3dB}
4	-80	1.13 f_{3dB}
5	-100	1.11 f_{3dB}

Figure 7.9: ENBW dependency on lock-in time constant, filter roll-off and 3 dB cutoff frequency.

Erklärung

Ich erkläre hiermit an Eides statt, dass ich die vorliegende Arbeit ohne unzulässige Hilfe Dritter und ohne Benutzung anderer als der angegebenen Hilfsmittel angefertigt habe; die aus anderen Quellen direkt oder indirekt übernommenen Daten und Konzepte sind unter Angabe des Literaturzitats gekennzeichnet.

Andere Personen waren an der inhaltlich-materiellen Herstellung der vorliegenden Arbeit nicht beteiligt. Insbesondere habe ich hierfür nicht die entgeltliche Hilfe eines Promotionsberaters oder anderer Personen in Anspruch genommen. Niemand hat von mir weder unmittelbar noch mittelbar geldwerte Leistungen für Arbeiten erhalten, die im Zusammenhang mit dem Inhalt der vorgelegten Dissertation stehen.

Die Arbeit wurde bisher weder im Inland noch im Ausland in gleicher oder ähnlicher Form einer anderen Prüfungsbehörde vorgelegt.

Regensburg, den 28. Juni 2017 Thomas Rück